UNIVERSIDADE DE LISBOA

INSTITUTO SUPERIOR TÉCNICO

Stationary ELM-free H-mode in ASDEX Upgrade

Luís Manuel Cerdeira Gil

Supervisor: Doctor Carlos Alberto Nogueira Garcia da Silva

Co-Supervisor: Doctor Tim Happel

Thesis approved in public session to obtain the PhD Degree in

Technological Physics Engineering

Jury Final Classification: Pass with Distinction and Honour

2021

Obra entregue para apreciação da prova de Doutoramento em Engenharia
Física Tecnológica
para obtenção do grau de Doutor concedido pela
Universidade de Lisboa, no Instituto Superior
Técnico, ao abrigo do D.L. 74/2006/, de 24 de março.

Lisboa, 18 de janeiro de 2021

O presidente do júri

Homologo

UNIVERSIDADE DE LISBOA
INSTITUTO SUPERIOR TÉCNICO

Stationary ELM-free H-mode in ASDEX Upgrade

Luís Manuel Cerdeira Gil

Supervisor: Doctor Carlos Alberto Nogueira Garcia da Silva
Co-Supervisor: Doctor Tim Happel

Thesis approved in public session to obtain the PhD Degree in
Technological Physics Engineering

Jury Final Classification: Pass with Distinction and Honour

Jury

Chairperson:

Luís Paulo da Mota Capitão Lemos Alves, Instituto Superior Técnico, Universidade de Lisboa, Portugal

Members of the Committee:

Amanda Hubbard, Plasma Science and Fusion Center, Massachusetts Institute of Technology, USA

Arne Kallenbach, Max-Planck-Institut für Plasmaphysik, Germany

Bruno Miguel Soares Gonçalves, Instituto Superior Técnico, Universidade de Lisboa, Portugal

Carlos Alberto Nogueira Garcia Silva, Instituto Superior Técnico, Universidade de Lisboa, Portugal

Funding Institution: Fundação para a Ciência e Tecnologia

2021

Acknowledgments

There are several individuals who made this work possible and whose contributions I would like to acknowledge. First and foremost, I thank my supervisor Dr. Carlos Silva for his constant and outstanding support, trust, and availability through these years. I am also grateful to Dr. Tim Happel for taking the role of co-supervisor and providing insight and detailed feedback on the work.

I would like to thank my colleagues from Instituto de Plasmas e Fusão Nuclear for all their help. In particular, António Silva and Jorge Santos for their efforts to keep the reflectometers working in good conditions despite all the adversities and José Vicente for sharing the operation duties. I also thank Luís Guimarãis for doing all of this while overflowing with humor, and for inspiring me to play a positive role within the international fusion community. Diogo Aguiam was helpful in showing more efficient ways to collaborate and Egor Seliunin contributed not only in this setting, but also by balancing the work with fun activities and trips. The rest of my colleagues and friends from APPLAuSE, including my other office mates Pedro Lourenço and André Lopes, also deserve a special thanks for the good moments we spent together, as well as for sharing the pain that comes with every PhD work and thesis.

I am grateful for the opportunity to work as a guest at the Max-Planck-Institut für Plasmaphysik, where I was well received, spent a lot of time and learned so much from so many people. I would like to highlight the patience and dedication of Thomas Pütterich, who was essential in preparing the experiments, and the support of Garrard Conway. I also thank Clemente Angioni, Gregor Birkenmeier, Volodymyr Bobkov, Alex Bock, Nicola Bonanomi, Dominik Brida, Andrés Cathey, Marco Cavedon, Pierre David, Severin Denk, Mike Dunne, Ralph Dux, Michael Faitsch, Rainer Fischer, Michael Griener, Stuart Henderson, Jörg Hobirk, Amanda Hubbard, TJ Jeronimas, Arne Kallenbach, Veronika Klevarová, Peter Manz, Marc Maraschek, Francisco Matos, Rachael McDermott, Pedro Molina, Roman Ochoukov, Ulrike Plank, Dmitrii Prisiazhniuk, François Ryter, Oleg Samoylov, Philip Schneider, Martin Schubert, Davide Silvagni, Karl Stimmel, Jörg Stober, Uli Stroth, Wolfgang Suttrop, Giovanni Tardini, Markus Teschke, Elisée Trier, Branka Vanovac, Eli Viezzer, Germán Vogel, Matthias Willensdorfer, and Elisabeth Wolfrum for all the work, discussions, advice, and good times spent in Germany.

I would also like to thank my friends outside the physics community for all the fun we had and for all the fun we did not have because of my PhD, which they nonetheless understood and encouraged. Above all, I am grateful to my family for the never-ending help and encouragement.

Special thanks to my mother and father for their unconditional support and to my brothers for keeping my spirits up and making me laugh even in the most stressful moments.

Lastly, I would like to acknowledge the financial support from Fundação para a Ciência e a Tecnologia through grant PD/BD/114326/2016 in the framework of the Advanced Program in Plasma Science and Engineering (APPLAuSE) at Instituto Superior Técnico.

Resumo

Um modo H estacionário sem modos localizados na periferia (ELMs) foi demonstrado com sucesso no tokamak ASDEX Upgrade (AUG) com acentuado aquecimento ressonante ciclotrónico dos eletrões. Obtém-se com um nível de deutério adequado e potência de aquecimento acima da transição L-H, mas abaixo do limiar dos ELMs. O regime é identificado como o modo H EDA e a sua capacidade de manter um pedestal estacionário sem ELMs deve-se provavelmente a instabilidades periféricas benignas, incluindo um modo quasi-coerente eletromagnético que parece responsável por um aumento de transporte.

Várias medidas foram tomadas para melhorar o desempenho do regime e a sua relevância para reatores. Moldar fortemente o plasma permite que a ausência de ELMs seja mantida com mais aquecimento, levando a um aumento de temperatura e pressão. A maior potência requer uma melhor dissipação de calor, que foi conseguida com dopagem de azoto. Este aumenta a radiação no diversor, baixando significativamente o fluxo de calor para as placas, sem degradar o confinamento no centro do plasma nem diluir consideravelmente o combustível. Dopagem de árgon provou ser eficaz no arrefecimento radiativo do pedestal, com impacto reduzido no centro do plasma, baixando a temperatura do diversor e ao mesmo tempo estendendo a janela de potência sem ELMs.

O modo H EDA no AUG possui várias características desejáveis para reatores futuros, tais como bom confinamento energético, alta densidade, baixo teor de impurezas, compatibilidade com paredes de tungsténio e dopagem de impurezas, possibilidade de acesso a baixo torque e potência, com aquecimento predominantemente eletrónico, sem necessidade de boronização recente e sem acumulação de impurezas, apesar de não ter ELMs. Isto constitui um conjunto único de características pela primeira vez atingidas em simultâneo num dispositivo de fusão.

Variações de parâmetros em modos H EDA mostraram que um nível mínimo de combustível é necessário para aceder ao regime. Aumentar mais o nível de gás leva a um pequeno aumento da densidade e diminuição do confinamento energético, mas permite a aplicação de maior aquecimento. Aumentar a corrente de plasma também estende a janela de potência sem ELMs e aumenta a densidade sem degradar o confinamento, subindo o produto triplo alcançável. Em termos de parâmetros adimensionais, o modo H EDA até agora só foi explorado a alto fator de segurança e colisionalidade. Contudo, distingue-se noutros parâmetros, apresentando baixa carga iónica efetiva e alto fator de melhoria de confinamento, pressão normalizada e fração de Greenwald. Tendo em conta as suas inúmeras vantagens, o modo H EDA merece continuar a ser desenvolvido e estudado em máquinas atuais e esperadas, com o objetivo final de avaliar com segurança a sua compatibilidade com reatores futuros.

Palavras-chave: Fusão Nuclear, Tokamak, sem ELMs, modo H, ASDEX Upgrade

Abstract

A stationary H-mode without edge localized modes (ELMs) has been successfully demonstrated in the ASDEX Upgrade (AUG) tokamak with significant electron cyclotron resonance heating. It is obtained via adequate fueling and heating power above the L-H transition, but below the ELM threshold. The regime is identified as the EDA H-mode and its ability to maintain a steady-state pedestal without ELMs is likely due to benign edge instabilities, including an ubiquitous electromagnetic quasi-coherent mode that appears to drive enhanced transport.

Several measures have been taken to improve the performance and reactor relevance of this regime. With strong shaping, it can be accessed within a wider ELM-free power window, allowing the achievement of higher temperature and pressure. The higher heating power calls for a better exhaust that was accomplished by nitrogen seeding. This increases divertor radiation, leading to much lower target heat fluxes without degrading core confinement nor significantly diluting the fuel. Furthermore, argon seeding proved effective in radiatively cooling the pedestal with minimal core impact, simultaneously lowering divertor temperature and extending the ELM-free power window.

The EDA H-mode in AUG features several desirable properties for future reactors, such as good energy confinement, high density, low impurity content, compatibility with tungsten walls and extrinsic impurity seeding, possibility of access at low input torque and power, with dominant electron heating, no need for a fresh boronization, and no impurity accumulation despite the absence of ELMs. This constitutes a unique set of characteristics simultaneously achieved for the first time in a fusion device.

Parameter scans in EDA H-modes showed that a minimum fueling level is required to access the regime. Further increasing the gas puff leads to a small density increase and slight reduction in energy confinement, but allows the application of more power. Increasing plasma current also extends the ELM-free power window and raises density without degrading confinement, increasing the achievable triple product. In terms of dimensionless quantities, the EDA H-mode in AUG has so far only been explored at high safety factor and collisionality. However, it performs quite well in other parameters, exhibiting a low effective ion charge and high confinement enhancement factor, Troyon-normalized pressure and Greenwald fraction. Considering its many advantages, the EDA H-mode is worth further developing and studying in current and upcoming devices, with the ultimate goal of reliably assessing its compatibility with future reactors.

Keywords: Nuclear fusion, Tokamak, ELM-free, H-mode, ASDEX Upgrade

Contents

List of Tables

List of Figures

Symbols

a Horizontal minor radius of the plasma, defined as $(R_{\mathrm{max}} - R_{\mathrm{min}})/2$

B Magnetic field

b Vertical minor radius of the plasma, defined as $(Z_{\mathrm{max}} - Z_{\mathrm{min}})/2$

β Ratio of the plasma pressure to the magnetic pressure

β_{N} Troyon-normalized ratio of the plasma pressure to the magnetic pressure

β_{p} Ratio of the plasma pressure to the poloidal magnetic pressure

B_{p} Poloidal magnetic field

B_{ϕ} Toroidal magnetic field

B_{t} Vacuum toroidal magnetic field at the plasma center

c_{N} Nitrogen concentration

c_{W} Tungsten concentration

δ Plasma triangularity

δ_{avg} Average triangularity of the plasma, defined as $\left(\delta_{\mathrm{low}} + \delta_{\mathrm{up}}\right)/2$

Δf Frequency width

δ_{low} Lower triangularity of the plasma, defined as $\left(R_{\mathrm{geo}} - R_{\mathrm{low}}\right)/a$

$\Delta_{\mathrm{ped},n_{\mathrm{e}}}$ Width of the electron density pedestal

$\Delta_{\mathrm{ped},T_{\mathrm{e}}}$ Width of the electron temperature pedestal

$\Delta\rho_{\mathrm{pol}_{\mathrm{sep}}}$ ρ_{pol} distance between the separatrixes of the lower and upper X-points

ΔR_{sep} Radial distance between the separatrixes of the lower and upper X-points at the outer midplane

δ_{up} Upper triangularity of the plasma, defined as $\left(R_{\mathrm{geo}} - R_{\mathrm{up}}\right)/a$

ΔZ_{eff} Variation of Z_{eff}due to impurities

E Electric field

e Elementary charge

e^- Electron

ε Inverse aspect ratio of the plasma, defined as a/R_{geo}

E_{r} Radial electric field

f Frequency

f_{ce} Eletron cyclotron frequency

f_{GW} Greenwald fraction

Γ_{D} Deuterium gas puff

q Heat flux density

$H_{98\mathrm{y}2}$ Confinement enhancement factor

I_{p} Plasma current

j_{sat} Ion saturation current density

κ Elongation of the plasma, defined as b/a

$k_{\perp}$ Perpendicular wavenumber

k_{θ} Poloidal wavenumber

l Electron cyclotron harmonic number

λ_q scrape-off layer (SOL) power decay length

$\ln\Lambda_e$ Coulomb logarithm

M Average ion mass

m_e Electron mass

μ_0 Vacuum magnetic permeability

n Toroidal mode number

N_a Density of ion a

n_{co} Cutoff density

n_e Electron density

$\overline{n_e}$ Line-averaged electron density

n_{GW} Greenwald density

ν Collision frequency

ν_e^* Normalized electron collisionality

ν^* Normalized collisionality

n_W Tungsten density

p Pressure

$\overline{p}$ Volume average pressure

p_e Electron pressure

P_{ECRH} Electron cyclotron resonance heating power

P_f Total fusion power

$P_{heat,ext}$ External heating power

ϕ Toroidal angle coordinate

P_{LH} Power threshold for the L-H transition

P_{rad} Radiated power

$P_{\mathrm{rad,div}}$ Power radiated in the divertor

$P_{\mathrm{rad,main}}$ Power radiated in the main chamber

$P_{\mathrm{rad,sep}}$ Power radiated within the separatrix

P_{tot} Total power lost by the plasma

Q Fusion gain, defined as the ratio of fusion power to auxilliary heating power

q Safety factor

q_{cyl} Cylindrical safety factor

Q_{E} Engineering gain factor, defined as the ratio of net output electric power to input electric power in a power plant

q_{95} Safety factor at $\rho_{\mathrm{pol}} = 0.95$

R Cylindrical radial coordinate

R_{geo} Geometric major radius of the plasma, defined as $(R_{\mathrm{max}} + R_{\mathrm{min}})/2$

ρ_{pol} Normalized poloidal flux radius

ρ_{s} Mixed Larmor radius, computed with the electron temperature and ion mass

ρ^* Normalized Larmor radius

R_{low} R of the vertically lowest point of the separatrix

R_{max} Maximum value of R along the separatrix

R_{min} Minimum value of R along the separatrix

R_{up} R of the vertically highest point of the separatrix

R_0 Plasma major radius

T Temperature

τ_{E} Energy confinement time

$\tau_{\mathrm{E,IPB98(y,2)}}$ Energy confinement time scaling IPB98(y,2)

τ_{eq} Temperature equilibration time

T_{div} Proxy for the divertor temperature, estimated from shunt current measurements

T_{e} Electron temperature

$T_{\mathrm{e,sep}}$ Electron temperature at the separatrix

θ Poloidal angle coordinate

T_{i} Ion temperature

V Plasma volume

$v_{\perp}$ Perpendicular velocity

ω_{b} Banana bounce frequency

ω_{ce} Angular electron cyclotron frequency

W_{MHD} Plasma stored energy

ω_{pe} Angular plasma frequency

Z Height coordinate

Z_a Charge number of ion a

Z_{eff} Effective ion charge

Z_{max} Maximum value of Z along the separatrix

Z_{min} Minimum value of Z along the separatrix

Acronyms

AUG ASDEX Upgrade

AXUV absolute extended ultraviolet

CHICA charge exchange impurity concentration analysis

CX charge exchange

CXRS charge exchange recombination spectroscopy

DCN deuterium cyanide

DCS discharge control system

DN double null

ECCD electron cyclotron current drive

ECE electron cyclotron emission

ECM edge coherent mode

ECRH electron cyclotron resonance heating

EHO edge harmonic oscillation

ELM edge localized mode

ETB edge transport barrier

FMCW frequency-modulated continuous-wave

FWHM full width at half maximum

GAM geodesic acoustic mode

HFS high-field side

HFSHD high-field side high density front

HRS high recycling steady

ICRF ion cyclotron range of frequencies

ICRH ion cyclotron resonance heating

IDA integrated data analysis

IR infrared

JET Joint European Torus

LFS low-field side

LHCD lower hybrid current drive

LHW lower hybrid wave

Li-BES lithium beam emission spectroscopy

LP Langmuir probe

LSN lower single null

MHD magnetohydrodynamic

MSE motional Stark effect

NBI neutral beam injection

NTM neoclassical tearing mode

P-B peeling-ballooning

PCR poloidal correlation reflectometry

PFC plasma facing component

PSL passive stabilization loop

QCE quasi-continuous exhaust

QCM quasi-coherent mode

QH-mode quiescent H-mode

RMP resonant magnetic perturbation

SOL scrape-off layer

TCV Tokamak à Configuration Variable

TS Thomson scattering

USN upper single null

VUV vacuum ultraviolet

WCM weakly coherent mode

Chapter 1

Introduction

1.1 Fusion power

1.1.1 World energy and climate situation

The current world population has reached almost 8 billion and is still growing, albeit at a slowing pace since 1965-1970. Nonetheless, this increase is projected to continue throughout the century, with the population peaking around 11 billion in 2100 [1]. Rapid population growth presents challenges for sustainable development, putting pressure on already strained resources.

One of such resources is primary energy, which forms the basis for a great part of human activity, owing to the high standard of living in the present day. The world energy consumption over the last 25 years is shown in figure 1.1, evidencing a concerning situation. There has been an in increase in total consumption of over 60 % which is not expected to slow down in the near future. Besides this, fossil fuels (oil, coal and natural gas) are the dominant sources, representing a combined share of more than 80 % [2].

A major problem of fossil fuels is that their reserves are quite limited, as shown by the low reserves-to-production ratio of table 1.1. This ratio is computed using the proved reserves and the production data of the same year, representing the duration of a resource if no new reserves were found and its production were to remain constant until full depletion. The proved reserves are generally taken to be those quantities that geological and engineering information indicates with reasonable certainty can be recovered in the future from known reservoirs under existing economic and operating conditions. Even though new reserves are being found and new technologies are unlocking previously unproven reserves, energy demand is also increasing, so

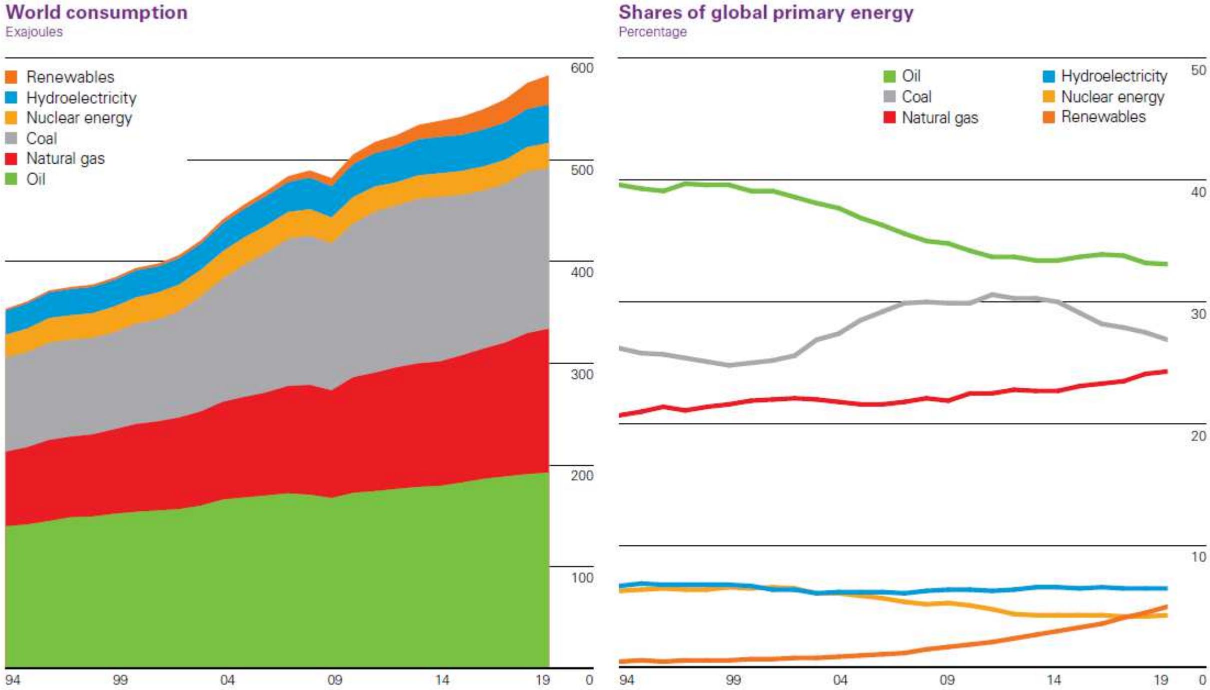

Figure 1.1: World primary energy consumption by source as a function of time, from 1994 to 2019: (left) absolute consumption in EJ, (right) relative share by source in %. Figure taken from [2].

Resource	Reserves / production (years)
Natural Gas	49.8
Oil	49.9
Coal	132

Table 1.1: Reserves-to-production ratio of natural gas, oil, and coal at the end of 2019. Data taken from [2].

the low reserves-to-production ratios constitute a concerning situation indeed.

Fossil fuels also pose serious pollution problems and are one of the main driving forces of climate change nowadays, due to emission of greenhouse gases [3, 4]. Figure 1.2 shows the evolution of global temperature spanning more than a century, where a strong increase over many decades is seen. Warming of the climate system is unequivocal and, since the 1950s, many of the observed changes and extreme events have broken longstanding records [3].

Direct measurements of atmospheric carbon dioxide, the main greenhouse gas contributing to global warming, have been made for a long time, as shown in figure 1.3. Its concentration has been raising at an ever-growing rate since the direct measurements began. Anthropogenic greenhouse gas emissions have increased so much since the pre-industrial era, that the concentrations of carbon dioxide, methane, and nitrous oxide are unprecedented in at least the last 800 000

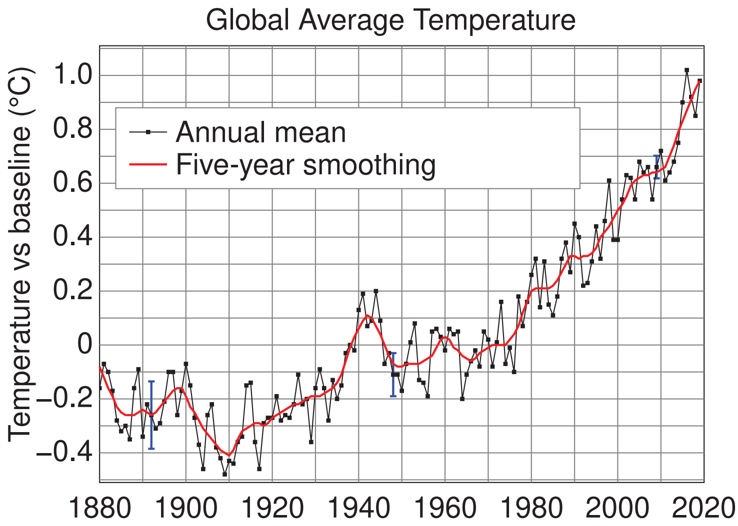

Figure 1.2: Land-ocean temperature temperature anomaly with respect to base period 1951-1980 as a function of time, from 1880 to 2019. The solid black line is the global annual mean and the solid red line is a five-year smooth. The blue bars represent the total annual uncertainty at a 95 % confidence interval [5]. Figure taken from [6].

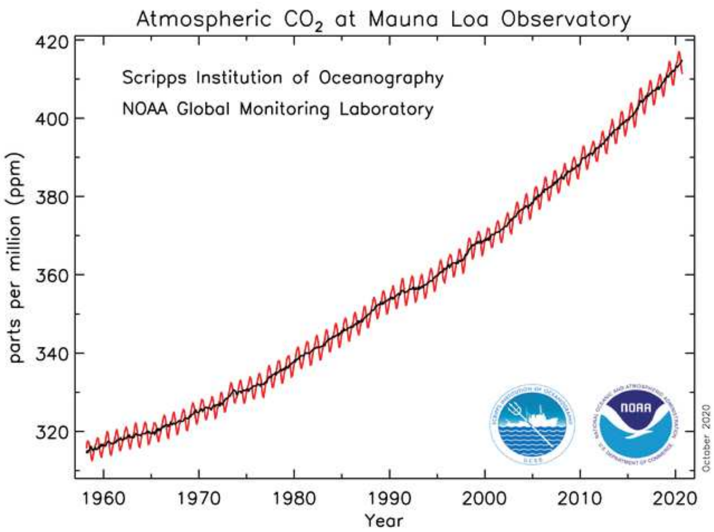

Figure 1.3: Atmospheric concentration of carbon dioxide as a function of time, measured at Mauna Loa Observatory, Hawaii. The red line represents the raw monthly mean values, whereas the black line has been corrected for the average seasonal cycle. Figure taken from [8].

years, whose levels are known from indirect ice core measurements [7].

Recent climate changes have had widespread impacts on human and natural systems across all continents and oceans. Continued emission of greenhouse gases will cause further warming and long-lasting effects in the climate system, leading to severe, pervasive and irreversible impacts for mankind. Limiting climate change and its risks will require substantial and sustained reductions in greenhouse gas emissions, which poses major technological, economic and social challenges [3].

The main energy sources besides fossil fuels are currently nuclear fission, hydroelectricity, and other renewables (solar and wind), as previously shown in figure 1.1. While being clean in terms of greenhouse gas emissions, each of these sources has its own problems [9]. Nuclear fission raises safety questions, has limited reserves, produces radioactive waste and may lead to nuclear proliferation. The main downside to hydroelectric power is that most of the suitable rivers already have dams, so its expansion is very limited. Solar and wind power do not suffer from any of these issues and are in fact the fastest growing energy sources, most likely playing a major role in the energy mix of the future. However, they still have a combined share of less than 10 % of global energy production and are subject to weather fluctuations which preclude the production of base load power. This limitation is exacerbated as the renewables' share of power generation increases. Furthermore, they require a very large area to produce a significant amount of power when compared to the other sources.

1.1.2 Nuclear fusion and tokamaks

A promising candidate to help solve the world energy problems is nuclear fusion. This process, which powers the sun and all other stars, consists in the merging of light elements into heavier ones, resulting in energy release. If mastered on Earth, nuclear fusion could provide a safe energy source with abundant reserves and low environmental impact [9]. However there are difficult scientific and technological challenges that must be surpassed before fusion power becomes a reality.

The main reaction of interest for energy production is the fusion of a deuterium nucleus (D) with a tritium nucleus (T), originating an energetic neutron (n) and a helium nucleus (α), written as

$$\mathrm{D} + \mathrm{T} \rightarrow \alpha\,(3.5\,\mathrm{MeV}) + \mathrm{n}\,(14.1\,\mathrm{MeV})\ . \tag{1.1}$$

Deuterium is a hydrogen isotope which exists naturally in ocean water and can be easily extracted at a low cost. If all the deuterium in the ocean was used to power fusion reactors using a standard steam cycle there would be enough energy generated to power the earth for about 2 billion years at the present rate of total world energy consumption [9]. Tritium however is a radioactive isotope of hydrogen with a half-life of about 12 years, so it is not found naturally and must be obtained by breeding with a lithium isotope whose reserves would last at least 20 000 years at the present energy consumption rate.

Another advantage is that fusion reactions produce no greenhouse gases and do not emit other harmful chemicals to the atmosphere. The only environmental issue of fusion is that the produced high energy neutrons can activate structural material, which becomes radioactive with a half-life on the order of 100 years. This is still much better than the multi-thousand year wastes originated by nuclear fission.

The last major advantage of fusion involves safety. In contrast with a fission reactor, where the entire energy content corresponding to several years of power production is in the core at any instant of time, a fusion reactor requires a very small instantaneous mass of fuel that is constantly fed at a low rate allowing it to be consumed as needed. This renders major accidents like those which have occurred with fission reactors impossible in a fusion reactor.

The problem with nuclear fusion is that nuclei are positively charged, so the repulsive electrostatic force between them must be overcome for the reactions to occur. This means the colliding particles must have an enormous amount of energy. Specifically, to burn D–T one is required to heat the fuel to the astounding temperature of 150 million degrees Celsius, hotter than the center of the sun. At these temperatures the fuel is fully ionized, becoming a collection of moving electrons and ions dominated by electromagnetic forces, which is called a plasma.

Ordinary material walls cannot hold by themselves such hot plasmas, so a clever idea is to also use magnetic fields to confine the plasma. In a uniform magnetic field charged particles are confined in the direction perpendicular to the magnetic field, describing helical trajectories. The parallel direction is however completely free. A possible method of magnetic confinement is to bend the magnetic field into a toroidal geometry, thereby confining the parallel direction by periodicity.

The most successful magnetic configuration so far is a toroidal confinement system called tokamak [10], represented schematically in figure 1.4. In a tokamak the principal magnetic field is the toroidal field created by external coils. However, this field alone does not allow confinement of the plasma and a poloidal field is necessary. In a tokamak this field is produced mainly by an electric current flowing in the toroidal direction in the plasma itself. This current is induced by transformer action in which the primary winding is in the center of the device and the plasma acts as the secondary winding.

In order to control the plasma-wall interaction, tokamaks preferentially use a magnetic configuration known as divertor [12], in which the field lines are directed to special target plates

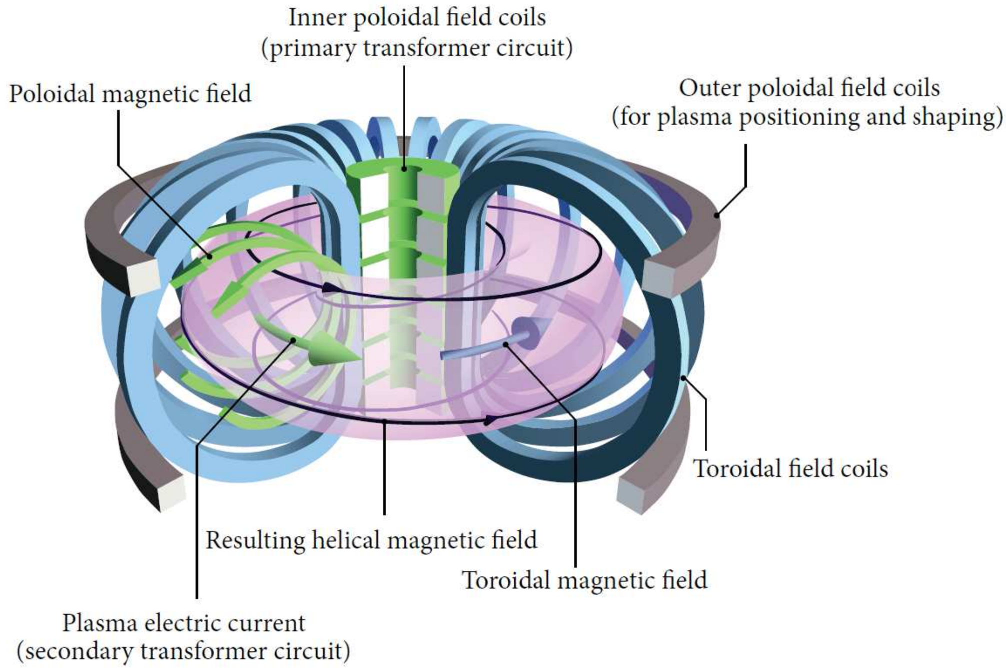

Figure 1.4: Schematic representation of a tokamak. Figure taken from [11].

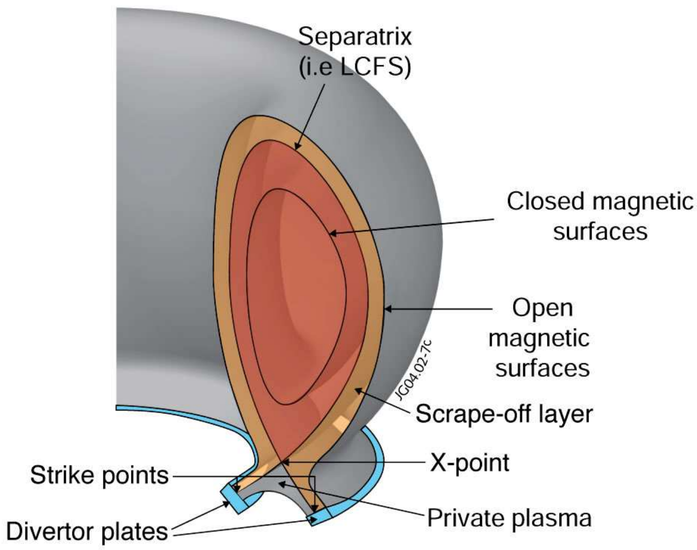

Figure 1.5: Schematic diagram of a magnetic divertor. Figure taken from [13].

far from the core plasma, as shown in figure 1.5. This allows a more efficient exhaust of reaction products, minimizes the influx of impurities from the wall to the plasma, and leads to improved performance.

But even with proper magnetic confinement and use of a divertor, there is always a continuous loss of energy in a fusion device, under the form of radiation and plasma transport, which has to be replenished by external or α-particle heating. The total power lost by the plasma, P_{tot}, is characterized by an energy confinement time, τ_{E}, defined by the relation

$$P_{\mathrm{tot}} = \frac{W_{\mathrm{MHD}}}{\tau_{\mathrm{E}}}, \tag{1.2}$$

where W_{MHD} is the plasma stored energy. Understanding and controlling energy confinement in tokamaks is fundamental to achieve efficient fusion power production.

1.1.3 H-mode and edge localized modes

In the absence of instabilities, transport of particles and energy in a toroidally symmetric tokamak plasma would be determined by Coulomb collisions and described by neoclassical theory [14, 15]. However, the experimentally measured losses do not agree with the calculated values, often exceeded by an order of magnitude or more [16]. This anomalous transport is caused by turbulence driven by instabilities and exhibits a significant degradation of energy confinement time with temperature [17], constituting one of the main obstacles in achieving the conditions for a desirable fusion reactor.

It was found, however, that a discontinuous improvement in confinement often occurs as the heating power is increased. This regime of higher confinement is called the H-mode and the previous lower level is called the L-mode. The H-mode was discovered in 1982 on the ASDEX tokamak [18], one of a small number of devices operating with an axisymmetric poloidal field divertor and strong additional heating by neutral beam injection (NBI) at the time. An example of an early H-mode is shown in figure 1.6, where the confinement improvement is evidenced by the much higher density when compared to a similar L-mode discharge.

The importance of the H-mode was recognized from the beginning, driving developments on devices across the world and leading to great accomplishments in the quest for fusion energy [19, 20]. For example, the highest ever controlled fusion power (16.1 MW) was achieved in the Joint European Torus (JET) tokamak using a mixture of deuterium and tritium in H-mode [21].

The physics of the L-H transition and confinement enhancement is not yet fully understood [22], but some characteristics are common to every H-mode. Its main defining feature is the development of an edge transport barrier, a region of reduced particle and energy losses just inside the separatrix [23], linked to a radial electric field well and flow shear [24–26] which suppress turbulence [27]. The reduced transport results in a sharp edge pressure gradient, as illustrated in figure 1.7(a), explaining why this region of the plasma is also referred to as the

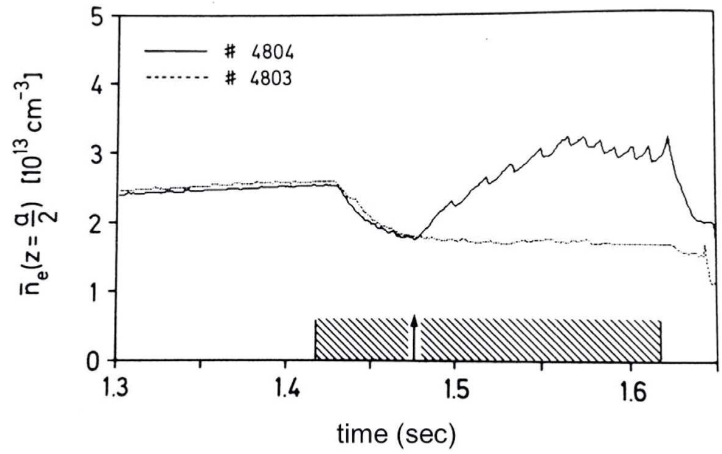

Figure 1.6: Time evolution of the line-averaged density in H-mode (solid) and L-mode (dashed) discharges with NBI in ASDEX. Figure taken from [19].

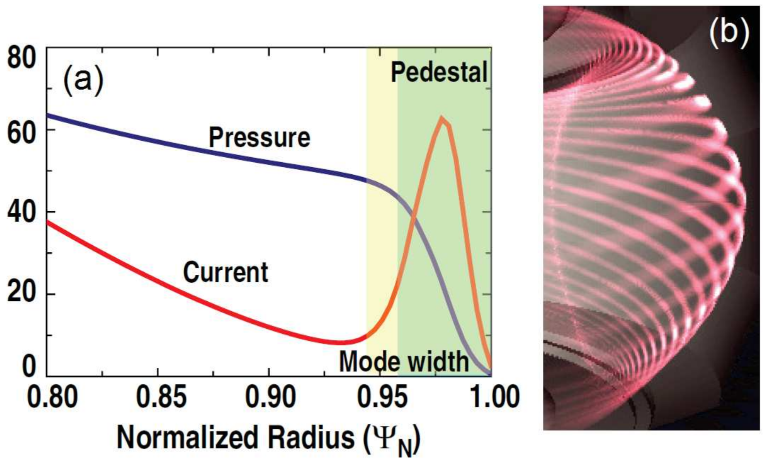

Figure 1.7: (a) Illustration of typical H-mode pressure and current profiles with the edge barrier or pedestal region dark shaded, and the P-B mode width (light shaded) extending across and beyond the pedestal. (b) Calculated 3D structure of an $n = 18$ P-B mode in the DIII-D tokamak. Figure adapted from [29].

pedestal [28].

The discovery of H-mode confinement represents a major improvement in tokamak operation, but also has some disadvantages. The strong pedestal gradients can excite localized instabilities in edge of the plasma, which cause a sudden relaxation of density and temperature, along with large heat and particle fluxes to plasma facing components (PFCs) [30]. These are known as ELMs [31–35]. ELMs act qualitatively as a pressure relief valve. When the edge pressure gradient becomes too high, ELM bursts occur, expelling plasma from the confined region to the SOL and divertor, thereby relieving the excess pressure.

Different types of ELMs exist [31, 33], as exemplified in figure 1.8. Type I ELMs are the largest and occur with high heating power. Their frequency of occurrence increases with power,

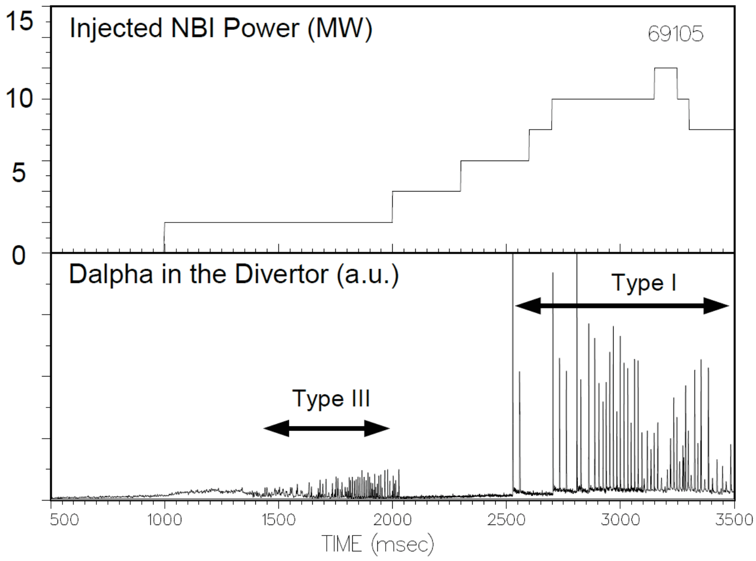

Figure 1.8: Typical sequence of ELMs, indicated by spikes in the Balmer alpha radiation (bottom panel), during a power ramp (upper panel) in DIII-D. At low power, close to P_{LH}, type III ELMs are found, whereas at higher power type I ELMs occur. Figure taken from [31].

typically ranging from a few dozen to a few hundred Hz. Type I ELMs pose a serious threat to PFCs when extrapolated to future large-scale devices, due to the unacceptably high heat loads on the divertor [36–38]. They are the manifestation of peeling-ballooning (P-B) modes [39, 40], magnetohydrodynamic (MHD) instabilities driven by the strong pedestal pressure gradient and resulting bootstrap current. Evidence for this picture include the fact that no device has been able to operate above the P-B instability threshold and numerous observations of ELMs which are triggered when the threshold is achieved [41]. An example of a calculated radial extent and 3D structure of a P-B mode is shown in figure 1.7.

Type III ELMs are much smaller and happen when the heating power is very close to the L-H power threshold, P_{LH}. Their frequency decreases with the applied power, although the amplitude may increase. In fact, at low heating power, type III ELMs are mostly indistinguishable from an edge phenomenon known as I-phase [42, 43], in which a complex interaction between turbulence and flows causes a pulsating behavior at typical frequencies of a couple kHz. At even lower power, plasmas can alternate between L-mode and I-phase. These regimes were originally known as dithering cycles and dithering H-mode [44, 45].

Between type III and type I ELMs there is usually a nonstationary ELM-free H-mode phase, visible in the bottom panel of figure 1.8. Traditional ELM-free H-modes tend to accumulate impurities due to the very high particle confinement time which is not counterbalanced by ELM-induced transport. This means that ELMs actually have a beneficial effect in terms of flushing impurities and helium ash out of the plasma. Fusion devices are therefore faced with the paradoxical challenge of operating in a way that avoids large heat loads to the divertor, ideally without ELMs, while at the same time keeping the plasma stationary and reasonably pure, which tends to require ELMs. This tradeoff is especially concerning in machines with high-Z wall materials, such as tungsten [46, 47], in which even a small amount of impurities can have a major impact in degrading core plasma performance and terminating discharges due to high radiative losses.

1.2 Requirements for a reactor scenario

1.2.1 General considerations

The ultimate goal of a fusion reactor is to leverage nuclear fusion to produce more power than it consumes. If adequate confinement conditions are provided, a state can be reached where the plasma energy is maintained against the losses solely by α-particle heating. This point is called ignition and the critical quantity to achieve it can be expressed as the product of the plasma pressure, p, by the energy confinement time, which must satisfy the Lawson criterion [48]. The critical ignition value depends on the temperature, T, and its minimum conditions are given by [9]

$$T_{\text{min}} = 15\,\text{keV}\,, \tag{1.3a}$$

$$(p\tau_{\text{E}})_{\text{min}} = 8.3\,\text{atm}\,\text{s}\,. \tag{1.3b}$$

Although an ignited plasma has the desirable feature that no externally applied heating is necessary, it is possible to reduce the requirements on $p\tau_{\text{E}}$ by using external power, thus turning the reactor into a power amplifier. The fusion gain of the plasma, Q, can be defined as

$$Q = \frac{P_{\text{f}}}{P_{\text{heat,ext}}}\,, \tag{1.4}$$

where P_{f} is the total fusion power, including alphas and neutrons, and $P_{\text{heat,ext}}$ is the external heating power. While Q constitutes a reasonable figure of merit from the physics point of view, the end goal of a reactor in practice is to produce electricity, which motivates the definition of an

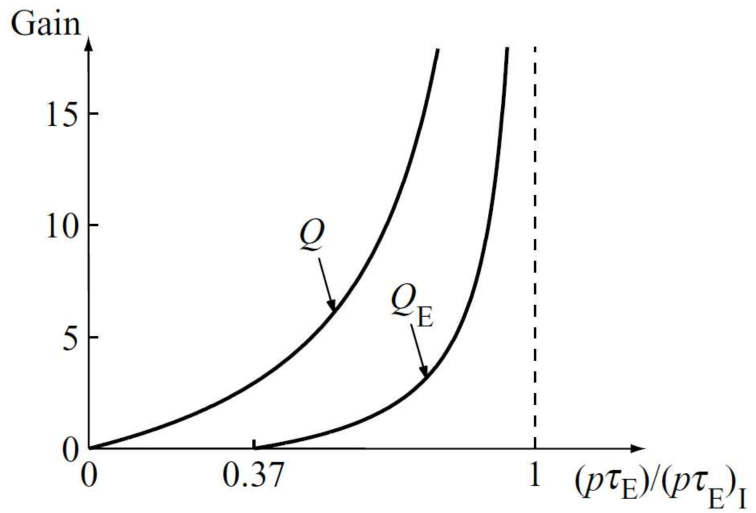

Figure 1.9: Physics gain factor Q and engineering gain factor Q_E as a function of proximity to ignition, expressed by the ratio of $p\tau_E$ in a given state to its required value for ignition. Figure taken from [9].

engineering gain factor:

$$Q_E = \frac{\text{net electric power out}}{\text{electric power in}}\,. \tag{1.5}$$

Q_E is always lower than Q because, regardless of the adopted methods, there are intrinsic and technical inefficiencies in every process of a power plant. This applies to both the conversion of electric power to plasma heating and also to the generation of electricity from fusion power. Using typical efficiencies of present-day technologies, the fusion engineering gain, Q_E can be estimated as a function of proximity to ignition, as illustrated in figure 1.9, together with Q. Electric power break-even, corresponding to $Q_E = 0$, requires $Q \approx 3$, and $Q = 10$ corresponds to $Q_E \approx 2$. While this would be enough to demonstrate nuclear fusion as a technically feasible method of energy production, the large capital investments will likely require even higher gain factors for economic viability. Therefore, plasma scenarios should aim to come as close as possible to ignition, since too much external power significantly degrades the overall gain of the reactor.

1.2.2 Main plasma

In general, increasing $p\tau_E$ requires an increase in the size of the device and/or magnetic field [49], both of which lead to an increase in the capital cost of a reactor. In present-day machines, the necessary absolute values are simply not attainable. This motivates the use of scaled parameters and figures of merit that allow an evaluation of the performance of plasma scenarios independently of design constraints of the devices. Some of these are empirical, whereas others are the result of dimensionless parameter scaling techniques [50], but both types are useful to extrapolate current knowledge to future devices. A set of definitions and conditions which should be achieved not only in large-scale reactors, but also in plasma scenarios of present-day tokamaks is given below.

Energy confinement

Energy confinement time is a critical component of $p\tau_{\mathrm{E}}$, but is incredibly hard to predict from first principles, mainly due to the complex physics of turbulent plasma transport. One of the most widely used empirical scalings for τ_{E}, derived from a multi-machine ELMy H-mode database, is given by [51]

$$\tau_{\mathrm{E,IPB98(y,2)}} = 0.0562 {I_{\mathrm{p}}}^{0.93} {B_{\mathrm{t}}}^{0.15} {P_{\mathrm{tot}}}^{-0.69} {\overline{n_{\mathrm{e}}}}^{0.41} M^{0.19} {R_{\mathrm{geo}}}^{1.97} \varepsilon^{0.58} \kappa^{0.78}, \tag{1.6}$$

where I_{p} is the plasma current in MA, B_{t} is the toroidal magnetic field in T, P_{tot} is the total power lost by the plasma in MW, $\overline{n_{\mathrm{e}}}$ is the line-averaged density in $10^{19}\ \mathrm{m}^{-3}$, M is the average ion mass in u, R_{geo} is the major radius in m, ε is the inverse aspect ratio, and κ is the elongation. Using this scaling to normalize the experimental energy confinement time τ_{E}, the following confinement enhancement factor can be defined:

$$H_{98\mathrm{y}2} = \frac{\tau_{\mathrm{E}}}{\tau_{\mathrm{E,IPB98(y,2)}}}. \tag{1.7}$$

The higher $H_{98\mathrm{y}2}$ is, the better. L-modes usually have $H_{98\mathrm{y}2} < 1$, and reactor scenarios are typically assumed to have $H_{98\mathrm{y}2} \geq 1$.

Pressure

The other main component of $p\tau_{\mathrm{E}}$ is the plasma pressure, which can be normalized to the magnetic pressure as follows:

$$\beta = \frac{p}{B^2/2\mu_0}, \tag{1.8}$$

where B is the magnetic field and μ_0 is the vacuum magnetic permeability. β is a measure of the efficiency with which the magnetic field confines the plasma. High β is desirable for economic power balance in a reactor but is difficult to achieve experimentally because of various plasma instabilities. Extensive ideal MHD numerical studies have shown that stability against external and internal kink modes, ballooning modes, localized modes, etc. requires β to be lower than a critical value known as Troyon limit [52, 53], that is approximately proportional to $I_\mathrm{p}/(aB_\mathrm{t})$, where a is the plasma minor radius. This leads to the following definition of the Troyon-normalized beta:

$$\beta_\mathrm{N} = 100\beta \frac{aB_\mathrm{t}}{I_\mathrm{p}}\,, \tag{1.9}$$

with a in m, B_t in T, and I_p in MA. The numerical factor causes β_N to be of order unity in tokamaks. In general, the exact β_N limit depends on several factors, such as the plasma shape (elongation, triangularity, etc.) and peakedness of pressure and current profiles. In practical terms, tokamak operation is usually limited to $\beta_\mathrm{N} \leq 3$ or even lower, if resistive instabilities like neoclassical tearing modes (NTMs) are considered.

Density

The fusion reaction rate is proportional to the square of plasma density, but has a nonmonotonic dependence on temperature [54]. Therefore, plasma pressure must not be arbitrarily partitioned between density and temperature if fusion power is to be maximized. However, there are limits to the density range over which magnetic confinement experiments can operate [55]. More specifically, when the edge density becomes too high, the plasma suffers a disruption, usually associated with a radiation collapse. A complete first principles understanding of the phenomenon does not exist yet, but an empirical limit for the line-averaged density of tokamaks known as the Greenwald density was determined from the analysis of a large volume of data and is given by [56]

$$n_\mathrm{GW} = \frac{I_\mathrm{p}}{\pi a^2}\,, \tag{1.10}$$

where n_GW is in $10^{20}\,\mathrm{m}^{-3}$, I_p in MA, and a in m. This can be used to normalize the plasma density, giving rise to the Greenwald fraction, defined as

$$f_\mathrm{GW} = \frac{\overline{n_\mathrm{e}}}{n_\mathrm{GW}}\,. \tag{1.11}$$

Reactor design studies show that the optimum density for fusion power production lies well above the Greenwald limit [49, 57], which is difficult to achieve experimentally. In practice, reactor scenarios are assumed to have f_GW around 1.

Temperature

The other component of pressure is temperature, which can be expressed by the related nondimensional plasma collisionality, generally defined as

$$\nu^* = \frac{\nu}{\varepsilon \omega_\mathrm{b}} , \tag{1.12}$$

where ν is the collision frequency and ω_b is the bounce frequency of trapped particles. Since a fusion plasma is composed by different types of particles, including impurities, there are multiple ways to define collisionalities. A commonly used expression for the electron collisionality is given by [58]

$$\nu_\mathrm{e}^* = 6.921 \times 10^{-18} \frac{q R_0 n_\mathrm{e} Z_\mathrm{eff} \ln \Lambda_\mathrm{e}}{T_\mathrm{e}{}^2 \varepsilon^{3/2}} , \tag{1.13}$$

where q is the safety factor, R_0 is the major radius in m, n_e is the electron density in m^{-3}, Z_eff is the effective ion charge, T_e is the electron temperature in eV, and $\ln \Lambda_\mathrm{e} = 31.3 - \ln \left(\sqrt{n_\mathrm{e}} / T_\mathrm{e} \right)$ is the Coulomb logarithm. The dominant dependence of collisionality on the inverse of temperature squared is characteristic of tokamaks, but the proportionality to density also plays a role. These quantities vary significantly along the radial direction, such that very low collisionality is required in the core of fusion plasmas, which inevitably leads to low pedestal top collisionality, but in a reactor allows for high collisionality at the separatrix and SOL.

Purity

The effective ion charge Z_eff is not only relevant for collisionality, but is also by itself an import measure of plasma impurity content. Making use of the overall charge neutrality of plasmas, it is given by

$$Z_\mathrm{eff} = \frac{\sum_a Z_a{}^2 N_a}{\sum_a Z_a N_a} = \frac{\sum_a Z_a{}^2 N_a}{n_\mathrm{e}} , \tag{1.14}$$

where Z_a and N_a are the charge number and density of each ion species in the plasma. With this definition, the Bremsstrahlung radiation losses are proportional to Z_eff [9], so it should be low to maintain good plasma performance. Besides this, a pure D-T plasma would have $Z_\mathrm{eff} = 1$, but most impurities, apart from hydrogen, raise the effective ion charge, making it a measure of fuel dilution, though in a way that depends on the impurity charge numbers. High fuel dilution is obviously undesirable since fusion power depends on the product of the density of the fuel species D and T. In practice, $Z_\mathrm{eff} < 2.5$ is usually considered necessary for a viable reactor scenario.

Current

Increasing plasma current generally leads to higher energy confinement time, density, temperature, pressure, and associated limits, making it arguably the most influential parameter in tokamak performance. However, there are stability limits to how much the current can be increased, often expressed in terms of the safety factor, defined as the number of toroidal turns made by a magnetic field line for each poloidal turn [10]:

$$q = \frac{\text{number of turns in toroidal direction}}{\text{number of turns in poloidal direction}} = \frac{1}{2\pi}\oint \frac{B_\phi}{RB_\mathrm{p}}\mathrm{d}s\,, \tag{1.15}$$

where R is the cylindrical radial coordinate, B_ϕ and B_p are the toroidal and poloidal components of the magnetic field, respectively, and the integral is carried out over a single poloidal circuit around the flux surface. The safety factor is a flux function that varies in the radial direction, being approximately proportional to $B_\mathrm{t}/I_\mathrm{p}$ at the plasma edge. In divertor magnetic configurations, q tends to infinity as it approaches the separatrix, so the edge safety factor is usually represented by q_{95}, its value at the flux surface with normalized poloidal flux radius $\rho_\mathrm{pol} = 0.95$. A too low safety factor leads to plasma instabilities and increased disruption probability, so $q_{95} \geq 3$ is usually required for reactor scenarios, effectively putting a limit on how high the plasma current can be.

Heating

In a fusion reactor, most of the plasma heating will come from alpha particles originated by the fusion reactions, whereas in present-day devices it is externally applied via injection of neutral beams or electromagnetic waves into the plasma. Alpha particles will transfer most of their energy to electrons and will apply no torque to plasma, but this is not necessarily the case with external heating methods. Current scenarios should therefore be compatible with heating conditions that mimic alpha heating, i.e. low torque and dominant electron heating, if they are to be extrapolated to burning plasmas. But even a reactor will require significant external heating to approach ignition until fusion reactions take over. Since external heating power is a limited resource, both economically and in terms of plasma accessibility, scenarios which can also be obtained at low heating power are desirable for reactors.

Stationarity

Besides approaching ignition within the constraints mentioned above, a fusion reactor will have to sustain plasma discharges for a long duration. Ideally a tokamak would be operated non-inductively for arbitrarily long periods, so that continuous energy production is ensured. But even if the device is operated inductively in a pulsed manner, a meaningful amount of energy must be produced per pulse in order to justify the resulting mechanical wear and stress on the machine. Because of this, nonstationary plasma scenarios are not viable candidates for fusion reactors, even if they achieve good transient performance. Integration of all the elements in a stationary plasma scenario turns out to be a difficult challenge, even in present-day machines.

1.2.3 Plasma-wall interaction

There are operational regimes in current devices that perform well in most of the core plasma requirements previously described, but unfortunately there are also constraints regarding power exhaust and plasma-wall interaction which will be much harder to satisfy in a reactor environment [59–61]. This remains one of the main challenges and active areas of research in magnetic confinement fusion [62].

Edge localized modes

It is clear that unmitigated type I ELMs are simply unacceptable in large-scale devices due to the extreme transient heat loads they deposit on the divertor target plates [36–38]. Even the toughest materials cannot withstand such harsh conditions without significant sputtering and surface melting, which dramatically shorten the lifetime of the divertor [59]. Although mitigated ELMs are not yet entirely ruled out, a fusion reactor may end up needing complete absence of ELMs of any form [63]. This requires the discovery and development of alternative ELM-free operational regimes [64, 65], which makes the achievement of fusion-relevant plasma conditions even more challenging.

Divertor detachment

ELM suppression or avoidance is a necessary but not sufficient condition to ensure benign plasma parameters at the divertor. In fact, even the ELM-free steady-state heat loads will be too high in a reactor if protection measures are not taken [66–68]. More specifically, a reactor scenario will have to operate in a state of divertor detachment [12, 69–71], in which directed heat fluxes are substantially mitigated via volumetric losses in layers of cold and dense plasma near the target plates. In a detached divertor, usually achieved by puffing large amounts of deuterium and/or radiating impurities, plasma pressure is no longer constant along SOL magnetic field lines, as collisions with the neutral divertor gas become a relevant sink of energy and momentum. Not all operational regimes, and especially those with high-performance, are compatible with detached divertors, so this constitutes another important constraint for a reactor scenario.

Plasma facing materials

At the moment, no existing plasma scenario in current devices simultaneously satisfies all the core, edge and divertor requirements for a reactor, even if only considering scaled parameters. When wall materials are added to the mix, the situation only gets worse. For a long time, tokamaks traditionally had PFCs made of graphite [72], which has some attractive properties, such as low Z, good thermal conduction and low cost. However, the high erosion rates and tritium retention, which poses safety and fuel efficiency issues, preclude the use of carbon PFCs in a fusion reactor. This prompted the utilization of high-Z metals with high melting points, such as molybdenum [73] and tungsten (W), in magnetic confinement devices. Tungsten is presently considered one of the most viable plasma facing materials for fusion reactors [74, 75], particularly in the divertor, in view of its good thermomechanical properties, resistance against sputtering, and low fuel retention. However, its high atomic number causes significant radiative losses in the plasma even at low impurity concentrations. The associated cooling can also initiate positive feedback loops that lead to tungsten accumulation in the core of plasma, resulting in severe confinement degradation and discharge collapse [47, 76–79]. This is especially relevant in the absence of an impurity flushing mechanism like ELMs. While the use of tungsten is a material constraint, it does impose severe limitations on the plasma operational regimes, because many performant scenarios obtained in graphite tokamaks are considerably worse or even not attainable in W-walled devices.

To sum up, the ideal plasma scenario must not only simultaneously achieve several stationary plasma parameters that translate to ignition proximity in a reactor, using heating methods similar to alpha particles, while avoiding ELMs and mitigating continuous heat loads by divertor detachment, but also do it in a way that is compatible with reactor-grade plasma facing materials like tungsten and derived alloys.

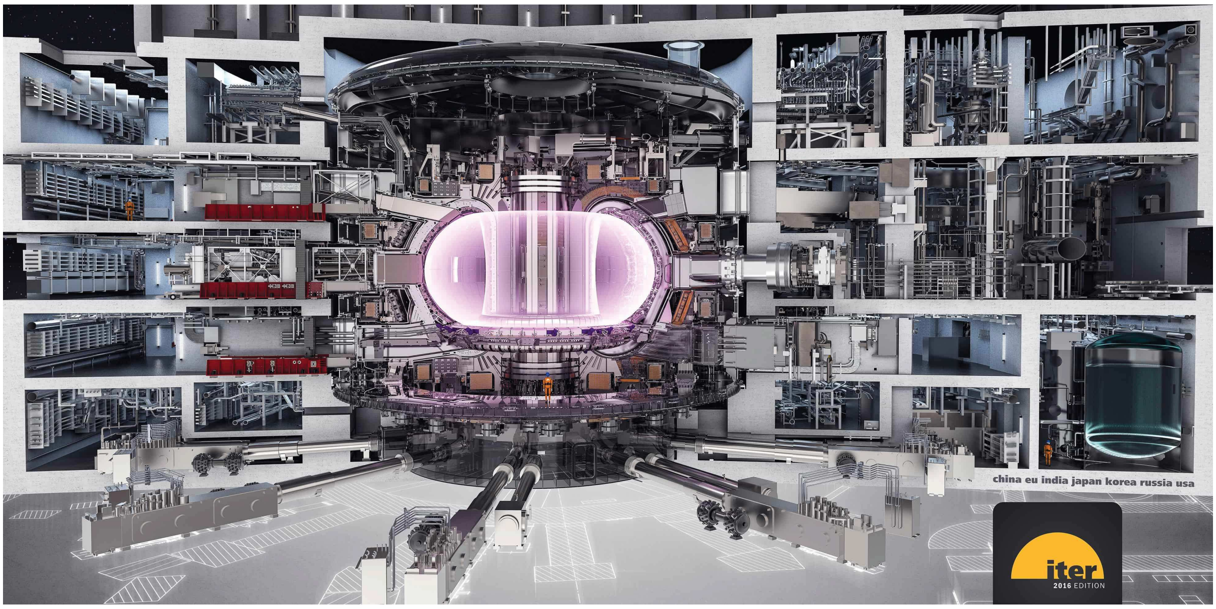

Figure 1.10: Schematic representation of the ITER tokamak and plant systems housed in their concrete home. Figure adapted from [82].

1.2.4 ITER

Plasma physics is obviously critical to achieve the goals of a fusion plasma [80], but the design of a reactor is largely determined by engineering, materials and nuclear physics constraints [9]. First, there are limits to the amount of power per unit area that can safely pass through the first wall without causing unacceptable damage to PFCs. This applies to both heat loss and neutron flux. Second, the magnetic field is limited by the properties of the superconducting magnets that generate it, since superconductivity can only be maintained up to certain values of current density, magnetic field, and temperature, that depend on the material. Third, the structural support system must be able to withstand the huge forces produced by the coils. Finally, the desired power output of the reactor significantly affects the size of the device, in conjunction with the other constraints. With conventional superconducting niobium–tin technology, and assuming a power output of 0.4-0.5 GW, the design inevitably converges to something similar to the ITER tokamak [81], represented schematically in figure 1.10.

ITER will be the world's largest fusion device and is currently under construction in Cadarache, southern France. It is one of the most ambitious energy projects ever undertaken, involving an international collaboration between China, the European Union, India, Japan, South Korea, Russia, and the United States [83]. The main goal of ITER is to create for the first time a plasma that produces net energy, namely a burning plasma with $Q = 10$. ITER aims to prove the scientific and technological viability of nuclear fusion as an energy source and thus pave the way

	Inductive	Hybrid	Non-inductive
R_{geo} (m)	6.2	6.2	6.35
a (m)	2	2	1.85
V (m^3)	831	831	793
ε	0.32	0.32	0.29
κ	1.85	1.85	2.0
δ	0.48	0.48	0.5
B_{t} (T)	5.3	5.3	5.17
I_{p} (m)	15	13.8	9
q_{95}	3	3.3	5.2
τ_{E} (s)	3.66	2.73	2.32
H_{98y2}	1	1	1.3
β_{N}	1.8	1.9	2.56
$\overline{n_{\mathrm{e}}}$ (10^{19} m^{-3})	10.1	9.3	6.7
f_{GW}	0.85	0.85	0.8
Z_{eff}	1.66	1.85	2.17
$P_{\mathrm{heat,ext}}$ (MW)	40	73	68
P_{rad} (MW)	47	55	38
P_{f} (MW)	400	400	338
Q	10	5.4	5
Burn time (s)	400	1070	Steady-state

Table 1.2: Main parameters of ITER inductive, hybrid and non-inductive scenarios. Table adapted from [86, 87].

for the first electricity producing fusion power plant that will follow [62].

ITER scenarios therefore constitute a realistic benchmarking reference for plasma scenarios of present-day devices. Table 1.2 shows an overview of the main parameters of the three types of scenarios planned for ITER: inductive, hybrid and non-inductive. Many of the absolute parameters are not achievable in current devices due to design limitations, namely the small size, but the scaled parameters should be aimed for by ongoing experiments. While most have been separately attained, no scenario so far has been able to simultaneously fulfill all the scaled requirements of ITER with benign plasma-wall interaction [84, 85]. It is not yet known whether the planned ITER scenarios will be possible, so a strong research effort must continue to be made in current machines to prepare ITER operation and also to develop suitable plasma scenarios for future reactors in general.

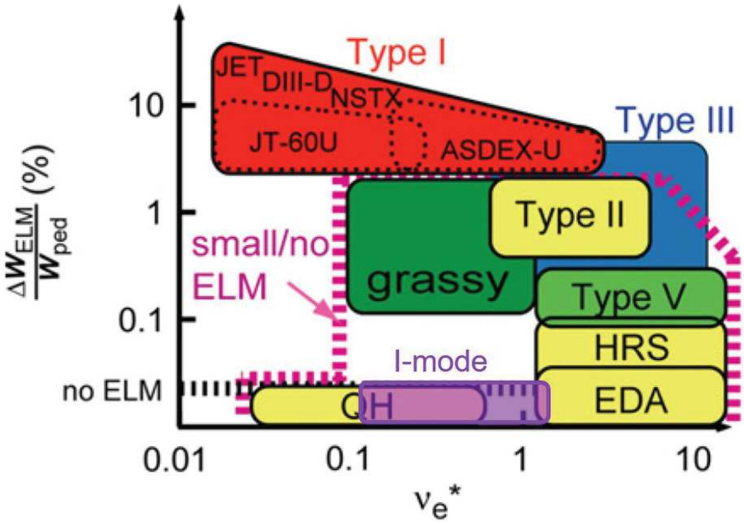

Figure 1.11: Normalized ELM energy loss versus pedestal electron collisionality for various ELMy, small-ELM and no-ELM regimes. Figure taken from [65].

1.3 ELM-free regimes

1.3.1 Overview

The standard H-mode [20] was traditionally regarded as the preferable operation regime for a fusion reactor, including ITER, due to its superior confinement properties, but this picture has significantly changed in the last years. The unacceptable heat loads due to ELMs are becoming more evident [36–38] and call for alternative solutions. Active ELM control techniques [88, 89], such as non axisymmetric magnetic perturbations [90–92], ELM pacing with pellets [93–95] and vertical kicks [96, 97] are possible approaches to the problem, but their effectiveness and applicability to reactor conditions is not yet entirely clear.

Alternatively, operational regimes with high confinement and benign ELM characteristics [64] can also be obtained without resorting to these techniques and are sometimes called ”natural” regimes [65]. A set of ”natural” ELMy, small-ELM and no-ELM regimes is shown in figure 1.11, separated by the ELM energy loss relative to the pedestal, as a function of ν_e^*. Small-ELM regimes, such as grassy [98] and type-II ELMs [99–101], can achieve good performance, but a fusion reactor might end up requiring complete absence of ELMs of any type. In such case, the set becomes more restricted, but there are still several candidates. The most well established of these, the EDA H-mode, QH-mode and I-mode, are reviewed below.

1.3.2 EDA H-mode

The enhanced D-alpha (EDA) H-mode [102] is a steady-state high confinement ELM-free regime discovered in the Alcator C-Mod tokamak by applying ion cyclotron resonance heating (ICRH) after a fresh boronization [103]. Its name originally comes from the observed high levels of D_α radiation when compared to the nonstationary ELM-free H-mode, but its main signature is the presence of a prominent edge fluctuation called the QCM [104, 105]. The EDA H-mode was studied mostly in C-mod [106], but a similar regime known as the high recycling steady (HRS) H-mode in JFT-2M [107, 108] is possibly the same [109]. In the EAST tokamak, a regime obtained with lithium wall coating and significant lower hybrid current drive (LHCD) [110] might also be related to the EDA H-mode. Past attempts to reproduce the EDA H-mode in other tokamaks such as DIII-D [111] and JET [112] were not able to produce desirable scenarios.

Access conditions to the EDA H-mode have been extensively investigated in C-mod through dedicated scans of I_p, B_t, density, power, and shape [102, 106, 113]. It was found that EDA access is roughly favored by $q_{95} \geq 3.5$, $\delta_\mathrm{avg} \geq 0.35$, and high L-mode target density, leading to high edge ν^* [114]. Away from these conditions, nonstationary ELM-free H-modes are more likely. No obvious dependence of this boundary on κ or input power was found over the ranges studied [106]. Furthermore, production of ohmic EDA H-modes [113] shows that the regime cannot be attributed to direct effects of radiofrequency heating or a high-energy minority ion tail.

EDA H-modes feature steep density and temperature gradients in the pedestal [104, 114], which can be maintained in a stationary ELM-free state if the pressure gradients do not exceed the P-B stability boundary due to excessive heating power [115, 116], above which small ELMs occur. This is in contrast to the nonstationary ELM-free H-mode, whose density and impurity content rise uncontrollably due to the extremely high particle confinement [117–119].

Evidence suggests the enhanced transport in EDA H-mode is caused by the QCM [104, 105, 120]. Its name comes from its larger frequency width in comparison to typical coherent MHD modes. The large density fluctuations of the QCM can be measured close to the separatrix by several diagnostics, including reflectometry, Langmuir probes, phase contrast imaging [121], and gas puff imaging [122]. The electromagnetic perturbation is also significant, but not detectable with standard set of magnetic probes mounted on the vacuum vessel wall, requiring fast scanning magnetic probes to be inserted in the plasma for the measurement, due to its relatively short poloidal wavelength [105, 120]. The QCM moves in the electron diamagnetic direction in the lab frame and usually appears as a downchirping oscillation at the transition to EDA H-mode, likely due to the evolving plasma rotation velocity. However, its exact location with respect to the radial electric field well and propagation direction in the plasma frame are not unequivocal [122]. The QCM was initially proposed to be a resistive X-point mode, a form of resistive ballooning mode strongly influenced by the magnetic geometry near the X-point [123], and later a separatrix-spanning electron drift-wave with interchange and electromagnetic contributions [120]. The true nature of the QCM has not yet been unambiguously identified [122] and its interplay with profiles and turbulence remains to be understood [106].

Despite the open questions about the EDA H-mode, it has been developed into a performant scenario with important accomplishments, such as the highest volume-averaged core plasma pressure ever achieved in a fusion device [124]. Besides this, it is obtainable in a device with high-Z (molybdenum) PFCs and is compatible with extrinsic impurity seeding and operation with a dissipative divertor and high radiative power fraction [125, 126]. Together with its high density and energy confinement, low Z_{eff}, and no need for torque, this makes the EDA H-mode a promising regime for future reactors. However, it has only been obtained at high collisionality, so it is not clear whether it will be accessible in large-scale devices with low collisionality.

1.3.3 QH-mode

The quiescent H-mode, usually referred to as QH-mode, is an ELM-free regime with good confinement originally discovered in the DIII-D tokamak with counter-current NBI [127]. It has also been reproduced in JT-60U [128] and in the carbon-walled ASDEX Upgrade (AUG) [129] and JET [130, 131]. The main signature of the QH-mode is an instability called edge harmonic oscillation (EHO).

The QH-mode is usually accessed at low density, with highly conditioned walls from a recent boronization, strong pumping, optimized wall clearance and a large edge rotational shear, traditionally provided from counter current NBI [132]. QH-modes can also be created with co-injection if enough torque is applied [133], but they are more challenging to obtain. It is also possible to apply external torque via the use of static non-axisymmetric nonresonant magnetic fields [134]. The key access condition seems to be a critical edge $E \times B$ shear, below which ELMs occur [134–137].

QH-modes typically feature low density, very high T_{i} and somewhat lower but still high T_{e}, with a deep radial electric field well [138] and a high pressure pedestal that can be maintained without ELMs, at constant radiated power and density [132]. This is believed to be possible due to the enhanced particle transport caused by the EHO [127, 132], a low frequency edge electromagnetic oscillation with several harmonics that can range from toroidal mode numbers $n = 1$ to 11 [129]. The EHO is thought to be a saturated kink-peeling mode, driven unstable by large edge current densities [139]. It has been nonlinearly simulated with several codes [140–144], showing in general good agreement with experiments.

The low density of the QH-mode is not optimal, but its operational range has been extended to reasonably high Greenwald fraction during density ramps [145, 146]. However, the high edge rotational shear required by the QH-mode may represent an accessibility challenge in future reactors due to the lack of torque [63]. That being said, a different type of QH-mode with no net input torque, known as the wide-pedestal QH-mode, has recently been achieved in DIII-D [136, 147–149]. In any case, regardless of its specific type, the QH-mode still has major obstacles to overcome, namely that it is only obtained with dominant ion heating from NBI, in devices with graphite walls, and with high Z_{eff}, which means high fuel dilution, considering the low Z of carbon. Recent attempts to obtain the QH-mode in AUG with tungsten PFCs have shown traces of the EHO, but no success so far in avoiding impurity accumulation. Furthermore, the QH-mode has not yet been shown to operate with a detached divertor. For these reasons, it is not known if it will be adequate for future reactors, despite its high performance in terms of energy confinement, pressure, and temperature in present-day devices.

1.3.4 I-mode

The I-mode [150], originally called improved L-mode [151], is an ELM-free regime with better energy confinement than L-mode and mostly accessed with the ion ∇B drift pointing away from the X-point. It has been obtained in C-Mod [150, 152], AUG [151, 153], DIII-D [154, 155], and EAST [156, 157]. In terms of edge fluctuations, the typical I-mode signature is a broadband peak above the background level known as the weakly coherent mode (WCM).

The I-mode is accessed when sufficient heating power is applied in L-mode without entering H-mode. The L-H transition is typically avoided by using high magnetic field and a configuration with the ion $B \times \nabla B$ drift pointing away from the active X-point, the so-called unfavorable configuration that significantly increases the H-mode power threshold. However, I-modes have occasionally been achieved in favorable ∇B configuration [158]. The I-mode has been obtained with a variety of heating methods, including ICRH [150], NBI [159], electron cyclotron resonance heating (ECRH) [160], and lower hybrid wave (LHW) heating [157], in devices with different wall materials, namely carbon [151, 154], molybdenum [150] and tungsten [160]. The power required to enter I-mode depends on density [153, 161], but only weakly on magnetic field [152, 153], when compared to the L-H threshold [162]. As a result, the I-mode power window is extended at high B_t. I-modes are often transient, specially at low B_t [152, 160], but can be made stationary by feedback controlling the plasma pressure through actuating on the input power [159]. The I-mode has been observed over a wide ν^* and q_{95} range, but only at low and medium density [150, 152, 153, 155, 160].

When transitioning from L to I-mode, the energy confinement increases, but the particle confinement remains mostly unaffected. As a result, a steep T_e and T_i pedestal develops, but the density profile remains shallow and impurity accumulation is prevented. Several I-mode characteristics are typically between those of L-mode and H-mode, such as energy confinement, E_r well [153, 163], pedestal pressure and SOL power decay length [68]. The I-mode pedestal remains well below the P-B threshold [153, 164–166], but intermittent bursts [153, 166] and pedestal relaxation events [155, 165, 167] might still pose a threat to the divertor in a reactor.

In addition to the temperature pedestal, a high frequency broadband fluctuation at the plasma edge called WCM [153, 158, 168–170] and a low frequency geodesic acoustic mode (GAM) [169, 170] are usually observed in I-mode. The non-linear coupling between the GAM and WCM can explain its broadband structure [169, 170], but their role in regulating transport is not yet clear. Suppression of large-scale, but not intermediate-scale turbulence, due to high T_i/T_e at the separatrix has been proposed as the main mechanism to explain the I-mode transport properties [171], but it has also been argued that neoclassical transport is sufficient [172].

The high temperature, no need for torque and compatibility with several wall materials make the I-mode a promising regime for future reactors. However, its high access power when compared to H-mode in favorable ∇B configuration, as well as the relatively low density and energy confinement are major inconveniences. Furthermore, I-mode seeding and detachment studies are scarce and did not produce encouraging results in C-Mod [173], but slight progress is currently being made in AUG.

1.4 Motivation and thesis outline

Nuclear fusion reactors will require scenarios with high plasma performance, but benign plasma-wall interaction, which is difficult to achieve because of ELMs, among other challenges. Several alternative high confinement ELM-free regimes have been obtained in current devices, but each of them has different advantages and drawbacks, so there is not yet a clear winner.

This thesis reports on the development of a stationary ELM-free H-mode recently achieved in the AUG tokamak, with the overall goal of approaching reactor relevance. The importance of this topic stems from the fact that performant ELM-free scenarios compatible with all plasma physics and engineering requirements for fusion do not exist in present-day devices, but are essential for future reactors. This is part of an international effort to bring nuclear fusion science and technology to a state of maturity and effectiveness, so that it can be applied in commercial power plants. It is an enormous challenge, but hopefully will help solve the world energy and climate issues.

The thesis is divided into six chapters, the first one being the current introductory chapter, where a basic overview of the world energy situation and the role of fusion energy is given, together with some of the main requirements of a plasma scenario for a fusion reactor and a review of notorious ELM-free regimes in current devices. Chapter 2 briefly describes the AUG tokamak, its heating systems and the relevant diagnostics for the work. Chapter 3 presents general features of the stationary ELM-free H-mode recently achieved in AUG, which is the main subject of the thesis, and concludes it is most likely the EDA H-mode. Chapter 4 explains different methods and experiments that were performed with the goal of bringing the regime closer to reactor relevance. Chapter 5 gives an overview of the operational space of the EDA H-mode in AUG, obtained experimentally with different parameter scans. Chapter 6 summarizes the results, makes conclusions and discusses future work.

Chapter 2

ASDEX Upgrade tokamak

All the experiments for this thesis were performed in the ASDEX Upgrade tokamak, currently one of the most relevant fusion devices in operation worldwide. This chapter presents an overview of AUG, including a brief explanation of its coils, PFCs and heating systems, followed by a description of most diagnostics used in this work.

2.1 Machine and heating systems

2.1.1 Overview

The AUG tokamak [174–176] is a fusion experiment operated by the Max-Planck-Institut für Plasmaphysik in Garching, Germany. It is the successor of the Axially Symmetric Divertor Experiment (ASDEX) and has has been in operation since 1991, being Germany's largest tokamak and second largest fusion device, after stellarator Wendelstein 7-X [177]. AUG is classified as a medium size tokamak and the overall goal of its scientific programme, run jointly with the EUROfusion consortium [178], is to improve the physics basis for the future large scale reactors ITER and DEMO [179].

The main design and maximum plasma parameters of AUG are listed in table 2.1. The high overall heating power, flexible heating mix, versatile shaping and comprehensive diagnostic set allow a wide range of studies with high-impact results [178, 180–186], covering topics such as particle and energy transport, turbulence, instabilities, integrated and advanced scenarios, SOL, divertor and power exhaust, wall materials, and theoretical models.

The confining magnetic field of AUG is essentially generated by 16 large copper toroidal field coils wrapped around the vessel. There are also 17 poloidal field coils illustrated in magenta

Major plasma radius	1.65 m
Minor plasma radii	0.5/0.8 m
Magnetic field	3.9 T
Plasma current	2 MA
Pulse length	10 s
Heating power	30 MW
Plasma volume	13 m^3
Plasma density	$2 \times 10^{20}\,m^{-3}$
Plasma temperature	8 keV
Main plasma types	D, H, He

Table 2.1: Main design and maximum plasma parameters of AUG.

in the cross-section of figure 2.1. These serve several purposes [187], roughly divided in the following manner: the ohmic OH coils are used for inducing the plasma current, which is a heat source and generates most of the confining poloidal magnetic field; the vertical field V coils shape the plasma and create the magnetic field configuration of the divertor; the internal and external CO coils correct the plasma position and control movements and instabilities, passively aided by an internal rigid conductor, the passive stabilization loop (PSL), colored in yellow. Three flywheel generators [188] supply the electrical power for the toroidal and poloidal field coils, as well as for auxiliary heating systems. In addition, the B-coils [189], a set of 16 in-vessel saddle coils mounted on the PSL, are used to generate non-asymmetric magnetic perturbations in order to affect plasma behavior [92] and compensate error fields.

The coil system of AUG can produce different magnetic topologies, including both limiter and divertor configurations. The X-point of the divertor can be created below or above the magnetic axis, giving rise to the lower single null (LSN) and upper single null (USN) configurations, respectively. Two X-points can also exist simultaneously in the double null (DN) configuration. AUG can produce plasma shapes similar to those planned for ITER, and experiments are typically performed in LSN configuration, exemplified in figure 2.1. The ion $B \times \nabla B$ drift usually points towards the active X-point, which favors the L-H transition, and the plasma current is opposite to the magnetic field. The lower divertor tiles require this fixed helicity, and reversing the plasma current involves special efforts executed only for a couple of weeks per campaign, in which unfavorable ∇B drift experiments are performed. The upper divertor can handle both helicities, allowing experiments with unfavorable ∇B drift at any time, but the lack of pumping and open geometry limit low density operation and power exhaust.

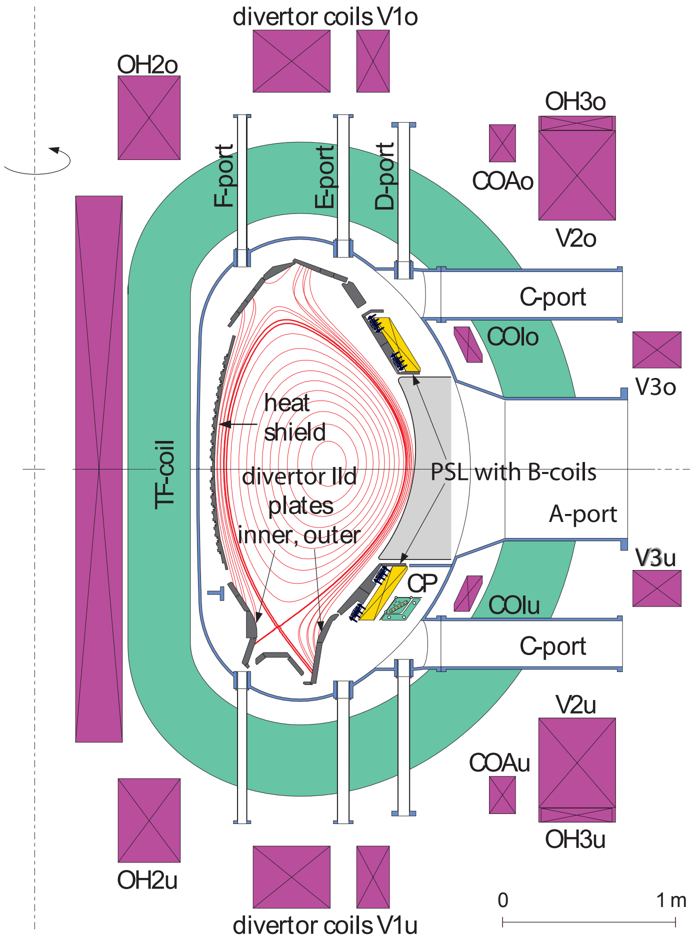

Figure 2.1: Cross section of AUG showing toroidal (green) and poloidal (magenta) field coils, vacuum vessel and ports, PFCs, and magnetic flux surfaces of a lower single null configuration. Figure taken from [190]

Besides similar magnetic geometries, also the divertor material of ITER (tungsten) is used in AUG. Tungsten is presently regarded as one of the most adequate plasma facing materials for fusion reactors [74], especially in the divertor, due to its good thermomechanical properties, resistance against sputtering, and low fuel retention. AUG has since long been in the forefront of operating with tungsten [77], achieving complete coverage of PFCs with W-coated graphite tiles in 2007 [191] and an outer divertor consisting of solid tungsten tiles in 2014 [192, 193]. Figure 2.2 shows the inside of the AUG vessel, where the the W-coated PFCs can be seen. The full tungsten wall of AUG is an extremely rare feature in present-day machines, contrasting with the typical graphite walls of most tokamaks [72], making it an extremely valuable asset for extrapolating to future devices.

Figure 2.2: Interior of AUG during installation work in the vessel, showing the W-coated PFCs and closed divertor. Figure taken from [194].

A major, though undesirable, effect of tungsten PFCs is the potential contamination of the plasma with a high Z impurity, which leads to significant radiative losses even at low concentration. Under certain conditions, accumulation of tungsten in the core of the plasma can occur, causing severe confinement degradation, development of strong MHD modes, and eventual termination of the discharges. Prevention of tungsten accumulation requires central heating with electromagnetic waves, which drives outward turbulent transport of tungsten, counteracting the neoclassical inward pinch [195]. A sufficiently high gas puff level is often also required to reduce the tungsten source from sputtering and increase flushing by ELMs. However, some scenarios, especially those requiring low density, are not compatible with such measures and need other means of reducing the influx of tungsten, namely a fresh boronization [46]. This procedure covers PFCs with a thin boron layer, whose effect of reducing the release of tungsten and deuterium from the walls usually lasts for a couple dozen discharges. Experience and knowledge gained in AUG is of paramount importance in developing solutions for the operation of future devices with high Z PFCs.

2.1.2 Heating systems

AUG has a powerful and diversified set of auxiliary heating systems [176], which at the moment consist of nominally up to 20 MW of NBI, 8 MW of ECRH, and 6 MW of ICRH, all designed for 10 s pulse duration. These allow a wide range of plasma scenarios and physics studies to be performed, including access to reactor-relevant divertor and SOL conditions.

Electron cyclotron resonance heating

Injection of electromagnetic waves is an effective plasma heating method if absorption resonances are taken advantage of. ECRH [196] follows this approach by making use of interactions with the gyro motion of electrons through the application of microwaves at harmonics of the electron cyclotron frequency, given by

$$\omega_{\mathrm{ce}} = 2\pi f_{\mathrm{ce}} = \frac{eB}{m_e}, \tag{2.1}$$

where ω_{ce} and f_{ce} are the angular and ordinary frequencies, respectively, e is the elementary charge, B is the local magnetic field, and m_e is the electron mass. The strong magnetic field of tokamaks translates to electron cyclotron frequencies in the range of dozens or hundreds of GHz, at which wavelengths are rather small, on the order of few millimeters. This makes ECRH particularly adequate for spatially localized heating, whose position is mostly defined by frequency of the wave and injection angle, as well as the radially varying magnetic field, that decreases from the HFS to the LFS.

The ECRH system of AUG [197–199] has been upgraded over the last 15 years and currently consists of a dual frequency system with 8 gyrotrons, making up a total nominal power of 6.4 MW at 105 GHz and 8 MW at 140 GHz. In practice, a maximum of 5.9 MW has been coupled to the plasma, although 6.5 MW at 140 GHz could be possible with future optimizations, after accounting for limitations on some gyrotrons and losses in beam preparation and transmission. The 8 transmission lines are mainly composed of air-filled oversized corrugated waveguides with overall lengths between 50 and 70 m and quasi-optical sections at both ends. These can focus the beam to the plasma center, steer it in poloidal and toroidal directions, and set it to any polarization state, in order to match the X or O-mode conditions at the plasma edge. Calculations of beam propagation and absorption in AUG are typically performed with the beam-tracing code TORBEAM [200], which also handles electron cyclotron current drive (ECCD), used for q-profile tailoring and non-inductive tokamak operation [201].

Standard ECRH operation at AUG is performed with the second harmonic of X-mode heating (X2) at $f = 140\,\mathrm{GHz}$, whose resonance passes through the center of the plasma at $|B_\mathrm{t}| = 2.5\,\mathrm{T}$. This scheme has the highest absorption rate, followed by O1, X3 and O2 [202]. Refocusing holographic mirrors installed on the inner column can be used to increase the absorbed fraction of O2 heating by providing a second pass of the beam through the plasma [197, 203]. The incomplete absorption of the alternative schemes, as well as cutoffs which reflect the waves in any of the methods, can lead to strong stray radiation and pose a risk to in-vessel components, especially microwave diagnostics. Several passive and active measures of machine protection against stray ECRH radiation are in place at AUG [204, 205], and an integration with the discharge control system (DCS) allows a practical real-time replacement of active gyrotrons in order to comply with predefined heating waveforms [206].

In general, the choice of the heating scheme depends on the available frequencies, the desired magnetic field and potential cutoffs. With X-mode injection from the LFS, the right-hand cutoff is the relevant one, which for harmonic numbers $l \geq 2$ enforces the following condition for wave propagation [196]:

$$\begin{aligned} {\omega_\mathrm{pe}}^2 &\leq l\,(l-1)\,{\omega_\mathrm{ce}}^2 \\ \Leftrightarrow n_\mathrm{e} &\leq n_\mathrm{co} = C l\,(l-1)\,B^2 \\ C &= 0.97 \times 10^{19}\,\mathrm{m^{-3}T^{-2}}, \end{aligned} \tag{2.2}$$

where ω_pe is the angular plasma frequency, n_e is the electron density and n_co is the cutoff density. With the standard AUG X2 heating at $|B_\mathrm{t}| = 2.5\,\mathrm{T}$, this results in $n_\mathrm{co} \approx 12 \times 10^{19}\,\mathrm{m^{-3}}$, which limits high density operation of certain plasma scenarios. As an alternative, and also to allow operation at lower B_t, X3 heating at 140 GHz is used relatively often in some scenarios with 1.8 T. X-mode operation at 105 GHz and O-mode heating schemes in general are rarer. Although relevant in AUG, ECRH limitations due to cutoffs are not expected to be a problem in ITER, due to the much higher B^2/n_e.

ECRH is an essential heating method in AUG due to its role in avoiding tungsten accumulation. In fact, it has been recognized as a basic system necessary for operation, being almost ubiquitous in AUG H-mode discharges. Besides this, the high versatility and available power, which exceeds the L-H threshold in favourable configuration by a factor of more than 3, or at least 2 at the highest densities, allows a wide variety of reactor-relevant studies to be performed with ECRH in AUG [199], such as H-mode operation with dominant electron heating and low torque, access of low collisionality in a full metal device, influence of T_e/T_i and rotational shear on transport, dependence of impurity accumulation on heating profiles, and advanced tokamak physics, related to nonstandard current profiles and non-inductive operation. ECRH is the main heating method used in the experiments performed for this thesis.

Neutral beam injection

NBI [207] is a popular and powerful heating method, responsible for the highest temperatures and triple products ever achieved in tokamaks [208]. It consists in injecting beams of highly energetic neutral particles in the vessel, which are unaffected by the magnetic field, therefore travelling in straight lines and penetrating the plasma. Once ionized by collisions with the background plasma, these particles become magnetically confined and form a high-energy tail on the plasma distribution function. They then slow down by further collisions, transferring their energy to the background plasma in the form of heat. The neutral beams are created from an initial source of ions that are accelerated with high voltages and then neutralized before entering the vessel.

The NBI system of AUG [176, 209, 210] consists of two similar injectors in boxes on opposite sectors of the tokamak, each equipped with four ion sources. With deuterium, each source can deliver up to 2.5 MW, making a total maximum of 20 MW, or a lower power of 13 MW with hydrogen. The maximum accelerating voltages of box 1 and 2 are 60 and 93 kV, respectively, but can be reduced to provide lower beam energies and heating power.

In terms of geometry, the neutral beams are co-current directed in standard AUG operation, but each source has a different injection angle in order to emphasize certain functionalities. They can currently be classified as: radial (2 sources), tangential (4 sources), and current drive (2 sources). This versatility allows for NBI to be used not only as a heating method, but also as a source of external torque and current drive [201].

NBI is the most powerful heating method of AUG and is used in the majority of its experiments. It is essential for scenarios with very high power, which in AUG allow the achievement of realistic SOL and divertor conditions expected in large-scale reactors [211]. Besides this, NBI is also crucial for diagnostics such as charge exchange recombination spectroscopy (CXRS) [212–214] and motional Stark effect (MSE) polarimetry [215].

Ion cyclotron resonance heating

ICRH [216] is an electromagnetic wave heating method based roughly on the same principle as ECRH, but using ion instead of electron resonances. The much higher mass of the ions results in lower cyclotron frequencies, on the order of dozens of MHz, and higher wavelengths, of several meters. This requires very different technology for generating, transmitting and launching the waves into the plasma. An important point to note is that the propagation of ICRH waves inside the plasma has a narrow cutoff region at the edge which causes excessive wave reflection, unless the large launcher antenna is placed very close to the plasma edge. As a consequence, plasma-surface interactions play an important role in this heating method, leading to the difficult challenge of avoiding plasma contamination, while simultaneously ensuring efficient power coupling.

The ICRH system of AUG [176, 217, 218] consists of four toroidally distributed antennas and corresponding transmission lines and radiofrequency generators, which cover the range of 30 to 120 MHz. Below 80 MHz, they have a nominal power of 1.5 MW each. Typical ICRH operation in AUG is performed at 36.5 MHz and, under optimal conditions, a total power up to 4.8 MW can be coupled to the plasma.

Enhanced sputtering of tungsten from the ICRH limiters was initially a serious problem in the W-coated AUG [217]. In 2012, the situation was significantly improved by coating the limiters of two antennas with boron [219]. However, such a solution is not adequate for a true reactor environment due to the high erosion rates of low-Z elements. Because of this, an alternative approach based on redesigning the other two antennas was developed [218]. The resulting pair of 3-strap antennas allows ICRH operation with relatively low tungsten content in the confined plasma by minimizing image currents at the antenna frames, despite maintaining W-coated limiters.

ICRH can be used used to prevent impurity accumulation in the plasma core, but is used less often in AUG than the other heating methods. It is typically employed in scenarios where ECRH is not applicable, for example due to cutoffs related to very high density operation, such as in the small-ELM regime [100] or high current scenarios. It is also used for example in experiments requiring varying ratios of electron and ion heating, as well as in investigations related to the ICRH physics and technology itself.

2.2 Diagnostics

The extreme conditions in a fusion plasma call for special diagnostic methods to investigate parameters such as temperatures, densities, energies, currents, impurities, etc [220]. It is desirable to measure the properties of the plasma with minimal perturbation of its state, so many techniques consist in analyzing the effects exerted by the plasma on its surroundings. Magnetic fields, neutral and charged particles, and electromagnetic waves emitted from the plasma in a wide spectral range, from radio frequency to X-rays, are measured to this end. Besides such passive methods, active methods in which the plasma is slightly disturbed by external agents and the consequential effects are analyzed, are also used to provide additional information, as long as their perturbative effect on the plasma is small.

AUG is equipped with an extensive set of diagnostic systems. A subset of these diagnostics is fundamental for the operation of the tokamak, allowing monitoring and control of critical plasma and machine parameters. The full set of diagnostics enables varied scientific investigations by providing essential measurements of several quantities, contributing to the improvement of operational scenarios and study of physics phenomena in the plasma. A top view of AUG showing the position of the heating systems and some of the diagnostics is presented in figure 2.3. These include for example magnetic coils, laser interferometry and scattering techniques, microwave reflectometry, etc. A brief description of the main diagnostics used in the thesis is given in this section, divided according to the type of final quantities they measure: electron parameters, ion/impurity parameters, magnetic fields and related quantities, radiation and divertor parameters.

2.2.1 Electron diagnostics

Interferometry

The refractive index of a plasma depends on the electron density and interferometry techniques are often used to measure the phase shift caused by the refractive index of varied media. In AUG a 195 μm wavelength deuterium cyanide (DCN) laser interferometer system is used to measure the line-averaged electron density along five lines of sight [222, 223]. Figure 2.4 shows a poloidal cross section of AUG where two interferometry lines of sight are visible, one passing through the core and the other through the edge of the plasma. Each line of sight is part of a phase-modulated Mach-Zehnder interferometer, that works by allowing electromagnetic waves

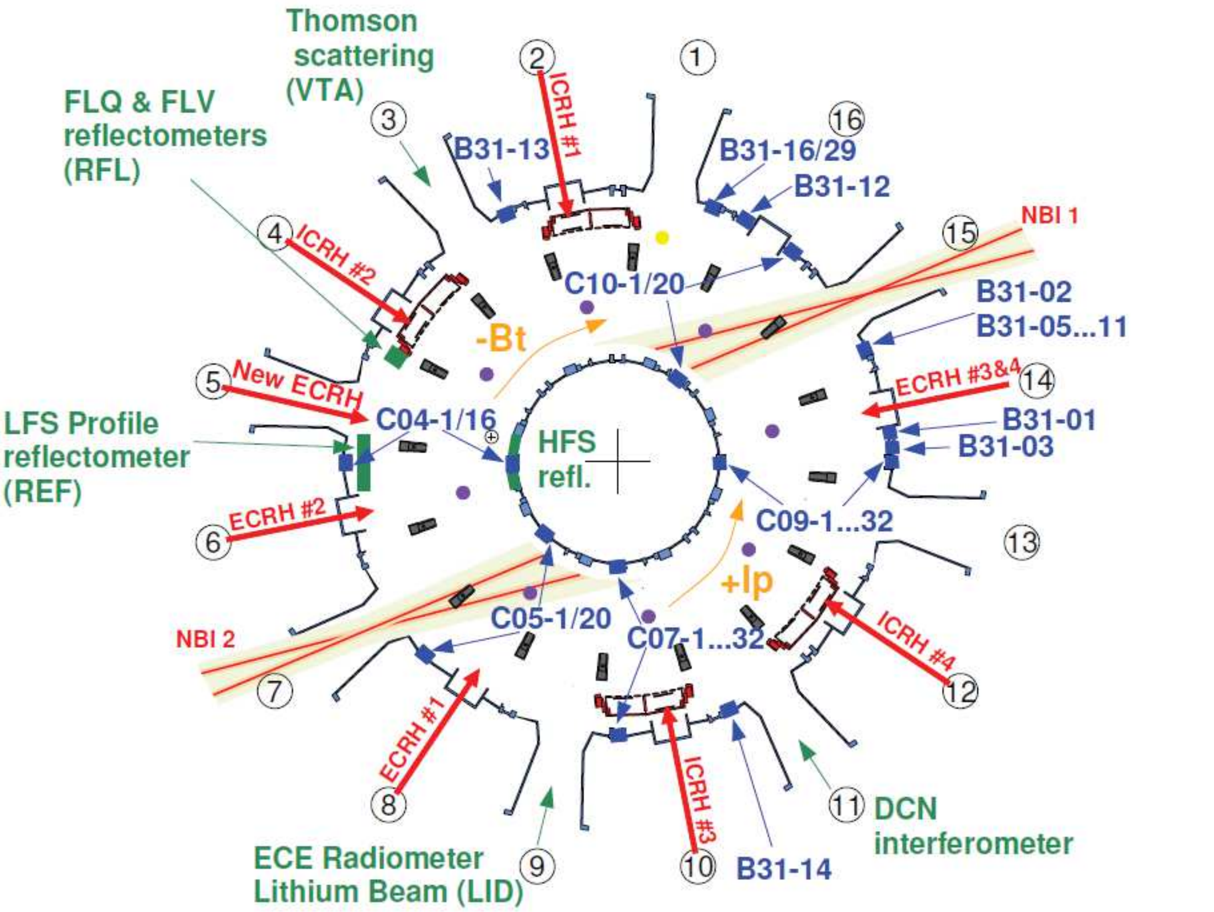

Figure 2.3: Top view of AUG showing the position of auxiliary heating systems and some diagnostics. Heating systems are indicated in red, magnetic pickup coils are indicated in blue and other diagnostics are indicated in green. Figure taken from [221].

to propagate simultaneously along two paths, one through the plasma and the other in vacuum, as a reference arm. The phase shift between the two waves is determined from their interference and is proportional to the line integrated electron density of the plasma. The AUG DCN laser interferometer measures the absolute line-integrated density with a 10 kHz sampling frequency, but the raw signal is significantly oversampled, at the same time allowing the detection of much faster modes in the plasma, up to a frequency of about 70 kHz.

Profile reflectometry

Reflectometry is a method based on the reflection of electromagnetic waves in the plasma which finds extensive use in magnetic confinement research [225, 226], being one of the few diagnostics expected to function in a true fusion reactor environment. Microwave radiation is launched into the plasma and reflected at a cutoff layer where a critical electron density is reached. The reflected wave is received at an antenna and phase changes due to propagation and reflection

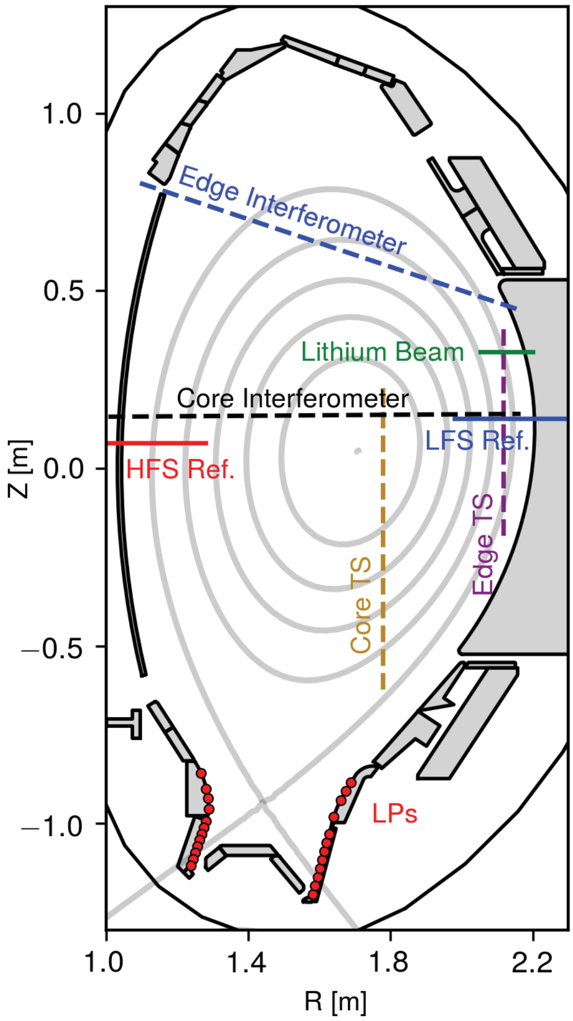

Figure 2.4: Poloidal cross section of AUG showing the lines of sight of several diagnostics and a typical magnetic equilibrium. Figure taken from [224].

in the plasma are measured by mixing the reflected radiation with a reference beam. Since the cutoff density depends on the frequency of the wave, relative positions of density layers can be determined and the electron density profile reconstructed by making measurements with a range of different probing frequencies.

A frequency-modulated continuous-wave (FMCW) O-mode reflectometer is used in AUG to measure electron density profiles with high temporal and spatial resolution [227, 228]. It is located at the midplane, with horizontal lines of sight, and has the unique capability of simultaneously probing the HFS and LFS of the plasma, as shown in figures 2.3 and 2.4. Four microwave bands (K, Ka, Q, and V) are operational, each with fundamental waveguides and a single antenna on each side for both emission and reception, covering the frequency range 17-73 GHz, corresponding to densities of $0.3\text{-}6.6 \times 10^{19}\ \mathrm{m^{-3}}$. The FMCW reflectometer works by continuously sweeping the frequency of the launched waves, resulting in signals containing rich information. The group delay, required to reconstruct the density profile with the Abel inversion [229], is extracted using several signal processing techniques [230]. Hyperabrupt varactor-tuned oscillators in the ranges 8-12 GHz and 12-18 GHz are used together with passive and active frequency multipliers to obtain the required frequency range for each channel, allowing sweeping in as fast as 10 µs, with 5 µs between sweeps. Hardening measures against stray ECRH radiation have been implemented [231], but non absorbed ECRH still poses a significant risk to the microwave components of reflectometers in AUG.

Fluctuation reflectometry

Reflectometry can also be used to monitor movements of single plasma layers by probing with fixed frequency microwaves. This allows the measurement of electron density fluctuations and has been used in fusion devices for a long time to study turbulence and MHD modes [232, 233].

The FMCW reflectometer designed for profile measurements in AUG can also operate at fixed frequency to measure fluctuations [227, 228]. In addition, two other conventional O-mode reflectometry systems dedicated to fluctuation measurements are installed: the fast frequency hopping reflectometer [234, 235] and the poloidal correlation reflectometry (PCR) diagnostic [236]. Contrary to the FMCW reflectometer, which uses homodyne single-ended detection in several bands, the fluctuation systems in AUG fully employ heterodyne I/Q detection, which improves the signal-to-noise ratio and allows separation of the phase and amplitude components of the signal [237]. All fixed-frequency conventional reflectometers in AUG have a 2 MHz sampling rate.

The hopping reflectometer system [234, 235] consists of Q-band (33-49.1 GHz) and V-band (49.4-69.0 GHz) channels, together covering the density range $1.3\text{-}5.9 \times 10^{19}\,\mathrm{m}^{-3}$. The two channels use separate waveguides and monostatic hog-horn antennas for emission and detection on the LFS, at and below the midplane, respectively. The hopping reflectometer is designed to allow a fast frequency change for arbitrary frequency steps.

The PCR system [236] operates over the Ka (26-38 GHz) and U (40-57 GHz) bands, corresponding to the density range $0.9\text{-}4.0 \times 10^{19}\,\mathrm{m}^{-3}$. Both channels use the same array of five waveguides and adjacent square-horn antennas at the LFS midplane, with the central one used for emission and the remaining 4 for detection. The use of several closely spaced antennas for detection of the microwaves allows correlations between signals to be computed and used to determine the propagation velocity and poloidal structure of modes and turbulent fluctuations [238].

Lithium beam emission spectroscopy

The lithium beam emission spectroscopy (Li-BES) diagnostic of AUG measures electron density profiles in the plasma edge [239, 240]. It is based on the electron impact excitation of neutral lithium atoms injected with 35-60 keV in the plasma above the LFS midplane, as illustrated in figure 2.4. The 670.8 nm light emitted by the 2p→2s transition of exited atoms is collected by two optical systems with spectral filters and photomultipliers in a region of about 20 cm from the wall towards the plasma. In order to separate the active contribution of the diagnostic from the passive background radiation, the lithium beam is repeatedly turned on and off [241]. Dozens of channels acquire the data with a maximum sampling rate of 200 kHz, which is used in a probabilistic framework with a collisional-radiative model to compute the density profiles at a typical resolution of 1 ms. Faster timescales down to 50 µs can be achieved if the quality of the signal is good and the raw data can also be used to analyze fast fluctuations. The radial extension of the measurement is limited by attenuation of the beam via ionization and charge exchange, especially in high density discharges.

Thomson scattering

When electromagnetic waves traverse a plasma they are elastically scattered by charged particles, mainly electrons. Incoherent Thomson scattering is carried out by free unbound electrons (as opposed to coherent scattering caused by plasma waves coupled to plasma ions) and the scattered radiation contains information about the electron population [242]. The total intensity of the scattered radiation is proportional to the electron density and the frequency width of its spectrum caused by Doppler shifts is related to the electron temperature.

There are two Thomson scattering systems in AUG [243, 244] used to simultaneously measure electron density and temperature profiles in the core and edge of the plasma with high radial resolution. Figure 2.4 shows their respective lines of sight. The core and edge systems have respectively 4 and 6 Nd-YAG lasers with a pulse energy below 1 J which fire alternately at a 20 Hz repetition rate each. Measurements are carried out by collecting the scattered light with 4 spectral channels from several volume elements (16 for the core and 10 for the edge). Thomson scattering measures electron density and temperature simultaneously and at the exact same locations, automatically resulting in a perfect relative radial alignment between the two quantities and serving as an important reference for the other profile diagnostics.

Electron cyclotron emission

The measurement of electron cyclotron emission (ECE) radiation is a well established method for determining electron temperatures in fusion plasmas [237]. Electrons gyrating in a magnetic field emit electromagnetic waves at harmonics of the cyclotron frequency, which in a tokamak depends mostly on major radius due to the spatially varying magnetic field. The intensity of the waves at a given detection location in general depends on the electron distribution at the source and along the path of the wave, but in case the plasma is optically thick, only the dependence on the temperature of the electrons that generated them remains. Therefore, by measuring the intensity of ECE radiation at specific frequencies, spatially and temporally resolved profiles of electron temperature can be determined. However, at the plasma edge the plasma is optically thin due to the low density and short path for absorption, so forward modelling of the radiation transport must be performed to avoid erroneous results [245].

At AUG, the electron cyclotron intensity spectrum is measured in second harmonic X-mode with a 60-channel heterodyne radiometer receiver [237], sampled at rates up to 1 MHz. It is equipped with five mixers and 60 filters which allow measurement of microwaves in the range 85-185 GHz with bandwidths of 300 and 600 MHz, resulting in an instrumental radial resolution of about 5 mm under typical conditions. The system is absolutely calibrated by measurements of black-body radiation emitted by laboratory sources at 77 and 773 K. It can measure temperature profiles and fluctuations from the core to the edge of the plasma, but is limited at high densities by the X-mode cutoff (equation 2.2). The ECE antennas are located slightly above the midplane and view the plasma from the low-field side, with lines of sight formed by a system of three lenses that focus Gaussian beams on the plasma edge.

Integrated data analysis

Integrated data analysis (IDA) [246] is not a diagnostic, but rather a method that combines data from several diagnostics within a Bayesian framework to reconstruct radial profiles of electron density and temperature. It uses forward models for each diagnostic, as well as priors related to smoothness, monotonicity or non-negativity constraints in order to suppress non-physical outputs. IDA can modularly combine data from all the diagnostics previously described and more, computing profiles parameterized by cubic splines and mapped to normalized poloidal flux radius coordinates, ρ_{pol}, together with uncertainty estimations. The profiles are typically reconstructed with 1 ms time resolution, but different resolutions can be used.

2.2.2 Ion diagnostics

Charge exchange recombination spectroscopy

Charge exchange recombination spectroscopy is an established diagnostic on many fusion experiments to measure the temperature, rotation, and density of impurity ions in the plasma [247, 248]. The technique relies on charge exchange reactions, which consist in the transfer of electrons from neutral particles to impurity ions, that subsequently de-excite and emit characteristic line radiation that is measured with spectrometers. The Doppler shift and width of these spectral lines is then used to compute the velocity and temperature of the ions that emitted the radiation. It is usually assumed that the impurity ions are in thermal equilibrium with the main ions, meaning that the temperature derived from CXRS measurements can also be considered the main ion temperature. In addition, the intensity of the spectral lines can be used to determine the impurity ion density if the neutral particle population is known [249]. With all these quantities, the radial electric field can be calculated through the impurity ion radial force balance equation. Since the natural neutral population is very low in fusion plasmas due to the extremely high temperatures, CXRS is typically combined with external sources of neutral particles, like gas puffs, neutral beams, or pellets, which increase the line radiation to useful levels and also localize the measurements.

Several beam-based CXRS systems are installed in AUG to measure the temperature, toroidal and poloidal rotation velocities of impurity ions such as He^{2+}, B^{5+}, C^{6+}, or N^{7+} with various spectrometers and lines of sight covering the plasma core and edge [212–214]. They require the use of specific NBI sources that intersect the CXRS lines of sight and have radial and temporal resolutions ranging from 0.5 to 5 cm and 0.05 to 20 ms, respectively, depending on which system is used and on the signal-to-noise ratio, affected also by the impurity concentration in the plasma. Impurity densities can be evaluated via forward modelling with the charge exchange impurity concentration analysis (CHICA) framework [249], that supports different models for the neutral beam densities.

Bremsstrahlung

The effective ion charge, Z_{eff}, is a useful parameter to quantify the purity of the plasma and can be computed if the concentrations of all impurities are known. While this can be measured for some species, it is very challenging and experimentally demanding to perform simultaneously for every single impurity species. Alternatively, the effective ion charge can also be estimated by background radiation measurements, since impurity ions in the plasma cause increased bremsstrahlung losses proportional to Z_{eff}.

In AUG, the line-integrated background radiation measured with a Czerny–Turner spectrometer mainly used for CXRS allows the quantification of Z_{eff} if the electron density and temperature profiles are known [250]. The main challenge is the differentiation of the bremsstrahlung background from spectral lines, solved with a robust adaptive method based on Bayesian probability theory [251].

Vacuum ultraviolet spectroscopy

The edge argon and neutral deuterium density can be estimated in AUG via impurity transport modelling with the STRAHL code and data from the SPRED spectrometer, a survey instrument for the vacuum ultraviolet (VUV) region [252]. It measures in the wavelength range of $12-90\,\mathrm{nm}$ and is situated at the mid plane, observing the plasma on a radial line of sight. The SPRED spectrometer is relatively calibrated by comparing VUV lines and visible lines measured with a calibrated visible spectrometer on a similar line of sight in cases where both diagnostics can detect line emission from the same impurity species, namely He^{+}, B^{2+}, C^{2+}, C^{3+}, and N^{3+}.

Grazing incidence spectroscopy

A grazing incidence spectrometer in the VUV region is used in AUG to measure the tungsten density in the plasma [253]. This is possible due to the very fine spectral resolution of the instrument, which can separate closely spaced lines of W emission. Even though there is only one line of sight, the tungsten concentration corresponding to parts of the plasma with different temperatures can be estimated by measuring line intensities of different transitions, if the electron density and temperature profiles are known.

Soft X-rays

The soft X-ray emission in AUG is measured by a set of 8 multi-head pinhole cameras surrounding the plasma with a total of 208 lines of sight [254]. Each head is equipped with an array of photodiodes shielded by a thin beryllium foil to suppress low energy photons, detecting radiation in the 2.3-13 keV range. The diode signals are acquired by two systems with sampling rates of 0.5 and 2 MHz, but low-pass filtered at 80 and 500 kHz, respectively. The extensive coverage provided by the diagnostic allows good quality tomographic reconstruction of two-dimensional soft X-ray emissivity profiles in the poloidal plane [254]. These can be used to infer the argon density in the core of the plasma by modelling impurity transport with the STRAHL code [252].

2.2.3 Magnetic diagnostics

Flux loops and equilibrium

Magnetic pickup coils are one of the most common diagnostics on magnetic confinement fusion devices [255, 256]. There are various types and geometries of coils with different purposes, but all are based on Faraday's law, by which voltages are induced in loops of wire proportionally to the time derivative of the magnetic flux enclosed by them. In AUG, numerous loops with different geometries, such as Rogowski coils, diamagnetic loops, saddle loops and poloidal flux loops at different positions are used to measure the plasma current, loop voltage, Ohmic power, stored energy, magnetic fields and fluxes required for equilibrium reconstructions and plasma position control.

With all this data, as well as the currents in toroidal and poloidal magnetic field coils, the MHD equilibrium of AUG plasmas is typically reconstructed by solving the Grad-Shafranov equation with the CLISTE code [257] on an intershot basis with a coarse temporal resolution. Reconstructions with finer time resolution, typically 1 ms, are computed posteriorly for more detailed analysis of experiments, and support the inclusion of measured plasma profiles in the calculation. In addition, the equilibrium can be reconstructed using more physics input with the IDE scheme [258], which couples the Grad-Shafranov and current diffusion equations. For the fastest computation time, enabling real-time use, the equilibrium is also estimated with a function parameterization approach for evaluating the flux distribution, in which necessary coefficients have previously been determined using a database of several thousand ideal equilibria. Accurate magnetic equilibria are not only useful to assess the plasma shape, but also to map measurements of different diagnostics to the same location and to normalized radial coordinates, for example the normalized poloidal flux radius, ρ_{pol}.

Fast pickup coils

AUG is equipped with an extensive set of high resolution magnetic pick-up coil arrays that measure the temporal derivative of magnetic field components in several locations outside the plasma, partly illustrated in figure 2.3. The signals are acquired with a 2 MHz sampling rate and low-pass filtered at 512 kHz, allowing the detection of a wide variety of fluctuations and MHD modes. There are many Mirnov coils measuring the poloidal magnetic field, as well as ballooning coils measuring the radial magnetic field, both along toroidal and poloidal rings, enabling the determination of mode numbers [259].

2.2.4 Radiation and divertor diagnostics

Bolometry

Bolometry is a standard diagnostic technique in fusion experiments used to measure the power radiated by the plasma. In AUG, two types of complementary bolometers are used: slow but absolutely calibrated metallic foil bolometers [260, 261] and fast absolute extended ultraviolet (AXUV) diodes with no intrinsic calibration [262]. Both systems use sets of pinhole cameras around the plasma, with a respective total of 112 and 256 lines of sight, covering the main chamber and the divertor. The foil bolometers absorb practically all energy of incident photons in a wide spectral range, from 1 eV (visible light) to 8 keV (soft X-rays), and have a time resolution of 1-2 ms, limited by the thermal inertia of the components. The AXUV diodes have a narrower sensitivity range, but much better temporal resolution of 5 µs, limited by the acquisition system, and can be relatively calibrated by comparison with the foil bolometers. The extensive poloidal coverage of the bolometers in AUG allows tomographic reconstructions of two-dimensional emissivity profiles and determination of the radiated power in different areas of the plasma, for example main chamber and divertor, or the confined region inside the separatrix.

D_α radiation

D_α radiation is the visible red light emitted by excited deuterium atoms when electrons fall from the third to second lowest energy level. In AUG, a volume integrated detection of the D_α

emission is installed in the lower divertor, in both the inner and outer regions. The intensity of the D_α emission depends simultaneously on the neutral deuterium and electron density and temperature at the divertor.

Divertor shunt currents

Large electric currents are often observed in the SOL and divertor of tokamaks, consisting of overlaid contributions of thermoelectric effects due to the temperature difference between the inner and outer divertor targets and Pfirsch-Schlüter currents [209]. In AUG, these currents are routinely measured using shunt resistors embedded in the divertor tile mountings, both inner and outer, being dominated by the thermoelectric contributions [263]. Since the inner divertor in AUG typically has very low temperature, the divertor shunt currents are directly related in good approximation to the outer divertor temperature. This allows them to be employed as a simple and robust diagnostic to estimate the outer divertor temperature and power loads, even usable for real-time feedback control schemes [264]. The divertor shunt currents are also used to detect several types of events related to transport to the divertor, such as the L-H transition, I-phase and ELMs.

Divertor Langmuir probes

Langmuir probes (LPs) are a standard diagnostic in fusion research, extensively used to investigate plasmas in the SOL and divertor areas [220, 265]. In AUG, several Langmuir probes are embedded in the divertor tiles of the outer and inner targets, as illustrated in figure 2.4. These flush-mounted probes are used mostly configured as triple probes although some additional single probes are available [266]. Standard triple probes have an acquisition rate of 25 kHz and a spatial resolution of 2.5-3.0 cm at the target. In triple probe configuration, simultaneous measurement of three points along the current-voltage characteristic of closely spaced probes allows a fast and convenient determination of the floating potential, electron temperature and ion saturation current. From this data, heat fluxes to the targets and the divertor detachment state can be evaluated.

Infrared thermograhpy

The heat flux onto the divertor targets can also be inferred from surface temperature measurements obtained with infrared cameras. In AUG, these are installed on the LFS and have a spectral response in the range 3.6-4.9 μm [267]. The lower outer target is usually measured with a spatial resolution of 0.6 mm/pixel, whereas the inner and upper outer targets have resolutions of 1.5 and 2.3 mm/pixel, respectively, due to the different view angles [68]. When mapped to the outer midplane, this corresponds to about 0.1-0.3 mm. The frame rate can be adjusted between 0.3 and 5.5 kHz, depending on the chosen digital resolution, allowing the separation of fast phenomena like ELMs. The cameras do not measure the heat flux directly, but rather the infrared radiation, that depends on the target temperature, from which the target heat flux is computed numerically by solving the two-dimensional nonlinear heat conduction equation [268].

Divertor spectroscopy

A Czerny Turner-like visible spectrometer with lines of sight to the AUG lower divertor is routinely used to evaluate the Stark broadening of the D_δ and D_ε spectral lines [269]. In this setting, the spectrometer measures in the 396-411 nm wavelength range, which is also useful for analysis of nitrogen emission lines. More specifically, N II and N III lines sensitive to the background plasma temperature and density can be measured and used to determine volumetric plasma parameters and the nitrogen concentration in the divertor [270, 271].

Chapter 3

Stationary ELM-free H-mode in AUG

This chapter reports on a regime newly achieved in AUG, the stationary ELM-free H-mode [272], which is the main subject of the thesis. It exhibits several desirable features for future reactors and therefore deserves a detailed description. The discovery and general characteristics of the regime are shown with results from several discharges and diagnostics. The quasi-coherent mode, its main signature in addition to the absence of ELMs, is then studied and interpreted. Finally, a brief comparison with other ELM-free scenarios is presented and the regime is identified as the EDA H-mode.

3.1 General features

The stationary ELM-free H-mode in AUG was discovered in power ramp discharges originally designed to study edge instabilities across the L-H transition and in H-mode. AUG experiments are typically performed at $B_\mathrm{t} = -2.5\,\mathrm{T}$ and often with $I_\mathrm{p} = 0.8\,\mathrm{MA}$, for which the minimum P_LH is about 1 MW [273]. The power of each NBI source at full voltage is 2.5 MW and therefore not optimal for detailed studies of phenomena close to the L-H transition. With reduced NBI voltage, the power can be decreased, but the deposition profile is affected and can peak at the plasma edge. While pulse width modulation techniques can be used for controlled time-averaged power ramps, these are still not ideal due to the large variations of the instantaneous heating power. ICRH does not suffer from this limitation, but poses other challenges related to the efficiency of coupling to the plasma and introduction of impurities due to sputtering. For these reasons, central ECRH, a reliable and almost ubiquitous technique in AUG discharges, was chosen as the preferential heating method for the studies in this thesis, with the exception of a few specific cases.

Each ECRH gyrotron in AUG usually delivers 0.6-0.8 MW to the plasma at full power. In order to produce slow power ramps, some gyrotrons must have their power reduced. For example, running two at the minimum power, 0.2 MW, and the others at 0.6 MW, with appropriate on/off cycles during a discharge, allows the total power to be ramped up to a maximum of 4 MW in fine steps of 0.2 MW [199]. Figure 3.1 shows an example of such a discharge, with an ECRH staircase up to about 1.2 MW and constant deuterium fueling. This is an LSN plasma with the ion ∇B drift pointing towards the X-point (favourable L-H configuration), toroidal magnetic field $B_\mathrm{t} = -2.5\,\mathrm{T}$, plasma current $I_\mathrm{p} = 0.8\,\mathrm{MA}$, corresponding to an edge safety factor $q_{95} = 5.3$, elongation $\kappa = 1.6 - 1.7$, upper and lower triangularity $\delta_\mathrm{up} = 0.10 - 0.12$ and $\delta_\mathrm{low} = 0.33 - 0.39$, respectively, with an average (mean) $\delta_\mathrm{avg} = 0.22 - 0.26$, and gas puff rate of 2.6×10^{21} $\mathrm{e^-/s}$ after the current ramp-up. As the heating power (figure 3.1(d)) is increased, the plasma undergoes several confinement regime transitions indicated by vertical dashed lines: from L-mode to an intermediate I-phase at 2.16 s, followed by an ELMy H-mode at 2.95 s. With another ECRH step the plasma then enters a regime without ELMs at 3.45 s, as evidenced by the disappearance of the large divertor shunt current spikes in figure 3.1(c). The transition to this ELM-free H-mode is accompanied by a strong density increase (figure 3.1(a)), reaching a Greenwald fraction $f_\mathrm{GW} = 0.8$ (figure 3.1(b)), and the appearance of a down-chirping edge instability hereafter referred to as the QCM (figure 3.1(e)). The stored energy in this phase of the discharge is also significantly higher. The density and total radiated power stop increasing after less than a second and the plasma remains stationary for about 10 energy confinement times ($\tau_\mathrm{E} = 0.2\,\mathrm{s}$), with an enhancement factor $H_{98\mathrm{y}2} = 1$ (figure 3.1(b)), until the end of the flattop, being limited in duration only by the inductive current drive.

This scenario is an example of the stationary ELM-free H-mode in AUG, which exhibits several desirable features for future reactors. High density, good energy confinement, possibility of access at low input torque, low input power, without the need of a fresh boronization and with dominant electron heating in a tungsten-walled machine, compatibility with extrinsic impurity seeding, and no impurity accumulation despite the absence of ELMs are its main advantages and constitute a unique set of characteristics not achieved simultaneously in any other known regime of tokamak operation.

Varying the plasma current, shape, heating power, fueling and seeding, steady-state H-modes without ELMs have been achieved in AUG with $H_{98\mathrm{y}2} = 0.9 - 1.3$, $f_\mathrm{GW} = 0.77 - 0.95$,

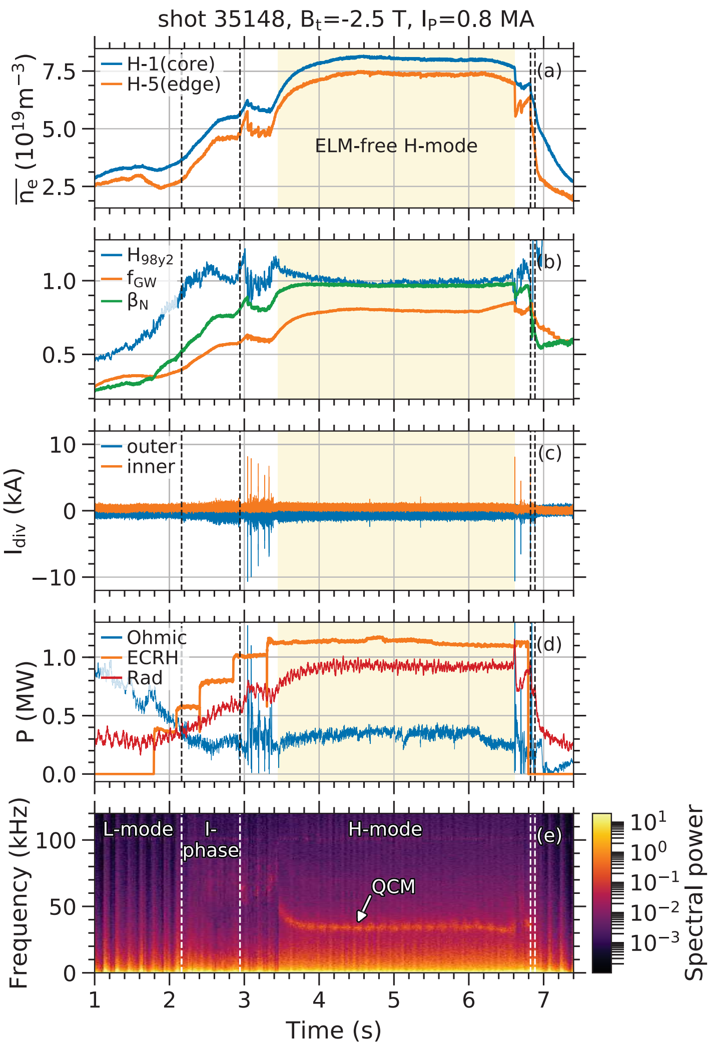

Figure 3.1: Time evolution of different quantities in a discharge with a stationary ELM-free H-mode: (a) line-averaged electron density, (b) performance indicators (confinement enhancement factor, Greenwald fraction and Troyon-normalized ratio of the plasma pressure to the magnetic pressure), (c) divertor shunt currents as ELM markers, (d) heating and radiated power, and (e) O-mode reflectometry phase spectra from edge cutoff layers with electron density $n_\mathrm{e} = 1.4 - 2.9 \times 10^{19}\,\mathrm{m}^{-3}$. The vertical dashed lines indicate regime transitions.

$Z_\mathrm{eff} = 1.1 - 2.0$, and a minimum access power at or slightly above P_LH. These values fit the requirements for ITER [274], making this a very promising mode of operation. However, the plasma can only sustain a limited amount of heating power in an ELM-free state. The Troyon-normalized plasma pressure, $\beta_\mathrm{N} = 0.8 - 1.7$, is slightly lower, and the normalized pedestal collisionality, $\nu_\mathrm{e}^* = 0.7 - 2.8$, and edge safety factor, $q_{95} = 4.5 - 7.8$, so far achieved are still higher than what is predicted for ITER. Different strategies employed to successfully attain these accomplishments are explained in chapter 4 and the overall parameter space is studied in more detail in chapter 5.

Many of the discharges performed for this work were slow power ramps like the one of figure

3.1 because they allow a significant amount of information to be gathered in an efficient way, especially when exploring a newly found regime or a virgin region of the parameter space of a fusion device. By using small power steps with long periods between them, threshold phenomena and stationarity can be studied simultaneously in the same discharge. However, this is actually not a requirement to access the ELM-free regime. In fact, applying all the power at once in a single step also works, as shown in figure 3.2. Shortly after the ECRH step (figure 3.2(c)), there is an L-H transition, with a strong increase in density (figure 3.2(a)), pressure and energy confinement (figure 3.2(b)). The QCM appears during this process and is maintained throughout the discharge (figure 3.2(d)). Most quantities stabilize after about 1.5 s and afterwards remain stationary. All this happens without the occurrence of a single ELM, which is a great advantage of this scenario. Some high-confinement regimes do not have such an easy and safe access strategy. However, the plasma tends to slightly underperform if all the heating power is applied in a single step when compared to a slow ramp, as exemplified by the H_{98y2} marginally below 1 (figure 3.2(b)). This phenomenon is not understood at the moment, but it is not well established and may be just a coincidence, since very few discharges with different power ramp rates were performed.

This discharge also had bremsstrahlung measurements that allowed an estimation of the effective ion charge Z_{eff}, used to assess the purity of the plasma (figure 3.2(b)). Aside from a temporary increase after the L-H transition, Z_{eff} remains stable and below 1.5, showing that there is no impurity accumulation, even though the particle confinement is high and there are no ELMs.

This steady-state ELM-free regime is in fact an H-mode, as it possesses an edge transport barrier leading to a pedestal in density, temperature, and therefore pressure, as shown in figure 3.3. These profiles were obtained in a discharge similar to the one of figure 3.2, but with short NBI blips of 20 ms, added for CXRS measurements of the ion temperature. The electron density and temperature profiles were measured with Thomson scattering (TS) and ECE diagnostics. All quantities were mapped to the outer midplane and radially aligned to have an electron temperature, T_{e}, at the separatrix consistent with the two-point model of the divertor SOL [275]. The SOL cross-sectional area, which is a parameter of this model, can be conveniently estimated using a cross-regime SOL power decay length λ_{q} scaling dependent on the volume-averaged plasma pressure in AUG [68], inspired by investigations at Alcator C-Mod [67]. The resulting T_{e}

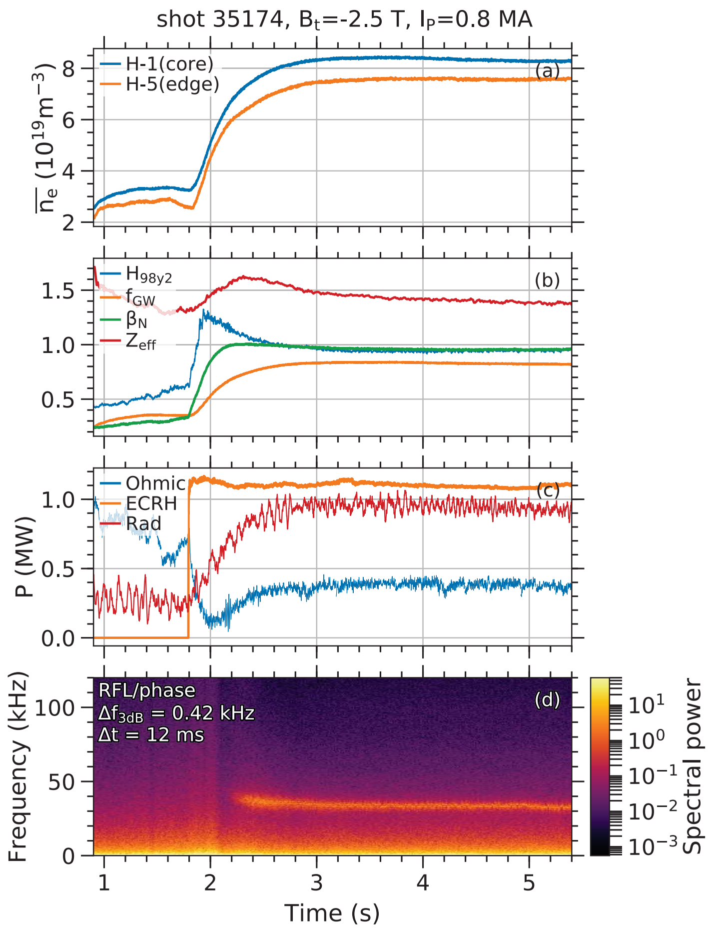

Figure 3.2: Time evolution of different quantities in a discharge with a single power step that allows the plasma to enter the stationary ELM-free H-mode without the occurrence of any ELMs: (a) line-averaged electron density, (b) performance indicators (confinement enhancement factor, Greenwald fraction, Troyon-normalized ratio of the plasma pressure to the magnetic pressure, and effective charge), (c) heating and radiated power, and (e) O-mode reflectometry phase spectra.

at the separatrix is then given by:

$$T_{\mathrm{e,sep}} = C \left(\frac{R_0}{a} \frac{{q_{\mathrm{cyl}}}^2}{\sqrt{\frac{1+\kappa^2}{2}}} \left(\frac{W_{\mathrm{MHD}}}{V} \right)^{0.52} \left(P_{\mathrm{tot}} - P_{\mathrm{rad,sep}} \right) \right)^{\frac{2}{7}}$$
$$C = 0.104\,\mathrm{eV}\,\mathrm{Pa}^{-\frac{1.04}{7}}\,\mathrm{W}^{-\frac{2}{7}}, \tag{3.1}$$

where R_0 and a are the plasma major and minor radii, respectively, q_{cyl} is the cylindrical safety factor, V is the volume and W_{MHD} is the plasma stored energy, P_{tot} is the total power lost by the plasma, and $P_{\mathrm{rad,sep}}$ is the power radiated within the separatrix. P_{tot} is computed by subtracting the time derivative of W_{MHD} from the total heating power, $P_{\mathrm{rad,sep}}$ is obtained from tomography of bolometry data, and the other quantities are readily available from the magnetic equilibrium

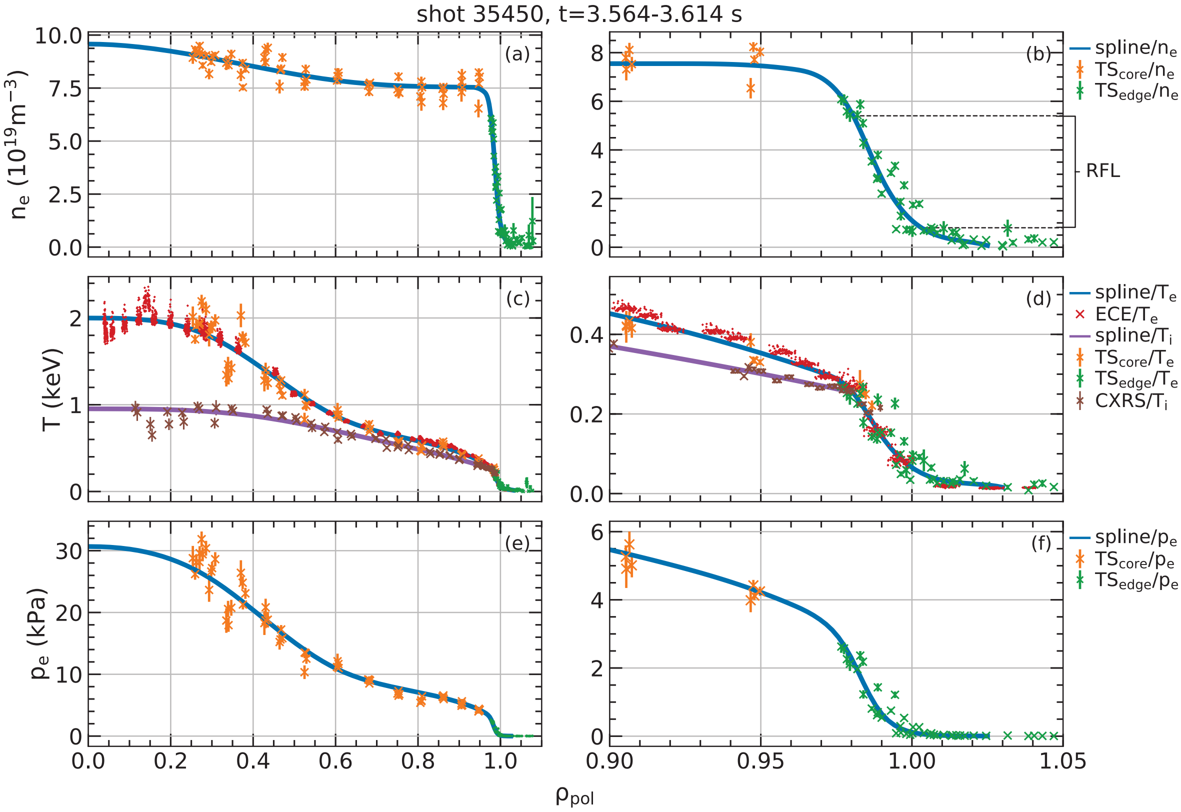

Figure 3.3: Radial profiles of (a)-(b) electron density, (c)-(d) electron and ion temperatures, and (e)-(f) electron pressure during a stationary ELM-free H-mode. The entire profiles are represented in the left-hand side panels (a), (c) and (e), and a zoom in the pedestal region is shown in the right-hand side panels (b), (d), and (f). The density range covered by the reflectometers which detect the QCM is indicated on the right-hand side of (b).

reconstruction. For this discharge, the resulting separatrix temperature, $T_{e,sep} = 65\,\mathrm{eV}$, is lower than the 100 eV usually assumed in AUG H-mode plasmas [276]. The main reason for the difference is that typical H-modes in AUG have about 3-8 MW of external heating power, whereas the discharge considered here has only 1.2 MW.

The core electron density, n_e, profile (figure 3.3(a)) is in general flat, but still with a slight degree of peaking, possibly due to the effect of central ECRH, as is usually observed in ELMy H-mode plasmas [277]. The electron temperature, T_e (figure 3.3(c)), and pressure, p_e (figure 3.3(e)), profiles are peaked due to the central heating. The temperature of the ions, T_i, in the inner core (figure 3.3(c)) is lower than that of the electrons because of the pure electron heating but they almost equilibrate in the outer core, for normalized poloidal flux radius $\rho_{pol} > 0.6$, and eventually equalize at the pedestal top (figure 3.3(d)). T_i directly affects nuclear fusion reaction rates, whereas T_e only indirectly does so, by driving heat transfer between electrons and ions. Therefore, T_i is the ultimate parameter to increase in a reactor, which, for a dominantly electronheated plasma, translates to coming as close as possible to T_e, not only in the pedestal, but also in the core, where the density and temperature are higher. The ion to electron temperature ratio, T_i/T_e, is governed both by the net collisional energy exchange between the two species, embodied in the temperature equilibration time, $\tau_{eq} \propto T^{3/2}/n_e$, and by the energy losses, represented by the energy confinement time, τ_E, with T_i/T_e roughly proportional to τ_E/τ_{eq}. The core $T_i/T_e = 0.5$ in this discharge is not ideal, but will probably be improved in large-scale reactors simply because of the higher τ_E due to their bigger size. The electron-ion coupling can in principle also be further increased by operating at a higher density. On the other hand, the temperature in a reactor will also be higher, resulting in a longer τ_{eq}, which goes in the opposite direction. Therefore this subject deserves more detailed studies and modelling in order to better extrapolate the results of the stationary ELM-free H-mode to future reactors.

The ability to maintain a steady-state edge pedestal without the relaxation caused by ELMs is a surprising and positive feature of this H-mode. It implies an alternative, more continuous edge transport mechanism, possibly related to the QCM, visible for example in the reflectometry spectrograms of figures 3.1(e) and 3.2(d). However, large ELMs reappear when the heating power is further increased, as exemplified in figure 3.4, from 3.95 s onward. Between 3.45 and 3.95 s the plasma was ELM-free, due to the optimal heating power, and there was no impurity accumulation. In fact, a strong reduction of the core tungsten density, n_W, measured by grazing incidence spectroscopy, is observed in this phase (figure 3.4(c)). Together with the electron density increase, this amounts to a significant reduction of the tungsten concentration, $c_W = n_W/n_e$, which drops below 10^{-5}. This happens even without ELMs to flush impurities and enables operation without fresh boronization for wall conditioning. While the tungsten source from sputtering is also reduced due to the absence of ELMs, this cannot solely account for the purity of the plasma, otherwise traditional ELM-free phases would not suffer from tungsten accumulation and radiative collapse.

Besides optimal heating power, adequate fueling is also required to maintain a steady-state ELM-free H-mode. In fact, when enough ECRH power is applied in L-mode but the gas puff is too low, the plasma transitions to a non-stationary ELM-free H-mode without the QCM, whose density uncontrollably increases until the occurrence of ELMs. By contrast, changing only the gas puff rate to a moderate value results in a well-behaved stationary ELM-free H-mode with the QCM. The influence of fueling on this regime is studied in more detail in section 5.1.

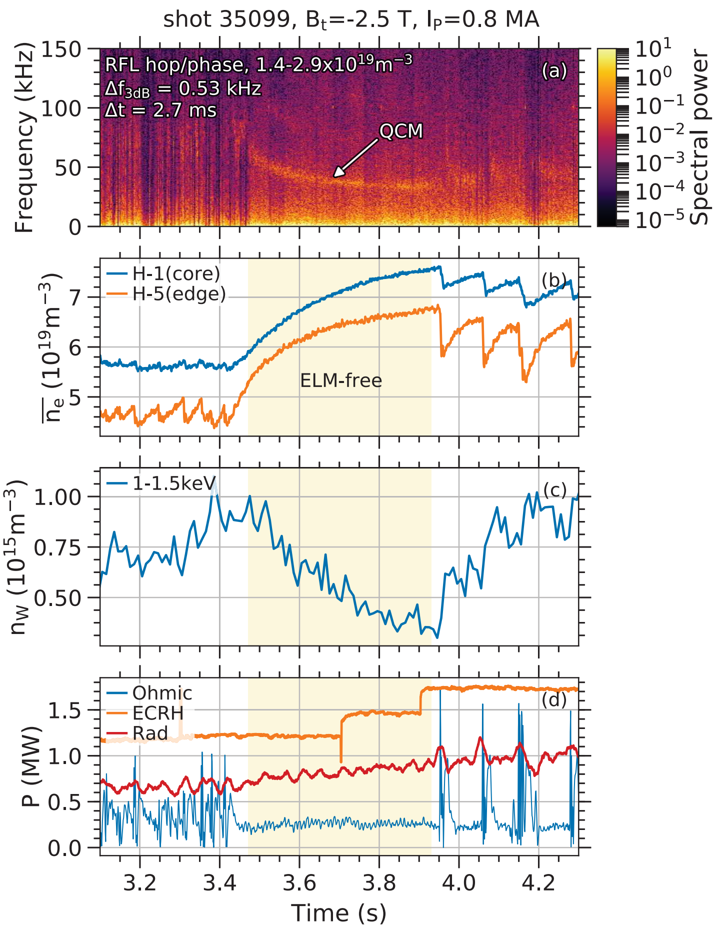

Figure 3.4: Time evolution of different quantities in a discharge with an ELM-free H-mode period and ELMs: (a) edge reflectometry phase spectra, (b) line-averaged electron density, (c) core tungsten density, (d) heating and radiated power. The sudden density drops and transient excursions of the ohmic power are due to ELMs.

3.2 Quasi-coherent mode

As mentioned in the previous section, the QCM is an instability that appears in stationary ELM-free H-mode plasmas, usually detected as a down-chirping oscillation of the edge plasma density. In fact, not a single discharge in this regime without the QCM has been observed, making it an ubiquitous feature that deserves some attention.

The QCM can be measured not only by reflectometers, but also by other diagnostics, such as magnetic pick-up coils, interferometry and ECE. Figure 3.5(a-b) shows spectrograms of a reflectometer and a magnetic pick-up coil in the outer midplane in an ELM-free plasma with constant heating power and fueling from 1.8 s onward, similar to that of figure 3.2. The QCM is visible as a relatively broad peak in frequency, starting at about 65 kHz at 2 s and gradually decreasing to 32 kHz within half a second. The coherence between the two signals as a function

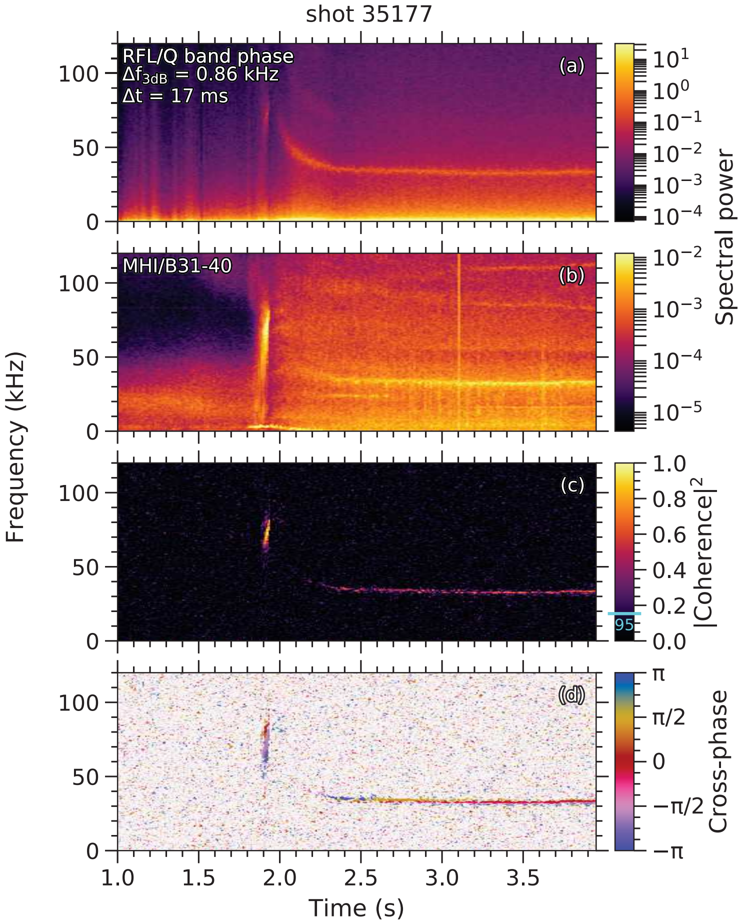

Figure 3.5: Spectrograms of O-mode reflectometry phase (a) and time derivative of the radial magnetic field at the LFS, measured by the pick-up coil closest to the plasma (b), and magnitude-squared coherence (c) and cross-phase (d) between them as a function of time, in a discharge with a stationary ELM-free H-mode.

of time and frequency, presented in figure 3.5(c), shows the same oscillation with a squared magnitude much higher than the neighboring frequencies, clearly above the 95 % confidence threshold [278], indicated as a horizontal blue line in the color scale, and with a stable cross-phase in time (figure 3.5(d)). This means that both diagnostics are in fact detecting the same mode. While the reflectometer signal is caused by density fluctuations, the pick-up coil measures the time derivative of the radial magnetic field, showing that the QCM is an electromagnetic instability. However, most of the pick-up coils cannot detect the mode, and the one of figure 3.5 is actually the coil closest to the plasma, indicating that the magnetic signal of the QCM has a strong radial attenuation.

With constant input parameters, the initial frequency of the QCM at the transition to the ELM-free regime can range from 40 to 80 kHz and then decreases to a constant average value between 20 and 40 kHz as the plasma evolves. Its name, quasi-coherent mode, comes from its

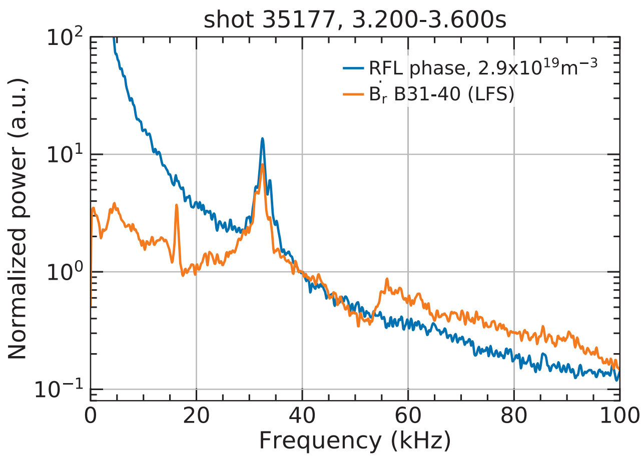

Figure 3.6: Normalized power spectra of reflectometry phase (blue) caused by density fluctuations and radial magnetic field fluctuations (orange) measured by the magnetic pick-up coil closest to the plasma on the LFS.

relatively large frequency width, exemplified in the Welch power spectra [279] of figure 3.6, computed over a long steady-state period of the discharge previously shown in figure 3.5. In this case, the full width at half maximum (FWHM) is $\Delta f = 6\,\mathrm{kHz}$, corresponding to 19 % of the central frequency $f = 32\,\mathrm{kHz}$. This relative width, $\Delta f/f$, measured over long timescales, can vary roughly from 5 to 50 %, depending on discharge parameters, being therefore much larger than the frequency width of typical coherent MHD modes. However, at short timescales, on the order of few milliseconds, the QCM can actually be quite coherent, with $\Delta f/f < 1\,\%$. But this instantaneous frequency varies considerably with time, even in stationary discharges, such that in longer timescales, comparable to those of more global plasma phenomena, its spectrum is usually rather broad.

The QCM is not the only instability detected by both reflectometry and magnetic pick-up coils in this type of ECRH-heated H-modes. In figure 3.5(c), at 1.8 s, a region with very high magnitude-squared coherence, close to 1, exists around 70 kHz. This is actually a group of regularly spaced peaks in frequency, known as edge coherent modes (ECMs) [280], which appear after the L-H transition, usually as an up-chirp, before the development of the QCM. When the heating power is slowly ramped up, like in the discharge of figure 3.1, or if the gas puff is too low, the ECMs can exist for a long time, during I-phases, nonstationary ELM-free H-modes and ELMy H-modes, disappearing and reappearing with each ELM. But if the heating power is applied at once with adequate fueling, like in the shots of figures 3.3 and 3.5, there is no ELMy phase and the ECMs live only for a short period of time after the L-H transition, before the QCM appears and the stationary ELM-free regime settles down.

As the QCM is only detected by few and widely spaced apart pick-up coils, it is not possible to determine its wavelength and mode numbers from the magnetic signals, as is usually done with MHD modes. In this case, PCR [238] is a diagnostic better suited for the task. The local perpendicular wavenumber of the mode, $k_\perp$, can be computed using the cross-phase between reflectometry phase signals of antenna pairs and the perpendicular distance between the reflection points at the cutoff surface with respect to the magnetic field lines. It is then combined with the frequency of the mode to determine its perpendicular velocity, $v_\perp$, and with the magnetic equilibrium to estimate the toroidal mode number, n, assuming straight field lines. These results, calculated with data from both microwave bands of the PCR diagnostic, are shown in figure 3.7 for the ECMs (a) and the QCM (b), obtained from two ECRH-heated plasmas with low and high fueling levels, respectively. The ECMs feature a multi-peak structure with $f = 60-110\,\mathrm{kHz}$, corresponding to $n = 6-10$, with $k_\perp = 0.15-0.3\,\mathrm{cm}^{-1} \approx 0.03\,\rho_\mathrm{s}{}^{-1}$, where ρ_s is the mixed Larmor radius, computed with the electron temperature and ion mass. They propagate in the electron diamagnetic direction in the lab frame with $v_\perp = 20-24\,\mathrm{km\,s^{-1}}$. The ECMs are strongly seen by many pick-up coils, so their properties can also be determined from the magnetic signals and they are consistent with the PCR results, showing the validity of the reflectometry technique. Contrary to the ECMs, the QCM is almost invisible to the coils and its properties must be determined mostly from PCR data alone, as exemplified in figure 3.7(b). In this period it has $k_\perp = 0.6-0.7\,\mathrm{cm}^{-1} \approx 0.06\,\rho_\mathrm{s}{}^{-1}$, $n = 20-23$, and $v_\perp = 5.5-6.4\,\mathrm{km/s}$, also in the electron diamagnetic direction in the lab frame. Although the exact values of these quantities depend on the plasma parameters for both instabilities, the QCM always appears at a higher density and is less coherent, smaller and slower (in the lab frame) than the ECMs. Possible reasons for the large velocity difference in the lab frame include different phase velocities of the instabilities, different location in the radial electric field well and changes in the $E\times B$ profile itself. The weak signature of the QCM in the pick-up coils may be explained by a strong radial decay of its magnetic component, possibly due to the high $k_\perp$. The relation between the two quantities can be derived for a field-aligned perturbation using Laplace's equation in a slab approximation [105].

The ECMs are detected by different diagnostics in the pedestal. Fixed-frequency O-mode reflectometers have measured them in the steep gradient region, close to the separatrix and even weakly in the SOL. An ultra-fast swept X-mode reflectometer has also localized them in the steep gradient region and up to the pedestal top, corresponding to $0.93 < \rho_\mathrm{pol} < 0.99$ [280]. While this radial localization is possible in the low density plasmas that have ECMs, the higher density of

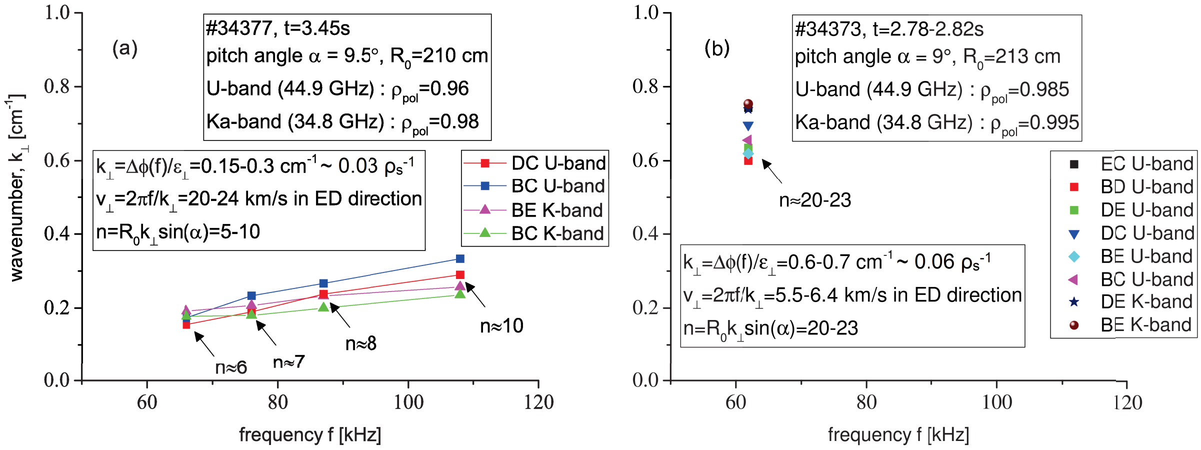

Figure 3.7: Perpendicular wavenumber as a function of frequency for ECMs (a) and QCM (b) computed with PCR.

the plasmas with the QCM renders the task much more challenging, because the reflectometers cannot probe up to the pedestal top in such cases. The QCM is measured by several diagnostics in the steep gradient region of the pedestal and close to the separatrix. Figure 3.3(b) shows the density range covered by the O-mode reflectometers that measure the QCM on the LFS. It goes from the near SOL to above the middle of the pedestal, but does not reach the pedestal top, being limited to $\rho_{\mathrm{pol}} \geq 0.98$. The Li-BES [240] and thermal helium beam diagnostics [281, 282] can also detect the QCM, but are limited to low densities and cannot penetrate the plasma beyond the steep gradient of the pedestal either. It is hypothetically possible that the QCM also exists at lower ρ_{pol}, but up to now the radial extent of the QCM has not been determined precisely and it is not known how far it extends to or even beyond the pedestal top.

A diagnostic that can measure density fluctuations, not only in the edge, but also in the core of AUG plasmas, is interferometry [223]. Using the different channels of the DCN laser interferometer [222], the radial localization of the modes can be roughly inferred, although not precisely due to the line-integrated nature of the interferometry principle and the limited number of chords. Figure 3.8 shows spectrograms of the interferometry signals for each of the channels, which cross different regions of the plasma, in a discharge with an ELM-free period. In this shot, the QCM is strongly seen only by the edge chords H-4 (figure 3.8(d)) and H-5 (figure 3.8(e)), with the outermost channel H-5 having the largest amplitude. This corroborates the idea that the QCM is radially localized to the edge of the plasma. The apparent double frequency band structure is just an artefact caused by the 10 kHz modulation of heterodyne detection scheme of the DCN system, the lower frequency branch being the correct one in this case. In most discharges, however, the QCM is also clearly seen in some of the core channels of

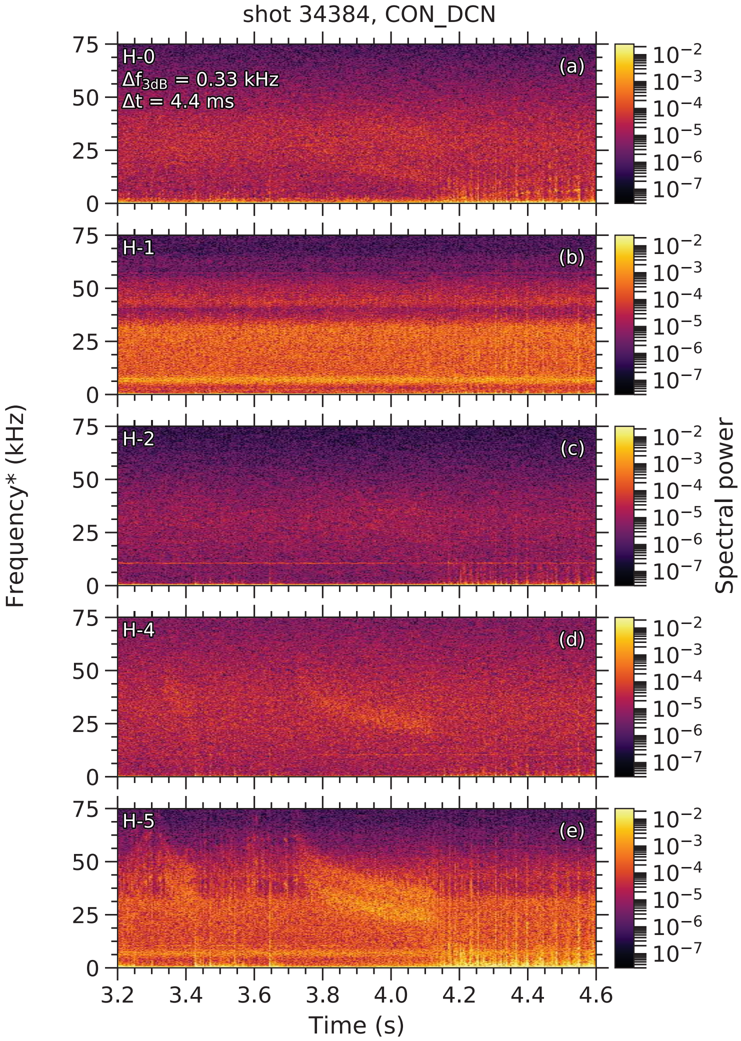

Figure 3.8: Interferometry spectrograms from the innermost (a) to the outermost (e) channel in a discharge with an ELM-free period and the QCM. The frequency has been downshifted by 10 kHz to account for the heterodyne detection of the DCN system.

the interferometer, but with a weaker signal than in the edge channels. Assuming the QCM is radially localized in the edge, its appearance in the core channels might be just due to the fact that the chords must always cross the edge region too. In fact, the QCM has never been detected in the core channels of the interferometer without being measured also by the edge channels.

ECE is also often used to detect and localize instabilities by measuring the fluctuations in the radiated power at the cyclotron frequency, which in ideal, optically thick conditions is proportional to the local electron temperature. The QCM is usually visible in a few channels of the ECE radiometer in the steep gradient region and close to the separatrix, corresponding to $0.98 \leq \rho_{\mathrm{pol}} \leq 1.01$. However, near the separatrix and in the SOL the plasma can be optically thin, such that the oscillating signals may actually be caused by density, rather than temperature fluctuations, so the data must be interpreted with care. Some ECE channels in the inner core of the plasma are also able to detect the QCM, but if it was really present in the whole plasma, it is unlikely that it would stay undetected by most magnetic pick-up coils. A hypothetical explanation for the surprising appearance of the QCM in the core ECE channels is the radiation from the core being affected by the edge density perturbation, possibly also via refraction. In order to test this hypothesis, two-dimensional radiation transport modelling would be required.

Besides frequency spectrum, toroidal mode numbers and radial localization, another important aspect to characterize instabilities is their poloidal structure in general and, more specifically, their ballooning nature or HFS / LFS symmetry. Few diagnostics can provide such information, but the O-mode FMCW reflectometer in AUG is such an exception, having the unique capability of measuring density profiles and fluctuations on both HFS and LFS [227, 283]. In ECRH discharges with low fueling, ECMs are often measured by this diagnostic in the confined region, at the HFS and LFS [280]. In contrast, the QCM has not yet been detected in the HFS, though the asymmetry in the measurements is likely also due to reasons other than an asymmetry in the mode itself. Figure 3.9 shows density profiles and spectrograms of the homodyne reflectometer signal, a proxy for density fluctuations, in both sides of the plasma, in a pair of identical discharges with a slow ECRH ramp, similar to the one of figure 3.1. ECMs are visible in the LFS (figure 3.9(d)), followed by the QCM that appears in the ELM-free H-mode with additional heating power. In the HFS (figure 3.9(b)), however, neither of the modes can be measured. Since the ECMs are detected on the HFS in different discharges, something could be perturbing the reflectometry measurements in this discharge. In fact, the density profiles of a paired shot in which the FMCW operated in swept mode can show this. The LFS profiles of figure 3.9(c)) have the expected H-mode shape, with an edge transport barrier (ETB) just inside the separatrix. As a result, the cutoff layer in which the density fluctuations are measured in the LFS, indicated by the blue line in the figure, is located at $\rho_{\mathrm{pol}} \approx 0.99$. But in the HFS (figure 3.9(a)) the profiles are very different and there is a steep gradient in the SOL. This is the high-field side high density front (HFSHD) [284], which has been shown to often reach the midplane and the reflectometer line of sight [285]. The HFSHD prevents the reflectometer beam from penetrating the plasma, resulting in cutoff layers at $\rho_{\mathrm{pol}} > 1.02$, explaining why not even the ECMs can be measured in the HFS. This means that no statement can be made about the poloidal structure of the QCM based on direct measurements, since the HFSHD has so far always been present in the stationary ELM-free H-mode discharges, not allowing a proper probing of the HFS. This, together with the impossibility of accurately determining the velocity of the QCM in the plasma frame of

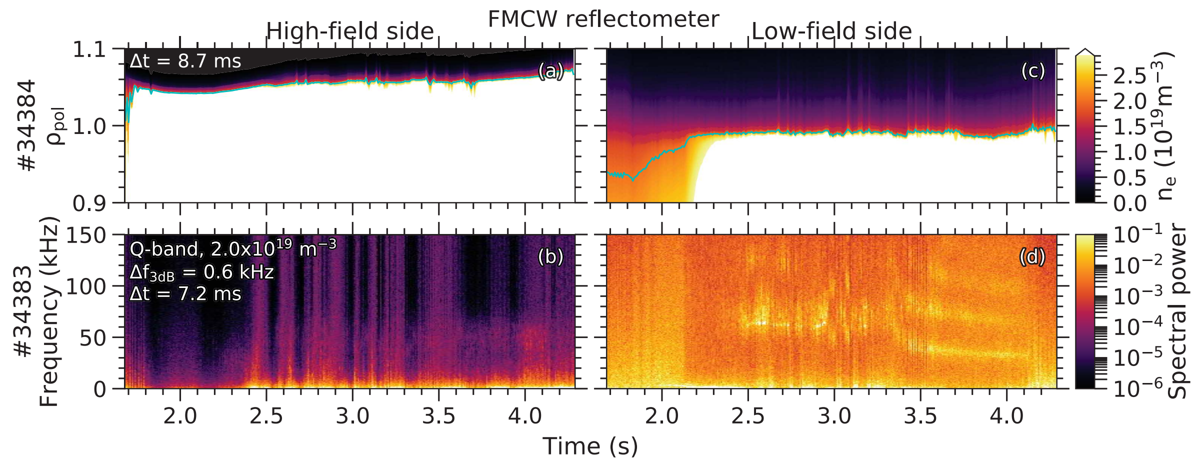

Figure 3.9: Density profiles from FMCW reflectometry (a,c) and fluctuations from fixed-frequency homodyne reflectometer power spectra (b,d) as a function of time in a pair of identical discharges with ELMy and ELM-free H-modes. The left-hand side (a-b) contains HFS measurements and the right-hand side (c-d) contains LFS measurements. The blue lines in (a,c) shows the radial location of the layer with the critical density corresponding to the cutoff frequency of the microwaves that lead to the fluctuation signals in (b,d).

AUG so far, due to the absence of E_r measurements, prevents an identification of its underlying instability.

Most known high confinement ELM-free regimes have edge instabilities believed to play an important role in the pedestal structure [64]. Given the ubiquity of the QCM in the stationary ELM-free H-mode in AUG and its presence in the plasma edge, it is natural to hypothesize that it regulates pedestal transport, possibly being one of the key ingredients to access and maintain the regime. In order to investigate this idea, it is useful to correlate the appearance and disappearance of the QCM with changes in plasma parameters. The discharge shown in figure 3.10 is particularly suitable for this analysis, because the heating power was kept very close to the lower threshold between ELMy and stationary ELM-free H-mode, resulting in a period of alternation between the two regimes, from 3.33-3.55 s. The ELMy H-mode features fast, high frequency ECMs, easily detected by the magnetic pick-up coils (figure 3.10(c)), while the stationary ELM-free H-mode features the QCM, with lower velocity, frequency, and wavelength, hardly seen by the coils, but clearly visible for example in an ECE channel close to the separatrix (figure 3.10(d)). The reflectometer (figure 3.10(a)) can detect both instabilities, which do not coexist, resulting in the spectral peaks jumping back and forth between low and high frequency. This alternation is correlated with changes in several edge and divertor parameters. Figure 3.10(e) shows the ECE radiation temperature measured by edge channels which display an oscillation synchronized with the mode alternation. When the QCM appears, the edge line-integrated density and temperature in ECE channels within the confined region decrease, while the temperature and density measured by divertor Langmuir probes increases, as shown in figure 3.10(f). A rise in the divertor shunt currents is also observed. Low frequency oscillations in the SOL ECE signals and in the poloidal magnetic field close to the divertor are concomitant with these effects. The changes in the divertor happen with a small time delay with respect to the changes in the pedestal, which suggests causality: the QCM appears to drive an increase of particle and energy transport in the pedestal region, expelling plasma to the divertor. This may explain the steady-state pedestal and absence of ELMs, as the enhanced transport could prevent the plasma from reaching the peeling-ballooning instability boundary.

The view just presented, while self-consistent and supported by experimental data, is based on indirect observations of effects presumably caused by the QCM. In order to directly measure the transport driven by the mode itself, different diagnostic techniques would have to be used. For example, inserting a Langmuir probe array in the plasma and measuring local electron density, temperature, and plasma potential fluctuations with high temporal resolution would allow an estimation of the particle and energy fluxes at the QCM frequency. However, it is extremely challenging to have the probe reach and go beyond the separatrix in these type of discharges in AUG, due to the extreme heat loads that the probe materials cannot sustain. But it might be possible, given that such measurements have been made in similar discharges in Alcator C-Mod [120]. Since the QCM is also visible in the near SOL, the reciprocating probe of AUG could be plunged just close enough to the separatrix to measure some of the QCM transport in specially designed low power discharges, but this has not been tried yet. In the future, the new heavy ion beam probe in AUG [286] may also contribute to this type of studies and even allow extensions to inner, hotter regions of the plasma, but at the moment it is still in commissioning. Therefore one cannot exclude the possibility that the enhanced transport attributed to the QCM is caused by different instabilities, not so easily detected. In fact, the stationary ELM-free H-mode is also accompanied by rich magnetic activity covering a wide frequency range, as exemplified in figure 3.11, taken from the same discharge of figure 3.5, but from a different pick-up coil. These fluctuations of the radial magnetic field at the LFS range from a few to hundreds of kilohertz and have a coherent, quasi-coherent, or even broadband turbulent nature. The role of these instabilities in the ELM-free H-mode is not yet understood, but they could hypothetically have a function similar to that of the QCM.

Besides experimental measurement and characterization, complementary strategies such as

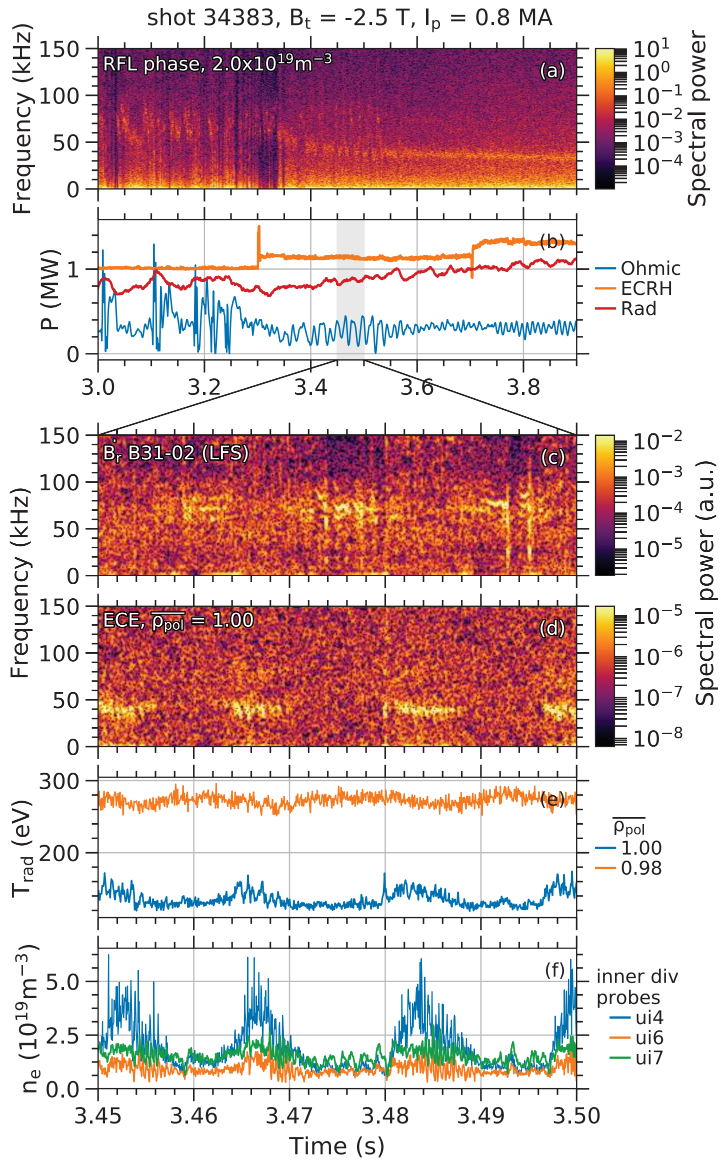

Figure 3.10: Time evolution of different quantities around the transition to the stationary ELM-free H-mode: (a) edge reflectometry phase spectra, (b) heating and radiated power, (c) LFS radial magnetic field spectra, (d) ECE spectra, (e) ECE radiation temperature, (f) electron density measured by Langmuir probes in the divertor. The time period in the shaded region of panel (b) is zoomed in panels (c)-(f) to highlight the regime alternation.

modelling and simulations should be employed to identify the different instabilities present in the stationary ELM-free H-mode. Transport, MHD, gyrofluid and gyrokinetic codes can be used not only to reproduce and make comparisons with the experiments, but also to provide quantities and investigate parameters not accessible with current devices and diagnostics. This will give useful insight and hopefully lead to a better understanding of the QCM and other instabilities present in the regime.

To summarize, the ubiquitous QCM appears to drive enhanced pedestal transport, likely

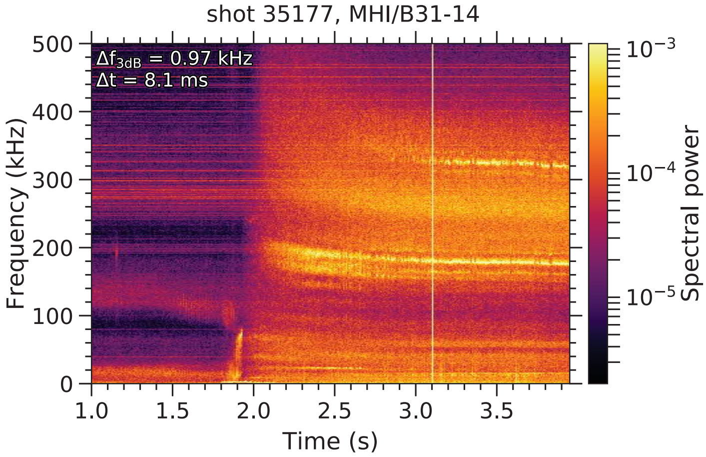

Figure 3.11: Spectrogram of a pick-up coil measuring the time derivative of the radial magnetic field at the LFS, showing rich activity in the stationary ELM-free H-mode.

providing the required pressure control to maintain the stationary ELM-free H-mode, although a definitive proof has not been achieved and other instabilities might also play an important role. More experimental data, modelling and studies are required to unequivocally identify the underlying instability of the QCM and fully understand its impact in the plasma.

3.3 Comparison with the EDA H-mode

The stationary ELM-free H-mode is a newly discovered regime in AUG, so it is important to compare it to other known regimes without ELMs, including those achieved in different machines. The comparison here is focused on the EDA H-mode [102, 103], I-mode [150] and quiescent H-mode (QH-mode) [127], which are some of the most researched ELM-free regimes in tokamaks. A special emphasis is placed on the EDA H-mode, which is the most similar to the AUG ELM-free H-mode.

The I-mode is obtained mostly with the ion ∇B drift pointing away from the active X-point (unfavourable L-H configuration), which is not the case for the stationary ELM-free H-mode, that has never been observed in such a magnetic configuration. Besides that, the I-mode features a marked temperature, but not density pedestal, whereas the ELM-free H-mode has a very clear pedestal in density, achieving values higher than most H-modes in general. The QH-mode also has a low density and is only obtained with high NBI power and torque, contrary to the stationary ELM-free H-mode in AUG, which so far requires a significant ECRH fraction. Furthermore, one of the most distinguishing features of the QH-mode is the presence of the EHO, a coherent MHD instability characterized by a fundamental toroidal mode number $n = 1$ and several harmonics, up to $n \approx 10$, clearly measured by magnetic pick-up coils, being therefore very different from the QCM.

Among the currently known ELM-free regimes, the EDA H-mode found in Alcator C-Mod is definitely the most similar to the stationary ELM-free H-mode in AUG, as they share several key characteristics. Both are obtained with significant electromagnetic wave heating and have good confinement, with a pedestal in density and temperature, but no or very small ELMs. The EDA H-mode also does not exist if the fueling is too low, resulting in transient, impurity accumulating plasmas [102, 103]. In terms of dimensionless parameters such as q_{95}, β_{N} and ν_{e}^{*}, the stationary ELM-free H-mode in AUG overlaps with a part of the EDA H-mode parameter space [106], although at a higher f_{GW} and typically lower δ_{avg} than in C-Mod. One should note, however, that a large portion of the parameter space for the regime in AUG remains to be explored. Practical differences between the two regimes include the use of ion cyclotron range of frequencies (ICRF) heating in C-Mod, compared with ECRH in AUG, and the need of a fresh boronization for wall conditioning in C-Mod, which is not required in AUG, possibly due to the impurity-expelling properties of ECRH.

The EDA H-mode also features an edge down-chirping QCM which has been shown to produce outward plasma transport [104, 105, 120], enabling steady-state ELM-free operation with a pedestal. In C-Mod, the QCM has a higher frequency in the lab frame than in AUG, usually starting above 200 kHz and subsequently decreasing to 50-150 kHz as the plasma evolves [104]. However, this quantity is not an intrinsic characteristic of the mode, as it depends on the plasma rotation. The QCM frequency width in C-Mod, $\Delta f/f = 5-20\,\%$, is similar to the AUG measurements. The poloidal wavenumber of the QCM is higher in C-mod, $k_\theta = 1.5-2\,\mathrm{cm}^{-1}$ [120, 122], which means the wavelength is lower, but so is the size of the machine, such that the mode numbers are comparable. Like in AUG, the magnetic signature of the QCM in C-Mod was not easily detectable in the wall-mounted pick-up coils, having been measured only by inserting fast-scanning magnetic probes near and up to the separatrix [105, 120]. Regarding radial localization, the C-Mod QCM is measured in the steep gradient region of the pedestal or at the separatrix and near SOL, which is consistent with AUG observations, although there is conflicting evidence about its position relative to the radial electric field well and velocity in the plasma frame [122]. The two main candidates for the QCM nature proposed in C-Mod, namely a resistive X-point mode [123] and an electron drift-wave with interchange and electromagnetic contributions [120], both seem to be consistent with AUG observations, since measurements of differentiating quantities are still lacking in AUG. Besides the QCM, high frequency coherent and broadband magnetic fluctuations up to 400 kHz have also been detected in EDA H-modes in C-Mod [287].

The overall similarities between the stationary ELM-free H-mode in AUG and the EDA H-mode in Alcator C-mod are numerous and significant. Further comparisons between AUG and C-Mod results are made throughout the thesis whenever appropriate. It is most likely that this is a single regime observed in two different machines, which constitutes a powerful opportunity to extend the understanding of its physics and increase the reliability of its extrapolation to large-scale reactors. For this reason, the stationary ELM-free H-mode in AUG is hereafter referred to as EDA H-mode.

Chapter 4

Path towards reactor relevance

The EDA H-mode in AUG is a promising regime with various positive qualities, but also important limitations which must be overcome in order to make it suitable for future energy-producing reactors. This chapter explains different methods and experiments performed with the goal of bringing the regime closer to reactor relevance, namely: extending the power window with strong shaping, detaching the divertor with nitrogen seeding, and cooling the pedestal with argon seeding.

4.1 Extending the power window with strong shaping

4.1.1 Shape

One of the main limitations of the EDA H-mode in AUG, especially in the form presented in chapter 3, is the inability to withstand large amounts of heating power in an ELM-free state. While the enhanced transport likely caused by the QCM is enough to maintain a stationary pedestal under the right conditions, large ELMs reappear when the heating power is increased too much. With a commonly used plasma shape in AUG, shown in figure 4.1(a), the ELM-free scenario only exists within a relatively narrow power window of roughly $\Delta P \approx 0.2\,\mathrm{MW}$, as previously exemplified in figure 3.4. This corresponds to about $\Delta P/P_{\mathrm{LH}} \approx 20\,\%$, where P_{LH} is the L-H power threshold, but it is difficult to determine the values precisely, since the minimum ECRH power per heating step in AUG is $0.2\,\mathrm{MW}$. As a result, this scenario is not robust and requires a fine control of the heating power to maintain stationarity without ELMs. Besides that, and more importantly, a burning or near-burning plasma in a fusion reactor will likely have a higher normalized heating power, P/P_{LH}, when alpha heating is included in the calculation.

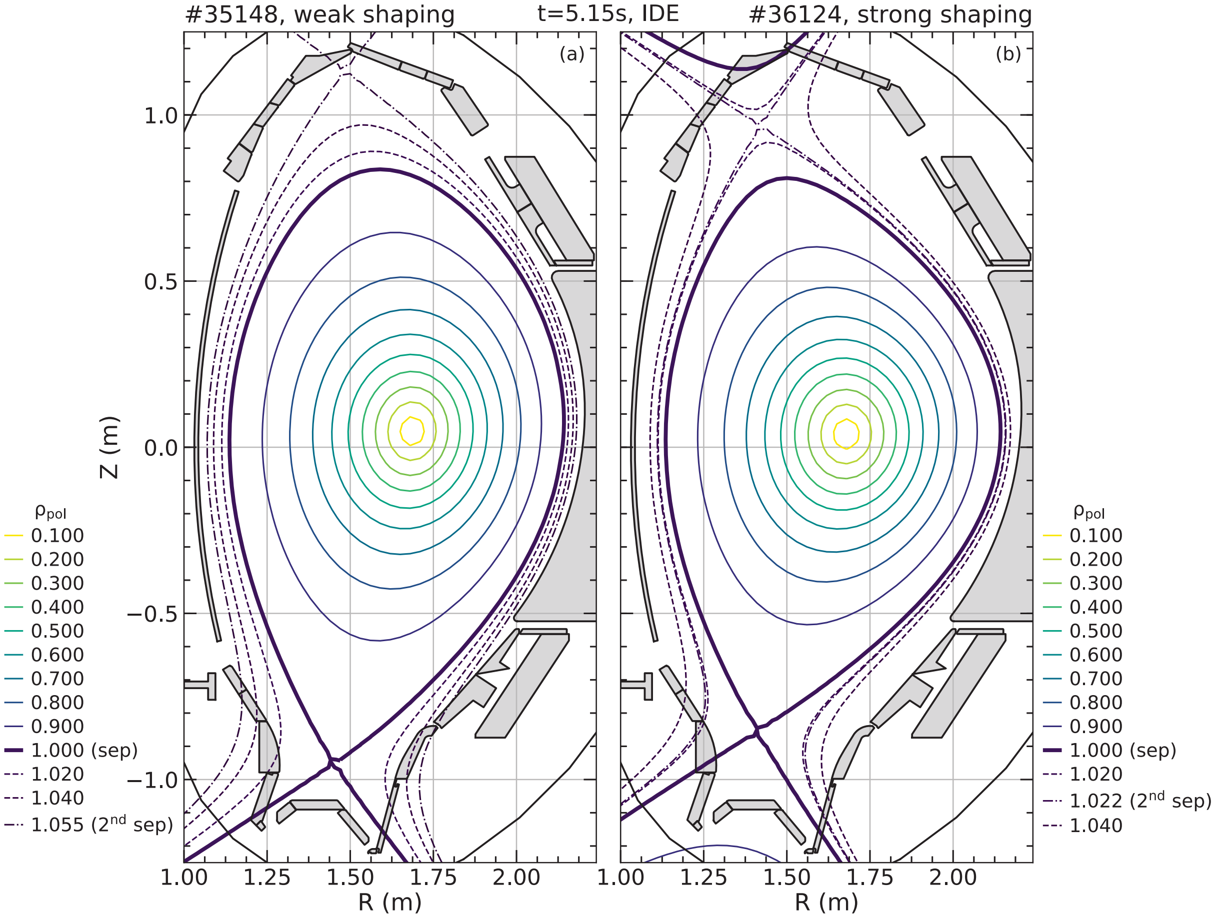

Figure 4.1: Poloidal section of AUG with flux surfaces of magnetic equilibria in (a) weakly shaped and (b) strongly shaped EDA H-modes. The primary separatrix is indicated by the thick solid lines and the secondary separatrix by the thin dash-dotted lines.

Therefore, any scenario in present-day machines should be able to withstand a significant amount of external heating power if it is to be taken seriously as a promising candidate for future devices.

Since ELMs are the limiting factor in terms of the power that can be handled by the EDA H-mode in AUG, a possible way to tackle the problem is to make the plasma less unstable to the instabilities that trigger ELMs. Although ELMs are not a completely understood phenomenon in tokamaks due to their multiplicity of types and rich dynamics, it is generally accepted that type I ELMs are well modelled by MHD peeling-ballooning modes [39], whose stability limits can be extended by strongly shaping the plasma. With this in mind, a new plasma shape with high triangularity was developed in AUG with the goal of increasing the power tolerated by the EDA H-mode. Figure 4.1(b) shows a poloidal section of the tokamak and this new plasma shape from the magnetic equilibrium reconstructed with the IDE package [258]. The flux surfaces are colored according to their ρ_{pol} and drawn in thin solid lines inside the confined region and dashed ones in the SOL. The primary separatrix is indicated by the thick solid line and the secondary separatrix by the thin dash-dotted line. The strongly shaped plasma is clearly more triangular than its weakly shaped counterpart of figure 4.1(a).

However, AUG was not designed specifically for high triangularity plasmas and the placement of its shaping coils imposes strong limitations on what can be achieved. For example, it is difficult to significantly increase the triangularity without affecting other important shaping parameters, such as elongation and proximity to double null. Table 4.1 shows a comparison of several shape parameters of the weakly and strongly shaped plasmas of figure 4.1. The geometric major radius R_{geo}, horizontal and vertical minor radii a and b, inverse aspect ratio ε, elongation κ, and lower, upper and average triangularities δ_{low}, δ_{up} and δ_{avg} of the plasma are defined as:

$$R_{\text{geo}} = \frac{R_{\text{max}} + R_{\text{min}}}{2}, \tag{4.1}$$

$$a = \frac{R_{\text{max}} - R_{\text{min}}}{2}, \tag{4.2}$$

$$b = \frac{Z_{\text{max}} - Z_{\text{min}}}{2}, \tag{4.3}$$

$$\varepsilon = \frac{a}{R_{\text{geo}}}, \tag{4.4}$$

$$\kappa = \frac{b}{a}, \tag{4.5}$$

$$\delta_{\text{low}} = \frac{R_{\text{geo}} - R_{\text{low}}}{a}, \tag{4.6}$$

$$\delta_{\text{up}} = \frac{R_{\text{geo}} - R_{\text{up}}}{a}, \tag{4.7}$$

$$\delta_{\text{avg}} = \frac{\delta_{\text{low}} + \delta_{\text{up}}}{2}, \tag{4.8}$$

where R_{max}, R_{min}, Z_{max}, Z_{min} are, respectively, the maximum and minimum values along the separatrix of the cylindrical radial and height coordinates R and Z, and R_{low} and R_{up} are the R values of the vertically lowest and highest points of the separatrix, which, like the plasma volume V, are all determined from the equilibrium reconstruction. The proximity to double null is parameterized by the radial distance between the separatrices of the lower and upper X-points in real space at the outer midplane, ΔR_{sep}, and in normalized poloidal flux radius, $\Delta\rho_{\text{pol}_{\text{sep}}}$.

The shapes in figure 4.1 correspond to time instants where the plasmas were in an EDA H-mode state, whereas the values in table 4.1 correspond to the full extent of the shape parameters along ECRH power ramps from L-mode to EDA H-mode. Contrary to typical high triangularity shapes used in AUG for H-mode studies, but hardly in L-mode, partly due to their large width, the strong shape presented here has the advantage of being usable both in L and H-mode

shot	35148	36124
time period (s)	2.0 – 6.0	2.9 – 6.7
shape	weak	strong
R_{geo} (m)	1.59 – 1.62	1.59 – 1.61
a (m)	0.49 – 0.51	0.49 – 0.50
b (m)	0.83 – 0.84	0.76 – 0.78
V (m^3)	12.7 – 13.4	11.5 – 12.0
ε	0.30 – 0.32	0.30 – 0.32
κ	1.62 – 1.71	1.52 – 1.58
δ_{low}	0.32 – 0.38	0.41 – 0.47
δ_{up}	0.10 – 0.11	0.25 – 0.28
δ_{avg}	0.22 – 0.24	0.33 – 0.38
ΔR_{sep} (m)	– (0.040 – 0.031)	– (0.018 – 0.011)
$\Delta\rho_{\mathrm{pol}_{\mathrm{sep}}}$	– (0.06 – 0.04)	– (0.03 – 0.01)

Table 4.1: Range of several shape parameters in weakly and strongly shaped plasmas along ECRH power ramps from L-mode to EDA H-mode: geometric major radius; horizontal and vertical minor radii; volume; inverse aspect ratio; elongation; lower, upper and average triangularities; radial distance between the separatrices of the lower and upper X-points at the outer midplane; ρ_{pol} distance between the separatrices of the lower and upper X-points.

without problems. The current in the shaping coils is kept constant throughout the power ramps, which means the actual resulting shape can still be slightly affected by the plasma response, influenced mostly by the heating power, which explains the non-negligible variation in some of the parameters. The horizontal parameters R_{geo}, a and consequently ε are almost identical in the weak and strong shapes, but the vertical parameters b and therefore κ are lower in the strongly shaped plasma. As a result, V is also lower. The reduced height and elongation of the strong shape are visible in figure 4.1, where the higher position of the inner strike point is also evident. The biggest change, however, is in the triangularity, as both δ_{low} and δ_{up} are significantly higher in the strong shape. Consequently, δ_{avg} reaches a value of almost 0.4, as opposed to less than 0.25 in the weak shape. Not decoupled from this increase in triangularity is the change in the topology of the secondary separatrix, which comes much closer to the primary separatrix, with the upper X-point clearly inside the vessel. This translates to ΔR_{sep} and $\Delta\rho_{\mathrm{pol}_{\mathrm{sep}}}$ being closer to zero, but still negative, as the plasma remains in a lower single null configuration. The proximity to double null results in less magnetic connection between HFS and LFS, but more connection from the outer midplane to the upper divertor. To sum up, there are clear differences between the typical weak shape and the special strong shape used in this experiment, but many parameters vary simultaneously, which makes the unequivocal identification of the critical ones very difficult. Although new plasma shapes could be designed in AUG to try disentangling the effect of some parameters, there will always be unavoidable correlations due to the structure of the machine. Future experiments in other devices with more shaping flexibility, such as Tokamak à Configuration Variable (TCV) [288], could prove useful in this regard, if the EDA H-mode can be achieved there.

4.1.2 Time evolution

Using the strong plasma shape described above, discharges with constant deuterium fueling and ECRH staircases similar to those presented in chapter 3 have been performed. Figure 4.2 shows the time evolution of several quantities in a pair of such discharges. The left-hand side panels (a)-(f) correspond to a discharge with a gradual power ramp starting from L-mode. As the heating power (d) is increased, the plasma transitions to H-mode at 4.38 s, with a brief I-phase lasting only 12 ms and a sudden increase in electron density (a) and stored energy (b). The first 13 ms of H-mode after the I-phase are accompanied by ECMs, which are then replaced by the QCM (e), marking the beginning of the EDA H-mode. After a few dozens of ms, a large number of modes start to appear in the magnetic signals (f) and later in the discharge their amplitude increases significantly. During the EDA H-mode, the stored energy increases with each ECRH step, but the density remains mostly constant, and the plasma is ELM-free, as evidenced by the absence of large spikes in the divertor shunt currents (c).

To probe the limits of the regime in terms of heating power, a similar discharge was conducted starting from a higher ECRH power, and its time evolution is shown in the right-hand side panels of figure 4.2(g)-(l). This discharge does not have the long L-mode phase because the higher power induces an earlier transition to H-mode, but the overall behavior of the plasma during the L-H transition and EDA H-mode along the ECRH staircase is very similar to the previous discharge, illustrating the reproducibility of the experiment. As the power (j) is further increased, ELMs start to appear at 4.2 s, as indicated by the spikes in the divertor shunt currents (i), and the density (g) gradually decreases. The QCM (k) and the modes picked up by the coils (l) become less evident, disappearing and reappearing with each ELM. Among the frequent ELMs, there are a few very large ones that lead to significant drops in the stored energy (h), with divertor current spikes that rise well above the envelope set by the smaller ELMs. At 5.5 s, the smaller ELMs start to disappear, and the plasma becomes dominated by the large ELMs, whose frequency

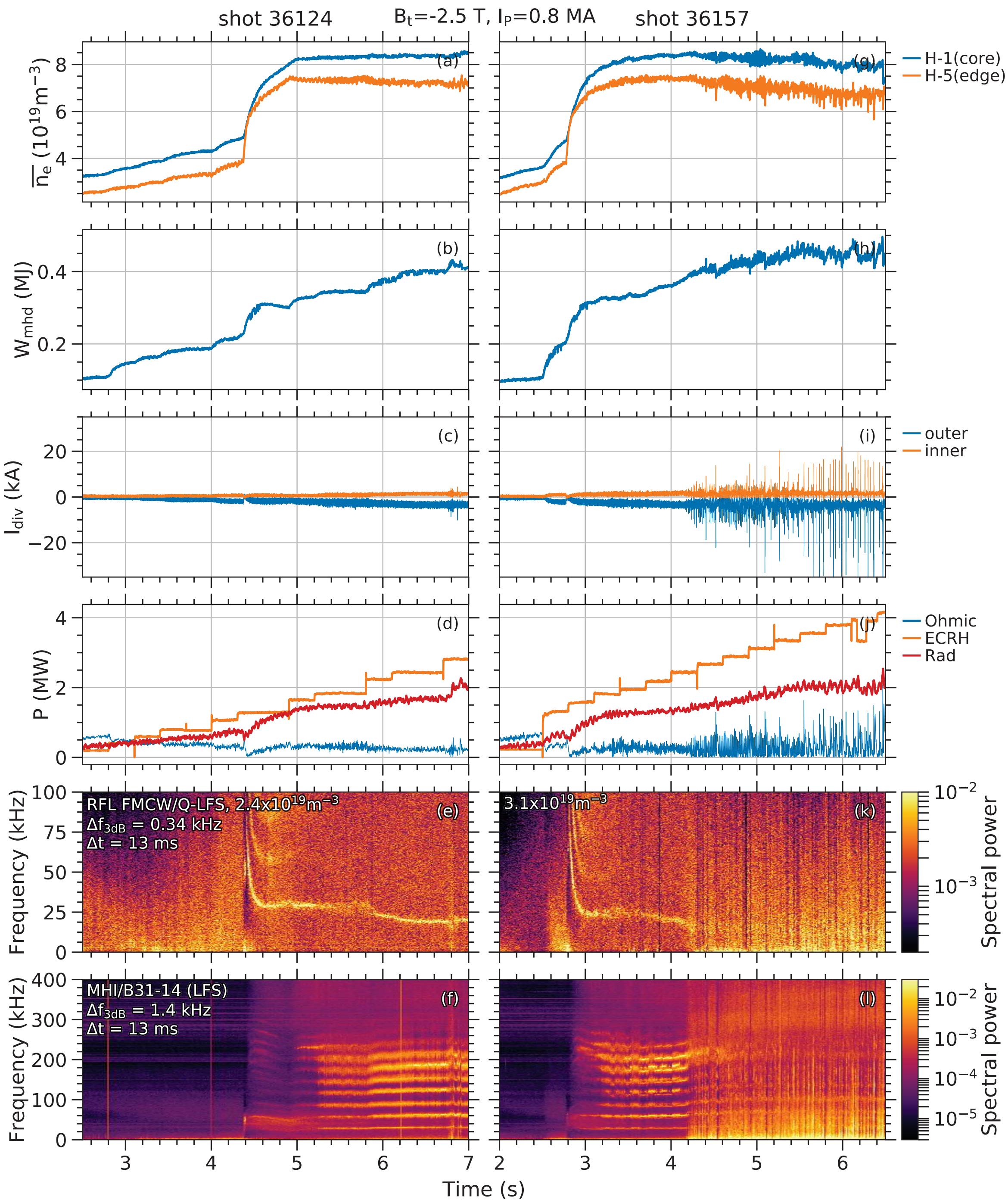

Figure 4.2: Time evolution of different quantities in strongly shaped power ramp discharges with EDA H-modes: (a)(g) line-averaged electron density, (b)(h) plasma stored energy, (c)(i) divertor shunt currents, (d)(j) heating and radiated power, (e)(k) O-mode reflectometry homodyne signal spectra, and (f)(l) spectra of the time derivative of the radial magnetic field measured by a magnetic pickup coil at the outer midplane. The left-hand side panels (a)-(f) correspond to a discharge with a gradual ECRH staircase starting from a very low power in L-mode and ending in an EDA H-mode, and the right-hand side panels (g)-(l) to a similar discharge, but with higher power, ending in an ELMy H-mode.

increases. By the same time, the stored energy appears to saturate.

The overall behaviour of the strongly shaped discharges is qualitatively similar to that of the weakly shaped ones, but there are a few differences worth noting. With strong shaping, the plasma transitions almost directly from L-mode to EDA H-mode, even when the power is gradually increased in a stepwise manner, having only a very brief I-phase and ELM-free H-mode with ECMs in between, together lasting less than a fifth of an energy confinement time. With slow power ramps in weakly shaped plasmas, the situation is different, and a long I-phase and ELMy H-mode with ECMs typically occur before the ELM-free EDA H-mode sets in. The ELMy phase can only be avoided in the weakly shaped scenario by abruptly applying the power at once. The ability to enter the EDA H-mode without passing through an ELMy phase, even in slow power ramps, is an important advantage of strong shaping.

Once in EDA H-mode, there is the usual QCM and rich magnetic activity in both weakly and strongly shaped plasmas. With the strong shape, however, the QCM is more coherent and the modes detected by the pickup coils are more intense, exhibiting different spectral features both in space and time. A detailed study of these instabilities is outside the scope of this work, but should be carried out in order to better characterize and understand the EDA H-mode and its dependence on shaping.

Lastly, operation with strong shaping leads to a significant extension of the ELM-free power range of the EDA H-mode in AUG. In order to quantitatively understand the impact of this aspect, an overlapped comparison of weakly and strongly shaped EDA H-mode discharges with power staircases up to a point near the ELMy threshold is presented in figure 4.3. Apart from the ECRH power in panel (d), the remaining quantities shown in the figure are nondimensional, such that the size differences between the shapes becomes irrelevant for the comparison. The time axis of the weakly shaped discharge has been shifted by 1 s to align the heating ramps of both discharges, allowing a direct comparison of the traces. The vertical dashed line marks the appearance of the QCM and beginning of the EDA H-mode. Left of this line, the weakly shaped discharge (orange) has a significantly higher f_{GW} (a) due to being in H-mode and I-phase, whereas the strongly shaped discharge (blue) is in L-mode. It is an L-mode with good confinement though, as β_{N} (b) is similar in both cases. As a consequence, the pedestal collisionality ν_{e}^{*} (c) is lower in the strongly shaped discharge due to the lower density. After the transition to EDA H-mode, the power is kept constant in the weak shaping case, because if another couple of ECRH steps were applied, large ELMs would occur. However, the strongly shaped plasma can handle several

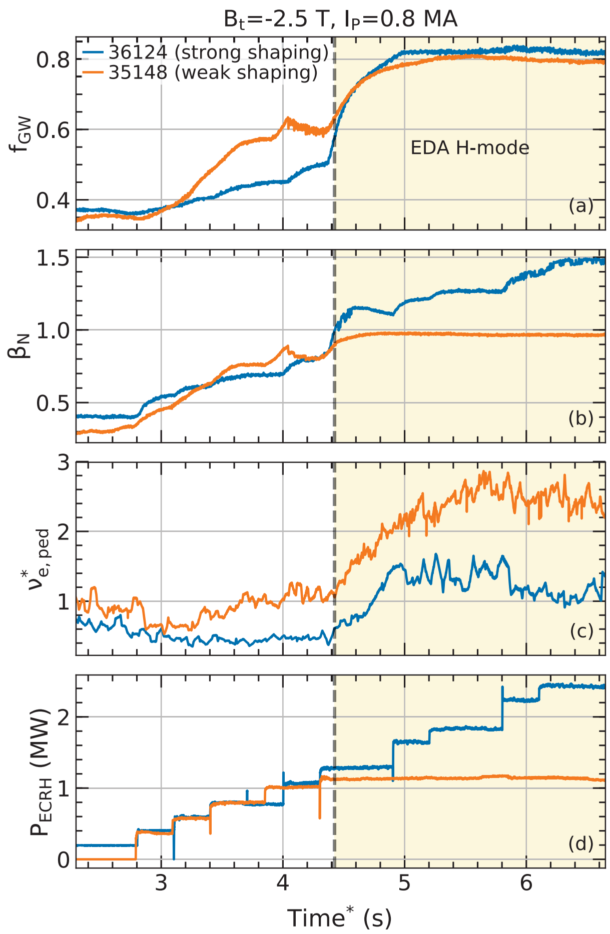

Figure 4.3: Comparison of weakly (orange) and strongly (blue) shaped discharges with an EDA H-mode: (a) Greenwald fraction, (b) Troyon-normalized beta, (c) normalized pedestal electron collisionality, (d) ECRH power. The time axis of the weakly shaped discharge has been shifted by 1 s to align the heating ramps of both discharges. The vertical dashed line marks the appearance of the QCM.

more steps, up to about twice the power, while remaining ELM-free. This leads to significantly higher core temperature and pressure, with the density remaining approximately constant after the initial increase.

With strong shaping, the EDA H-mode can be accessed within a much wider power window, corresponding to $P/P_{\rm LH} \approx 1-2$ in this case, although even wider ranges can be achieved by varying the gas puff. This increased robustness makes the regime highly reproducible without requiring a fine control of the input power. In Alcator C-mod, the EDA H-mode is said to be favored by high triangularity [102, 106, 116], but an extension of the ELM-free power window with shaping has not been specifically reported. In AUG, both weakly and strongly shaped EDA H-modes have high and similar $f_{\rm GW}$, but the extended power window of the strongly shaped scenario allows remarkably higher ELM-free $\beta_{\rm N}$ and lower $\nu_{\rm e}^*$ to be achieved. This represents a great improvement in the performance of the regime and an important step towards reactor relevance.

4.1.3 Radial profiles

Radial electron profiles of a strongly shaped EDA H-mode with 2.4 MW of ECRH power as a function of ρ_{pol} are shown in figure 4.4, with diagnostic data and spline fits for easier visualization and computation of derived quantities. The electron density was measured by TS and Li-BES, the electron temperature by TS and ECE, and the electron pressure computed for each diagnostic from the corresponding n_{e} and T_{e} data points or overall spline fits. All profiles were mapped to the outer midplane with the IDE equilibrium and radially aligned in accordance to the $T_{\mathrm{e,sep}}$ estimate from the two-point model of the divertor SOL [275]. The core density (figure 4.4(a)) is mostly flat, whereas the temperature (b) and therefore pressure (c) are peaked in the core. There is a clear edge pedestal in all three quantities (d)-(f), but no ELMs occur at this heating power. This is qualitatively similar to the profiles of the weakly shaped EDA H-mode presented in chapter 3, but the higher heating power allowed by the strong shaping leads to important quantitative differences.

For a better profile comparison between the weakly and strongly shaped EDA H-modes, three discharges of each scenario were chosen in order to mitigate the effects of some systematic uncertainties of the measurements in the interpretation. Table 4.2 shows the chosen discharges and time periods for each shape, as well as some of their main input parameters: deuterium gas puff Γ_{D}, ECRH power P_{ECRH}, and total power lost by the plasma P_{tot}, which includes the ohmic contribution and subtracts the time derivative of W_{MHD} to better approximate complete stationarity. Γ_{D} is very similar among all cases, with less than 10 % total variation. P_{ECRH} and P_{tot} are very different between the shapes, as each one is exploiting the respectively available ELM-free power range, but very similar inside each shaping scenario, also with less then 10 % total variation. P_{tot} is roughly 30 % higher than P_{ECRH} for the low power, weak shaping case, but less then 10 % higher in the high power, strong shaping case, because the higher temperature reduces the ohmic power. As a result, P_{ECRH} and P_{tot} are, respectively, about 110 % and 70 % higher in the strong shaping examples than in the weak shaping ones. This dataset can therefore be divided in two subgroups: weakly shaped, low-powered plasmas, and strongly shaped, high-powered plasmas.

The electron profiles of the plasmas in table 4.2 were fit with the same diagnostics and

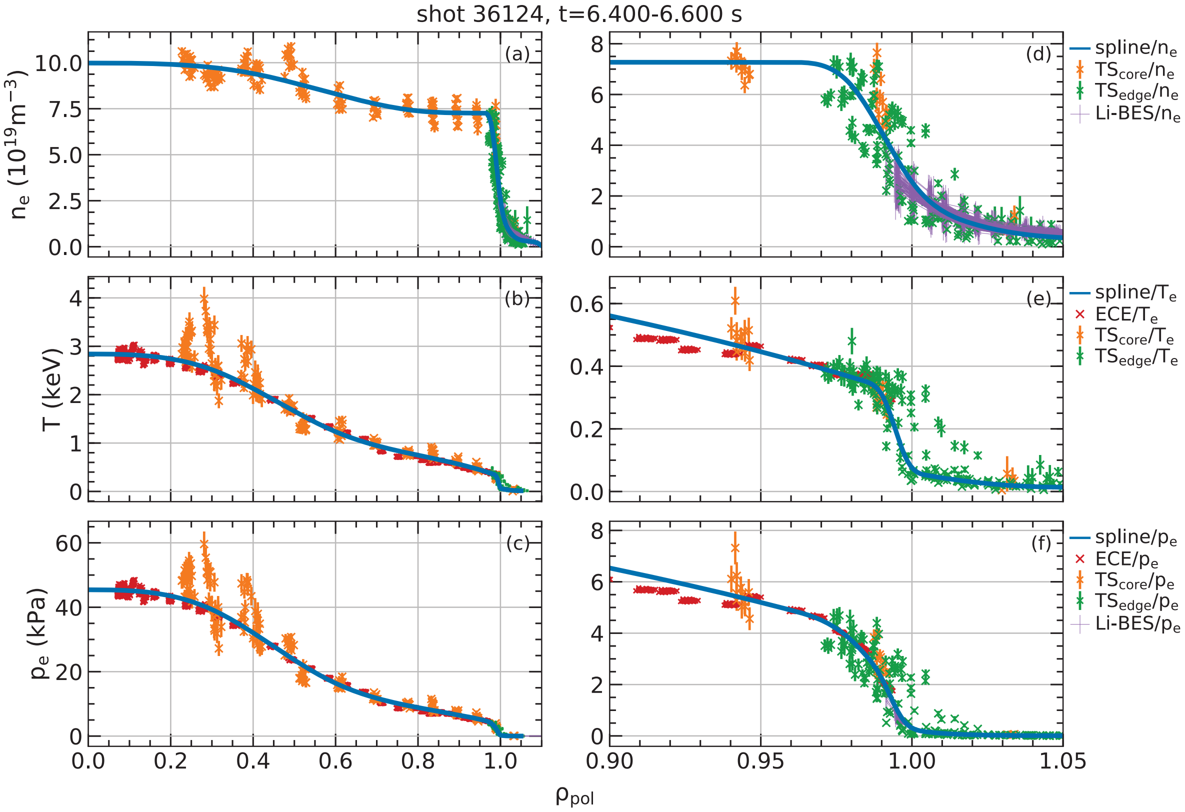

Figure 4.4: Radial profiles of electron (a,d) density, (b,e) temperature, and (c,f) pressure during a strongly shaped EDA H-mode. The entire profiles are represented in the left-hand side panels (a)-(c) and a zoom in the pedestal region is shown in the right-hand side panels (d)-(f).

shot	time period (s)	shape	Γ_D (10^{21} e$^-$/s)	P_{ECRH} (MW)	P_{tot} (MW)
35148	5.40 – 5.60	weak	2.62	1.13	1.49
35174	3.40 – 3.60	weak	2.58	1.12	1.51
35450	3.40 – 3.60	weak	2.60	1.22	1.60
36124	6.40 – 6.60	strong	2.59	2.43	2.62
36157	4.00 – 4.18	strong	2.53	2.43	2.53
37412	3.00 – 3.20	strong	2.45	2.44	2.66

Table 4.2: Chosen discharges and time periods for profile comparison of weakly and strongly shaped EDA H-modes, as well as some corresponding input parameters: deuterium gas puff, ECRH power and total power lost by the plasma.

procedure of figure 4.4. The resulting splines are overlappingly plotted in figure 4.5. The core density (a) tends to be slightly higher at mid-radius for strong shaping, but similar to the weak shaping case otherwise. The core temperature (b) and pressure (c) are much higher in the high-powered, strongly shaped plasmas, reaching about 3 keV and 45 kPa on the magnetic axis, respectively, being 50 % higher than the 2 keV and 30 kPa of the low-powered, weakly shaped scenario. Apart from this scaling factor, the shape of the core profiles is quite similar. Regarding the edge density profile (d), the strong shape has a slightly higher separatrix and lower pedestal top n_e, and therefore a slightly lower gradient. However, this difference is very small when compared to the edge temperature profiles (e), whose pedestal top values are about 50 % higher in the high-powered, strong shaping case. The pedestal temperature width is also narrower, which translates to significantly higher pedestal temperature gradients. As a consequence, the pressure pedestal has a higher gradient and top values in the high-powered, strongly shaped case, but it is more rounded, due to the different pedestal widths in density, $\Delta_{\mathrm{ped},n_e}$, and temperature, $\Delta_{\mathrm{ped},T_e}$. In C-mod, a dramatic increase of the EDA H-mode $\Delta_{\mathrm{ped},n_e}$ with higher triangularity has been reported [114]. In AUG at strong shaping, $\Delta_{\mathrm{ped},n_e}$ is significantly higher than $\Delta_{\mathrm{ped},T_e}$, but this appears to be mainly due to a reduction of the $\Delta_{\mathrm{ped},T_e}$, as a change of $\Delta_{\mathrm{ped},n_e}$ with shaping does not seem to be so evident in normalized coordinates. A more detailed study of the pedestal structure in EDA H-modes and its dependence on shaping and other parameters will be the subject of future work, especially when new experiments specifically designed for higher quality measurements and better diagnostic coverage are performed.

No ELMs occur in the strong shaping scenario despite the much higher heating power and pedestal pressure gradients and top values when compared to the weak shaping case, that cannot achieve such values without having ELMs. A possible explanation for this effect is the extension of the P-B stability limit with strong shaping [39]. In AUG, pedestal stability can be investigated using a combination of tools [289]. First, a pressure-constrained high resolution CLISTE/HELENA equilibrium is reconstructed from experimental magnetic and profile measurements, together with appropriate bootstrap current models. The ideal MHD stability of the equilibrium is computed with the MISHKA solver for a wide range of mode numbers. Then, the pressure and current density profiles are artificially modified, keeping constant the total plasma current, and pedestal stability is reassessed. This process is repeated until the plasma is found to be unstable. Preliminary pedestal stability calculations of EDA H-modes in AUG seem to show that the beneficial effects of strong shaping are, at least in part, due to the extension of the P-B boundary. More specifically, the pedestal appears limited by ballooning modes with high mode numbers, at a relatively low current density. Experimentally, it is not yet known at which point the effect of strong shaping in AUG EDA H-modes saturates, and it is not possible to find it out due to current and force limits in the shaping coils. Future experiments in TCV may be able to tackle this question.

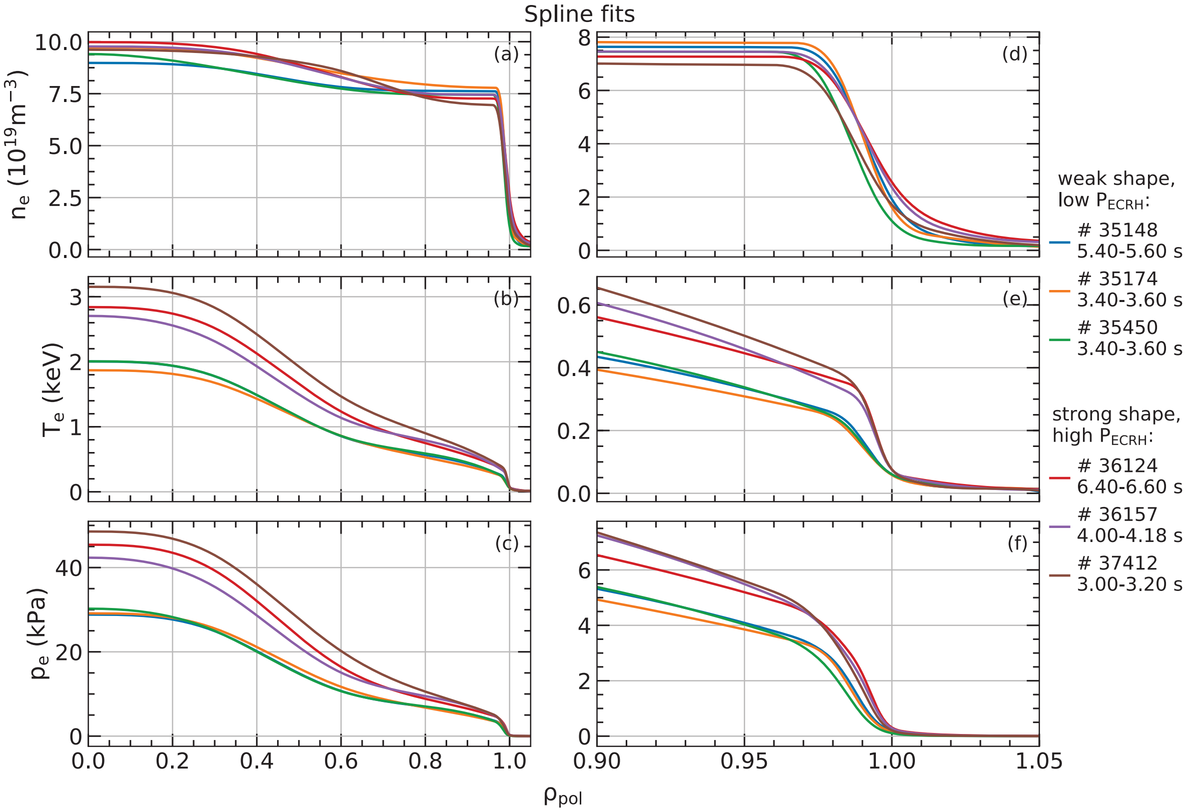

Figure 4.5: Comparison of electron profiles between low-powered, weakly shaped (blue, orange, green) and high-powered, strongly shaped (red, purple, brown) EDA H-modes close to the respective upper power limits: (a,d) density, (b,e) temperature, and (c,f) pressure. The entire profiles are represented in the left-hand side panels (a)-(c) and a zoom in the pedestal region is shown in the right-hand side panels (d)-(f). Some of the main input parameters of the discharges are shown in table 4.2.

4.1.4 Pulsations

While strong shaping significantly expands the operational space of the EDA H-mode, the behavior of the plasma edge is not uniform throughout the extended heating power range. Figure 4.6 shows a comparison of different phases in the same strongly shaped discharge at different ECRH powers. The middle column corresponds to a calm, ELM-free EDA H-mode at $P_{tot} = 2.5\,\text{MW}$. The QCM, detected by interferometry (h), and the multiple modes detected by pickup coils on the outer midplane (j) are present as usual. The edge line-averaged density (j), divertor currents (k) and poloidal magnetic field B_p near the divertor (l) are mostly constant. This quietude results in a continuous exhaust to the divertor, evidenced by the uniform behavior of the heat flux inferred from infrared (IR) thermography measurements (n), whose maximum local value (m) varies little in time.

At a lower heating power, with $P_{tot} = 2.1\,\text{MW}$, the EDA H-mode has somewhat different

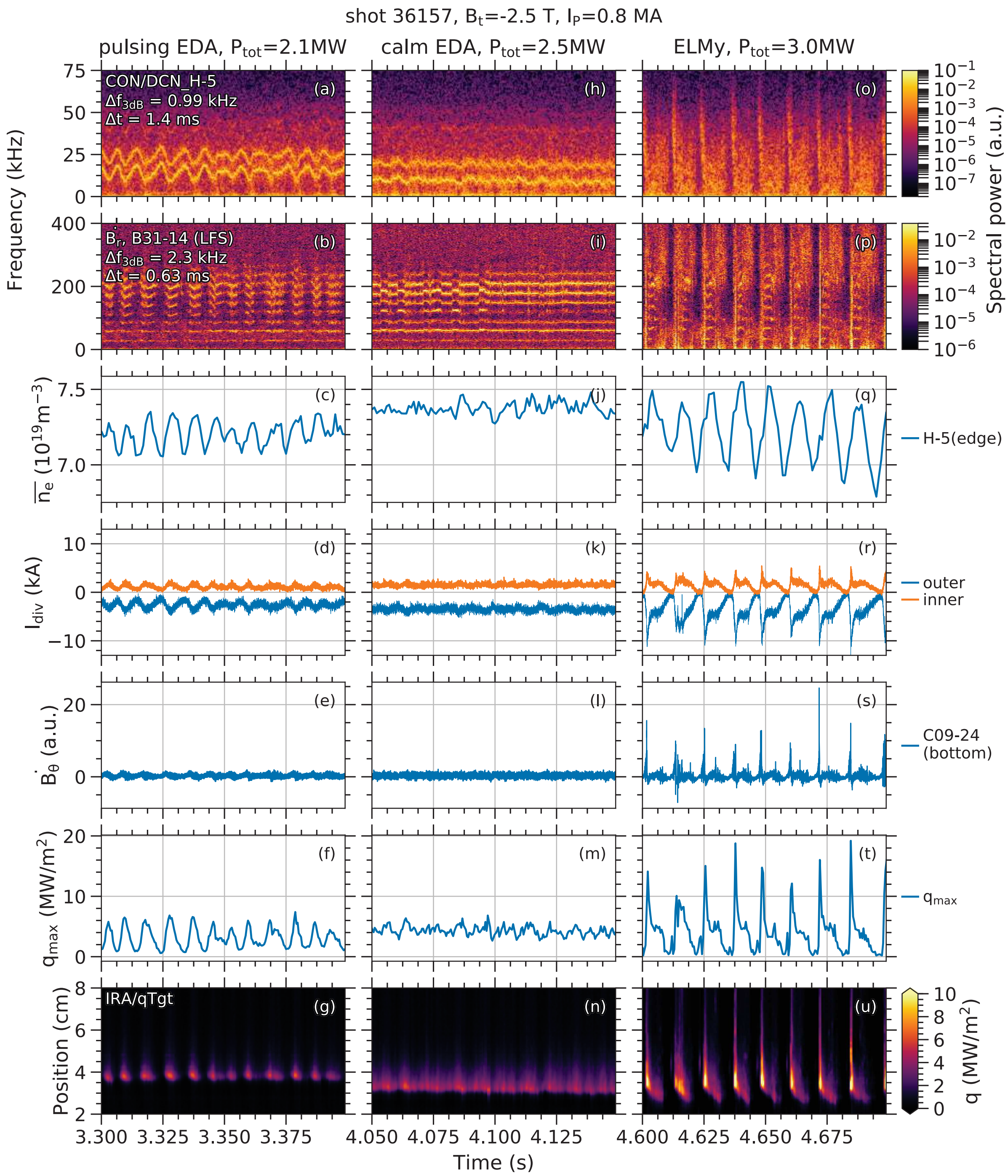

Figure 4.6: Comparison of different phases in the same strongly shaped discharge with ECRH by order of increasing heating power: (a)-(g) pulsing EDA H-mode, (h)-(n) calm EDA H-mode, (o)-(u) ELMy H-mode. The following quantities are shown as a function of time: (a)(h)(o) spectra of edge interferometry measuring line-integrated density fluctuations, (b)(i)(p) spectra of the radial magnetic field time derivative measured by a pickup coil at the LFS midplane, (c)(j)(q) edge line-averaged density, (d)(k)(r) divertor shunt currents, (e)(l)(s) time derivative of the poloidal magnetic field measured by a pickup coil near the divertor, (f)(m)(t) maximum local heat flux on the divertor inferred from IR thermography measurements, (g)(n)(u) heat flux as function of position on the divertor.

dynamics, as the left-hand side column of figure 4.6(a)-(g) shows. The plasma is in a pulsating state, with the frequency of the QCM and magnetic modes undergoing regular oscillations, synchronized with the edge density and divertor shunt currents. The divertor $\dot{B}_{\mathrm{p}}$ also has a small but clear oscillation. The heat loads on the divertor are not continuous, but rather oscillate in phase with the pulsations, at a frequency on the order of 120 Hz.

This may sound like a description of ELMs, but appears to be something different when compared to actual ELMs shown in the right-hand side column of figure 4.6(o)-(u), corresponding to $P_{\mathrm{tot}} = 3.0\,\mathrm{MW}$. In this phase, the QCM is hardly seen and the interferometry and magnetic spectra are regularly interrupted by the ELMs, which cause strong spikes in the divertor currents. The variation of the edge density is significantly more intense and the divertor $\dot{B}_{\mathrm{p}}$ exhibits not only an oscillation, but also a very strong spike with each ELM. The dynamic of the heat load profile is also quite different, with ELMs suddenly depositing very large amounts of power, both in a localized manner at the strike point and in a wider region of the divertor. The strike point subsequently moves and the heat load reduces until it becomes negligible before the next cycle. As a result, the maximum heat load has instantaneous peaks almost 5 times higher than its time-averaged value. And these ELMs are actually not that large, because a few ECRH steps later, at $P_{\mathrm{tot}} = 3.6\,\mathrm{MW}$, the maximum instantaneous heat load reaches values 15 times higher than the time average.

The nature and cause of the pulsations in the EDA H-mode is not yet known and the conditions to access this state are not clear, although it seems to be favored by low heating power. While undoubtedly more benign than ELMy H-modes, the pulsating EDA H-mode could still pose a risk to PFCs, because the extreme conditions of a reactor environment will lead to such extreme heat loads to the divertor that any bursty expulsion of plasma must be taken seriously. For this reason, the pulsations of the EDA H-mode should be better investigated in future studies, with the goal of understanding their origin, dynamics and dependence on plasma parameters. This reinforces the importance of thoroughly exploring the multidimensional parameter space of the regime and will hopefully allow a proper assessment of the eventual risks. Ultimately one will have to decide if the pulsations must be absolutely avoided, with the implication that only the totally calm EDA H-mode must be aimed for, or if the extrapolated heat loads are tolerable and the pulsating EDA H-mode can also be considered, offering a wider operational space.

To sum up, strong shaping of the plasma opened a window for operating with more heating power in the EDA H-mode without the occurrence of ELMs. As a consequence, significantly higher pedestal and core temperature and pressure values, as well as gradients, can be achieved. The main physical explanation for this effect appears to be the extension of the peeling-ballooning stability boundary with strong shaping, confirmed via pedestal MHD stability analysis of experimental equilibria. The final outcome of operating with a strong shape is a more direct access to the EDA H-mode, wider parameter space, resulting in increased robustness, and achievement of higher β_N and lower ν_e^*, which bring the regime one step closer to reactor relevance. All discharges presented hereinafter are by default strongly shaped, unless otherwise noted.

4.2 Detaching the divertor with nitrogen seeding

Getting rid of the huge instantaneous heat loads to PFCs caused by ELMs is definitely an important achievement, though not sufficient to solve the exhaust problem of fusion devices. The power flux to the divertor in the EDA H-mode, while mostly continuous, is not negligible, and is actually higher than the inter-ELM flux of ELMy plasmas in similar conditions, as previously exemplified in figure 4.6. In order for a scenario to be usable in a reactor, it must not only have its peak heat load excursions minimized, but also its time-averaged value reduced to a level low enough to be continuously sustained by the divertor materials. This remains one of the main challenges and active areas of research in magnetic confinement fusion [59, 61, 62].

Heat fluxes to the target plates in tokamaks are typically mitigated by puffing large amounts of deuterium and/or radiating impurities, which lower the temperature of the divertor plasma [12, 71]. When it is sufficiently reduced, to the order of or below 5 eV, the power flux is very low and impurity sputtering becomes unimportant [69]. This is usually accompanied by divertor detachment [70], in which layers of cold and dense plasma, associated with large volumetric losses, form near the target plates. In a detached state, plasma pressure is no longer constant along SOL magnetic field lines, as collisions with the neutral divertor gas become a relevant sink of energy and momentum. The benign conditions of a detached plasma at the target plates, namely the substantially reduced heat load and erosion, lead to a dramatic increase of the lifetime of PFCs, making this state desirable, if not mandatory, for any reactor scenario.

In order to investigate the compatibility of the EDA H-mode in AUG with a detached divertor, dedicated experiments were performed with impurity seeding as a way of increasing energy exhaust by line radiation. Among the different possible substances, nitrogen (N) was chosen due to its exceptional radiative characteristics [290], namely a strong peak around $T_\mathrm{e} = 5 - 20\,\mathrm{eV}$, ideal for the divertor, and low radiation at high temperatures, to avoid impairing core plasma performance. In addition, nitrogen seeding has proven an effective way of detaching the divertor in AUG ELMy H-modes in the past, both partially [211] and completely [291], albeit usually at the cost of degrading energy confinement.

4.2.1 Time evolution

Figure 4.7 shows an overview of EDA H-mode discharges with slow nitrogen seeding ramps and constant deuterium gas puff. The ECRH power is rapidly increased in the beginning to enter the EDA H-mode and then kept constant. Nitrogen is injected only about 2 s after the L-H transition in order for the plasma to be stationary before the effect of seeding is assessed. The left-hand side column corresponds to a discharge that starts with a low nitrogen puff (h), less than half of the deuterium fueling rate in terms of electrons, and is slowly increased over the course of several seconds, surpassing the deuterium puff towards the end of the discharge. As a result, the nitrogen concentration in the divertor, c_N, estimated from spectroscopy measurements [270], gradually increases from below 0.5 % to over 2 %. At the same time, the divertor temperature T_{div} (e), estimated from the shunt currents (c), strongly decreases from 30 eV to very low values. This does not happen in a smooth manner throughout the entire ramp, as the plasma undergoes an alternation phase between calm and pulsating EDA H-mode, also visible in the behavior of the QCM (d). As expected with the nitrogen puff, the radiated power in the divertor, $P_{rad,div}$, and as a whole increase (g), but the main chamber radiation, $P_{rad,main}$, remains approximately constant. The electron density (a) and β_N (b) vary little, apart from an accidental gyrotron trip and a couple of NBI blips for diagnostic purposes. This means the energy confinement time is not degraded and H_{98y2} stays above 1, but Z_{eff} nonetheless increases from 1.5 to 2, indicating some fuel dilution in the core.

The discharge just described did not reach the limit of the regime in terms of seeding, so a similar one was performed, but starting at a much higher nitrogen puff rate, and its time evolution is illustrated in the right-hand side column of figure 4.7. The higher seeding levels cause T_{div} (m) to drop even further, up to the point where it becomes negative. This has to do with the model used for its computation, which assumes there is a strong temperature difference between outer and inner targets that is responsible for the shunt currents. This is valid in most cases when the outer divertor is attached, since the inner divertor is naturally much colder and usually in a detached state. However, when the outer divertor is cooled and starts to approach detachment,

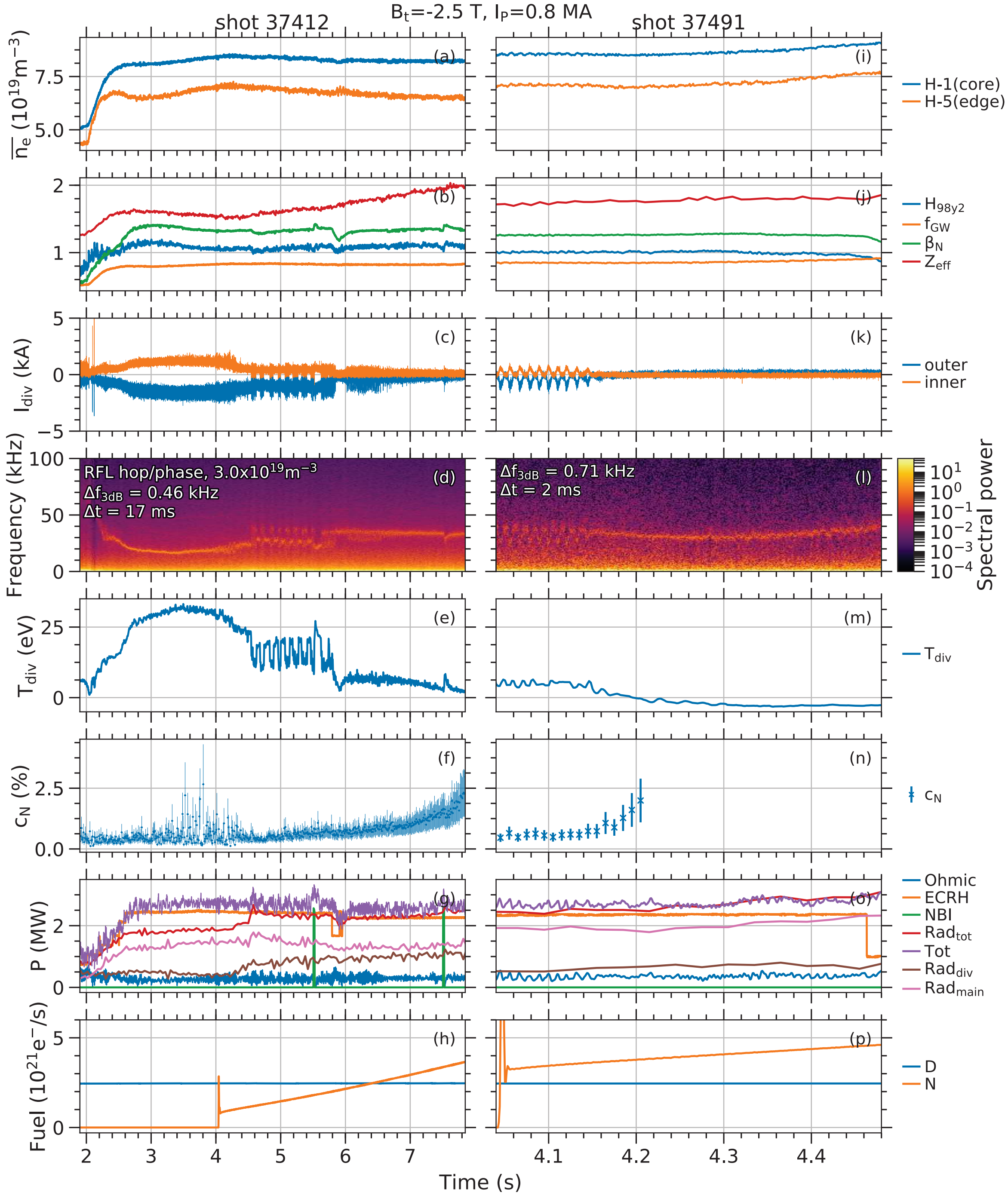

Figure 4.7: Time evolution of different quantities in EDA H-mode discharges with nitrogen seeding ramps: (a)(i) line-averaged electron density, (b)(j) performance indicators, (c)(k) divertor shunt currents, (d)(l) O-mode reflectometry phase spectra, (e)(m) proxy for the divertor temperature based on shunt currents, (f)(n) divertor nitrogen concentration estimated from spectroscopy measurements, (g)(o) heating and radiated power, and (h)(p) gas puff rates. The left-hand side panels (a)-(h) correspond to a discharge with a slow N seeding ramp starting from a low gas puff value, and the right-hand side panels (i)-(p) to a similar discharge, but starting from a higher value.

the temperature difference between the targets becomes much smaller and other contributions to the shunt currents stop being negligible, causing the model to break down. In any case, negative T_{div} is an indication of a detached or close to detached divertor. As a consequence of the low divertor temperature, the model for the spectroscopy-based nitrogen concentration also breaks down and its measurement becomes unavailable (n). In this phase, the total radiated power is almost equal to the total heating power (o), which means the fraction conducted to the target plates is very low. Contrary to the discharge with less nitrogen seeding, the electron density (i) in this plasma with a seemingly close to detached divertor gradually increases, and f_{GW} goes from 0.8 to 0.9. A possible explanation for this effect is the momentum loss of the plasma flow towards the target plate caused caused by collisions with the divertor neutrals, which would lead to an upstream reduced plasma outflow rate, i.e. the particle confinement time would be increased [69]. A similar n_{e} increase has also been observed in AUG ELMy H-modes with partial detachment of the outer divertor [291]. As this happens in the EDA H-mode, β_{N} remains unaffected, but the core n_{e} then becomes too close to the ECRH cutoff and stray ECRH radiation causes several gyrotrons to be turned off, resulting afterwards in a back-transition to L-mode. At $I_{\mathrm{p}} = 0.8\,\mathrm{MA}$ in AUG, this technicality is actually the limiting factor for divertor detachment in the EDA H-mode. In principle this will not be a problem in ITER for example, because the crucial quantity B^2/n_{e} will be much larger. Nonetheless, an EDA H-mode scenario at lower I_{p} and therefore lower n_{e} has been developed in AUG to avoid the ECRH cutoff, but has not yet been used in seeding experiments.

4.2.2 Divertor profiles

The density increase, high radiation fraction and strong reduction in T_{div} achieved with nitrogen seeding in the EDA H-mode indicate that the divertor is approaching detachment, but the best way to evaluate this is to analyze divertor Langmuir probe data. With the strong shaping used in these shots, the inner strike point is higher than in typical configurations, so very few probes cover the region. This is not a problem though, because the heat loads on the inner divertor are not the bottleneck for heat exhaust, as it is much easier to detach than the outer divertor, especially in favorable ∇B drift configuration. In fact, the inner divertor in these plasmas is detached even before nitrogen is injected.

The analysis that follows therefore focuses on the outer divertor, where hardest challenges lie. Figure 4.8 compares spatial profiles of the divertor plasma measured by Langmuir probes as a function of the distance to the outer strike point along the target plate, for different levels of nitrogen. The profiles are rather peaked at the strike point and no strike point sweeps were performed. As a result, the spatial resolution is not ideal, but some useful observations can nevertheless be made. Without nitrogen seeding, at $c_\mathrm{N} \lesssim 0.5\,\%$, the divertor is clearly attached, with the electron temperature (b) above 5 eV throughout the entire profile. In this shot with low nitrogen, a probe unfortunately malfunctioned, so T_e and derived quantities could not be evaluated at the strike point. With some nitrogen seeding, at $c_\mathrm{N} \approx 1\,\%$, T_e decreases, but is still above 5 eV. The ion saturation current density, j_sat, slightly increases, which indicates that the rollover, characteristic of detachment [12], has not yet been reached. As the nitrogen content in the divertor increases, stronger changes start happening. With $c_\mathrm{N} \approx 2\,\%$, T_e becomes close to 5 eV, except at the strike point, which is still higher. There is a strong reduction in j_sat, indicating the rollover that corresponds to the beginning of detachment. As the nitrogen is further increased above the measurement threshold in these conditions, $c_\mathrm{N} \gtrsim 2.5\,\%$, T_e continues to drop and becomes lower than 5 eV for most of the profile. Only the strike point remains slightly above this value, but j_sat is further reduced. As a result, the electron density (c), pressure (d) and heat flux density q (e) are significantly lower, and the divertor is approaching detachment. The required divertor nitrogen concentration to achieve this is on the same order of magnitude as what has been observed in ELMy H-modes of similar power in AUG [271].

The results convincingly show that nitrogen seeding in the EDA H-mode in AUG leads to substantial reductions in parallel heat flux and target temperature, causing the divertor to approach detachment without noticeable confinement degradation. That being said, the corresponding $Z_\mathrm{eff} = 1.8 - 2.0$ and $\Delta Z_\mathrm{eff} \approx 0.5$ are not negligible. Experiments in Alcator C-mod have produced similar results, also showing nitrogen to be effective for operating with a dissipative divertor in EDA H-mode and moderate or no confinement degradation [125, 126]. Future seeding experiments are planned in AUG at lower I_p to avoid the ECRH cutoff, with the goal of investigating the limits of the EDA H-mode regarding nitrogen seeding and divertor detachment.

4.3 Cooling the pedestal with argon seeding

The previous sections demonstrated two effective techniques for bringing the EDA H-mode in AUG closer to reactor relevance: strong shaping to increase the power that can be applied while maintaining an ELM-free state and nitrogen seeding to decrease the heat loads reaching the

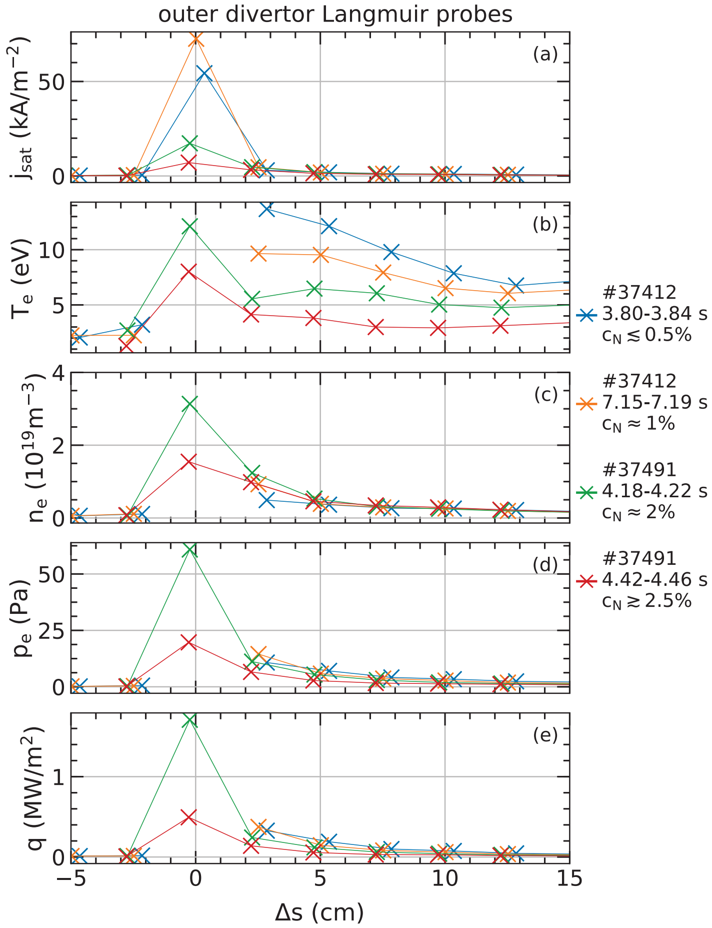

Figure 4.8: Outer target profiles of different quantities as a function of distance from the strike point along the divertor, measured by Langmuir probes in EDA H-modes with different nitrogen concentrations: (a) ion saturation current density, (b) electron temperature, (c) electron density, (d) electron pressure, (e) heat flux density.

divertor. Both goals are extremely important for the success of a reactor scenario, but they are unfortunately not synergistic. On the contrary, as more heating power applied to the plasma core will inevitably lead to more power reaching the divertor. The techniques just mentioned dealt with each problem independently, but there are ways to tackle both issues at the same time too.

Heat loads to PFCs can be reduced not only by increasing radiation in the SOL, but also by increasing radiation inside the separatrix, which has the additional effect of cooling the confined plasma. This is in principle not desirable, as very high temperature is basically the main requirement for the occurrence of fusion reactions, and therefore high radiation in the inner core of the plasma should be avoided. However, if the increased radiation can be confined to the pedestal region, where fusion reactions are anyway negligible, serious drops in the performance of the scenario can be prevented. Cooling the pedestal would then have the added benefit of reducing the edge pressure and therefore stabilize ELMs, allowing more heating power to be used in the core without the edge reaching the peeling-ballooning boundary. Besides this, the extreme power fluxes foreseen in large-scale reactors cannot be entirely radiated away by the SOL alone, so enhanced core radiation by impurity seeding is a key component of current DEMO scenarios [63, 292]. Therefore, increased radiative losses in the pedestal would simultaneously help fulfilling two very important goals of bringing the EDA H-mode to a state that can be considered for a fusion reactor: extending the ELM-free power range to achieve higher temperature in the inner core, while at the same time reducing the heat loads to the divertor.

The practical question is what is the best way to increase radiation in the pedestal region without severely hampering core performance. Among different potential seeding species, argon (Ar) stands out as a prime candidate due to its strong radiative peak at $T_e = 0.1-0.5\,\mathrm{keV}$ [290], fitting the pedestal temperature of the EDA H-mode in AUG quite well. Besides that, it is also a very effective divertor radiator [293], with a peak at $T_e = 10-40\,\mathrm{eV}$, but unfortunately does have a much higher radiation than nitrogen for core temperatures of a few keV. On the other hand, argon features high divertor enrichment [294] and does not suffer from some of the disadvantages of nitrogen, such as strong wall sticking and ammonia formation [295], which may lead to enhanced tritium inventories. In the end, the optimal strategy for a reactor may be a mix of impurities to better control both divertor and pedestal parameters, but argon will likely play a key role in the final solution.

4.3.1 Time evolution

Power ramp experiments with argon seeding for pedestal radiative cooling have been performed with the main goal of increasing the ELM-free power range and performance of the EDA H-mode in AUG in a divertor-friendly way. A comparison of two similar ECRH discharges with and without argon seeding is presented in figure 4.9. Both have a small nitrogen puff, much lower than the deuterium puff (f)(l). The argon level of the seeded discharge, on the right-hand side column, was feedback-controlled in real time to maintain a constant estimate of the power through the separatrix, $P_{\mathrm{tot}} - P_{\mathrm{rad,main}}$. Although also low in absolute value when compared to the fueling rate, it has a strong effect on the plasma and is definitely not negligible. Before argon is puffed, at 2.6 s, both discharges have an identical behavior, with an L-H transition around around 2.15 s and subsequent appearance of the QCM (c)(i), marking the EDA H-mode, as the heating power (e)(k) is increased.

The unseeded discharge, in the left-hand side column of figure 4.9, can remain ELM-free for

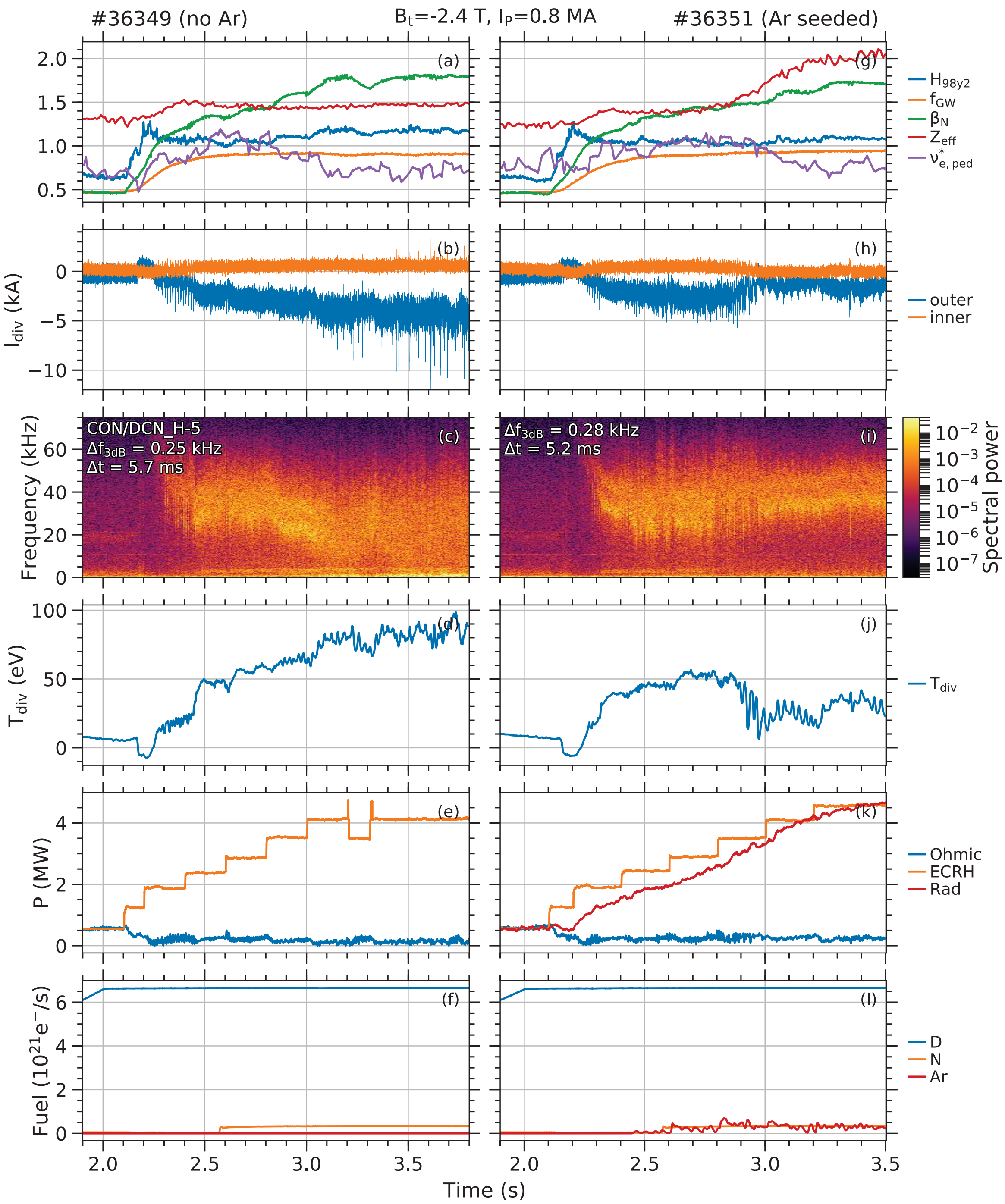

Figure 4.9: Time evolution of different quantities in EDA H-mode ECRH ramp discharges with and without argon seeding: (a)(g) performance indicators, (b)(h) divertor shunt currents, (c)(i) spectra of edge interferometry measuring line-integrated density fluctuations, (d)(j) proxy for the divertor temperature based on shunt currents, (e)(k) heating and radiated power, and (f)(l) gas puff rates. The left-hand side panels (a)-(f) correspond to a discharge without argon, and the right-hand side panels (g)-(l) to a similar discharge but with argon seeding.

a couple more ECRH steps, up to 3 s, but does not withstand the last step to 4 MW of external heating power, with ELMs appearing in the divertor shunt currents (b). The power threshold is higher than in the discharges shown in section 4.1 due to the higher deuterium gas puff rate.

With increased P_{ECRH}, T_{div} (d) also continues to rise, reaching 75-95 eV. Although the discharge has good performance (a), with high density ($f_{\mathrm{GW}} = 0.9$), pressure ($\beta_{\mathrm{N}} = 1.8$), and energy confinement ($H_{98\mathrm{y}2} = 1.15$), the hot divertor and occurrence of ELMs are a showstopper for a reactor.

In contrast, the argon-seeded discharge, in the right-hand side column of figure 4.9, can withstand all the ECRH steps plus one, up to 4.6 MW, without ELMs and with a much colder divertor ($T_{\mathrm{div}} = 20-40\,\mathrm{eV}$). It also has good performance, with $f_{\mathrm{GW}} = 0.95$, but a slightly lower $\beta_{\mathrm{N}} = 1.7$ and $H_{98\mathrm{y}2} = 1.1$ compared to the unseeded ELMy plasma. However, when compared to the unseeded ELM-free plasma, which can only sustain lower heating power, the high-powered argon-seeded EDA H-mode reaches higher f_{GW} and β_{N}, lower ν_{e}^{*}, and half of T_{div}. This clearly shows the beneficial effects of argon seeding in the EDA H-mode, simultaneously leading to ELM avoidance and divertor protection. There is some fuel dilution in the core though, with $\Delta Z_{\mathrm{eff}} \approx 0.6$ after seeding. As with nitrogen, there is a point where more argon seeding leads to divertor detachment, which causes core density to increase and reach the ECRH cutoff, at $I_{\mathrm{p}} = 0.8\,\mathrm{MA}$. For this reason, future experiments with argon seeding at lower I_{p} are also planned to properly investigate the limits of the regime.

The extended EDA H-mode power window achieved with strong shaping, higher deuterium puff and argon seeding allowed experiments with a full voltage NBI source to be performed without exceeding the ELM threshold. Figure 4.10 shows a comparison of a pair of unseeded and argon-seeded discharges with an approximately even mix of ECRH and NBI. The unseeded discharge, on the left-hand side column, is an EDA H-mode with 2.3 MW of ECRH, on top of which an NBI source with 2.4 MW is applied at 2.6 s (e). Just 30 ms after the the application of NBI, the plasma starts to have large ELMs (b), stronger than those with pure ECRH, and the density decreases (a). With argon seeding (right-hand side column of figure 4.10), the plasma is able to remain ELM-free throughout the NBI ramp, done by pulse width modulation, up to a full source, which, together with ECRH and ohmic power, make up $P_{\mathrm{tot}} = 5\,\mathrm{MW} > 4P_{\mathrm{LH}}$. A large portion of this power is lost by radiation, with argon increasing both $P_{\mathrm{rad,div}}$ and $P_{\mathrm{rad,main}}$, leading to lower T_{div} when compared to the unseeded ELMy plasma. Despite the argon-induced enhanced radiation, the ELM-free EDA H-mode maintains $H_{98\mathrm{y}2} > 1$ and almost reaches $\beta_{\mathrm{N}} = 1.7$, but has a slightly lower density, with f_{GW} just under 0.9, than the pure ECRH case.

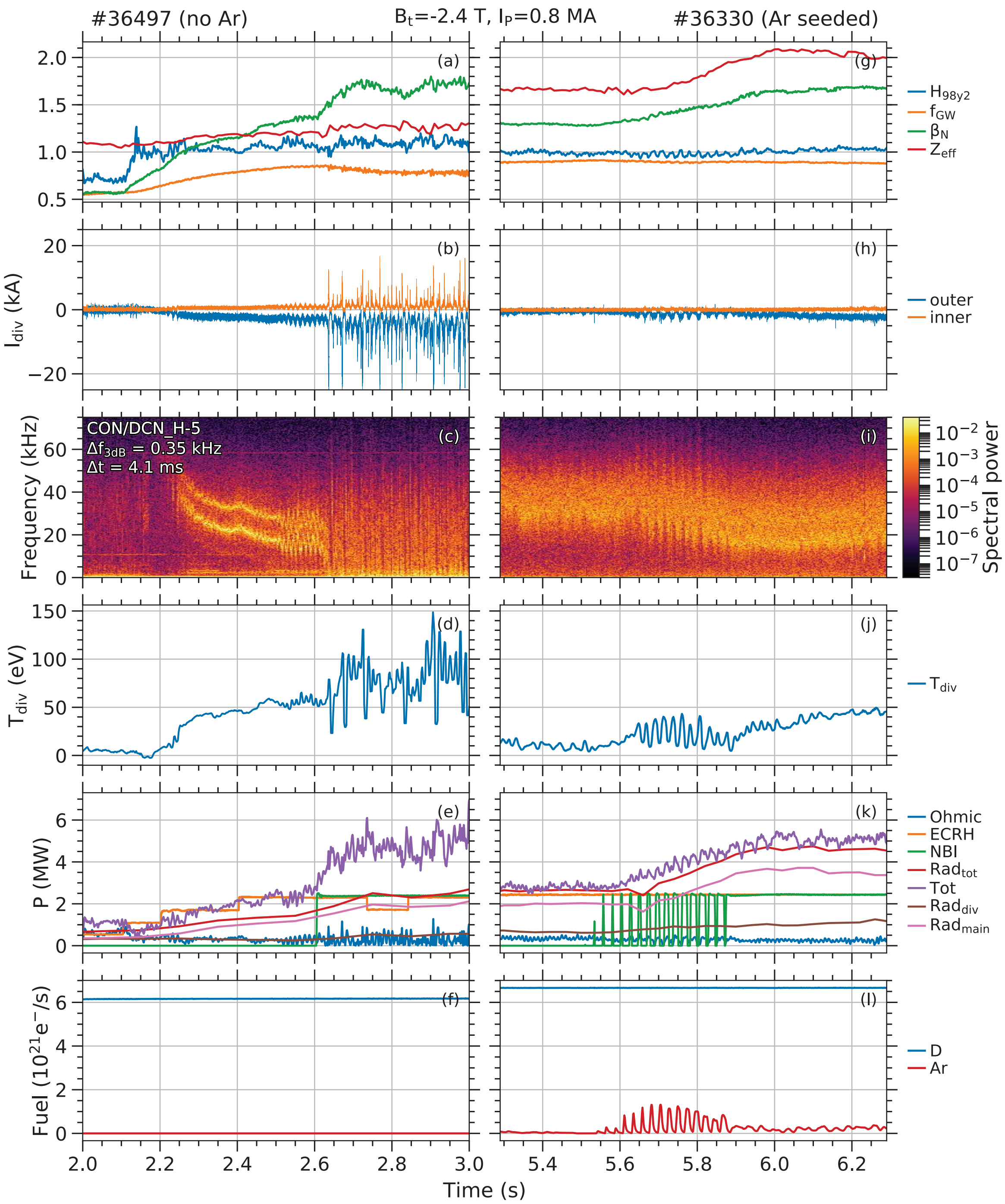

Figure 4.10: Time evolution of different quantities in EDA H-mode ECRH+NBI discharges with and without argon seeding: (a)(g) performance indicators, (b)(h) divertor shunt currents, (c)(i) spectra of edge interferometry measuring line-integrated density fluctuations, (d)(j) proxy for the divertor temperature based on shunt currents, (e)(k) heating and radiated power, and (f)(l) gas puff rates. The left-hand side panels (a)-(f) correspond to a discharge without argon, and the right-hand side panels (g)-(l) to a similar discharge but with argon seeding.

4.3.2 Profiles and radiation

By continuously applying full voltage NBI it is possible to obtain better quality CXRS measurements. Radial profiles of different quantities in the argon-seeded EDA H-mode with an even mix of ECRH and NBI, including not only the usual electron profiles, but also CXRS measurements of impurity (N^{7+}) temperature and rotation up to the separatrix, are shown in figure 4.11. The profiles were mapped to the outer midplane with the IDE equilibrium and radially aligned in accordance to the $T_{\mathrm{e,sep}}$ estimate from the two-point model. Like in the unseeded ECRH examples, core n_{e} (a) is mostly flat, but T_{e} (b) and p_{e} (c) are peaked. In this discharge, the CXRS signal in the inner core, for $\rho_{\mathrm{pol}} < 0.5$, was too low, so T_{i} was extrapolated inwards using the $T_{\mathrm{e}}/T_{\mathrm{i}}$ ratio of a similar discharge in which the spectrometer was measuring a different impurity. Despite having higher core temperature and pressure than the unseeded discharges with lower power, the pedestal in this high power argon-seeded discharge is not higher, explaining why there are no ELMs. The toroidal and poloidal impurity rotations have the typical inversions at the pedestal [296] and were used to compute the radial electric field, E_{r}, from the impurity radial force balance equation. An estimate of the impurity density profile from CXRS measurements was also included [249], but has a small impact in the calculation. The result, illustrated in figure 4.11(l), shows the E_{r} well (orange points and blue line) at the pedestal, reaching a minimum of almost $-20\,\mathrm{kV/m}$ in the steep gradient region. This is deeper than typical values at the L-H transition [297], but is, in absolute value, lower than the estimate from the main ion pressure gradient (red line), which is usually a good approximation in AUG [298]. A possible explanation for the discrepancy is the strong edge toroidal rotation, whose term in the force balance equation (green line) contributes with an almost constant offset that shifts E_{r} to more positive values, while barely affecting the $E \times B$ shear, which is believed to be the relevant quantity for turbulence suppression [27]. These profiles are currently being used in core and edge gyrokinetic GENE [299, 300] simulations to study the turbulence properties of the EDA H-mode. Future dedicated experiments with different parameters and small radial movements of the plasma for increased radial resolution, as well as other strategies for optimal CXRS measurements are also planned.

In order to confirm the existence of enhanced radiation in the pedestal, which seems to keep the plasma free of ELMs without significantly affecting core performance, tomography reconstructions of radiation from bolometry measurements were made to compute radial profiles of the radiated power in discharges with and without argon seeding, as shown in figure 4.12. These have the same $P_{\mathrm{tot}} = 5\,\mathrm{MW}$, with an even mix of ECRH and NBI, but the unseeded

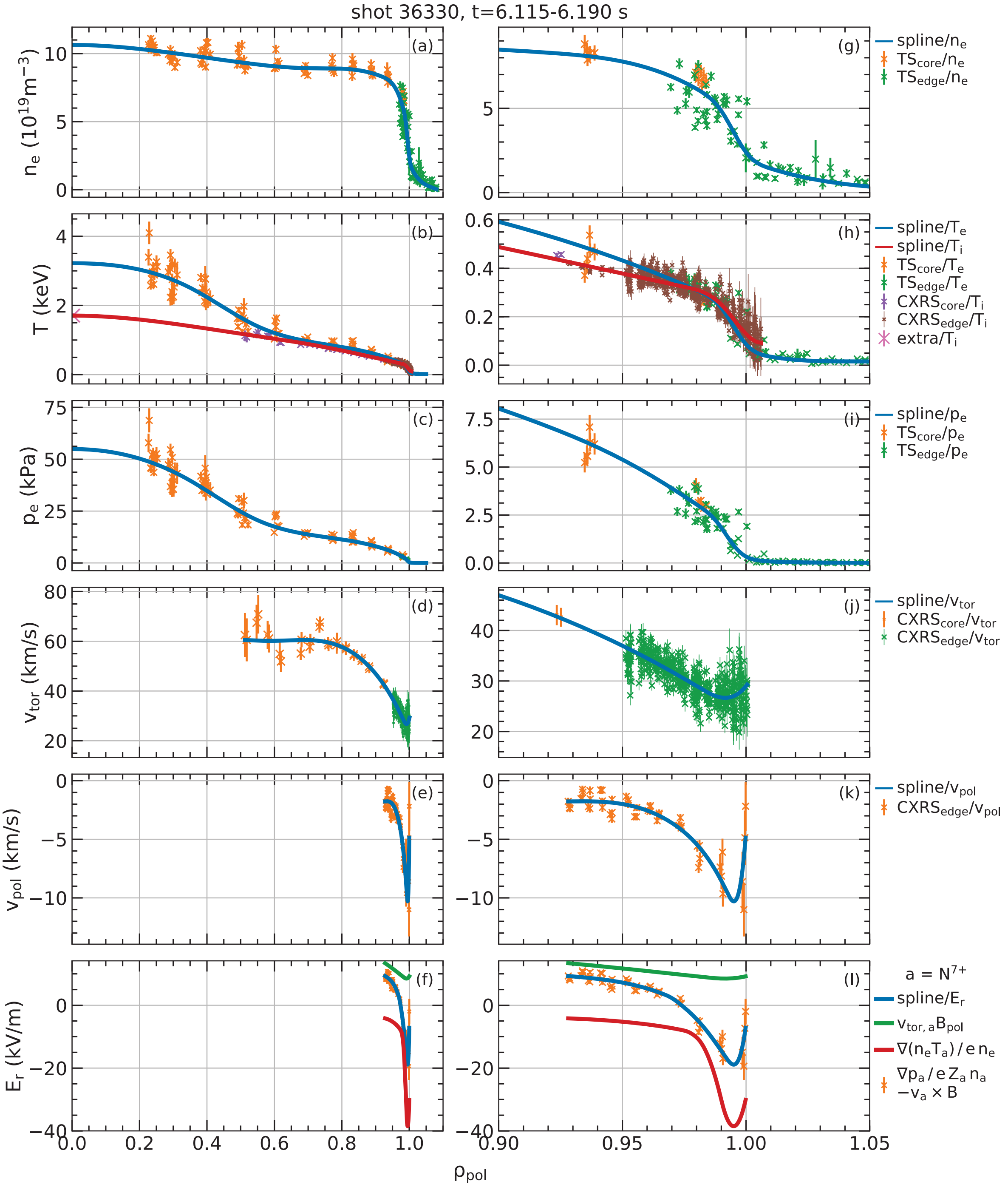

Figure 4.11: Radial profiles of different quantities in an argon seeded EDA H-mode with an even mix of ECRH and NBI: (a)(g) electron density, (b)(h) electron and ion (impurity) temperatures, (c)(i) electron pressure, (d)(j) impurity toroidal velocity, (e)(k) impurity poloidal velocity, and (f)(l) radial electric field. The entire profiles are represented in the left-hand side panels (a)-(f), and a zoom in the pedestal region is shown in the right-hand side panels (g)-(l).

discharge (blue) is an ELMy H-mode, while the argon-seeded discharge (orange) is an ELM-free EDA H-mode. With argon seeding, the average local radiation volume emissivity (a) is slightly higher in the core, but much higher in the pedestal region. As a result, the total radiated power

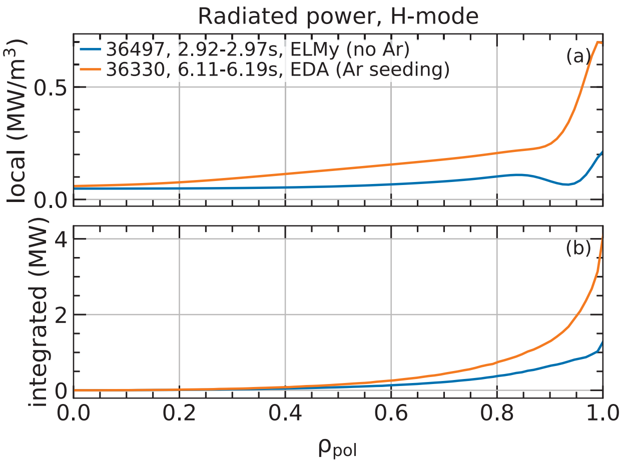

Figure 4.12: Radial profile of (a) local and (b) integrated radiated power from bolometry tomography in two discharges with the same even mix of ECRH and NBI, but different impurity seeding: (blue) an ELMy H-mode without seeding and (orange) an EDA H-mode with argon seeding.

up to each flux surface (b) represents, at the separatrix, a high fraction of the heating power in the argon seeded case, with the bulk contribution coming from the pedestal, but a low fraction in the unseeded case. This explains how the seeded scenario simultaneously avoids ELMs and has a colder divertor that the unseeded one.

The mechanism by which argon radiates in the pedestal can be quite complex, involving both atomic and plasma physics, since it depends on the distribution of the abundances of each charge state, which is governed by ionisation and recombination rates, as well as radial transport. The impurity transport code STRAHL has been used to model these phenomena, including not only collisions with electrons, but also charge exchange (CX) reactions with neutral deuterium atoms [252]. Figure 4.13 shows the results from STRAHL modelling of the argon-seeded mixed heating EDA H-mode using as input the density and temperature profiles of figure 4.11.

The core argon density (a), including all ionization states, was inferred from the soft X-ray volume emissivity profile (b), obtained from tomographic inversion of measured line-of-sight integrals [254]. The contribution of tungsten and deuterium ions to the soft X-rays was included in the calculation, using the tungsten concentration deduced from spectra measured in the VUV range by a grazing incidence spectrometer [253], being rather small when compared to the argon contribution in this discharge. The core argon density is lower than the electron density by almost 3 orders of magnitude, which means fuel dilution is low.

In the pedestal, where soft X-ray emission is almost non-existent due to the lower temperature, the argon density is determined together with the neutral deuterium density by fitting the modelled

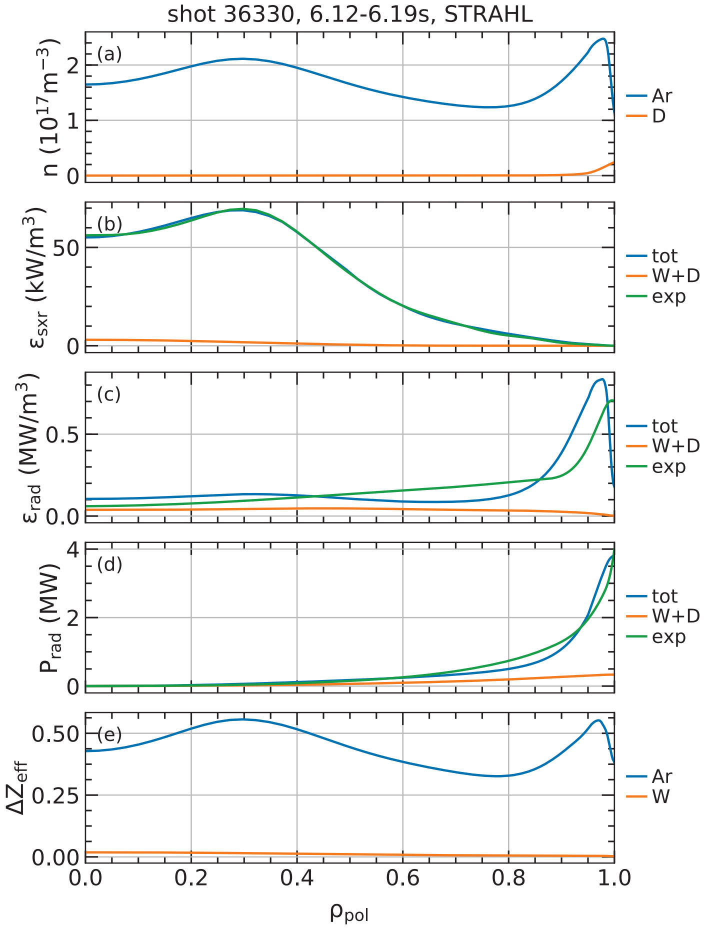

Figure 4.13: Radial profiles of different quantities resulting from a STRAHL run of an argon seeded EDA H-mode and comparison with experimental measurements: (a) argon and neutral deuterium density, (b) soft X-ray volume emissivity, (c) total radiation volume emissivity, (d) total radiated power, (e) variation of Z_{eff} due to impurities.

radiation to the experimental bolometry data of figure 4.12 and to spectral lines in the VUV range measured by the SPRED spectrometer. Inclusion of neutral deuterium and CX reactions is crucial for the accuracy of the model, as it can significantly alter the ionization balance of lower argon charge states, affecting the radiated power in the pedestal by a factor of possibly more than 2.

The resulting total radiation volume emissivity (c) and integrated radiated power (d) show good agreement with the experimental values, with residual differences easily ascribed to uncertainties in the tomography reconstructions and presence of other impurities, such as boron, carbon and nitrogen. The resulting $\Delta Z_{eff} \approx 0.4$ from the modelled argon density is comparable to the experimentally observed variation with seeding in this discharge, computed from Bremsstrahlung measurements, which corroborates the results of the model. The total measured $Z_{eff} \approx 2$ is higher than what results from the contribution of argon and tungsten alone, suggesting that other impurities are indeed present in the plasma. Nevertheless, argon can explain most of the measured radiation, demonstrating its fundamental role in cooling the pedestal, not only from an empirical, but also from a theoretical point of view.

4.3.3 Unseeded heating mix

Argon seeding leads to radiative pedestal cooling, which allowed the EDA H-mode to be maintained with a full NBI source and equal amount of ECRH power. However, seeding is not required to obtain a stationary ELM-free plasma with mixed heating, as long as the the total power is adequate. Figure 4.14 shows an example of a discharge with constant ECRH and a slow NBI ramp by pulse width modulation of a reduced voltage source. The L-H transition occurs with one of the first NBI blips (d) and the QCM then appears (c), as a mark of the EDA H-mode maintained until the end of the ramp. P_{tot} (d) and β_{N} (a) gradually increase, with some modulations due to the non-smooth heating ramp, but no ELMs occur, as evidenced by the absence of large spikes in the divertor shunt currents (b), when compared for example with figure 4.10(b). $H_{98\mathrm{y}2}$ is slightly lower than in the pure ECRH case, but the achievement is still important, because it opens the possibility for useful mixed heating EDA H-mode studies under various conditions in the future, not only to benefit from CXRS measurements, but also to have access to a wider range of input parameters, namely torque and ion heating, to better understand the physics in play. In fact, an identical discharge with NBI only was also tried, but did not achieve a stationary EDA H-mode, which suggests that some ECRH is a crucial ingredient for this regime in AUG. Possible reasons include poorer impurity flushing in the core due to the lack of localized electron heating, too much torque and different $T_{\mathrm{e}}/T_{\mathrm{i}}$ ratios, but more experiments are needed to properly investigate this.

4.3.4 Summary

To summarize, the EDA H-mode has been achieved in AUG with pure ECRH and with a mix of ECRH and NBI, both with and without argon seeding. Argon has a strong influence in the plasma, especially in the pedestal, where it causes significant radiation, including CX with neutral deuterium. This causes a localized cooling effect which lowers the pedestal, with a small impact in the inner core, allowing more heating power to be applied without the occurrence of ELMs. As a result, higher β_{N} can be achieved in this ELM-free regime, with low fuel dilution. Besides this, pedestal radiative cooling by argon seeding leads to less power entering the SOL,

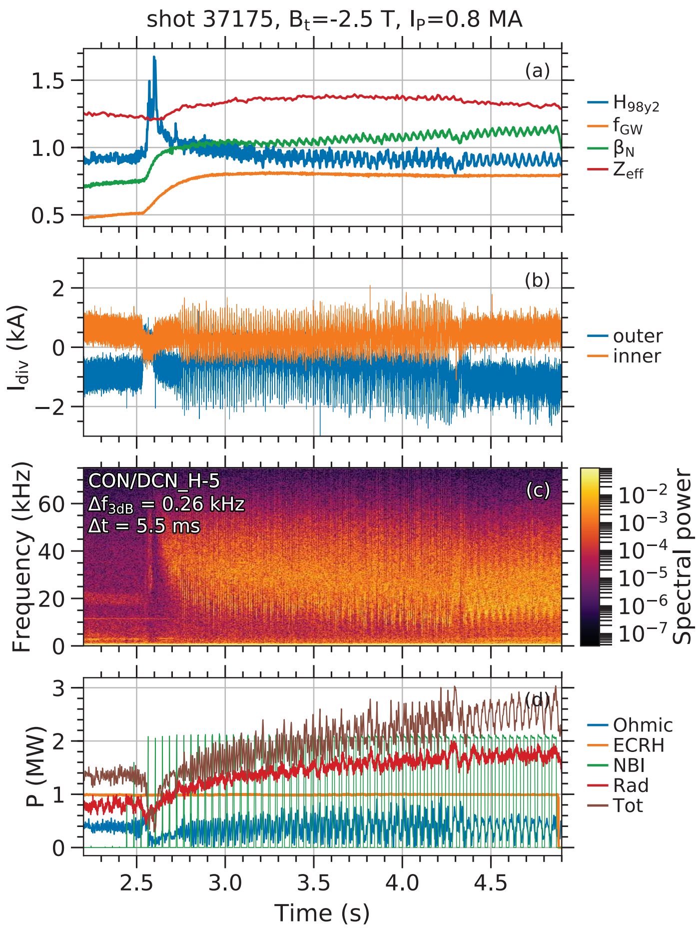

Figure 4.14: Time evolution of different quantities in an unseeded EDA H-mode with a mix of ECRH and NBI: (a) performance indicators, (b) divertor shunt currents, (c) spectra of edge interferometry measuring line-integrated density fluctuations, and (d) heating and radiated power.

and argon itself also radiates in the divertor, easing the conditions to reach detachment and mitigate heat loads to PFCs. In Alcator C-mod, argon seeding in the EDA H-mode resulted in too much confinement degradation [125, 126], with nitrogen and neon being deemed more effective for radiative exhaust. In AUG however, argon is an important asset as an actuator for tailoring radiation profiles in the pedestal and divertor. Together with strong shaping and possibly other seeding species, such as nitrogen, it may lead to a performant EDA H-mode ELM-free scenario with a benign divertor. A large portion of the parameter space remains to be explored and different optimization strategies are still available, so future experiments are required to continue the path towards reactor relevance, which appears to be well paved.

Chapter 5

Parameter space and dependences

This chapter presents results of experiments performed in AUG to explore the parameter space of the EDA H-mode. Plasma behavior, access windows and dependences of global confinement, core and edge parameters on heating power, fueling and plasma current are analyzed in strongly shaped plasmas. Finally, an overview including more discharges and dimensionless quantities that can be compared with scenarios in other devices is shown and discussed.

5.1 Fueling and heating power

One of the simplest, but most important actuators in tokamak operation is the gas puff used to control fueling levels. It can have a strong impact in the behavior of the plasma, with varying influence across different confinement regimes. The EDA H-mode in AUG is no exception, as its access and performance are significantly affected by the gas puff. Heating power is also one of the main control knobs in fusion devices and has been shown in previous chapters to be of paramount importance in achieving EDA H-modes, as well as avoiding ELMs. For this reason, a combined study of the influence of fueling level and heating power has been performed in plasmas with ECRH around a strongly shaped EDA H-mode scenario of AUG at $B_\mathrm{t} = -2.5\,\mathrm{T}$ and $I_\mathrm{p} = 0.8\,\mathrm{MA}$.

5.1.1 Input parameters and general behavior

There are multiple ways to explore the two-dimensional parameter space of fueling and heating power, but some caveats exist. A straightforward strategy would be to perform discharges at constant power and gas puff, and then vary the applied values from shot to shot, covering for

shot	time period (s)	Γ_D (10^{21} e$^-$/s)	P_{ECRH} (MW)	P_{tot} (MW)
36257	2.600 – 5.870	0.91	0.72 – 3.38	1.07 – 3.73
36157	2.600 – 6.800	2.53	1.31 – 4.15	0.75 – 5.70
36124	2.900 – 7.090	2.58	0.40 – 3.00	0.80 – 3.29
37193	2.100 – 5.900	4.67	0.64 – 3.42	0.93 – 3.62
36349	2.167 – 4.000	6.65*	1.24 – 4.16	0.77 – 4.39
36151	3.000 – 6.210	7.23	0.86 – 2.94	0.94 – 3.18

Table 5.1: Discharges performed as part of the fueling and heating power scan, with the relevant time periods and corresponding input parameter ranges: deuterium gas puff, ECRH power and total power lost by the plasma. *This shot also has nitrogen seeding.

example an equally spaced grid with a given resolution and extent. While this approach would result in a very clean experiment with high quality data, it has the problem of requiring a large number of discharges, basically the product of the number of samples in each parameter. This is unpractical in a highly demanded device like AUG, with frequently overbooked experimental campaigns covering a wide range of topics.

A possible solution is to vary the parameters during each discharge, at a cost of risking non-stationarity and less statistics in each sampled point. This tradeoff was readily embraced, but further decisions had to be made, namely which trajectory to follow when varying the parameters during the discharges. Besides the obvious choice of keeping one input parameter constant and ramping or stepwise increasing the other one, defined trajectories along output parameters, such as n_e or β, are often employed in fusion experiments by resorting to real-time feedback control. However, these more sophisticated methods can be problematic with the occurrence of confinement regime transitions that lead to sudden changes in the plasma parameters, sometimes causing the controllers to respond erratically or suffer large feedback oscillations.

For this reason, the simple approach of using feed-forward trajectories in the input parameters was chosen. The last remaining decision was which parameter to keep constant during each shot. Since heating power has the most potential to damage machine components, it was gradually increased during each discharge, while keeping the deuterium puff, Γ_D, constant, which was then varied from shot to shot. Table 5.1 shows the discharges performed as part of this fueling and heating scan, with the relevant time periods and corresponding input parameter ranges.

A comparison of three of these ECRH staircase discharges at different fueling levels is shown in figure 5.1. The discharge in the middle column exhibits the typical behavior previously described in section 4.1.2, with a strong density increase (e) following the L-H transition and

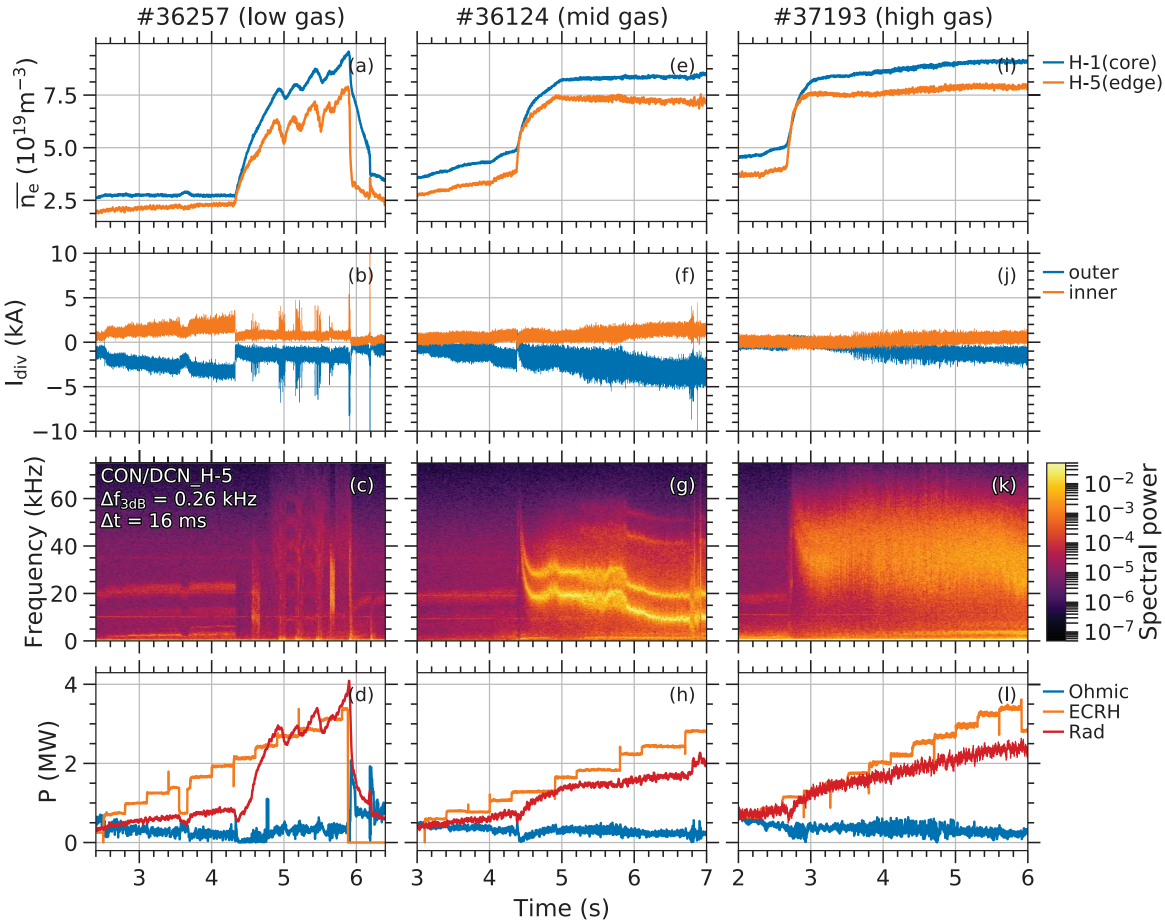

Figure 5.1: Time evolution of different quantities in ECRH staircase discharges at different fueling levels, taken from table 5.1, by order of increasing gas puff: (a)(e)(i) line-averaged electron density, (b)(f)(j) divertor shunt currents, (c)(g)(k) spectra of edge interferometry measuring line-integrated density fluctuations, (d)(h)(l) heating and radiated power. The left-hand side panels (a)-(d) correspond to a discharge without low gas puff, the middle column panels (e)-(h) to one with medium gas puff, and the right-hand side panels (i)-(l) to one with high gas puff.

the appearance of the QCM shortly after (g), marking the EDA H-mode. After a few hundred ms, the density stops increasing and the EDA H-mode is maintained for a long time until the occurrence of ELMs (f) at a much higher power (h).

With stronger gas puff, on the right-hand side column of figure 5.1, the plasma has a similar behavior, but the density (i) is higher, the QCM is broader in frequency (k) and no ELMs occur (j) even at higher heating power (l). The cause of QCM broadening with fueling is not yet known and could in principle be related to changes in the behavior of the mode itself or to perturbations caused by other instabilities and filaments excited by the altered profiles. These plasmas with more gas puff show some similarities with the strongly shaped scenarios of type II ELMs [99], also called small ELMs [100], and, more recently, quasi-continuous exhaust (QCE) regime of AUG. Very high n ballooning modes, made unstable by the high separatrix density, have been proposed as the cause of exhaust and filamentary activity in this regime [101]. In Alcator C-mod, small grassy ELMs have been observed when edge temperature and pressure gradients increase too much for the EDA H-mode to be maintained [115], but the plasmas were found to be stable to infinite n ballooning modes when bootstrap current was included. Experiments in AUG are planned to extend the EDA H-mode to input parameters closer to those of the small ELM scenarios and properly investigate the relations between the two regimes.

When the fueling is too low, the behavior of the plasma completely changes, as exemplified in the left-hand side column of figure 5.1. In this case, the L-mode density is lower (a), requiring a higher heating power (d) for the L-H transition, and the subsequent evolution is very different. The density (a) and radiated power (d) rise uncontrollably until sequences of ELMs occur (b) and the process is repeated several times up to a point where the ECRH cutoff is approached and the external heating is turned off. ECMs are present (c) in this nonstationary H-mode, but the QCM is not observed. This shows that there is a lower boundary in gas puff for accessing the EDA H-mode and a steady-state scenario.

In order to better understand the EDA H-mode access window in terms of fueling and power, the discharges of table 5.1 were analyzed and divided in time periods according to their respective confinement regimes, labelled as: L-mode, I-phase, nonstationary ELM-free H-mode with ECMs, evolving EDA H-mode, developed EDA H-mode, evolving ELMy H-mode, and developed ELMy H-mode. These were further divided in subperiods of approximately 50 ms to sample the plasma and input parameters along the heating power ramps. The explored parameter space is illustrated in figure 5.2, with the different regimes coded by color. The ECRH power window (a) to access EDA H-mode is strongly affected by the deuterium gas puff, being non-existent at low fueling and expanding as fueling levels increase. It starts around ≈ 1 MW and is limited by ELMy H-modes at high power. At high gas puff, the ELMy boundary was only achieved in one of the discharges, at ≈ 4 MW, but this shot also had nitrogen seeding, which might affect the results, so it will not be used in the analyses that follow. In this EDA H-mode scenario, it is difficult to increase the heating power with strong gas puff because the density is so high that it approaches the ECRH cutoff. Future fueling and power scans at lower plasma current are planned to overcome this limitation.

While the ECRH power, P_{ECRH}, is the direct input parameter of the performed experiments, it does not represent the total power heating the plasma, since there is also an ohmic contribution. Besides this, the plasma does not reach its final state instantaneously when the heating power is

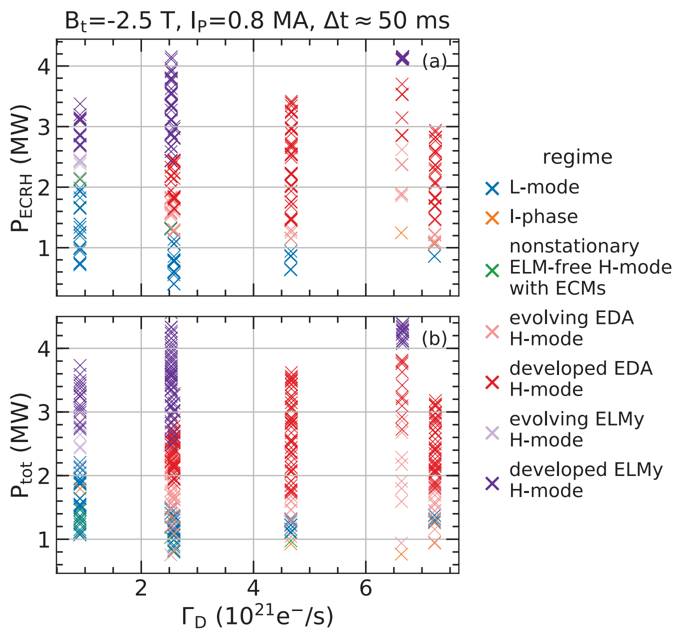

Figure 5.2: Explored parameter space in fueling and power scans showing the window to access EDA H-mode as a function of deuterium gas puff in terms of: (a) ECRH power, (b) total power lost by the plasma. The various confinement regimes are indicated by different colors.

increased, since it takes time for the profiles to build up and the dynamics to correspondingly adapt. For this reason, a more adequate quantity to characterize the plasma state might be the total power lost by the plasma, P_{tot}, which incorporates all the heating sources and deducts the time derivative of the stored energy, mitigating some transient effects. Figure 5.2(b) shows the scanned parameter space expressed in terms of this variable. The overall picture is similar to the P_{ECRH} space, but an important difference exists in points after regime transitions, such as non stationary ELM-free H-modes and the evolving EDA H-modes. The sudden confinement improvement leads to an increase in $\mathrm{d}W_{\mathrm{MHD}}/\mathrm{d}t$, causing a drop in P_{tot}, which then overlaps with the lower input power L-mode regime. In any case, the EDA H-mode in AUG does not exist with too low fueling and its power window broadens with increasing gas puff. In C-mod, the EDA H-mode also requires a minimum L-mode density, controlled by fueling, below which the resulting H-modes are transient and accumulate impurities [102, 103].

5.1.2 Core and pedestal

Besides affecting EDA H-mode access, fueling and heating power also influence plasma density, temperature and pressure profiles, as shown in figure 5.3, populated with data from IDA reconstructions, which combine several diagnostics [246]. The left-hand side column presents

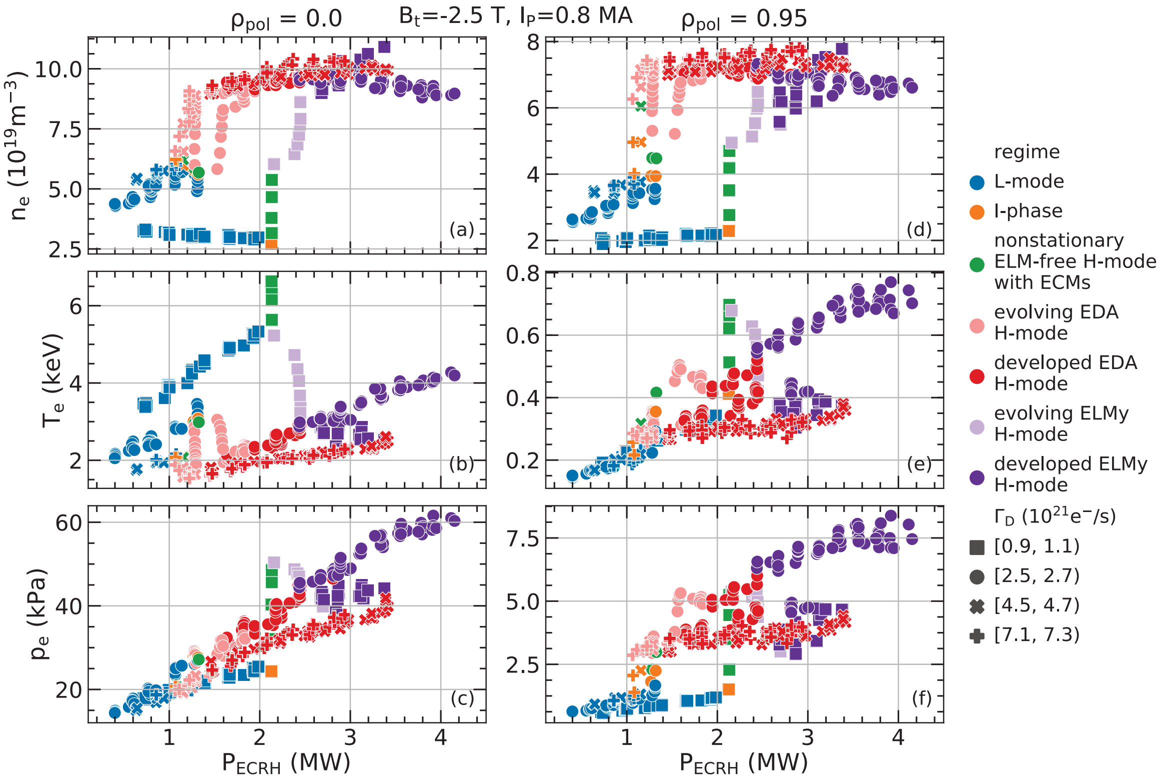

Figure 5.3: Core and edge electron plasma parameters from IDA in fueling and heating power scans as a function of ECRH power: (a,d) density, (b,e) temperature, and (c,f) pressure. The left-hand side panels (a)-(c) were evaluated at the magnetic axis ($\rho_{\mathrm{pol}} = 0$) to represent the core and the right-hand side panels (d)-(f) at the edge ($\rho_{\mathrm{pol}} = 0.95$), as a proxy for pedestal parameters. The various confinement regimes are indicated by different colors and the deuterium gas puff levels by different symbols.

core values evaluated at the magnetic axis and the right-hand side column contains a proxy for pedestal top values, evaluated at $\rho_{\mathrm{pol}} = 0.95$. This location is slightly more interior than the actual pedestal top, but results in more robust quantities with respect to misalignment of diagnostics and systematic biases, which become more relevant closer to the separatrix.

Core density (figure 5.3(a)) in L-mode increases with fueling and power, except in the low fueling case, where it is stays approximately constant. With the transition to EDA H-mode, possible at moderate and high gas puff, the core density suffers an abrupt increase and after the regime develops it shows a positive, but weak dependence on both heating power and fueling. When the ELMy H-mode is achieved, the power dependence is reversed and density decreases due to transport caused by ELM. In the lowest fueling case that does not achieve EDA H-mode, however, the density in the nonstationary ELM-free H-mode and then ELMy H-mode continues to rise between ELMs as the power is increased, surpassing even the highest fueling discharge. The edge density presented in figure 5.3(d) shows an overall similar behavior, but with a more marked difference between developed EDA H-mode and L-mode, at ratio of about 2. Besides this, the edge density in EDA H-mode stays constant with heating power, an observation shared also by C-mod experiments [114]. A weak scaling of pedestal density with the L-mode target density, which is controlled by the gas puff, was also found in C-mod [114].

Core temperature, shown in figure 5.3(b), decreases with fueling and increases with power in all L-modes, but decreases during the initial phases of the EDA H-mode, where the plasma profiles are still evolving and the density is strongly increasing. After it stabilizes, the temperature then increases with power and continues to do so even when ELMs appear. The exception is again the lowest fueling case, which achieves extremely high core electron temperature in L-mode and nonstationary ELM-free H-mode, but then decreases even as the heating power is increased, though this could be an effect of impurity transport which happens at long timescales rather than a reaction to the power itself. In EDA H-mode, with adequate fueling, no such effects are observed, and the core temperature is inversely correlated with gas puff. The edge temperature (figure 5.3(e)) is almost independent of gas puff in L-mode, but increases with power. Contrary to the core, edge temperature increases with the transition to EDA H-mode, despite the simultaneous density rise, evidencing an edge transport barrier in both channels. Like in the core, edge temperature in EDA H-mode is then positively correlated with power and negatively correlated with fueling. In C-mod, the pedestal temperature in EDA H-mode was found to moderately decrease with L-mode target density and sublinearly increase with heating power [114]. This appears to be consistent with AUG data, but the strength of the dependence seems to vary significantly with fueling and the narrow investigated range prevents robust quantitative comparisons from being made.

As a result of electron density and temperature behavior, core pressure shown in figure 5.3(c) exhibits a positive dependence on power across all confinement regimes, apart from the transient phases of the lowest fueling shot. The core gain from EDA H-mode when compared to L-mode is modest, but the edge improvement is significant, as evidenced in figure 5.3(f). Once in EDA H-mode, the edge pressure is inversely correlated with fueling and has a positive but weak dependence on heating power. These results are qualitatively consistent with those of C-mod [114].

The strong influence of confinement regime on edge parameters motivates looking at the data from a different perspective. Figure 5.4 shows the edge electron temperature as a function of density with the various regimes coded by different colors and the gas puff by symbols as in the

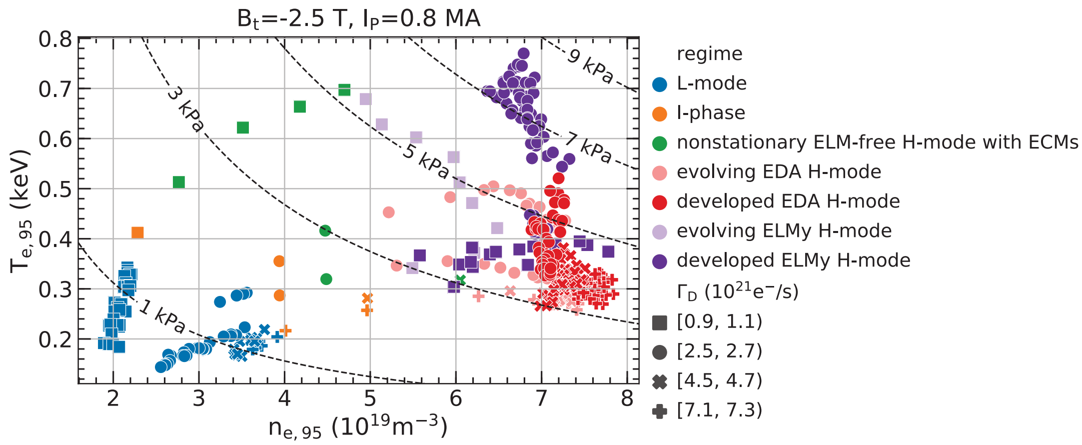

Figure 5.4: Edge operational space of different confinement regimes in terms of electron temperature and density obtained from IDA data evaluated at $\rho_{pol} = 0.95$ of discharges in a fueling and heating power scan. The regimes are coded by color and the gas puff levels by symbol. The dashed lines indicate constant pressure.

previous analysis. The L-mode exists in a region of low edge temperature, density, and therefore pressure, whereas the H-modes have high edge pressure. The I-phase, very short-lived in these strongly shaped plasmas, appears in between. The EDA H-mode has a very high density and its edge pressure lies between 3 and 7 kPa for the discharges in this scan. Only the medium fueling shots were able to go from EDA to ELMy H-mode as temperature and pressure increased with heating power. It is not clear whether the temperature and pressure boundaries of the high fueling discharges would reach or even surpass those of the medium fueling cases, possibly populating a region of higher edge density and temperature.

The low gas puff discharge follows a trajectory of high temperature, transiently peaking at the nonstationary ELM-free H-mode, just before ELMs appear and the plasma starts to move in the direction of the region occupied by the EDA H-mode. The ELMy plasma eventually overlaps with this region, showing that edge temperature and density evaluated at $\rho_{pol} = 0.95$ are not enough to uniquely determine the confinement regime. Besides the possible influence of other quantities in this location, the critical parameters to access EDA H-mode could also be localized closer to the separatrix, but such analysis is more subtle and challenging due to the existence of several sources of uncertainty and bias in the experimental data. Future analysis and experiments with better quality measurements are planned to investigate this possibility. Furthermore, the simple 1D approach to the profiles adopted in this discussion might simply not capture all the relevant phenomena in play, especially when one considers the strong influence of plasma shape in accessing the EDA H-mode, previously described in section 4.1. A 2D model of the plasma may be required to accurately explain the parameter space of the EDA H-mode.

5.1.3 Global confinement

A global view of confinement and its dependence on the scanned parameters also provides useful information, as illustrated in figure 5.5. The plasma stored energy, W_{MHD}, increases with power in each confinement regime. In EDA H-mode, it appears to exhibit an offset linear dependence on power, although the limited scanned range does not preclude a sublinear relation without offset, as computed in C-mod experiments [114]. This translates to an energy confinement time, τ_{E}, that decreases with power, but the degradation is not as severe as the prediction from the IPB98(y,2) scaling [51], since $H_{98\mathrm{y}2}$ increases with power in the developed EDA H-mode. Such behavior has also been observed in EDA H-modes of C-mod [126, 301]. This suggests that $H_{98\mathrm{y}2}$ might not be the ideal quantity to assess confinement quality of EDA H-modes and make extrapolations to future reactors. In fact, even in the ELMy H-mode regime, from which most of the scaling was derived, weaker dependences of confinement with power are sometimes found in single machine scans [302]. Another very important quantity, arguably the ultimate figure of merit to evaluate the performance of fusion plasmas, due to its requirement for ignition, is the triple product $\overline{nT}\tau_{\mathrm{E}} = \overline{p}\tau_{\mathrm{E}}$, shown in figure 5.5(d). In developed EDA H-mode, the average pressure increases with power, but the energy confinement time decreases, and, as a result, the triple product stays approximately constant.

It is interesting to note that significantly higher τ_{E}, $H_{98\mathrm{y}2}$, and $\overline{p}\tau_{\mathrm{E}}$ are achieved transiently during the initial phases of the EDA H-mode, when the density is still evolving. Also the nonstationary ELM-free H-mode can for brief moments attain incredible performance, with high $\overline{p}\tau_{\mathrm{E}}$ and $H_{98\mathrm{y}2} > 1.6$. In fact, the current world record of magnetic confinement fusion power was achieved in such a scenario using a deuterium-tritium mixture in JET [21]. However, these transient regimes rapidly encounter MHD instabilities, ELMs, or impurity accumulation and cannot be maintained in a sustainable way to be used in a reactor for energy production. Even if inductive scenarios end up being the optimal choice and are employed while operating the devices in a pulsed manner, the plasma regime itself needs to be stationary in order to produce a meaningful amount of energy per pulse. In this sense, the EDA H-mode continues to be a promising regime due to its steady-state ELM-free capabilities. The L-mode also has these characteristics and can actually exhibit decent confinement, as shown in figure 5.5(b,c), but it is only able to achieve low heating power and achieve low triple product, so it remains an inferior

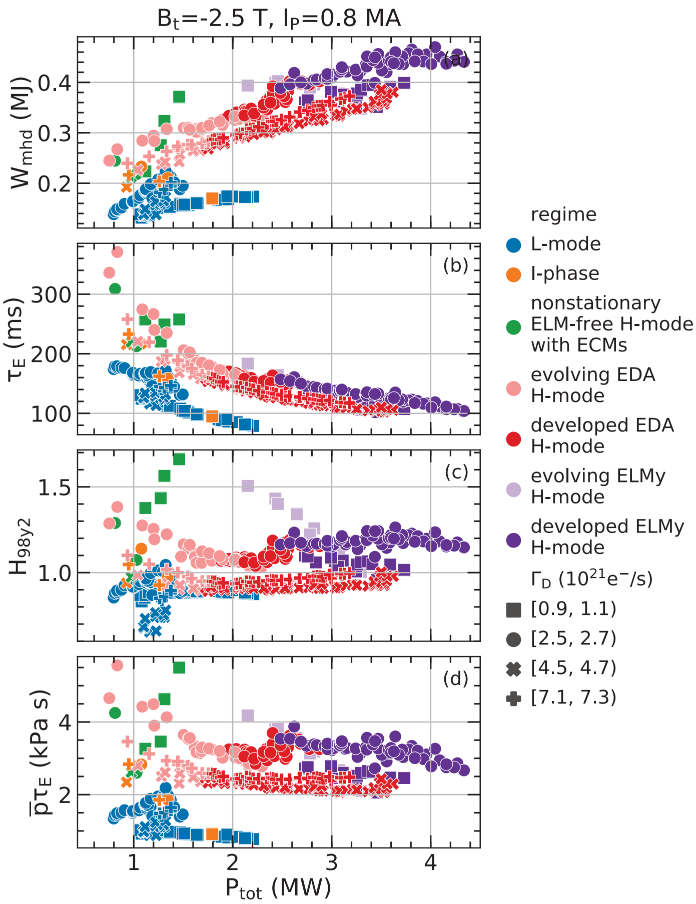

Figure 5.5: Global confinement quantities as a function of the total power lost by the plasma for different fueling levels: (a) stored energy, (b) energy confinement time, (c) confinement enhancement factor, (d) triple product. The different regimes are coded by color and the gas puff levels by symbol.

alternative.

In terms of fueling dependence, figure 5.5 shows that, for the same power, stored energy in EDA H-mode sightly decreases with gas puff. This means energy confinement time is also slightly lower, which is opposite to the IPB98(y,2) scaling, that predicts a weak improvement of τ_E with density. As a result, H_{98y2} in EDA H-mode decreases with strong gas puff. In C-mod, the stored energy of EDA H-modes also showed a negative, but weak, relation with L-mode target density [114]. The decrease in triple product may be an argument against operating with high gas puff, but the expanded ELM-free power window that results is an advantage worth considering. In fact, for the same triple product, higher heating power does lead to higher fusion power output, so strong fueling may turn out to be beneficial in the end. Besides that, heat exhaust constraints may also force operation with high gas puff values. Further experiments are required and currently planned to investigate the upper power limit of EDA H-modes with strong fueling and the associated effects on the plasma. These discharges will possibly approach the parameter space of the small ELM regime, but with differences in torque which have not yet been well studied and could have a strong impact in the physics of the scenarios.

5.2 Plasma current and heating power

The previous section has shown that heating power affects several parameters of the EDA H-mode, but has a small influence on the triple product once the plasma reaches steady-state. If this dependence is general, it suggests that, after the L-H transition and evolving period, a future reactor operating in EDA H-mode should not heavily rely on power to get closer to ignition. Instead, the scenario should be designed to achieve the desired triple product mostly by resorting to other input parameters. One of such parameters is the plasma current, I_p, known to have a strong impact in many aspects of both L-mode and H-mode plasmas, including confinement and performance. For this reason, a combined study of the influence of plasma current and heating power has been performed in plasmas with ECRH around a strongly shaped EDA H-mode scenario of AUG at $B_\mathrm{t} = -2.5\,\mathrm{T}$ and $\Gamma_\mathrm{D} \approx 2.5 \times 10^{21}\,\mathrm{e}^-/\mathrm{s}$.

5.2.1 Input parameters

To explore the two-dimensional parameter space of plasma current and heating power, the same strategy used in the fueling scan of section 5.1 was employed. The ECRH power was gradually increased in steps during each discharge while the current was kept constant, being varied from shot to shot. Table 5.2 shows the discharges performed as part of this scan, with the relevant time periods and corresponding input parameter ranges. The discharges were analyzed and divided in time periods according to their respective confinement regimes. These were then further divided in subperiods of approximately 50 ms to sample the plasma and input parameters along the heating power ramps.

Overall, the plasmas show similar qualitative behavior, but important quantitative differences with variations in plasma current. Figure 5.6 shows the explored parameter space with the different regimes coded by color. The EDA H-mode power window is almost non-existent at 0.5 MA, but expands significantly as the current is increased. This is a positive result, since high I_p, or equivalently low safety factor, assuming constant B_t, is in general considered a requirement for reactor scenarios. In C-mod, the EDA H-mode is more likely at high edge safety factor

shot	time period (s)	I_p (MA)	P_{ECRH} (MW)	P_{tot} (MW)
36980	2.100 – 5.500	0.5	0.63 – 2.32	0.77 – 2.46
35970	2.600 – 8.290	0.6	0.41 – 3.93	0.53 – 4.30
38049	2.100 – 8.590	0.7	0.56 – 3.65	0.75 – 3.99
36124	2.900 – 7.090	0.8	0.40 – 3.00	0.80 – 3.29
36157	2.600 – 6.800	0.8	1.31 – 4.15	0.75 – 5.70

Table 5.2: Discharges performed as part of the current and heating power scan, with the relevant time periods and corresponding input parameter ranges: plasma current, ECRH power and total power lost by the plasma.

[102, 104, 106], which at first sight might seem to contradict the AUG results, but actually does not. At $q_{95} < 3.5$ in C-mod, nonstationary ELM-free H-modes are more likely than EDA H-modes, but the AUG strongly shaped EDA H-modes at 0.8 MA have $q_{95} = 4.9$, being well inside the favorable range of C-mod. In fact, nonstationary ELM-free H-modes are not a problem in these AUG discharges if enough gas puff is used, at least up to this current. Unfortunately, EDA H-modes at higher I_p could not be properly investigated in AUG because the resulting high density reaches the ECRH X2 cutoff. O2 heating might be a solution to this limitation, but is in general more challenging and has not yet been tried in EDA H-mode. ICRH is also a possible alternative that is planned for future experiments. In any case, force and/or current limits of the poloidal field coils are approached at higher I_p, preventing plasma currents above 0.9 MA to be safely reached with the strong plasma shaping used in these EDA H-modes, regardless of the heating method. Another approach to lower the safety factor in EDA H-mode is to lower the magnetic field. This is not compatible with the standard AUG heating scheme of X2 ECRH, but has been done in other scenarios with X3 ECRH [199]. Future experiments are also planned in AUG to try obtaining the EDA H-mode with this alternative heating scheme at lower B_t.

5.2.2 Core and pedestal

Plasma current has a strong impact not only on the power window to access EDA H-mode, but also in the resulting electron density, temperature and pressure profiles, as shown in figure 5.7. The dependence of the different core and edge quantities on heating power does not change significantly with plasma current, being mostly identical to what was previously described in section 5.2.2. An exception is the constant density at 0.5 MA in ELMy H-mode, which decreases with power for the other currents. In EDA H-mode, however, the influence of power is consistent

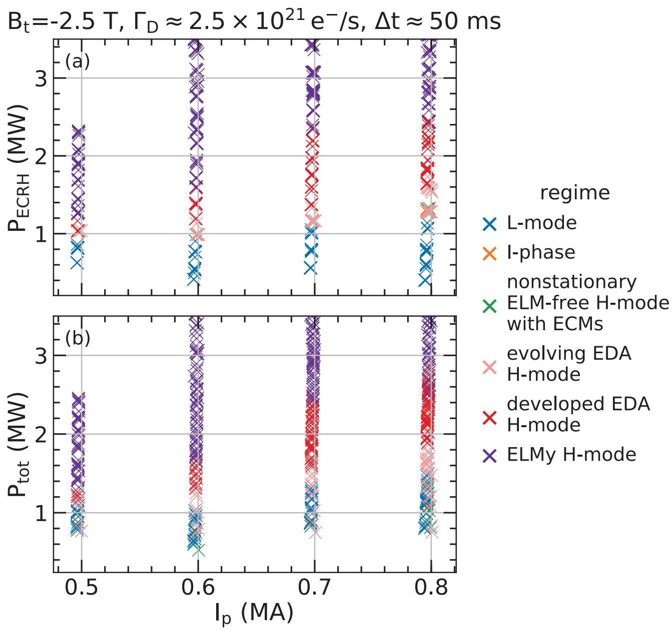

Figure 5.6: Explored parameter space in plasma current and power scans showing the window to access EDA H-mode in terms of: (a) ECRH power, (b) total power lost by the plasma. The various confinement regimes are indicated by different colors.

across all scanned I_p values.

To better visualize the dependence of the profiles on plasma current, the same data is presented as a function of I_p in figure 5.8, but just for the developed EDA H-mode and with the power coded in color. The density is strongly affected by plasma current, achieving very high values and approaching the ECRH cutoff as I_p is increased. This technical limit is what prevents higher plasma current from being scanned in X2-heated AUG EDA H-modes. In the core (a), the marginal density increase appears to become modest at 0.8 MA, but not in the edge (d), where the relation between n_e and I_p remains linear with a negative offset. The pedestal density of EDA H-modes in C-mod also has an approximately linear dependence on plasma current [114], but no offset has been reported.

The core temperature, shown in figure 5.8(b), exhibits a non-monotonic dependence on current, with the 0.6 MA discharge achieving the highest values despite the low heating power. Since only one discharge was performed at this current, it is not clear whether the effect is robust or if it was an outlier. The same can be said for the edge temperature (e), though the difference is less pronounced. More discharges at low current are planned to properly assess the question.

The resulting electron pressure also suffers from this effect, but the robust behavior of the density still allows a general trend of increasing pressure with plasma current to be visible. This

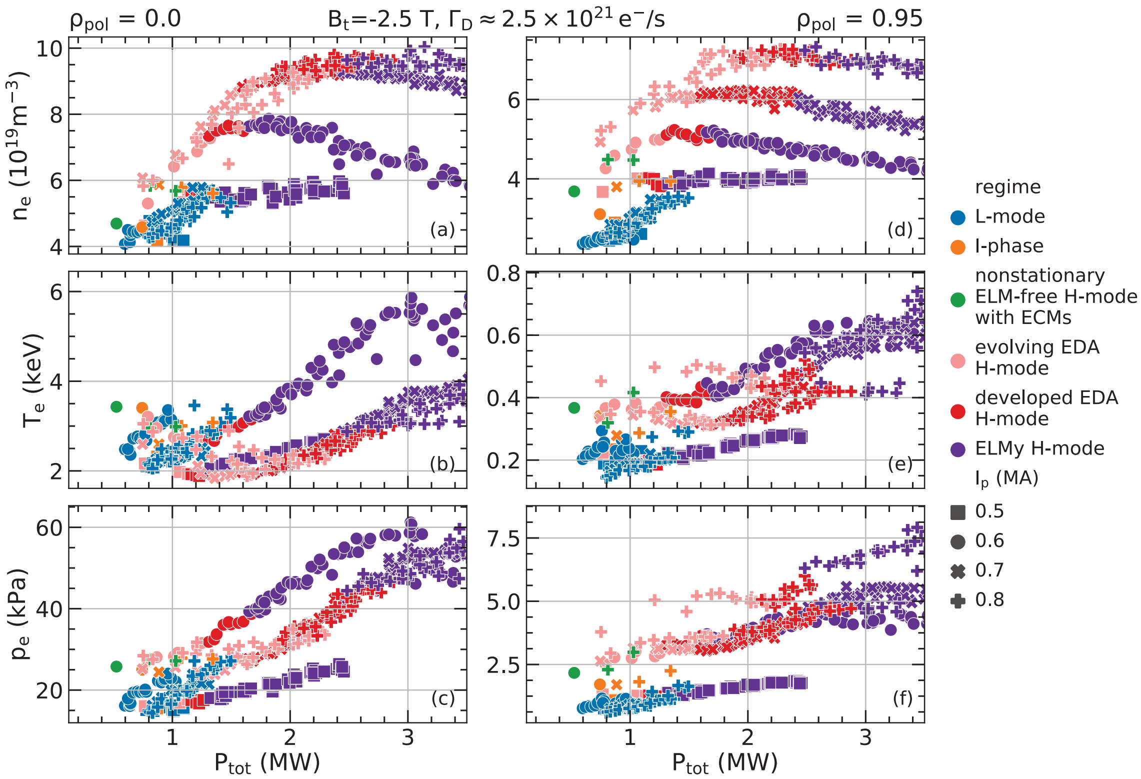

Figure 5.7: Core and edge electron plasma parameters from IDA in current and heating power scans: (a,d) density, (b,e) temperature, and (c,f) pressure. The left-hand side panels (a)-(c) were evaluated at the magnetic axis ($\rho_{pol} = 0$) to represent the core and the right-hand side panels (d)-(f) at the edge ($\rho_{pol} = 0.95$), as a proxy for pedestal parameters. The various confinement regimes are indicated by different colors and the plasma current by different symbols.

is especially evident when the higher heating power sustainable in EDA H-mode by operating at higher current is taken advantage of.

The EDA H-modes at different plasma current are clearly separated in the edge electron temperature-density space, as illustrated in figure 5.9. Neither of these quantities nor the edge electron pressure represent a fundamental critical parameter for accessing and maintaining the regime, since its boundaries in this operational space vary with current.

An alternative non-dimensional parameter space which makes use of edge temperature and density, as well as plasma current, can be constructed by using the edge collisionality, ν_e^*, and the ratio of plasma pressure to poloidal magnetic pressure, β_p. Such a diagram, illustrated in figure 5.10, achieves a better ordering of the regimes at different currents. This means that ν_e^* and β_p are closer to the true underlying quantities for achieving EDA H-mode, but are still not ideal by themselves, since there is some overlap with the ELMy H-mode for the lower current discharges. In C-mod, EDA H-modes also tend to have high edge collisionality [106, 114]. It has been proposed that the QCM is a resistive X-point mode, a form of resistive ballooning mode that

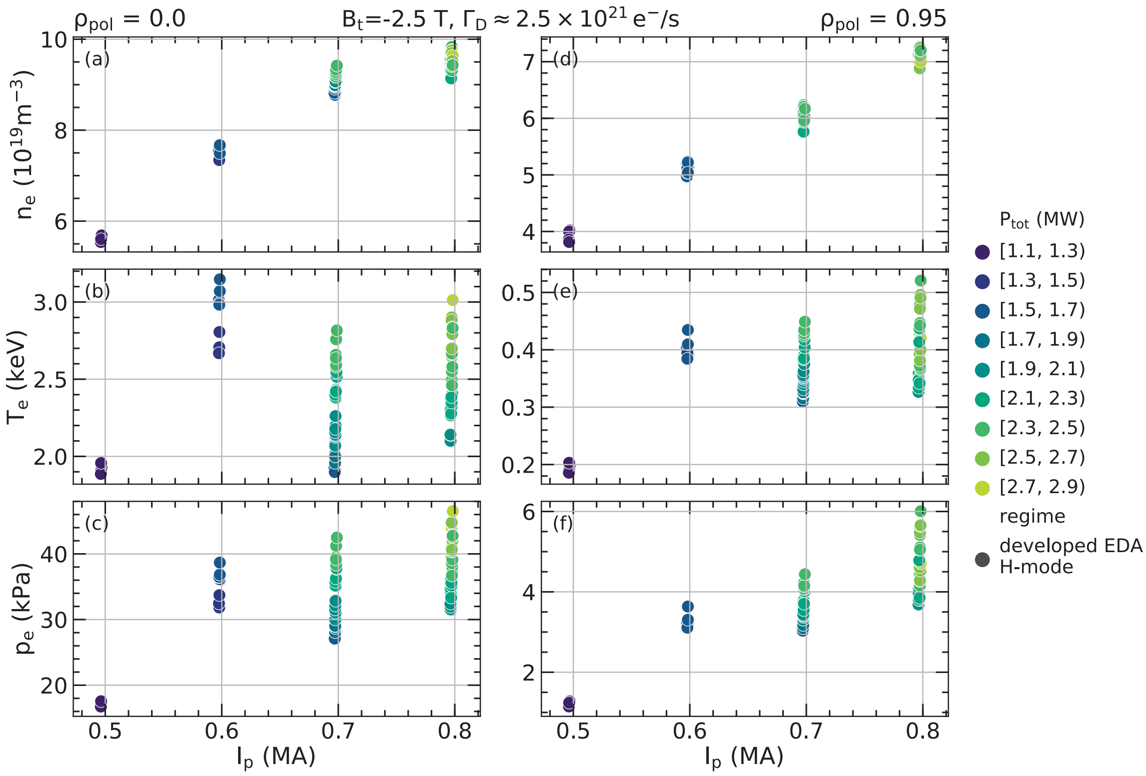

Figure 5.8: Core and edge electron plasma parameters from IDA as a function of current in developed EDA H-mode: (a,d) density, (b,e) temperature, and (c,f) pressure. The left-hand side panels (a)-(c) were evaluated at the magnetic axis ($\rho_{\text{pol}} = 0$) to represent the core and the right-hand side panels (d)-(f) at the edge ($\rho_{\text{pol}} = 0.95$), as a proxy for pedestal parameters. The total power lost by the plasma is indicated by different colors.

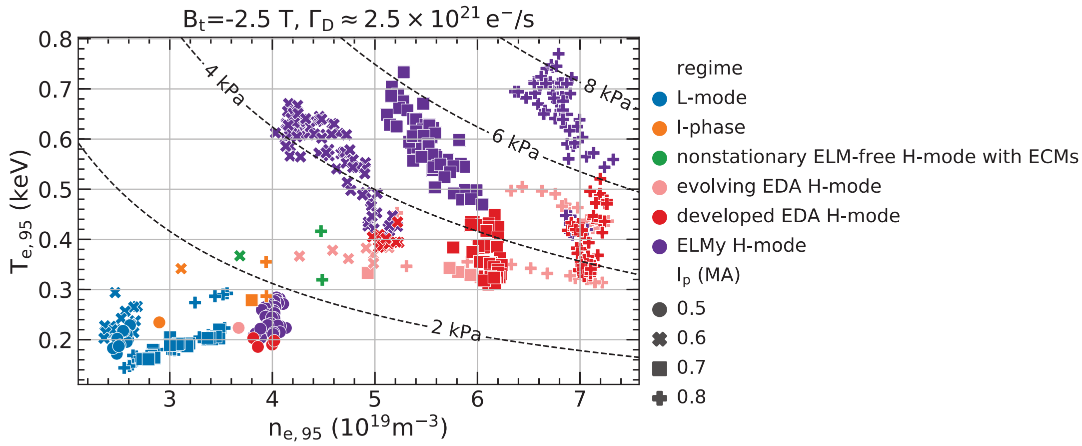

Figure 5.9: Edge operational space of different confinement regimes in terms of electron temperature and density obtained from IDA data evaluated at $\rho_{\text{pol}} = 0.95$ of discharges in a current and heating power scan. The regimes are coded by color and the plasma current levels by symbol. The dashed lines indicate constant pressure.

is strongly influenced by the magnetic geometry near the X-point [123], which would require high edge collisionality to exist. If this is true, it could be a serious limitation in extrapolating

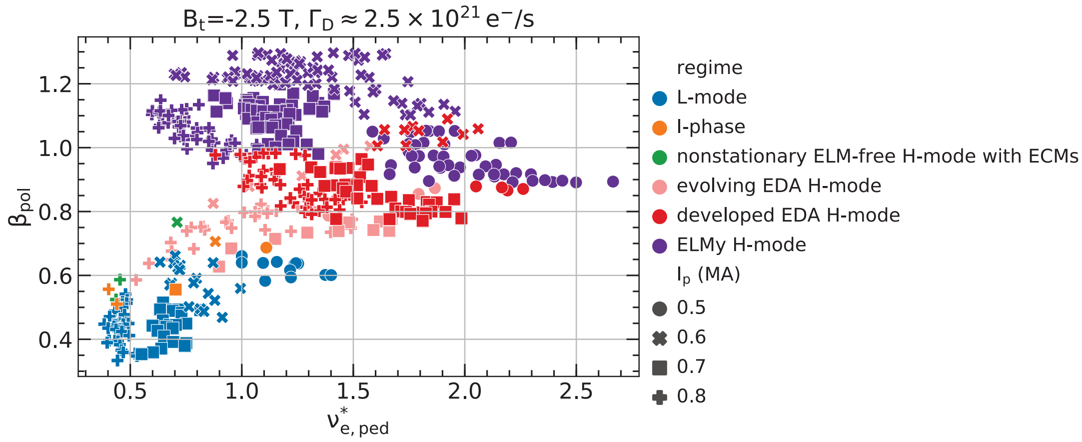

Figure 5.10: Non-dimensional operational space of different confinement regimes in terms of poloidal beta and collisionality from a current and heating power scan. The regimes are coded by color and the plasma current levels by symbol.

the EDA H-mode to a reactor scenario, which will have much higher core temperature and likely lower edge collisionality. That being said, if high collisionality is actually only required at the separatrix, but not at the pedestal top, the QCM could still exist in a reactor. Anyway, this discussion is somewhat speculative, since EDA H-mode experiments in different machines are scarce and the nature of the QCM as well as its definitive role in the regime are not conclusively proven. Nonlinear MHD simulations of EDA H-mode discharges in AUG using the JOREK code [303, 304], including collisionality effects and realistic X-point geometry, are planned to investigate the existing instabilities and contribute to this topic.

5.2.3 Global confinement

Regarding global confinement, not only heating power, but also plasma current has a significant impact in different confinement regimes, as shown in figure 5.11. The dependences on heating power, more evident in the left-hand side column in which the various quantities are expressed as a function of power, do not change significantly with plasma current and are for the most part identical to what was previously described in section 5.1.3. The current, however, strongly influences the absolute values of several quantities, so a subset of the data pertaining only to developed EDA H-modes is presented in the right-hand side column as a function of I_p, to allow a better visualization the associated dependences.

The line-averaged density (figure 5.11(a)(h)) increases approximately linearly with current, prompting the use of the Greenwald density [56] as a normalization parameter. The resulting

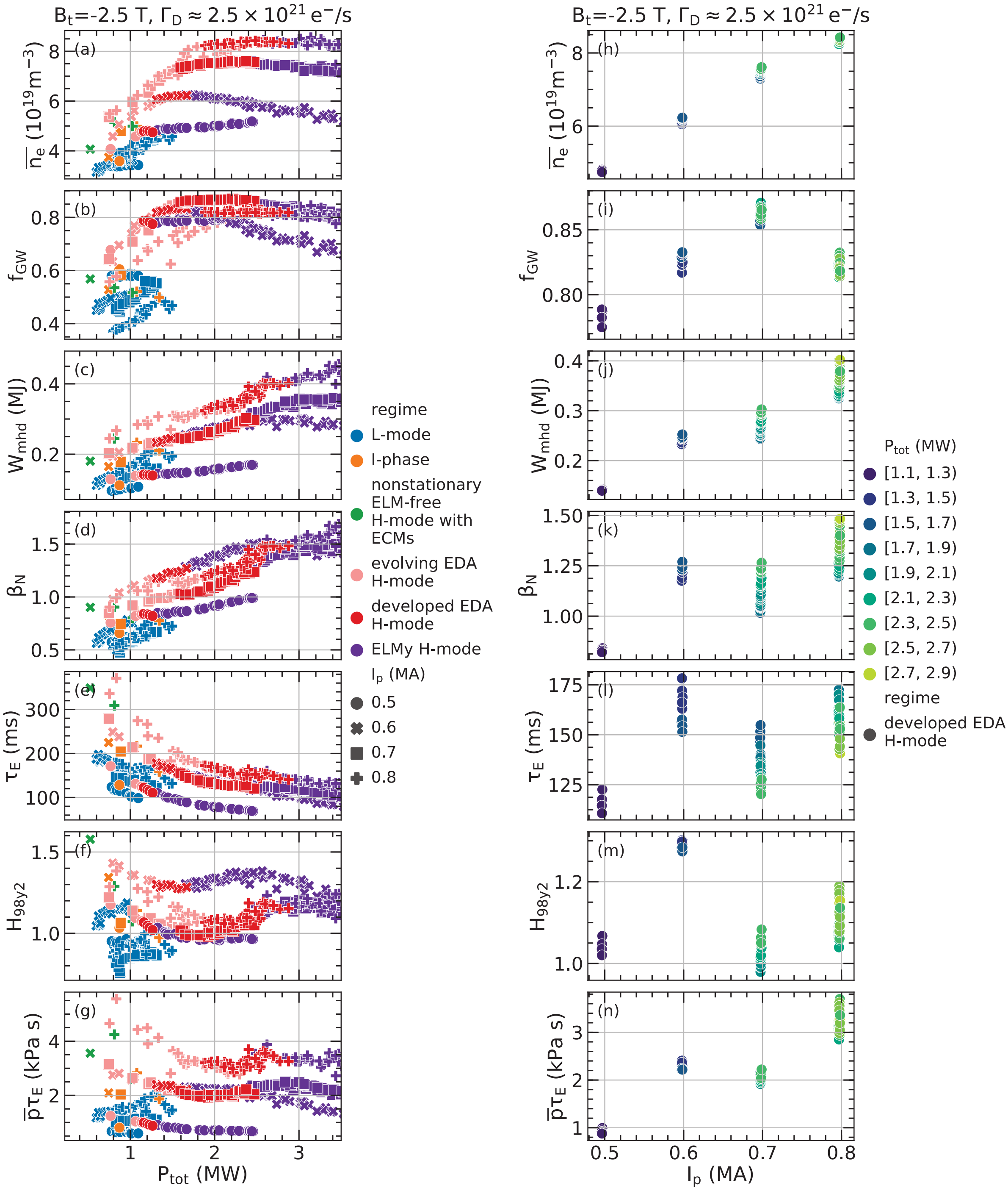

Figure 5.11: Global confinement quantities as a function of the total power lost by the plasma (a)-(g) and plasma current (h)-(n): (a)(h) line-averaged electron density, (b)(i) Greenwald fraction, (c)(j) stored energy, (d)(k) Troyon-normalized ratio of the plasma pressure to the magnetic pressure, (e)(l) energy confinement time, (f)(m) confinement enhancement factor, (g)(n) triple product. On the left-hand side column (a)-(g) the different regimes are coded by color and the plasma current levels by symbol. On the right-hand side column (h)-(n) only data from developed EDA H-mode is present and the power is coded by color.

Greenwald fraction (figure 5.11(b)(i)) shows only a very weak, residual trend with plasma current, and therefore seems an appropriate quantity to describe the natural density achieved by the EDA H-mode in AUG at constant gas puff.

The plasma stored energy (figure 5.11(c)(j)) also increases with current, being in qualitative agreement with C-mod observations [114]. Troyon normalization [52, 53] is not enough to characterize the dependence, since β_N continues to increase with plasma current, as figure 5.11(d)(k) shows. The expansion of the power window with I_p also contributes to the maximum achievable β_N.

In terms of energy confinement time (figure 5.11(e)(l)), the situation is not entirely clear due to the very high τ_E of the 0.6 MA discharge, but a general increase with plasma current seems to exist. This translates to a good confinement enhancement factor (figure 5.11(f)(m)), around and above 1, throughout the investigated current range, but with a non-monotonic dependence reaching a very high value of 1.3 in the 0.6 MA discharge. Since few discharges at different currents were performed, it is not yet clear whether this was a spurious outlier or if the dependence of EDA H-mode confinement on I_p really exhibits such complex behavior. Further experiments are planned to better cover this current range and also include variations in gas puff, since it affects confinement in EDA H-mode too.

Lastly, the triple product increases strongly with plasma current, as figure 5.11(g)(n) shows. Despite the uncertainty in confinement regarding the 0.6 MA discharge, it is clear that increasing I_p is beneficial for the absolute plasma performance in EDA H-mode, at least in the investigated range, which was limited only by the ECRH cutoff. This is a technical constraint due to the specific frequency employed by the AUG ECRH system, rather than a true limit of the plasma scenario. Such a limit will certainly exist at some plasma current value, but this point has not yet been reached in AUG EDA H-modes. Future experiments with ICRH are envisaged to try circumventing the ECRH limitation and investigate other physics aspects, such as the impact of ion heating. The door is also open for further improvement and optimization of this stationary ELM-free regime with plasma current in other fusion devices.

5.3 Overview and summary

Heating power, fueling and plasma current have been shown to significantly influence the qualitative and quantitative behavior of the EDA H-mode in AUG. In order to have a combined overview of the regime using data from all the scans and enable a more direct comparison with other tokamaks, input parameters and resulting plasma quantities are better expressed in

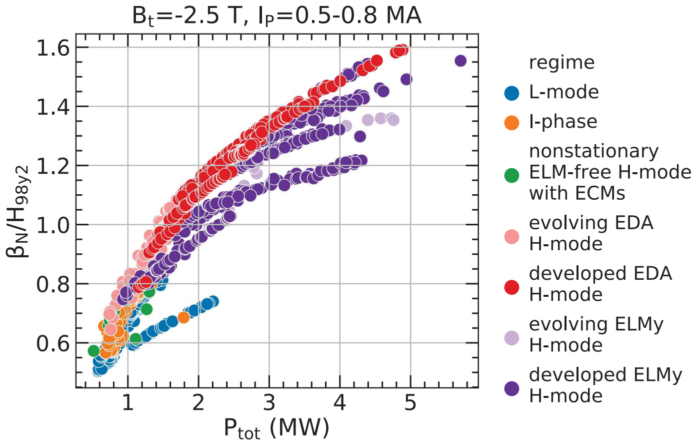

Figure 5.12: Normalized heating power as a function of the total power lost by the plasma in different confinement regimes. The data comes from heating power, fueling, and plasma current scans, as well as additional discharges with EDA H-modes, including weakly shaped plasmas.

non-dimensional form. Plasma current can be readily replaced by the inversely related edge safety factor, q_{95}, while fueling effects can be expressed via the edge collisionality, ν_e^*.

A not so standard, but very versatile quantity, β_N/H_{98y2}, is used here to represent the heating power. This comes from considering the definition of the energy confinement time, τ_E, which gives rise to the expression

$$P_{tot} = \frac{3}{2}\frac{\overline{p}V}{\tau_E}, \tag{5.1}$$

and directly replacing the average pressure, $\overline{p}$, and τ_E by their respective normalized, dimensionless quantities β_N and H_{98y2}, while ignoring all other factors. The resulting normalized heating power, β_N/H_{98y2}, is plotted as a function of the total power lost by the plasma, P_{tot}, in figure 5.12, using data from all the scans in this chapter, as well as additional performed EDA H-mode discharges, including some of the weakly shaped plasmas. The two quantities are well correlated, but β_N/H_{98y2} can better separate L-mode from H-mode, exemplifying its value across a wide range of parameters and confinement regimes.

Several dimensionless quantities related to performance and confinement are shown in figure 5.13 as a function of normalized heating power, edge collisionality and safety factor. β_N/H_{98y2} in EDA H-mode covers a range from 0.8 to 1.6, which is relatively wide, but falls short of the ITER inductive scenario value of 1.8 [86]. Future EDA H-mode experiments in AUG with high fueling and avoidance of the ECRH cutoff might be able to reach this value, especially if combined with other heating methods to increase the total available heating power.

In terms of edge collisionality, the developed EDA H-mode so far goes from 0.7 to 2.8,

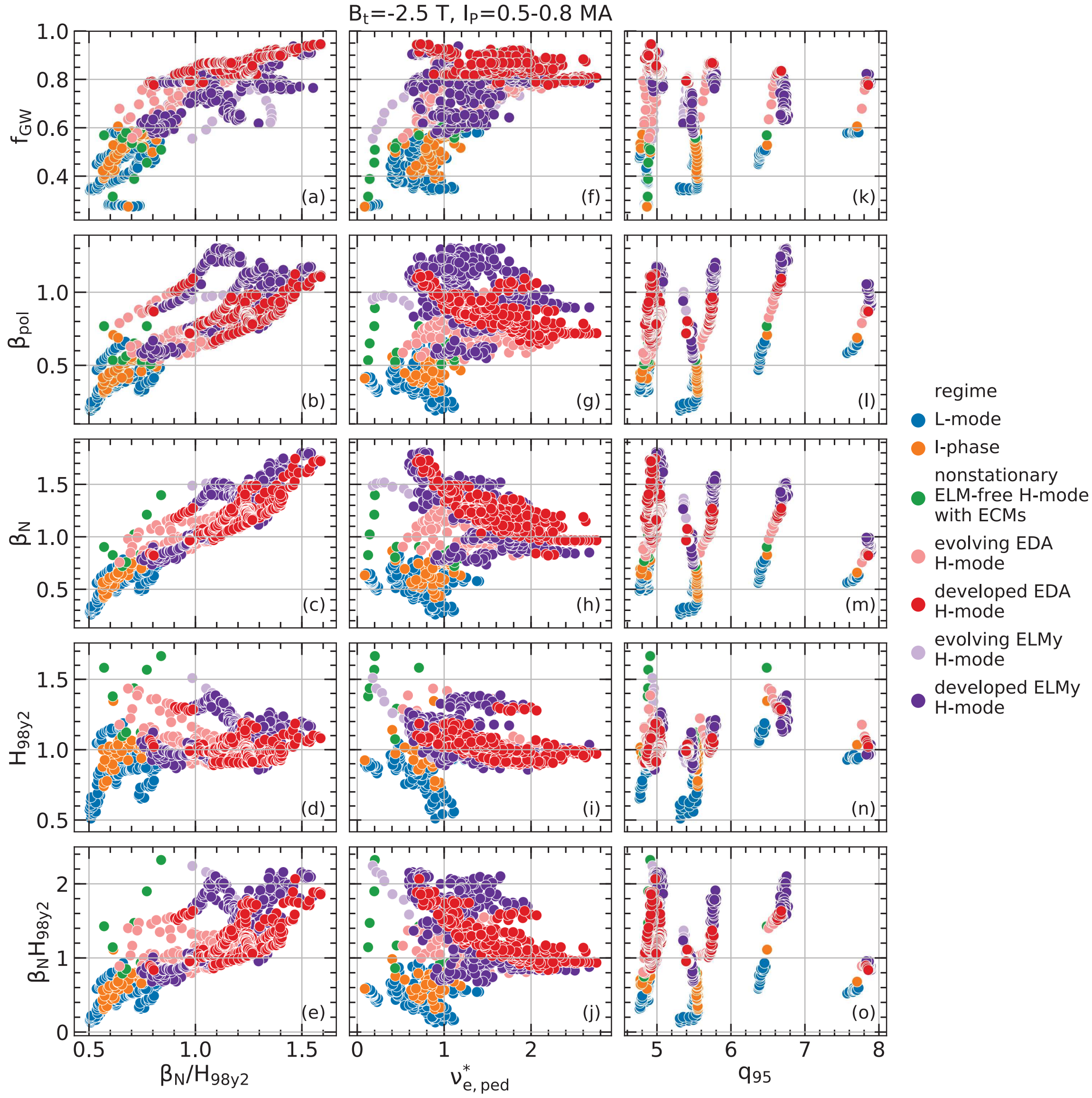

Figure 5.13: Dimensionless quantities related to performance and confinement as a function of normalized heating power (a)-(e), edge collisionality (f)-(j) and safety factor (k)-(o): (a,f,k) Greenwald fraction, (b,g,l) poloidal beta, (c,h,m) Troyon-normalized beta, (d,i,n) confinement enhancement factor, and (e,j,o) proxy for the triple product. The various confinement regimes are indicated by different colors.

which is significantly higher that ITER predictions, unachievable in present-day machines at high density. Marginal reductions of collisionality might still be made in AUG, but EDA H-mode experiments in larger devices are needed to explore lower ν_e^* ranges without significant perturbation of other dimensionless parameters. This is of course apart from ρ^*, which would be lower, but in any case would not achieve ITER values due to the sheer size and magnetic field requirements. Since JET is currently focused on the upcoming deuterium-tritium operation [305], with an overbooked program, and will then come to the end of its life, the next large candidate for such experiments would be JT-60SA [306, 307], whose construction has been recently completed and which will benefit from the additional advantage of having ECRH.

The edge safety factor, q_{95}, of the EDA H-modes obtained in AUG ranges from 4.8 to 7.8, which is higher than the ITER value of 3 in the inductive scenario, but contains $q_{95} = 5.2$ of the steady state scenario [86] and $q_{95} = 5.5$ of CFETR scenarios [308]. In the high safety factor cases, however, requirements on other quantities like β_N and $H_{98\mathrm{y}2}$ are more stringent. In C-mod, EDA H-modes are more likely at $q_{95} > 3.5$ [102, 104, 106] although a record low of 2 has been achieved [104]. In AUG, such low safety factors in EDA H-mode could not be properly investigated at $B_\mathrm{t} = 2.5\,\mathrm{T}$, because this requires high I_p, which leads to very high density and ECRH cutoff with X2 heating. With the current ECRH system, a possible strategy to lower the safety factor is to lower the magnetic field to about 1.8 T, which allows the use of X3 heating. This introduces additional challenges due to the lower absorption, but experiments following this approach are planned for the upcoming campaign. This is a crucial aspect to investigate in EDA H-mode, since a scenario that can withstand low safety factor allows higher plasma current to be used, which leads to strong gains in fusion performance.

The Greenwald fraction, shown in figure 5.13(a,f,k), exhibits in developed EDA H-mode a positive correlation with $\beta_\mathrm{N}/H_{98\mathrm{y}2}$ and a negative, but weak, correlation with q_{95}. f_GW is overall quite high, ranging from 0.77 to 0.95, being in most cases above the other confinement regimes. This satisfies ITER requirements of $f_\mathrm{GW} = 0.85 - 0.94$, depending on the exact scenario [87], being one of the main strong points of the EDA H-mode in AUG. In fact, this is a difference from C-mod EDA H-modes, which had $f_\mathrm{GW} < 0.7$ [124, 301, 309]. Such values only occur in AUG during the initial phases of the regime, where the plasma is still evolving with a strong density increase. High Greenwald fraction with good confinement is an important achievement of the EDA H-mode in AUG, because a low density reactor is not so efficient for energy production and confinement in typical H-modes across several devices tends to worsen with high f_GW [274].

Figure 5.13(b,g,l) shows that β_p in developed EDA H-mode increases with normalized heating power and decreases with edge collisionality, ranging from 0.6 to 1.1, which covers $\beta_\mathrm{p} = 0.65$ predicted for ITER inductive operation [87]. The EDA H-mode region in the $\beta_\mathrm{p} - \nu_\mathrm{e}^*$ space partially overlaps with type I and type II ELMs regimes in AUG and JET, and also with type III ELMs in JT-60U [64]. These quantities are therefore not sufficient to accurately predict ELM conditions in different devices.

β_N in EDA H-mode spans a range of 0.8-1.7 and follows in general similar trends as β_p, but also increases with decreasing q_{95}, as shown in figure 5.13(c,h,m). It almost reaches the ITER inductive and hybrid targets of $\beta_\mathrm{N} = 1.8 - 1.9$ [86]. In C-mod, the EDA H-mode tended to have $\beta_\mathrm{N} < 1.3$ [106, 115], with the highest ever achieved volume averaged absolute pressure plasma having $\beta_\mathrm{N} = 1.43$ [124]. Higher β_N has been attained in AUG, but the explored plasma current and magnetic field was limited. If this high normalized pressure can be maintained or even surpassed at higher I_p and B_t, the EDA H-mode will constitute a highly desirable ELM-free regime in large-scale devices. In C-mod, experiments with very high $B_\mathrm{t} = 7.8\,\mathrm{T}$ showed that the parameter space in which the EDA H-mode occurs is consistent with lower magnetic field experience [310]. This is an encouraging result for extrapolating the AUG scenario to future reactors with higher magnetic field.

Developed EDA H-modes exhibit good energy confinement, with $H_{98\mathrm{y}2} = 0.9 - 1.3$, as figure 5.13(d,i,n) shows. This satisfies ITER assumptions of $H_{98\mathrm{y}2} \approx 1$ in inductive and hybrid scenarios, and even $H_{98\mathrm{y}2} = 1.3$ of the more demanding steady-state scenario [86]. In C-mod, EDA H-modes had $H_{98\mathrm{y}2} \approx 1$ [104]. The high energy confinement of this ELM-free regime across a wide range of inputs is a great asset, especially when one considers that typical ELMy H-modes of the metal-walled AUG and JET tokamaks tend to exhibit good confinement only at much higher heating power and β_N [311].

Finally, a nondimensional proxy for the triple product, $\beta_\mathrm{N} H_{98\mathrm{y}2}$, is presented in figure 5.13(e,j,o). In developed EDA H-mode, it shows similar trends to β_N and its total range $\beta_\mathrm{N} H_{98\mathrm{y}2} = 0.8 - 2.1$ satisfies the demands of ITER inductive and hybrid scenarios, but not the very high requirement of the steady-state scenario [86]. It is still a remarkable feat for an ELM-free regime in a tokamak with high Z metallic walls.

When looking to figure 5.13 as a whole, it is evident that L-mode and I-phase are well separated from EDA H-mode in most parameter combinations. The same cannot be said for the ELMy H-mode, which shows some overlap with EDA H-mode, especially aggravated with the inclusion of weakly shaped discharges. This illustrates the complexity of the multidimensional parameter space occupied by these regimes, which makes experiments, physical understanding and accurate predictions of the EDA H-mode for future reactors quite challenging. In any case, the maximum potential of the EDA H-mode has not yet been reached, but the results are promising. Further experimental, modelling and theoretical investigations of this stationary ELM-free regime, both in AUG and other devices, should be undertaken to make the most of it.

Comparing with the parameter space of C-Mod, AUG EDA H-modes have expanded the maximum achieved f_{GW} from 0.7 [124, 301] to 0.95 and β_{N} from 1.4 [124] to 1.7, constituting a great improvement in these parameters, which are now starting to approach reactor requirements. Strong plasma shaping, up to $\delta_{\mathrm{avg}} = 0.4$, was one of the key ingredients for increasing the maximum pressure of EDA H-modes in AUG without ELMs, but this average triangularity is in fact lower than the highest C-Mod values, $\delta_{\mathrm{avg}} \approx 0.7$ [116]. The extension happened in the other direction, with AUG also having EDA H-modes at $\delta_{\mathrm{avg}} = 0.25$, whereas C-Mod required $\delta_{\mathrm{avg}} > 0.3$ [102, 104, 116]. In terms of safety factor, the lowest value achieved in AUG EDA H-modes so far was $q_{95} > 4.5$, which is not as low as the usual C-Mod boundary, $q_{95} > 3.5$ [102, 104, 106]. That said, the AUG boundary comes from technical limitations of the chosen heating method and shaping coils, rather than a limit of the plasma itself. The pedestal collisionality, ν_{e}^{*}, is high in EDA H-modes of both devices, with the lowest values being only slightly below 1 [106, 114].

To summarize, heating power, fueling and plasma current scans have been performed in EDA H-modes of AUG at fixed magnetic field. The regime exists in a power window which can be extended by increasing fueling and current, and above which ELMs occur. Core electron density and core and edge temperature and pressure increase with heating power, with a global confinement degradation less severe than the IPB98(y,2) scaling. High gas puff leads to a slight decrease of energy confinement and increase of density. Plasma current has a strong impact in increasing core and edge density, but the effect on temperature is not entirely clear, though few discharges were performed and spurious outliers might exist. Still, the achievable pressure and triple product increase significantly with current while maintaining good confinement. In terms of dimensionless parameters, the EDA H-mode in AUG has only been explored at high q_{95}, due to technical limitations in the chosen heating method, and high ν_{e}^{*}, which could represent an obstacle in extrapolating it to large-scale devices. However, the fundamental physics constraints are complex and not yet understood, so no final judgement can yet be made. On a positive note, the EDA H-mode in AUG achieves high f_{GW}, β_{N}, $H_{98\mathrm{y}2}$ and $\beta_{\mathrm{N}}H_{98\mathrm{y}2}$, satisfying several requirements of planned ITER scenarios. This constitutes a remarkable feat considering it is a stationary ELM-free H-mode obtained with dominant electron heating and no torque in a tokamak with tungsten walls. This makes the EDA H-mode a very promising regime for future reactors, which justifies further experiments and studies, not only in AUG, but in all tokamaks, in order to enhance its performance and improve the empirical and physical understanding of its phenomena and constraints.

Chapter 6

Summary and outlook

6.1 Summary

This thesis took advantage of the extensive heating, shaping and diagnostic capabilities of the AUG tokamak to show the discovery, development, optimization and study of a stationary ELM-free H-mode with several desirable properties for future reactors. These include good energy confinement, high density, low impurity content, compatibility with tungsten walls and extrinsic impurity seeding, possibility of access at low input torque and power, with dominant electron heating, no need for a fresh boronization, and no impurity accumulation despite the absence of ELMs, constituting a unique set of characteristics simultaneously achieved for the first time in a fusion device. This regime is identified as the EDA H-mode, previously obtained in Alcator C-Mod.

The main conditions to access the EDA H-mode in AUG are a significant ECRH fraction, adequate heating power, above the L-H threshold in favorable ∇B configuration, but below the ELM threshold, and an appropriate fueling level, above a limit below which nonstationary plasmas are obtained.

The EDA H-mode exhibits an edge transport barrier in density, temperature, and therefore pressure, as expected in an H-mode. The core density profile is mostly flat, whereas the electron temperature is peaked, due to the central heating, resulting in high pressure. The temperature of the ions in the inner core is lower than that of the electrons because of the heating method, but they almost equilibrate from mid-radius outwards.

The ability to maintain a stationary pedestal without the relaxation caused by ELMs is one of the main distinguishing features of the regime when compared to a standard H-mode. This requires an alternative transport mechanism which seems to be related to the QCM, an ubiquitous electromagnetic instability in EDA H-modes.

Once the transition to EDA H-mode occurs, the QCM is usually detected by several diagnostics as a down-chirping oscillation in the edge electron density, moving in the electron diamagnetic direction in the lab frame, and whose frequency settles as the plasma approaches steady-state. It can also be observed in a few magnetic pick-up coils, though faintly, possibly because of a strong radial decay of the magnetic signal due to its high mode number. The QCM is coherent on short timescales, but over long timescales it has a relatively broad frequency width that gives rise to its name.

The appearance and disappearance of the QCM are correlated with corresponding changes in edge and divertor plasma parameters. This suggests an enhanced particle and energy transport driven by the QCM in the pedestal region, expelling plasma to the SOL, which could be the key to stationary ELM-free operation in EDA H-mode. That said, there are also multiple high frequency modes detected by pick-up coils which might play an important role in the regime.

Several measures have been taken to improve the performance and reactor relevance of the EDA H-mode. With strong shaping, it can be accessed within a wider ELM-free power window. This increased robustness makes the regime more easily reproducible, without requiring a fine control of the input power, and allows the achievement of much higher pedestal and core temperature and pressure. Furthermore, a direct access to EDA H-mode without passing through an ELMy period is enabled by the strong shaping even in slow power ramps, although pulsating phases can occur.

The higher heating power made possible with strong shaping calls for a better power exhaust at the divertor. This was achieved by seeding nitrogen in EDA H-mode, causing increased divertor radiation and leading to much lower target temperature and heat fluxes, without degrading core confinement nor significantly diluting the fuel. However, as detachment is approached, core electron density increases and the ECRH cutoff is reached, preventing further plasma heating. This is not a limit of the plasma state itself, but rather a specific restriction of the heating system which is not expected to be a problem in future reactors.

Argon was also applied to EDA H-mode plasmas, resulting in a significant increase of radiation at the pedestal, well matched by impurity transport modelling, with minimal impact in the core. This additional loss channel leads not only to a decrease in divertor temperature, but also to an extension of the ELM-free power window, allowing higher core pressure to be attained, while maintaining low fuel dilution. The high density and compatibility of the EDA H-mode with extrinsic impurity seeding constitute one of the best power exhaust solutions among high confinement ELM-free regimes nowadays.

While most EDA H-modes in AUG have been obtained exclusively with ECRH, the regime has also been successfully demonstrated with an even mix of ECRH and NBI, both with and without argon seeding. Pure wave heating is therefore not required to access EDA H-mode, proving its robustness and versatility, which can be useful for exploiting the full heating and diagnostic capabilities of current and future fusion devices.

A high ECRH fraction and strong shaping are favorable, but not sufficient conditions to access EDA H-mode in AUG. Fueling scans show that a minimum fueling level is also required to maintain a steady-state ELM-free regime. In fact, when enough ECRH power is applied but the gas puff is too low, the plasma transitions to a nonstationary H-mode with ECMs, in which the density and radiated power rise uncontrollably until the occurrence of ELMs. By contrast, changing only the gas puff rate to a moderate value results in a well-behaved stationary ELM-free H-mode with the QCM. Further increasing the fueling level leads to a small density increase and slight reduction in energy confinement, but extends the ELM-free power window, so might be worth the tradeoff. These studies were constrained by the ECRH cutoff, so the limits of the regime at high fueling rates could not be fully investigated.

A scan in plasma current was also performed, showing that it extends the power window of the EDA H-mode. In addition, increasing plasma current clearly raises core and edge density, but the effect on temperature is not entirely clear, due to the small number of discharges and possibility of spurious outliers. Still, the achievable pressure and triple product increase with current over the scanned range while maintaining good confinement. High current investigations were limited by the ECRH cutoff due to the high density.

The effect of heating power on EDA H-mode plasmas was similar in most discharges of the fueling and current scans, basically leading to an increase in core and edge electron temperature and pressure, and a slight increase in core density, with an energy confinement degradation less severe than the IPB98(y,2) scaling.

In terms of dimensionless parameters, the EDA H-mode in AUG has so far only been explored at high safety factor, due to the ECRH cutoff, so it is not yet known how the results hold in low q scenarios predicted for reactors. Besides this, it has only been obtained at high collisionality, which may represent a major obstacle in its extrapolation to a burning plasma. However, the multidimensional parameter space of the EDA H-mode is complex and its physics is not well understood, so these issues might not be showstoppers in the end, especially if the critical parameters to access the regime are located close to the separatrix, where conditions in a reactor will be more similar to those of present-day devices. In other dimensionless parameters, the EDA H-mode in AUG performs quite well, achieving high H_{98y2}, β_N, f_{GW}, $\beta_N H_{98y2}$, and low Z_{eff}. Considering it is a stationary ELM-free regime with great power exhaust capabilities, obtained with dominant electron heating and no torque in a full-W tokamak, one can conclude that the EDA H-mode is indeed a promising regime for future reactors, well worth further developing and studying in current and upcoming devices.

6.2 Outlook

Great progress has been made in the development of the EDA H-mode in AUG, but each study raised countless questions and opened multiple new doors for additional investigations. After all, a good portion of socratic wisdom is unavoidable when hard challenges are tackled.

Starting with the plasma edge, that appears to be one of the most critical regions for the EDA H-mode, a general question can be posed: how is the pedestal structure determined? Several instabilities exist, but their interactions and role in regulating plasma transport is not well understood. The QCM is always present in the regime, but the transport it drives is hard to quantify and observations have been somewhat indirect. Experimentally, inserting a Langmuir probe array would allow an estimation of the particle and energy fluxes at the QCM frequency. However, this is very challenging due to the extreme heat loads that the probe materials cannot sustain. Still, a plunge close enough to the separatrix may provide useful information and specially designed low power discharges are planned to this end. Another possibility is to exploit the heavy ion beam probe that will soon start operating in AUG, possibly allowing an extension of transport and instability studies to inner, hotter regions of the plasma. Besides this, data from the thermal helium beam diagnostic is currently being analyzed to search for connections between filaments and the QCM, in hope of finding further transport evidence.

From the theoretical point of view, understanding the QCM and its influence on the plasma would first require an identification of its nature. This, in turn, still needs a better experimental characterization. More specifically, it is important to determine the propagation direction and velocity of the QCM in the plasma frame, which is difficult since it requires precise, aligned and simultaneous measurements of the radial electric profile and radial localization of the QCM, as well as its wavelength and frequency, preferably over a range of EDA H-modes with different plasma parameters. In principle this can be done without resorting to probes by using a set of more passive diagnostic methods in AUG, as long as great care is taken to optimize the discharges for high quality measurements, and is part of the plan for the future. If successful, this could also unequivocally determine if the typical downchirping of the QCM is just a consequence of changes in plasma rotation or if the mode characteristics also evolve. Regarding radial localization, the puzzle of the QCM also appearing in core ECE channels should be better investigated, for example with 2D radiation transport modelling, and also with the ECE imaging diagnostic, which will be used to study instabilities in ELM-free regimes in the upcoming AUG campaign. Another important aspect to characterize is the poloidal profile of the QCM amplitude, namely HFS/LFS asymmetries, which would allow an evaluation of its ballooning character. This may be possible with the AUG reflectometers, but requires further scenario development to mitigate the HFSHD in EDA H-mode.

If a thorough experimental characterization of the QCM is performed, there is hope to find it unambiguously also in modelling efforts. More specifically, nonlinear MHD and gyrokinetic simulations of EDA H-modes, with the JOREK and GENE codes, are currently planned and being performed to better understand the regime. This may finally reveal the true nature of the QCM, its saturation mechanisms, and how it affects plasma transport and the pedestal structure. Understanding its underlying instability will also help mapping out the parameter space of the QCM and EDA H-mode. In addition, these simulations may be able to explain how the QCM interacts with other instabilities and why it has a relatively broad frequency peak over long timescales.

In fact, the importance of other instabilities in the EDA H-mode is not known, so practically all the experimental, analysis and modelling strategies mentioned above should be applied to study also the numerous MHD modes frequently observed in the regime. Even more information could be available, since these modes are detected by many pick-up coils around the plasma.

In the end, knowledge about the QCM and other instabilities may be leveraged to develop better EDA H-modes, not only by varying standard discharge parameters, but also by implementing new strategies that might not be evident beforehand. As an example, application of ICRH beat waves and resonant magnetic perturbations (RMPs) in EDA H-modes are currently planned for the upcoming AUG campaign, based on the hypothesis that they might influence the QCM and enhance its effects.

Proper edge conditions seem fundamental for the EDA H-mode, but the plasma core is what ultimately matters for fusion performance, though both regions are correlated. In AUG, relatively high electron to ion temperature ratios are obtained in EDA H-modes, which is not ideal in a reactor, since nuclear fusion occurs between ions. However, the temperature difference is due to the dominant applied electron heating, which will also exist in future reactors from the alpha particles. That said, the much larger machine size will hopefully lead to a better temperature equilibration. On the other hand, the higher absolute temperature of a burning plasma will also result in less electron-ion energy transfer, so the net result should be better investigated with transport modelling. This is important not only to predict the performance of EDA H-modes in large-scale devices, but also to evaluate how different the plasma profiles are expected to be and whether this could have an impact in accessing the regime.

In order to better investigate these issues in current devices, more experiments with different heating methods should be performed. Further exploration of the EDA H-mode in AUG with different ratios of ECRH and NBI is currently planned. Besides this, a preliminary pure ICRH discharge has been performed, but results suggest the regime might be more challenging to obtain than with pure ECRH, possibly due to the higher tungsten content in the plasma. Nonetheless, the EDA H-mode should in principle be obtainable with pure ICRH in AUG, since that is how it was actually discovered in C-Mod. Scenarios with pure ICRH, as well as mixes with the other heating methods should also be developed in AUG. This may allow a separation of torque and T_e/T_i effects, as well as access to other magnetic field values, contributing to a better understanding of the required conditions to obtain EDA H-mode. In addition, ohmic EDA H-modes should be performed to extend the operational space of the regime, especially in terms of B_t. At the other side of the spectrum, current drive methods should be tried in EDA H-mode in order to evaluate the potential of the regime for non-inductive operation, which would be very beneficial for the lifetime and economic viability of a fusion reactor. Another aspect related to external heating that should be better studied is the influence of its application rate, i.e., which differences exist when slowly increasing the heating power, as compared to fully applying it at once. In addition, decreasing power ramps would also be interesting to study hysteresis in the transition to EDA H-mode and develop safe ramp-down procedures. These experiments are relevant not only for physics investigations, but also to prepare the operation of large-scale devices, where machine safety measures are stricter.

Plasma shaping has also been shown to strongly affect the EDA H-mode. However, in AUG only two different shapes have been used in the experiments, which limits both the extrapolation and physical understanding of the phenomena in play. Besides this, the weak and strong shapes used vary in several parameters, including triangularity and closeness to double null. This means that, even from a purely empirical perspective, the critical shaping aspects affecting the regime are not unequivocally known. The AUG coil system makes it very difficult to disentangle the parameters, so it would be useful to study the intricacies of shaping in EDA H-mode also with other devices. More specifically, experiments in TCV are planned to conduct such a study, but the EDA H-mode must first be obtained in this machine. In any case, it is very important to better study this topic and determine whether plasma shaping can be further exploited to improve the performance of the EDA H-mode, since this may have a strong impact on its reactor relevance. Linear and nonlinear MHD modelling might prove especially helpful in interpreting and predicting results of such experiments.

Besides affecting the P-B stability boundary, plasma shaping in EDA H-mode also influences the properties of other instabilities, like the QCM and the high frequency modes detected by the pickup coils, as well as the pedestal structure. In addition, strong shaping allows an almost direct transition from L-mode to EDA H-mode without any ELMs, even when the power is gradually increased, and revealed the existence of pulsating EDA H-mode phases under certain power ranges, but none of these phenomena is understood. It is important to study the pulsations, namely their parameter space, nature and cause, in order to determine whether they might represent a risk to PFCs in large-scale reactors.

That said, power exhaust is actually one of the main strong points of the EDA H-mode, since it is compatible with extrinsic impurity seeding. Nitrogen and argon proved to be very effective radiators in the divertor and pedestal, respectively, but the experiments in AUG were limited by the ECRH cutoff. For this reason, new experiments at a lower plasma current, and therefore density, are planned to further develop seeded EDA H-mode regimes and properly investigate their limits from the plasma physics point of view. This includes also mixes of seeding species, in order to try achieving an integrated scenario with simultaneous ELM-free, high power operation and a detached divertor.

Also deuterium fueling scans in EDA H-mode were hampered by the ECRH cutoff at high gas puff rates, so they are planned at lower current in the upcoming campaign. Besides this, even within the ranges already scanned, there are effects in confinement and in the QCM not yet understood, so they must be further studied. These might be related to filaments and phenomena observed also in the small ELM regime, so the connection between the two regimes should be investigated, namely by bringing their operational spaces closer. EDA H-mode experiments in AUG were performed almost exclusively in deuterium, but a preliminary discharge with a deuterium-hydrogen mix suggests that it might be more difficult to obtain a stationary scenario with hydrogen, since the L-H power threshold increases, but the ELM boundary remains mostly unaffected. EDA H-mode experiments in hydrogen and helium are also planned for the upcoming campaign to study dependences of the regime on the main ion mass.

Plasma current scans in AUG EDA H-modes were scarce and produced some clear and some ambiguous results. They were also limited by the ECRH cutoff, preventing the achievement of low safety factor which is crucial for fusion performance. Magnetic field scans could not be performed at all with the standard X2 ECRH scheme. For these reasons, the development of EDA H-mode scenarios with alternative ECRH schemes in AUG, such as X3 and O2 heating, is one of the priorities in the upcoming campaign, as it may allow lower B_t, higher I_p, and therefore lower q to be achieved.

Despite considerable progress made in developing the EDA H-mode in AUG since its first observation, its parameter space remains largely unexplored. This is partly because of the ECRH limitations, but also due to the fact that the regime is recent in AUG and simply did not yet have enough time and discharges to be thoroughly explored, so its full potential is most likely yet to be reached. For this reason, general parameter scans, such as plasma current, magnetic field, shaping, heating power and fueling are still very worth doing. These are useful not only by themselves, but also have a synergistic effect by serving as the basis for developing the required scenarios to be used in all the other possible investigations mentioned so far.

However, even if all these experiments are conducted in AUG, some parameters or combinations of parameters will never be achieved simply due to the size of the machine. Because of this, performing EDA H-mode experiments in larger devices is of paramount importance. JT60-SA is presently the ideal candidate for such studies, and should encourage future experiments in ITER if the results are positive. In the meantime, if SPARC is constructed it should also try achieving the EDA H-mode, since the device will likely fulfill the requirements and could represent a major breakthrough in fusion research. To conclude, the EDA H-mode is too promising not to be further developed and studied in present and upcoming devices, giving rise to many exciting opportunities for future research. This will allow a more reliable assessment of its compatibility with large-scale reactors, which will hopefully come in time for the design of a demonstration fusion power plant.

Bibliography

[1] United Nations Department of Economic and Social Affairs Population Division. World Population Prospects 2019: Highlights. Technical report, United Nations, 2019. URL https://population.un.org/wpp2019/Publications/Files/WPP2019{_}Highlights.pdf.

[2] BP. Statistical Review of World Energy, 2020 — 69th Edition. Technical report, BP, 2020. URL https://www.bp.com/content/dam/bp/business-sites/en/global/corporate/pdfs/energy-economics/statistical-review/bp-stats-review-2020-full-report.pdf.

[3] IPCC. Climate Change 2014: Synthesis Report. Technical report, IPCC, Geneva, Switzerland, 2014.

[4] S. C. Sherwood, M. J. Webb, J. D. Annan, et al. An Assessment of Earth's Climate Sensitivity Using Multiple Lines of Evidence. *Reviews of Geophysics*, 58(4):1–92, 2020. URL https://onlinelibrary.wiley.com/doi/10.1029/2019RG000678.

[5] Nathan J. L. Lenssen, Gavin A. Schmidt, James E. Hansen, et al. Improvements in the GISTEMP Uncertainty Model. *Journal of Geophysical Research: Atmospheres*, 124(12): 6307–6326, 2019. URL https://onlinelibrary.wiley.com/doi/abs/10.1029/2018JD029522.

[6] NASA Goddard Institute for Space Studies. Global Temperature Anomaly, 2020. URL https://commons.wikimedia.org/wiki/File:Global{_}Temperature{_}Anomaly.svg.

[7] J. Jouzel. A brief history of ice core science over the last 50 yr. *Climate of the Past*, 9(6): 2525–2547, 2013. URL https://cp.copernicus.org/articles/9/2525/2013/.

[8] National Oceanic and Atmospheric Administration. Trends in Atmospheric Carbon Dioxide, 2020. URL http://www.esrl.noaa.gov/gmd/ccgg/trends/.

[9] Jeffrey P. Freidberg. *Plasma Physics and Fusion Energy*. Cambridge University Press, 2007.

[10] John Wesson. *Tokamaks*. Oxford University Press, third edition, 2004.

[11] S. Li, H. Jiang, Z. Ren, and C. Xu. Optimal Tracking for a Divergent-Type Parabolic PDE System in Current Profile Control. *Abstract and Applied Analysis*, 2014:1–8, 2014. URL http://www.hindawi.com/journals/aaa/2014/940965/.

[12] C. S. Pitcher and P. C. Stangeby. Experimental divertor physics. *Plasma Physics and Controlled Fusion*, 39(6):779–930, 1997. URL https://iopscience.iop.org/article/10.1088/0741-3335/39/6/001.

[13] EUROfusion. Divertor schematic. URL https://www.euro-fusion.org/fileadmin/user{_}upload/Archive/wp-content/uploads/2011/07/fig05.jpg.

[14] F. L. Hinton and R D Hazeltine. Theory of plasma transport in toroidal confinement systems. *Reviews of Modern Physics*, 48(2):239–308, 1976. URL https://link.aps.org/doi/10.1103/RevModPhys.48.239.

[15] Per Helander and Dieter J. Sigmar. *Collisional Transport in Magnetized Plasmas*. Cambridge University Press, 2005.

[16] A. J. Wootton, B. A. Carreras, H. Matsumoto, et al. Fluctuations and anomalous transport in tokamaks. *Physics of Fluids B: Plasma Physics*, 2(12):2879–2903, 1990. URL http://scitation.aip.org/content/aip/journal/pofb/2/12/10.1063/1.859358.

[17] Robert J Goldston. Energy confinement scaling in Tokamaks: some implications of recent experiments with Ohmic and strong auxiliary heating. *Plasma Physics and Controlled Fusion*, 26(1A):87–103, 1984. URL http://stacks.iop.org/0741-3335/26/i=1A/a=308?key=crossref.306d85348801dc49512e8870950be622.

[18] F. Wagner, G. Becker, K. Behringer, et al. Regime of Improved Confinement and High Beta in Neutral-Beam-Heated Divertor Discharges of the ASDEX Tokamak. *Physical Review Letters*, 49(19):1408–1412, 1982. URL http://link.aps.org/doi/10.1103/PhysRevLett.49.1408.

[19] F. Wagner. The history of research into improved confinement regimes. *The European Physical Journal H*, 43(4-5):523–549, 2018. URL http://link.springer.com/10.1140/epjh/e2016-70064-9.

[20] F Wagner. A quarter-century of H-mode studies. *Plasma Physics and Controlled Fusion*, 49(12B):B1–B33, 2007. URL http://stacks.iop.org/0741-3335/49/i=12B/a=S01?key=crossref.4b1659cd2933e3e40b713717cd852006.

[21] M. Keilhacker, A. Gibson, C. Gormezano, et al. High fusion performance from deuterium-tritium plasmas in JET. *Nuclear Fusion*, 39(2):209–234, 1999. URL https://iopscience.iop.org/article/10.1088/0029-5515/39/2/306.

[22] J W Connor and H R Wilson. A review of theories of the L-H transition. *Plasma Physics and Controlled Fusion*, 42(1):R1–R74, 2000. URL http://stacks.iop.org/0741-3335/42/i=1/a=201?key=crossref.ddfa91e32a275bdc2af0805f72040f61.

[23] F. Wagner, G. Fussmann, T. Grave, et al. Development of an Edge Transport Barrier at the H-Mode Transition of ASDEX. *Physical Review Letters*, 53(15):1453–1456, 1984. URL http://link.aps.org/doi/10.1103/PhysRevLett.53.1453.

[24] R. J. Groebner, K. H. Burrell, and R. P. Seraydarian. Role of edge electric field and poloidal rotation in the L - H transition. *Physical Review Letters*, 64(25):3015–3018, 1990. URL http://link.aps.org/doi/10.1103/PhysRevLett.64.3015.

[25] A.R Field, G. Fussmann, and J.V Hofmann. Measurement of the radial electric field in the ASDEX tokamak. *Nuclear Fusion*, 32(7):1191–1208, 1992. URL https://iopscience.iop.org/article/10.1088/0029-5515/32/7/I09.

[26] K H Burrell, T N Carlstrom, E J Doyle, et al. Physics of the L-mode to H-mode transition in tokamaks. *Plasma Physics and Controlled Fusion*, 34(13):1859–1869, 1992. URL https://iopscience.iop.org/article/10.1088/0741-3335/34/13/014.

[27] P. W. Terry. Suppression of turbulence and transport by sheared flow. *Reviews of Modern Physics*, 72(1):109–165, 2000. URL https://link.aps.org/doi/10.1103/RevModPhys.72.109.

[28] Hajime Urano. Pedestal structure in H-mode plasmas. *Nuclear Fusion*, 54(11):116001, 2014. URL http://stacks.iop.org/0029-5515/54/i=11/a=116001.

[29] P.B. Snyder, R.J. Groebner, J.W. Hughes, et al. A first-principles predictive model of the pedestal height and width: development, testing and ITER optimization with the EPED

model. *Nuclear Fusion*, 51(10):103016, 2011. URL http://stacks.iop.org/0029-5515/51/i=10/a=103016?key=crossref.334289a0972991b200871ad1b82fa95c.

[30] Hartmut Zohm. The physics of edge localized modes (ELMs) and their role in power and particle exhaust. *Plasma Physics and Controlled Fusion*, 38(8):1213–1223, 1996. URL https://iopscience.iop.org/article/10.1088/0741-3335/38/8/012.

[31] H Zohm. Edge localized modes (ELMs). *Plasma Physics and Controlled Fusion*, 38 (2):105–128, 1996. URL http://stacks.iop.org/0741-3335/38/i=2/a=001?key=crossref.f28892e44e8eadadb5c7b755b5fc53e6.

[32] J W Connor. A review of models for ELMs. *Plasma Physics and Controlled Fusion*, 40 (2):191–213, 1998. URL https://iopscience.iop.org/article/10.1088/0741-3335/40/2/003.

[33] Wilson Howard. Edge Localized Modes in Tokamaks. *Fusion Science and Technology*, 53 (2T):161–169, 2008. URL https://www.tandfonline.com/doi/full/10.13182/FST08-A1702.

[34] J. W. Connor, A. Kirk, H. R. Wilson, and Sadruddin Benkadda. Edge Localised Modes (ELMs): Experiments and Theory. In *AIP Conference Proceedings*, volume 1013, pages 174–190. AIP, 2008. URL http://aip.scitation.org/doi/abs/10.1063/1.2939030.

[35] A. W. Leonard. Edge-localized-modes in tokamaks. *Physics of Plasmas*, 21(9):090501, 2014. URL http://scitation.aip.org/content/aip/journal/pop/21/9/10.1063/1.4894742.

[36] R.P. Wenninger, M. Bernert, T. Eich, et al. DEMO divertor limitations during and in between ELMs. *Nuclear Fusion*, 54(11):114003, 2014. URL https://iopscience.iop.org/article/10.1088/0029-5515/54/11/114003.

[37] T. Eich, B. Sieglin, A.J. Thornton, et al. ELM divertor peak energy fluence scaling to ITER with data from JET, MAST and ASDEX upgrade. *Nuclear Materials and Energy*, 12:84–90, 2017. URL https://linkinghub.elsevier.com/retrieve/pii/S2352179116302927.

[38] R.A. Pitts, X. Bonnin, F. Escourbiac, et al. Physics basis for the first ITER tungsten divertor. *Nuclear Materials and Energy*, 20(July):100696, 2019. URL https://doi.org/10.1016/j.nme.2019.100696.

[39] P. B. Snyder, H. R. Wilson, J. R. Ferron, et al. Edge localized modes and the pedestal: A model based on coupled peeling–ballooning modes. *Physics of Plasmas*, 9(5):2037–2043, 2002. URL http://aip.scitation.org/doi/10.1063/1.1449463.

[40] P. B. Snyder, H. R. Wilson, and X. Q. Xu. Progress in the peeling-ballooning model of edge localized modes: Numerical studies of nonlinear dynamics. *Physics of Plasmas*, 12 (5):056115, 2005. URL http://aip.scitation.org/doi/10.1063/1.1873792.

[41] R.J. Groebner, C.S. Chang, J.W. Hughes, et al. Improved understanding of physics processes in pedestal structure, leading to improved predictive capability for ITER. *Nuclear Fusion*, 53(9):093024, 2013. URL http://stacks.iop.org/0029-5515/53/i=9/a=093024?key=crossref.8753903f11d6cecec5e724fe3d2d6708.

[42] G. D. Conway, C. Angioni, F. Ryter, P. Sauter, and J. Vicente. Mean and Oscillating Plasma Flows and Turbulence Interactions across the L-H Confinement Transition. *Physical Review Letters*, 106(6):065001, 2011. URL http://link.aps.org/doi/10.1103/PhysRevLett.106.065001.

[43] G. Birkenmeier, M. Cavedon, G.D. Conway, et al. Magnetic structure and frequency scaling of limit-cycle oscillations close to L- to H-mode transitions. *Nuclear Fusion*, 56 (8):086009, 2016. URL http://stacks.iop.org/0029-5515/56/i=8/a=086009?key=crossref.a3b09a1a38a0b63b51e427a12981ef3d.

[44] H. Zohm, F. Ryter, C. Fuchs, et al. Dynamic behaviour of the H-mode in ASDEX upgrade. *Plasma Physics and Controlled Fusion*, 36(7A):A129–A134, 1994. URL https://iopscience.iop.org/article/10.1088/0741-3335/36/7A/016.

[45] H. Zohm. Dynamic behavior of the L - H transition. *Physical Review Letters*, 72(2): 222–225, 1994. URL https://link.aps.org/doi/10.1103/PhysRevLett.72.222.

[46] A. Kallenbach, R. Dux, M. Mayer, et al. Non-boronized compared with boronized operation of ASDEX Upgrade with full-tungsten plasma facing components. *Nuclear Fusion*, 49(4):045007, 2009. URL https://iopscience.iop.org/article/10.1088/0029-5515/49/4/045007.

[47] R. Dux, V. Bobkov, A. Herrmann, et al. Plasma-wall interaction and plasma behaviour in the non-boronised all tungsten ASDEX Upgrade. *Journal of Nuclear Materials*, 390-391 (1):858–863, 2009. URL http://dx.doi.org/10.1016/j.jnucmat.2009.01.225.

[48] J D Lawson. Some Criteria for a Power Producing Thermonuclear Reactor. *Proceedings of*

the Physical Society. Section B, 70(1):6–10, 1957. URL http://stacks.iop.org/0370-1301/70/i=1/a=303?key=crossref.e1697fd64b8a71aa295438657a972463.

[49] ITER Physics Basis Editors, ITER Physics Expert Group Chairs an Co-Chairs, ITER Joint Central Team Unit, and Physics. Chapter 1: Overview and summary. *Nuclear Fusion*, 39 (12):2137–2174, 1999. URL https://iopscience.iop.org/article/10.1088/0029-5515/39/12/301.

[50] T. C. Luce, C. C. Petty, and J. G. Cordey. Application of dimensionless parameter scaling techniques to the design and interpretation of magnetic fusion experiments. *Plasma Physics and Controlled Fusion*, 50(4):043001, 2008. URL https://iopscience.iop.org/article/10.1088/0741-3335/50/4/043001.

[51] ITER Physics Expert Group on Confinement and Transport, ITER Physics Expert Group on Confinement Modelling, and ITER Physics Basis Editors. Chapter 2: Plasma confinement and transport. *Nuclear Fusion*, 39(12):2175–2249, 1999. URL https://iopscience.iop.org/article/10.1088/0029-5515/39/12/302.

[52] F Troyon, R Gruber, H Saurenmann, S Semenzato, and S Succi. MHD-Limits to Plasma Confinement. *Plasma Physics and Controlled Fusion*, 26(1A):209–215, 1984. URL https://iopscience.iop.org/article/10.1088/0741-3335/26/1A/319.

[53] F Troyon, A Roy, W A Cooper, F Yasseen, and A. Turnbull. Beta limit in tokamaks. Experimental and computational status. *Plasma Physics and Controlled Fusion*, 30(11):1597–1609, 1988. URL https://iopscience.iop.org/article/10.1088/0741-3335/30/11/019.

[54] H.-S Bosch and G.M Hale. Improved formulas for fusion cross-sections and thermal reactivities. *Nuclear Fusion*, 32(4):611–631, 1992. URL https://iopscience.iop.org/article/10.1088/0029-5515/32/4/I07.

[55] Martin Greenwald. Density limits in toroidal plasmas. *Plasma Physics and Controlled Fusion*, 44(8):201, 2002. URL https://iopscience.iop.org/article/10.1088/0741-3335/44/8/201.

[56] M. Greenwald, J.L. Terry, S.M. Wolfe, et al. A new look at density limits in tokamaks. *Nuclear Fusion*, 28(12):2199–2207, 1988. URL https://iopscience.iop.org/article/10.1088/0029-5515/28/12/009.

[57] Robert J Goldston. Reactor compatibility of the H-mode. *Plasma Physics and Controlled Fusion*, 38(8):1161–1172, 1996. URL https://iopscience.iop.org/article/10.1088/0741-3335/38/8/008.

[58] O. Sauter, C. Angioni, and Y. R. Lin-Liu. Neoclassical conductivity and bootstrap current formulas for general axisymmetric equilibria and arbitrary collisionality regime. *Physics of Plasmas*, 6(7):2834–2839, 1999. URL http://aip.scitation.org/doi/10.1063/1.873240.

[59] A. Loarte, B. Lipschultz, A.S Kukushkin, et al. Chapter 4: Power and particle control. *Nuclear Fusion*, 47(6):S203–S263, 2007. URL https://iopscience.iop.org/article/10.1088/0029-5515/47/6/S04.

[60] H. Zohm, C. Angioni, E. Fable, et al. On the physics guidelines for a tokamak DEMO. *Nuclear Fusion*, 53(7):073019, 2013. URL https://iopscience.iop.org/article/10.1088/0029-5515/53/7/073019.

[61] A. Loarte and R. Neu. Power exhaust in tokamaks and scenario integration issues. *Fusion Engineering and Design*, 122:256–273, 2017. URL https://doi.org/10.1016/j.fusengdes.2017.06.024.

[62] EUROfusion. European Research Roadmap to the Realisation of Fusion Energy - long version. Technical report, 2018. URL https://www.euro-fusion.org/fileadmin/user{_}upload/EUROfusion/Documents/TopLevelRoadmap.pdf.

[63] M. Siccinio, W. Biel, M. Cavedon, et al. DEMO physics challenges beyond ITER. *Fusion Engineering and Design*, 156(March):111603, 2020. URL https://doi.org/10.1016/j.fusengdes.2020.111603.

[64] N. Oyama, P. Gohil, L. D. Horton, et al. Pedestal conditions for small ELM regimes in tokamaks. *Plasma Physics and Controlled Fusion*, 48(5A):A171–A181, 2006. URL http://stacks.iop.org/0741-3335/48/i=5A/a=S16?key=crossref.aaca50d075955e7fc67d3cf4bdfcdc5e.

[65] E. Viezzer. Access and sustainment of naturally ELM-free and small-ELM regimes. *Nuclear Fusion*, 58(11):115002, 2018. URL http://stacks.iop.org/0029-5515/58/i=11/a=115002?key=crossref.32a8217e77eafbb62faa56d86e888d55.

[66] T. Eich, B. Sieglin, A. Scarabosio, et al. Inter-ELM Power Decay Length for JET and ASDEX Upgrade: Measurement and Comparison with Heuristic Drift-Based Model. *Physical Review Letters*, 107(21):215001, 2011. URL https://link.aps.org/doi/10.1103/PhysRevLett.107.215001.

[67] D. Brunner, B. LaBombard, A.Q. Kuang, and J.L. Terry. High-resolution heat flux width measurements at reactor-level magnetic fields and observation of a unified width scaling across confinement regimes in the Alcator C-Mod tokamak. *Nuclear Fusion*, 58(9):094002, 2018. URL https://iopscience.iop.org/article/10.1088/1741-4326/aad0d6.

[68] D Silvagni, T Eich, M Faitsch, et al. Scrape-off layer (SOL) power width scaling and correlation between SOL and pedestal gradients across L, I and H-mode plasmas at ASDEX Upgrade. *Plasma Physics and Controlled Fusion*, 62(4):045015, 2020. URL https://iopscience.iop.org/article/10.1088/1361-6587/ab74e8.

[69] P.C Stangeby. Can detached divertor plasmas be explained as self-sustained gas targets? *Nuclear Fusion*, 33(11):1695–1705, 1993. URL https://iopscience.iop.org/article/10.1088/0029-5515/33/11/I10.

[70] G.F. Matthews. Plasma detachment from divertor targets and limiters. *Journal of Nuclear Materials*, 220-222:104–116, 1995. URL http://linkinghub.elsevier.com/retrieve/pii/0022311594004501.

[71] A. W. Leonard. Plasma detachment in divertor tokamaks. *Plasma Physics and Controlled Fusion*, 60(4):044001, 2018. URL https://iopscience.iop.org/article/10.1088/1361-6587/aaa7a9.

[72] V. Philipps, R. Neu, J. Rapp, et al. Comparison of tokamak behaviour with tungsten and low- Z plasma facing materials. *Plasma Physics and Controlled Fusion*, 42(12B):B293–B310, 2000. URL https://iopscience.iop.org/article/10.1088/0741-3335/42/12B/322.

[73] J.N. Brooks, L. El-Guebaly, A. Hassanein, and T. Sizyuk. Plasma-facing material alternatives to tungsten. *Nuclear Fusion*, 55(4):043002, 2015. URL https://iopscience.iop.org/article/10.1088/0029-5515/55/4/043002.

[74] H. Bolt, V. Barabash, W. Krauss, et al. Materials for the plasma-facing components of

fusion reactors. *Journal of Nuclear Materials*, 329-333(1-3 PART A):66–73, 2004. URL https://linkinghub.elsevier.com/retrieve/pii/S0022311504001242.

[75] V. Philipps. Tungsten as material for plasma-facing components in fusion devices. *Journal of Nuclear Materials*, 415(1):S2–S9, 2011. URL http://dx.doi.org/10.1016/j.jnucmat.2011.01.110.

[76] R Neu, K Asmussen, K Krieger, et al. The tungsten divertor experiment at ASDEX Upgrade. *Plasma Physics and Controlled Fusion*, 38(12A):A165–A179, 1996. URL https://iopscience.iop.org/article/10.1088/0741-3335/38/12A/013.

[77] R. Neu, R. Dux, A. Geier, et al. Impurity behaviour in the ASDEX Upgrade divertor tokamak with large area tungsten walls. *Plasma Physics and Controlled Fusion*, 44(6):313, 2002. URL https://iopscience.iop.org/article/10.1088/0741-3335/44/6/313.

[78] R. Neu. High- Z plasma facing components in fusion devices: boundary conditions and operational experiences. *Physica Scripta*, T123:33–44, 2006. URL https://iopscience.iop.org/article/10.1088/0031-8949/2006/T123/005.

[79] R. Neu, A. Kallenbach, M. Balden, et al. Overview on plasma operation with a full tungsten wall in ASDEX Upgrade. *Journal of Nuclear Materials*, 438(SUPPL):S34–S41, 2013. URL https://linkinghub.elsevier.com/retrieve/pii/S0022311513000147.

[80] M Shimada, D.J Campbell, V Mukhovatov, et al. Chapter 1: Overview and summary. *Nuclear Fusion*, 47(6):S1–S17, 2007. URL http://stacks.iop.org/0029-5515/47/i=6/a=S01?key=crossref.9f5018b333c98316af6e827446ba6d15.

[81] R Aymar, P Barabaschi, and Y Shimomura. The ITER design. *Plasma Physics and Controlled Fusion*, 44(5):304, 2002. URL https://iopscience.iop.org/article/10.1088/0741-3335/44/5/304.

[82] ITER Organization. PHOTOS TECHNICAL. URL https://www.iter.org/album/Media/7-Technical.

[83] Kaname Ikeda. ITER on the road to fusion energy. *Nuclear Fusion*, 50(1):014002, 2010. URL http://stacks.iop.org/0029-5515/50/i=1/a=014002?key=crossref.6f4f01cd3f89161161cf9721d787809f.

[84] V. Mukhovatov, M. Shimada, K. Lackner, et al. Chapter 9: ITER contributions for Demo plasma development. *Nuclear Fusion*, 47(6), 2007.

[85] A.C.C. Sips, J. Schweinzer, T.C. Luce, et al. Assessment of the baseline scenario at q 95 ˜ 3 for ITER. *Nuclear Fusion*, 58(12):126010, 2018. URL https://iopscience.iop.org/article/10.1088/1741-4326/aade57.

[86] V Mukhovatov, M Shimada, A N Chudnovskiy, et al. Overview of physics basis for ITER. *Plasma Physics and Controlled Fusion*, 45(12A):A235–A252, 2003. URL https://iopscience.iop.org/article/10.1088/0741-3335/45/12A/016.

[87] B J Green, ITER International Team Teams, and Partici. ITER: burning plasma physics experiment. *Plasma Physics and Controlled Fusion*, 45(5):687–706, 2003. URL https://iopscience.iop.org/article/10.1088/0741-3335/45/5/312.

[88] Y. Liang. Overview of Edge-Localized Mode Control in Tokamak Plasmas. *Fusion Science and Technology*, 59(3):586–601, 2011. URL https://www.tandfonline.com/doi/full/10.13182/FST11-A11699.

[89] R. Maingi. Enhanced confinement scenarios without large edge localized modes in tokamaks: control, performance, and extrapolability issues for ITER. *Nuclear Fusion*, 54(11):114016, 2014. URL https://iopscience.iop.org/article/10.1088/0029-5515/54/11/114016.

[90] T. E. Evans, R. A. Moyer, P. R. Thomas, et al. Suppression of Large Edge-Localized Modes in High-Confinement DIII-D Plasmas with a Stochastic Magnetic Boundary. *Physical Review Letters*, 92(23):235003, 2004. URL https://link.aps.org/doi/10.1103/PhysRevLett.92.235003.

[91] Y. M. Jeon, J.-K. Park, S. W. Yoon, et al. Suppression of Edge Localized Modes in High-Confinement KSTAR Plasmas by Nonaxisymmetric Magnetic Perturbations. *Physical Review Letters*, 109(3):035004, 2012. URL https://link.aps.org/doi/10.1103/PhysRevLett.109.035004.

[92] W. Suttrop, A. Kirk, R. Nazikian, et al. Experimental studies of high-confinement mode plasma response to non-axisymmetric magnetic perturbations in ASDEX Upgrade. *Plasma*

Physics and Controlled Fusion, 59(1):014049, 2017. URL https://iopscience.iop.org/article/10.1088/0741-3335/59/1/014049.

[93] P.T Lang, G.D Conway, T. Eich, et al. ELM pace making and mitigation by pellet injection in ASDEX Upgrade. *Nuclear Fusion*, 44(5):665–677, 2004. URL https://iopscience.iop.org/article/10.1088/0029-5515/44/5/010.

[94] L.R. Baylor, S.K. Combs, C.R. Foust, et al. Pellet fuelling, ELM pacing and disruption mitigation technology development for ITER. *Nuclear Fusion*, 49(8):085013, 2009. URL https://iopscience.iop.org/article/10.1088/0029-5515/49/8/085013.

[95] P.T. Lang, A. Loarte, G. Saibene, et al. ELM control strategies and tools: status and potential for ITER. *Nuclear Fusion*, 53(4):043004, 2013. URL https://iopscience.iop.org/article/10.1088/0029-5515/53/4/043004.

[96] A W Degeling, Y R Martin, J B Lister, et al. Magnetic triggering of ELMs in TCV. *Plasma Physics and Controlled Fusion*, 45(9):1637–1655, 2003. URL https://iopscience.iop.org/article/10.1088/0741-3335/45/9/306.

[97] E. de la Luna, I.T. Chapman, F. Rimini, et al. Understanding the physics of ELM pacing via vertical kicks in JET in view of ITER. *Nuclear Fusion*, 56(2):026001, 2016. URL https://iopscience.iop.org/article/10.1088/0029-5515/56/2/026001.

[98] Y. Kamada, T. Oikawa, L. Lao, et al. Disappearance of giant ELMs and appearance of minute grassy ELMs in JT-60U high-triangularity discharges. *Plasma Physics and Controlled Fusion*, 42(5A):A247–A253, 2000. URL https://iopscience.iop.org/article/10.1088/0741-3335/42/5A/329.

[99] J. Stober, M. Maraschek, G.D Conway, et al. Type II ELMy H modes on ASDEX Upgrade with good confinement at high density. *Nuclear Fusion*, 41(9):1123–1134, 2001. URL https://iopscience.iop.org/article/10.1088/0029-5515/41/9/301.

[100] G.F. Harrer, E. Wolfrum, M.G. Dunne, et al. Parameter dependences of small edge localized modes (ELMs). *Nuclear Fusion*, 58(11):112001, 2018. URL https://iopscience.iop.org/article/10.1088/1741-4326/aad757.

[101] B. Labit, T. Eich, G.F. Harrer, et al. Dependence on plasma shape and plasma fueling for small edge-localized mode regimes in TCV and ASDEX Upgrade. *Nuclear Fusion*, 59(8): 086020, 2019. URL https://iopscience.iop.org/article/10.1088/1741-4326/ab2211.

[102] M. Greenwald, R. Boivin, P. Bonoli, et al. Characterization of enhanced Dα high-confinement modes in Alcator C -Mod. *Physics of Plasmas*, 6(5):1943–1949, 1999. URL http://aip.scitation.org/doi/10.1063/1.873451.

[103] Y. Takase, R. L. Boivin, F. Bombarda, et al. Radiofrequency-heated enhanced confinement modes in the Alcator C-Mod tokamak. *Physics of Plasmas*, 4(5):1647–1653, 1997. URL http://aip.scitation.org/doi/10.1063/1.872269.

[104] A. E. Hubbard, R. L. Boivin, R. S. Granetz, et al. Pedestal profiles and fluctuations in C-Mod enhanced D-alpha H-modes. *Physics of Plasmas*, 8(5):2033–2040, 2001. URL http://aip.scitation.org/doi/10.1063/1.1348329.

[105] J A Snipes, B LaBombard, M Greenwald, et al. The quasi-coherent signature of enhanced D α H-mode in Alcator C-Mod. *Plasma Physics and Controlled Fusion*, 43(4):L23–L30, 2001. URL http://iopscience.iop.org/0741-3335/43/4/101.

[106] M. Greenwald, N. Basse, P. Bonoli, et al. Confinement and Transport Research in Alcator C-Mod. *Fusion Science and Technology*, 51(3):266–287, 2007. URL https://www.tandfonline.com/doi/full/10.13182/FST07-A1422.

[107] K. Kamiya, H. Kimura, H. Ogawa, et al. Observation of High Recycling Steady H-mode edge and compatibility with improved core confinement mode on JFT-2M. *Nuclear Fusion*, 43(10):1214–1219, 2003. URL http://stacks.iop.org/0029-5515/43/i=10/a=024?key=crossref.ce693a7b312cd2cab34304566876df90.

[108] K. Kamiya, M. Bakhtiari, S. Kasai, et al. High recycling steady H-mode regime in the JFT-2M tokamak. *Plasma Physics and Controlled Fusion*, 46(5A):A157–A163, 2004. URL https://iopscience.iop.org/article/10.1088/0741-3335/46/5A/017.

[109] A. E. Hubbard, K. Kamiya, N. Oyama, et al. Comparisons of small ELM H-Mode regimes on the Alcator C-Mod and JFT-2M tokamaks. *Plasma Physics and Controlled Fusion*, 48(5A):A121–A129, 2006. URL http://stacks.iop.org/0741-3335/48/i=5A/a=S11?key=crossref.f8ee84a68ab363afe856b4d1877f71a1.

[110] Y. Ye, G.S. Xu, B.N. Wan, et al. A stationary long-pulse ELM-absent H-mode regime in EAST. *Nuclear Fusion*, 57(8):086041, 2017. URL https://iopscience.iop.org/article/10.1088/1741-4326/aa7809.

[111] D. A. Mossessian, R. J. Groebner, R. A. Moyer, et al. Edge dimensionless identity experiment on DIII-D and Alcator C -Mod. *Physics of Plasmas*, 10(3):689–698, 2003. URL http://aip.scitation.org/doi/10.1063/1.1538252.

[112] J. Stober, P. J. Lomas, G. Saibene, et al. Small ELM regimes with good confinement on JET and comparison to those on ASDEX Upgrade, Alcator C-mod and JT-60U. *Nuclear Fusion*, 45(11):1213–1223, 2005.

[113] M Greenwald, R Boivin, P Bonoli, et al. Studies of EDA H-mode in Alcator C-Mod. *Plasma Physics and Controlled Fusion*, 42(5A):A263–A269, 2000. URL http://stacks.iop.org/0741-3335/42/i=5A/a=331?key=crossref.c08f4e8003e3a21558bba070e46cef53.

[114] J. W. Hughes, D. A. Mossessian, A. E. Hubbard, B. LaBombard, and E. S. Marmar. Observations and empirical scalings of the high-confinement mode pedestal on Alcator C-Mod. *Physics of Plasmas*, 9(7):3019–3030, 2002. URL http://aip.scitation.org/doi/10.1063/1.1486224.

[115] D A Mossessian, P B Snyder, M Greenwald, et al. H-mode pedestal characteristics and MHD stability of the edge plasma in Alcator C-Mod. *Plasma Physics and Controlled Fusion*, 44(4):423–437, 2002. URL http://stacks.iop.org/0741-3335/44/i=4/a=303?key=crossref.2d5225ddd59a1804c8b392181dc225f4.

[116] D. A. Mossessian, P. Snyder, A. Hubbard, et al. High-confinement-mode edge stability of Alcator C-mod plasmas. *Physics of Plasmas*, 10(5):1720–1726, 2003. URL http://aip.scitation.org/doi/10.1063/1.1561618.

[117] T. Sunn Pedersen, R.S Granetz, A.E Hubbard, et al. Radial impurity transport in the H mode transport barrier region in Alcator C-Mod. *Nuclear Fusion*, 40(10):1795–1804, 2000. URL http://stacks.iop.org/0029-5515/40/i=10/a=310?key=crossref.618667ac4e6224b23d39e5311aa12da6.

[118] J. E. Rice, J. L. Terry, E. S. Marmar, et al. Impurity Transport in Alcator C-Mod Plasmas.

Fusion Science and Technology, 51(3):357–368, 2007. URL https://www.tandfonline.com/doi/full/10.13182/FST07-A1427.

[119] J.E. Rice, M.L. Reinke, C. Gao, et al. Core impurity transport in Alcator C-Mod L-, I- and H-mode plasmas. *Nuclear Fusion*, 55(3):033014, 2015. URL https://iopscience.iop.org/article/10.1088/0029-5515/55/3/033014.

[120] B. LaBombard, T. Golfinopoulos, J. L. Terry, et al. New insights on boundary plasma turbulence and the quasi-coherent mode in Alcator C-Mod using a Mirror Langmuir Probea). *Physics of Plasmas*, 21(5):056108, 2014. URL http://dx.doi.org/10.1063/1.4873918.

[121] N. P. Basse, E. M. Edlund, D. R. Ernst, et al. Characterization of core and edge turbulence in L- and enhanced Dα H-mode Alcator C-Mod plasmas. *Physics of Plasmas*, 12(5):052512, 2005. URL http://aip.scitation.org/doi/10.1063/1.1899161.

[122] C Theiler, J L Terry, E Edlund, et al. Radial localization of edge modes in Alcator C-Mod pedestals using optical diagnostics. *Plasma Physics and Controlled Fusion*, 59(2):025016, 2017. URL http://stacks.iop.org/0741-3335/59/i=2/a=025016?key=crossref.66ad4edaee1a2e07af2b6bbda74ffb6e.

[123] a Mazurenko, M Porkolab, D Mossessian, et al. Experimental and Theoretical Study of Quasicoherent Fluctuations in Enhanced <math display=”inline”> <msub> <mi>D</mi> <mi>α</mi> </msub> </math> Plasmas in the Alcator C-Mod Tokamak. *Physical Review Letters*, 89(22):225004, 2002. URL http://link.aps.org/doi/10.1103/PhysRevLett.89.225004.

[124] J.W. Hughes, P.B. Snyder, M.L. Reinke, et al. Access to pedestal pressure relevant to burning plasmas on the high magnetic field tokamak Alcator C-Mod. *Nuclear Fusion*, 58(11):112003, 2018. URL http://stacks.iop.org/0029-5515/58/i=11/a=112003?key=crossref.a28758d3716876daba628e1750629c48.

[125] J. A. Goetz, B. LaBombard, B. Lipschultz, et al. High confinement dissipative divertor operation on Alcator C-Mod. *Physics of Plasmas*, 6(5):1899–1906, 1999. URL http://aip.scitation.org/doi/10.1063/1.873447.

[126] A. Loarte, J. W. Hughes, M. L. Reinke, et al. High confinement/high radiated power H-mode experiments in Alcator C-Mod and consequences for International Thermonuclear Experimental Reactor (ITER) Q DT = 10 operation. *Physics of Plasmas*, 18(5):056105, 2011. URL http://aip.scitation.org/doi/10.1063/1.3567547.

[127] K. H. Burrell, M. E. Austin, D. P. Brennan, et al. Quiescent double barrier high-confinement mode plasmas in the DIII-D tokamak. *Physics of Plasmas*, 8(5):2153–2162, 2001. URL http://aip.scitation.org/doi/10.1063/1.1355981.

[128] Y. Sakamoto, H. Shirai, T. Fujita, et al. Impact of toroidal rotation on ELM behaviour in the H-mode on JT-60U. *Plasma Physics and Controlled Fusion*, 46(5A):A299–A304, 2004. URL https://iopscience.iop.org/article/10.1088/0741-3335/46/5A/033.

[129] W Suttrop, M Maraschek, G D Conway, et al. ELM-free stationary H-mode plasmas in the ASDEX Upgrade tokamak. *Plasma Physics and Controlled Fusion*, 45(8):1399–1416, 2003. URL https://iopscience.iop.org/article/10.1088/0741-3335/45/8/302.

[130] W. Suttrop, V. Hynönen, T. Kurki-Suonio, et al. Studies of the 'Quiescent H-mode' regime in ASDEX Upgrade and JET. *Nuclear Fusion*, 45(7):721–730, 2005. URL https://iopscience.iop.org/article/10.1088/0029-5515/45/7/021.

[131] E. R. Solano, P. J. Lomas, B. Alper, et al. Observation of Confined Current Ribbon in JET Plasmas. *Physical Review Letters*, 104(18):185003, 2010. URL https://link.aps.org/doi/10.1103/PhysRevLett.104.185003.

[132] K H Burrell, M E Austin, D P Brennan, et al. Quiescent H-mode plasmas in the DIII-D tokamak. *Plasma Physics and Controlled Fusion*, 44(5A):325, 2002. URL https://iopscience.iop.org/article/10.1088/0741-3335/44/5A/325.

[133] K.H. Burrell, T.H. Osborne, P.B. Snyder, et al. Edge pedestal control in quiescent H-mode discharges in DIII-D using co-plus counter-neutral beam injection. *Nuclear Fusion*, 49(8):085024, 2009. URL https://iopscience.iop.org/article/10.1088/0029-5515/49/8/085024.

[134] A.M. Garofalo, W.M. Solomon, J.-K. Park, et al. Advances towards QH-mode viability for ELM-stable operation in ITER. *Nuclear Fusion*, 51(8):083018, 2011. URL https://iopscience.iop.org/article/10.1088/0029-5515/51/8/083018.

[135] K. H. Burrell, T. H. Osborne, P. B. Snyder, et al. Quiescent H-Mode Plasmas with Strong Edge Rotation in the Cocurrent Direction. *Physical Review Letters*, 102(15):155003, 2009. URL https://link.aps.org/doi/10.1103/PhysRevLett.102.155003.

[136] Xi Chen, K.H. Burrell, T.H. Osborne, et al. Bifurcation of quiescent H-mode to a wide pedestal regime in DIII-D and advances in the understanding of edge harmonic oscillations. *Nuclear Fusion*, 57(8):086008, 2017. URL http://stacks.iop.org/0029-5515/57/i=8/a=086008?key=crossref.f7ba8442b0274120fd45526dd2c50bdc.

[137] T.M. Wilks, A.M. Garofalo, P.H. Diamond, et al. Scaling trends of the critical E × B shear for edge harmonic oscillation onset in DIII-D quiescent H-mode plasmas. *Nuclear Fusion*, 58(11):112002, 2018. URL https://iopscience.iop.org/article/10.1088/1741-4326/aad143.

[138] G D Conway, J Schirmer, S Klenge, et al. Plasma rotation profile measurements using Doppler reflectometry. *Plasma Physics and Controlled Fusion*, 46 (6):951–970, 2004. URL http://stacks.iop.org/0741-3335/46/i=6/a=003?key=crossref.bc56d3ab826fb70cbd11ae3bdd7445a1.

[139] P.B Snyder, K.H Burrell, H.R Wilson, et al. Stability and dynamics of the edge pedestal in the low collisionality regime: physics mechanisms for steady-state ELM-free operation. *Nuclear Fusion*, 47(8):961–968, 2007. URL https://iopscience.iop.org/article/10.1088/0029-5515/47/8/030.

[140] F. Liu, G.T.A. Huijsmans, A. Loarte, et al. Nonlinear MHD simulations of Quiescent H-mode plasmas in DIII-D. *Nuclear Fusion*, 55(11):113002, 2015. URL https://iopscience.iop.org/article/10.1088/0029-5515/55/11/113002.

[141] Xi Chen, K.H. Burrell, N.M. Ferraro, et al. Rotational shear effects on edge harmonic oscillations in DIII-D quiescent H-mode discharges. *Nuclear Fusion*, 56(7):076011, 2016. URL https://iopscience.iop.org/article/10.1088/0029-5515/56/7/076011.

[142] J. R. King, S. E. Kruger, K. H. Burrell, et al. MHD modeling of a DIII-D low-torque QH-mode discharge and comparison to observations. *Physics of Plasmas*, 24(5):055902, 2017. URL http://dx.doi.org/10.1063/1.4977467.

[143] J. R. King, K. H. Burrell, A. M. Garofalo, et al. NIMROD modeling of quiescent H-mode: Reconstruction considerations and saturation mechanism. *Nuclear Fusion*, 57(2), 2017.

[144] F. Liu, G T A Huijsmans, A. Loarte, et al. Nonlinear MHD simulations of QH-mode DIII-D plasmas and implications for ITER high Q scenarios. *Plasma Physics and Controlled Fusion*, 60(1):014039, 2018. URL https://iopscience.iop.org/article/10.1088/1361-6587/aa934f.

[145] W.M. Solomon, K.H. Burrell, M.E. Fenstermacher, et al. Extending the physics basis of quiescent H-mode toward ITER relevant parameters. *Nuclear Fusion*, 55(7):073031, 2015. URL https://iopscience.iop.org/article/10.1088/0029-5515/55/7/073031.

[146] A. M. Garofalo, K. H. Burrell, D. Eldon, et al. The quiescent H-mode regime for high performance edge localized mode-stable operation in future burning plasmasa). *Physics of Plasmas*, 22(5):056116, 2015. URL http://dx.doi.org/10.1063/1.4921406.

[147] K. H. Burrell, K. Barada, X. Chen, et al. Discovery of stationary operation of quiescent H-mode plasmas with net-zero neutral beam injection torque and high energy confinement on DIII-D. *Physics of Plasmas*, 23(5):056103, 2016. URL http://aip.scitation.org/doi/10.1063/1.4943521.

[148] Xi Chen, K.H. Burrell, T.H. Osborne, et al. Stationary QH-mode plasmas with high and wide pedestal at low rotation on DIII-D. *Nuclear Fusion*, 57(2):022007, 2017. URL http://stacks.iop.org/0029-5515/57/i=2/a=022007?key=crossref.186310b65bf05bdbe03d94264cf551bc.

[149] Xi Chen, K.H. Burrell, T.H. Osborne, et al. Expanding the parameter space of the wide-pedestal QH-mode towards ITER conditions. *Nuclear Fusion*, 60(9):092006, 2020. URL https://iopscience.iop.org/article/10.1088/1741-4326/ab9fa5.

[150] D.G. Whyte, A.E. Hubbard, J.W. Hughes, et al. I-mode: an H-mode energy confinement regime with L-mode particle transport in Alcator C-Mod. *Nuclear Fusion*, 50(10):105005, 2010. URL http://stacks.iop.org/0029-5515/50/i=10/a=105005?key=crossref.76e3332b73592f6e6b157a67f119a92d.

[151] F. Ryter, W. Suttrop, B. Brüsehaber, et al. H-mode power threshold and transition in ASDEX Upgrade. *Plasma Physics and Controlled Fusion*, 40(5):725–729, 1998. URL https://iopscience.iop.org/article/10.1088/0741-3335/40/5/032.

[152] A.E. Hubbard, S.-G. Baek, D. Brunner, et al. Physics and performance of the I-mode regime over an expanded operating space on Alcator C-Mod. *Nuclear Fusion*, 57(12): 126039, 2017. URL https://iopscience.iop.org/article/10.1088/1741-4326/aa8570.

[153] T. Happel, P. Manz, F. Ryter, et al. The I-mode confinement regime at ASDEX Upgrade: global properties and characterization of strongly intermittent density fluctuations. *Plasma Physics and Controlled Fusion*, 59(1):014004, 2017. URL https://iopscience.iop.org/article/10.1088/0741-3335/59/1/014004.

[154] A. Marinoni, J.C. Rost, M. Porkolab, et al. Characterization of density fluctuations during the search for an I-mode regime on the DIII-D tokamak. *Nuclear Fusion*, 55(9):093019, 2015. URL https://iopscience.iop.org/article/10.1088/0029-5515/55/9/093019.

[155] A.E. Hubbard, T. Osborne, F. Ryter, et al. Multi-device studies of pedestal physics and confinement in the I-mode regime. *Nuclear Fusion*, 56(8):086003, 2016. URL https://iopscience.iop.org/article/10.1088/0029-5515/56/8/086003.

[156] X. Feng, A.D. Liu, C. Zhou, et al. I-mode investigation on the Experimental Advanced Superconducting Tokamak. *Nuclear Fusion*, 59(9):096025, 2019. URL https://iopscience.iop.org/article/10.1088/1741-4326/ab28a7.

[157] Y.J. Liu, Z.X. Liu, A.D. Liu, et al. Power threshold and confinement of the I-mode in the EAST tokamak. *Nuclear Fusion*, 60(8):082003, 2020. URL https://iopscience.iop.org/article/10.1088/1741-4326/ab88e0.

[158] A. E. Hubbard, D. G. Whyte, R. M. Churchill, et al. Edge energy transport barrier and turbulence in the I-mode regime on Alcator C-Mod. *Physics of Plasmas*, 18(5):056115, 2011. URL http://aip.scitation.org/doi/10.1063/1.3582135.

[159] T Happel, M Griener, D Silvagni, et al. Stationarity of I-mode operation and I-mode divertor heat fluxes on the ASDEX Upgrade tokamak. *Nuclear Materials and Energy*, 18: 159–165, 2019. URL https://doi.org/10.1016/j.nme.2018.12.022.

[160] F. Ryter, R. Fischer, J.C. Fuchs, et al. I-mode studies at ASDEX Upgrade: L-I and I-H transitions, pedestal and confinement properties. *Nuclear Fusion*, 57(1):016004, 2017. URL https://iopscience.iop.org/article/10.1088/0029-5515/57/1/016004.

[161] A.E. Hubbard, D.G. Whyte, R.M. Churchill, et al. Threshold conditions for transitions to I-mode and H-mode with unfavourable ion grad B drift direction. *Nuclear Fusion*, 52(11): 114009, 2012. URL https://iopscience.iop.org/article/10.1088/0029-5515/52/11/114009.

[162] Y R Martin, T Takizuka, and ITPA CDBM H-mode Threshold Database Working Group. Power requirement for accessing the H-mode in ITER. *Journal of Physics: Conference Series*, 123:012033, 2008. URL http://stacks.iop.org/1742-6596/123/i=1/a=012033?key=crossref.433acb98b7d8b044ce2b33de88f46da5.

[163] C. Theiler, R.M. Churchill, B. Lipschultz, et al. Inboard and outboard radial electric field wells in the H- and I-mode pedestal of Alcator C-Mod and poloidal variations of impurity temperature. *Nuclear Fusion*, 54(8):083017, 2014. URL https://iopscience.iop.org/article/10.1088/0029-5515/54/8/083017.

[164] J.W. Hughes, P.B. Snyder, J.R. Walk, et al. Pedestal structure and stability in H-mode and I-mode: a comparative study on Alcator C-Mod. *Nuclear Fusion*, 53(4):043016, 2013. URL https://iopscience.iop.org/article/10.1088/0029-5515/53/4/043016.

[165] J. R. Walk, J. W. Hughes, A. E. Hubbard, et al. Edge-localized mode avoidance and pedestal structure in I-mode plasmas. *Physics of Plasmas*, 21(5):056103, 2014. URL http://dx.doi.org/10.1063/1.4872220.

[166] T Happel, P Manz, F Ryter, et al. Turbulence intermittency linked to the weakly coherent mode in ASDEX Upgrade I-mode plasmas. *Nuclear Fusion*, 56(6):064004, 2016. URL http://stacks.iop.org/0029-5515/56/i=6/a=064004.

[167] D Silvagni, T Eich, T Happel, et al. I-mode pedestal relaxation events at ASDEX Upgrade. *Nuclear Fusion*, 60(12):126028, 2020. URL https://iopscience.iop.org/article/10.1088/1741-4326/abb423.

[168] A.E. White, P. Phillips, D.G. Whyte, et al. Electron temperature fluctuations associated with the weakly coherent mode in the edge of I-mode plasmas. *Nuclear Fusion*, 51(11): 113005, 2011. URL http://stacks.iop.org/0029-5515/51/i=11/a=113005?key=crossref.37e29be42195088af0e0712974d62fc7.

[169] I. Cziegler, P. H. Diamond, N. Fedorczak, et al. Fluctuating zonal flows in the I-mode

regime in Alcator C-Mod. *Physics of Plasmas*, 20(5):055904, 2013. URL http://aip.scitation.org/doi/10.1063/1.4803914.

[170] P. Manz, P. Lauber, V.E. Nikolaeva, et al. Geodesic oscillations and the weakly coherent mode in the I-mode of ASDEX Upgrade. *Nuclear Fusion*, 55(8):083004, 2015. URL http://stacks.iop.org/0029-5515/55/i=8/a=083004?key=crossref.009744030ad4b292d40e752f4ebb21a7.

[171] Peter Manz, Tim Happel, Ulrich Stroth, Thomas Eich, and Davide Silvagni. Physical mechanism behind and access to the I-mode confinement regime in tokamaks. *Nuclear Fusion*, 60(9):096011, 2020. URL https://iopscience.iop.org/article/10.1088/1741-4326/ab9e17.

[172] Silvia Espinosa and Peter J. Catto. Theoretical explanation of I-mode impurity removal and energy confinement. *Plasma Physics and Controlled Fusion*, 60(9):094001, 2018. URL http://stacks.iop.org/0741-3335/60/i=9/a=094001?key=crossref.8d28fd26d66becdcd80ebced898c2783.

[173] M.L. Reinke, D. Brunner, T. Golfinopoulos, et al. Radiative heat exhaust in Alcator C-Mod I-mode plasmas. *Nuclear Fusion*, 59(4):046018, 2019. URL https://iopscience.iop.org/article/10.1088/1741-4326/ab04cf.

[174] H. Vernickel, M. Blaumoser, K. Ennen, et al. ASDEX upgrade: A poloidal divertor tokamak adapted to reactor requirements. *Journal of Nuclear Materials*, 128-129(C):71–77, 1984. URL https://linkinghub.elsevier.com/retrieve/pii/0022311584903301.

[175] Albrecht Herrmann and Otto Gruber. Chapter 1: ASDEX Upgrade - Introduction and Overview. *Fusion Science and Technology*, 44(3):569–577, 2003. URL https://www.tandfonline.com/doi/full/10.13182/FST03-A399.

[176] Bernhard Streibl, Peter Thomas Lang, Fritz Leuterer, Jean-Marie Noterdaeme, and Albrecht Stäbler. Chapter 2: Machine Design, Fueling, and Heating in ASDEX Upgrade. *Fusion Science and Technology*, 44(3):578–592, 2003. URL https://www.tandfonline.com/doi/full/10.13182/FST03-A400.

[177] R.C. Wolf, A. Ali, A. Alonso, et al. Major results from the first plasma campaign of

the Wendelstein 7-X stellarator. *Nuclear Fusion*, 57(10):102020, 2017. URL https://iopscience.iop.org/article/10.1088/1741-4326/aa770d.

[178] H. Meyer, C. Angioni, C.G. Albert, et al. Overview of physics studies on ASDEX Upgrade. *Nuclear Fusion*, 59(11):112014, 2019. URL https://iopscience.iop.org/article/10.1088/1741-4326/ab18b8.

[179] H. Zohm. Recent ASDEX Upgrade research in support of ITER and DEMO. *Nuclear Fusion*, 55(10):104010, 2015. URL https://iopscience.iop.org/article/10.1088/0029-5515/55/10/104010.

[180] O. Gruber, R. Arslanbekov, C. Atanasiu, et al. Overview of ASDEX Upgrade results. *Nuclear Fusion*, 41(10):1369–1389, 2001. URL https://iopscience.iop.org/article/10.1088/0029-5515/41/10/306.

[181] H Zohm, C Angioni, R Arslanbekov, et al. Overview of ASDEX Upgrade results. *Nuclear Fusion*, 43(12):1570–1582, 2003. URL https://iopscience.iop.org/article/10.1088/0029-5515/47/10/S11.

[182] S. Günter, C. Angioni, M. Apostoliceanu, et al. Overview of ASDEX Upgrade results—development of integrated operating scenarios for ITER. *Nuclear Fusion*, 45(10):S98–S108, 2005. URL https://iopscience.iop.org/article/10.1088/0029-5515/45/10/S08.

[183] O. Gruber. Overview of ASDEX Upgrade results. *Nuclear Fusion*, 47(10):S622–S634, 2007. URL https://iopscience.iop.org/article/10.1088/0029-5515/47/10/S11.

[184] U. Stroth, J. Adamek, L. Aho-Mantila, et al. Overview of ASDEX Upgrade results. *Nuclear Fusion*, 53(10):104003, 2013. URL http://stacks.iop.org/0029-5515/53/i=10/a=104003?key=crossref.236751437b5a8ac5e7063de763951121.

[185] E. Wolfrum, E. Viezzer, A. Burckhart, et al. Overview of recent pedestal studies at ASDEX Upgrade. *Nuclear Fusion*, 55(5):053017, 2015. URL http://dx.doi.org/10.1088/0029-5515/55/5/053017.

[186] A. Kallenbach. Overview of ASDEX Upgrade results. *Nuclear Fusion*, 57(10):102015, 2017. URL https://iopscience.iop.org/article/10.1088/0029-5515/47/10/S11.

[187] W. Köppendörfer, M. Blaumoser, K. Ennen, et al. The ASDEX Upgrade toroidal field magnet and poloidal divertor field coil system adapted to reactor requirements. *Nuclear Engineering and Design. Fusion*, 3(3):265–272, 1986. URL https://linkinghub.elsevier.com/retrieve/pii/S0167899X86800179.

[188] C. Sihler, P. Fu, M. Huart, B. Streibl, and W. Treutterer. Paralleling of two large flywheel generators for the optimisation of the ASDEX Upgrade power supply. *Fusion Engineering and Design*, 58-59:41–45, 2001. URL https://linkinghub.elsevier.com/retrieve/pii/S0920379601002812.

[189] W. Suttrop, O. Gruber, S. Günter, et al. In-vessel saddle coils for MHD control in ASDEX Upgrade. *Fusion Engineering and Design*, 84(2-6):290–294, 2009. URL https://linkinghub.elsevier.com/retrieve/pii/S0920379608004912.

[190] Max Planck Institute for Plasma Physics. AUG cross section, . URL https://www.aug.ipp.mpg.de/aug/local/aug{_}only/AUG{_}Aufbau/Drawing{_}Gallery/.

[191] R Neu, M. Balden, V. Bobkov, et al. Plasma wall interaction and its implication in an all tungsten divertor tokamak. *Plasma Physics and Controlled Fusion*, 49(12B):B59–B70, 2007. URL https://iopscience.iop.org/article/10.1088/0741-3335/49/12B/S04.

[192] A. Herrmann, H. Greuner, N. Jaksic, et al. Solid tungsten Divertor-III for ASDEX Upgrade and contributions to ITER. *Nuclear Fusion*, 55(6):063015, 2015. URL https://iopscience.iop.org/article/10.1088/0029-5515/55/6/063015.

[193] A. Herrmann, I. Zammuto, M. Balden, et al. Experiences with a solid tungsten divertor in ASDEX Upgrade. *Nuclear Materials and Energy*, 12:205–209, 2017. URL https://linkinghub.elsevier.com/retrieve/pii/S2352179116300771.

[194] Max Planck Institute for Plasma Physics. Introduction: The ASDEX Upgrade tokamak, . URL https://www.ipp.mpg.de/16208/einfuehrung.

[195] C. Angioni, E. Fable, M. Greenwald, et al. Particle transport in tokamak plasmas, theory and experiment. *Plasma Physics and Controlled Fusion*, 51(12):124017, 2009. URL https://iopscience.iop.org/article/10.1088/0741-3335/51/12/124017.

[196] R. Prater. Heating and current drive by electron cyclotron waves. *Physics of Plasmas*, 11 (5):2349–2376, 2004. URL http://aip.scitation.org/doi/10.1063/1.1690762.

[197] Martin Schubert, Jörg Stober, Albrecht Herrmann, et al. Extension of electron cyclotron heating at ASDEX Upgrade with respect to high density operation. *EPJ Web of Conferences*, 157:03047, 2017. URL http://www.epj-conferences.org/10.1051/epjconf/201715703047.

[198] D. Wagner, J. Stober, M. Kircher, et al. The Multi-Frequency ECRH System at ASDEX Upgrade - Current Status and Plans -. In *2018 43rd International Conference on Infrared, Millimeter, and Terahertz Waves (IRMMW-THz)*, volume 2018-Septe, pages 1–2. IEEE, 2018. URL http://ieeexplore.ieee.org/document/5612556/.

[199] J Stober, M Reisner, C Angioni, et al. Exploring fusion-reactor physics with high-power electron cyclotron resonance heating on ASDEX Upgrade. *Plasma Physics and Controlled Fusion*, 62(2):024012, 2020. URL https://iopscience.iop.org/article/10.1088/1361-6587/ab512b.

[200] E. Poli, A. Bock, M. Lochbrunner, et al. TORBEAM 2.0, a paraxial beam tracing code for electron-cyclotron beams in fusion plasmas for extended physics applications. *Computer Physics Communications*, 225:36–46, 2018. URL https://doi.org/10.1016/j.cpc.2017.12.018https://linkinghub.elsevier.com/retrieve/pii/S001046551730423X.

[201] Albrecht Stäbler, Jörg Hobirk, Fritz Leuterer, Fernando Meo, and Jean-Marie Noterdaeme. Chapter 13: Current Drive in ASDEX Upgrade. *Fusion Science and Technology*, 44(3):730–742, 2003. URL https://www.tandfonline.com/doi/full/10.13182/FST03-A411.

[202] H. Höhnle, J. Stober, A. Herrmann, et al. Extension of the ECRH operational space with O2 and X3 heating schemes to control tungsten accumulation in ASDEX Upgrade. *Nuclear Fusion*, 51(8):083013, 2011. URL https://iopscience.iop.org/article/10.1088/0029-5515/51/8/083013.

[203] Martin Schubert, Burkhard Plaum, Jörg Stober, et al. Beam tracing study for design and operation of two-pass electron cyclotron heating at ASDEX Upgrade. *EPJ Web of Conferences*, 203:02009, 2019. URL https://www.epj-conferences.org/10.1051/epjconf/201920302009.

[204] M. Schubert, F. Honecker, F. Monaco, et al. Monitoring millimeter wave stray radiation during ECRH operation at ASDEX Upgrade. *EPJ Web of Conferences*, 32:02013, 2012. URL http://www.epj-conferences.org/10.1051/epjconf/20123202013.

[205] Martin Schubert, Albrecht Herrmann, Francesco Monaco, et al. Machine safety issues with respect to the extension of ECRH systems at ASDEX Upgrade. *EPJ Web of Conferences*, 87:02010, 2015. URL http://www.epj-conferences.org/10.1051/epjconf/20158702010.

[206] O. Kudlacek, W. Treutterer, F. Janky, B. Sieglin, and M. Maraschek. Actuator management development on ASDEX-Upgrade. *Fusion Engineering and Design*, 146:1145–1148, 2019. URL https://linkinghub.elsevier.com/retrieve/pii/S0920379619302017.

[207] D. Stork. Neutral beam heating and current drive systems. *Fusion Engineering and Design*, 14(1-2):111–133, 1991. URL https://linkinghub.elsevier.com/retrieve/pii/092037969190238L.

[208] Mitsuru Kikuchi. The large tokamak JT-60: a history of the fight to achieve the Japanese fusion research mission. *The European Physical Journal H*, 43(4-5):551–577, 2018. URL http://link.springer.com/10.1140/epjh/e2018-90054-2.

[209] A. STÄBLER, J.-H. FEIST, E. SPETH, et al. DESIGN OF THE NEUTRAL BEAM INJECTION SYSTEM FOR ASDEX-UPGRADE. In *Fusion Technology 1988*, pages 620–624. Elsevier, 1989. URL https://linkinghub.elsevier.com/retrieve/pii/B9780444873699500962.

[210] A. Stäbler, O. Vollmer, J.H. Feist, et al. PERFORMANCE OF THE FIRST ASDEX UPGRADE NEUTRAL BEAM INJECTOR. In *Fusion Technology 1994*, pages 593–596. Elsevier, 1995. URL https://linkinghub.elsevier.com/retrieve/pii/B9780444822208501163.

[211] A. Kallenbach, M. Bernert, M. Beurskens, et al. Partial detachment of high power discharges in ASDEX Upgrade. *Nuclear Fusion*, 55(5):053026, 2015. URL https://iopscience.iop.org/article/10.1088/0029-5515/55/5/053026.

[212] E. Viezzer, T. Pütterich, R. Dux, and R. M. McDermott. High-resolution charge exchange measurements at ASDEX Upgrade. *Review of Scientific Instruments*, 83(10):103501, 2012. URL http://aip.scitation.org/doi/10.1063/1.4755810.

[213] M. Cavedon, T. Pütterich, E. Viezzer, et al. A fast edge charge exchange recombination spectroscopy system at the ASDEX Upgrade tokamak. *Review of Scientific Instruments*, 88(4):043103, 2017. URL http://dx.doi.org/10.1063/1.4979801.

[214] R. M. McDermott, A. Lebschy, B. Geiger, et al. Extensions to the charge exchange recombination spectroscopy diagnostic suite at ASDEX Upgrade. *Review of Scientific Instruments*, 88(7):073508, 2017. URL http://dx.doi.org/10.1063/1.4993131.

[215] E. Viezzer, R. Dux, and M. G. Dunne. A new beam emission polarimetry diagnostic for measuring the magnetic field line angle at the plasma edge of ASDEX Upgrade. *Review of Scientific Instruments*, 87(11):11E528, 2016. URL http://dx.doi.org/10.1063/1.4959952.

[216] D. G. Swanson. Radio frequency heating in the ion-cyclotron range of frequencies. *Physics of Fluids*, 28(9):2645–2677, 1985. URL https://aip.scitation.org/doi/10.1063/1.865224.

[217] Vl Bobkov, F. Braun, R. Dux, et al. Operation of ICRF antennas in a full tungsten environment in ASDEX Upgrade. *Journal of Nuclear Materials*, 390-391(1):900–903, 2009. URL http://dx.doi.org/10.1016/j.jnucmat.2009.01.231.

[218] V. Bobkov, F. Braun, R. Dux, et al. First results with 3-strap ICRF antennas in ASDEX Upgrade. *Nuclear Fusion*, 56(8):084001, 2016. URL https://iopscience.iop.org/article/10.1088/0029-5515/56/8/084001.

[219] V. Bobkov, M. Balden, R. Bilato, et al. ICRF operation with improved antennas in ASDEX Upgrade with W wall. *Nuclear Fusion*, 53(9):093018, 2013. URL https://iopscience.iop.org/article/10.1088/0029-5515/53/9/093018.

[220] I. H. Hutchinson. *Principles of Plasma Diagnostics*. Cambridge University Press, second edition, 2002. URL http://ebooks.cambridge.org/ref/id/CBO9780511613630.

[221] Sílvia Cristina da Graça Ramos. *MHD and fast particle mode studies using fast frequency hopping reflectometers on the ASDEX Upgrade tokamak*. PhD thesis, Instituto Superior Técnico, 2009.

[222] A. Mlynek, G. Schramm, H. Eixenberger, et al. Design of a digital multiradian phase detector and its application in fusion plasma interferometry. *Review of Scientific Instruments*, 81(3):033507, 2010. URL http://scitation.aip.org/content/aip/journal/rsi/81/3/10.1063/1.3340944.

[223] A. Mlynek, L. Casali, O. Ford, and H. Eixenberger. Fringe jump analysis and implementation of polarimetry on the ASDEX Upgrade DCN interferometer. *Review of Scientific Instruments*, 85(11):11D408, 2014. URL http://dx.doi.org/10.1063/1.4890574.

[224] Luís Manuel Rodrigues Guimarãis. *Poloidal asymmetries at the ASDEX Upgrade Tokamak*. PhD thesis, Instituto Superior Técnico, Universidade de Lisboa, 2018.

[225] M E Manso. Reflectometry in fusion devices. *Plasma Physics and Controlled Fusion*, 35 (SB):B141–B155, 1993. URL https://iopscience.iop.org/article/10.1088/0741-3335/35/SB/011.

[226] E Mazzucato. Microwave reflectometry for magnetically confined plasmas. *Review of Scientific Instruments*, 69(6):2201, 1998. URL http://scitation.aip.org/content/aip/journal/rsi/69/6/10.1063/1.1149121.

[227] A. Silva, M E Manso, L Cupido, et al. Ultrafast broadband frequency modulation of a continuous wave reflectometry system to measure density profiles on ASDEX Upgrade. *Review of Scientific Instruments*, 67(12):4138–4145, 1996. URL http://scitation.aip.org/content/aip/journal/rsi/67/12/10.1063/1.1147517.

[228] M Manso, F Serra, B Kurzan, et al. H-mode studies with microwave reflectometry on ASDEX Upgrade. *Plasma Physics and Controlled Fusion*, 40(5):747–752, 1998. URL https://iopscience.iop.org/article/10.1088/0741-3335/40/5/036.

[229] F. Simonet. Measurement of electron density profile by microwave reflectometry on tokamaks. *Review of Scientific Instruments*, 56(5):664, 1985. URL http://scitation.aip.org/content/aip/journal/rsi/56/5/10.1063/1.1138200.

[230] P Varela, M.E Manso, A Silva, the CFN Team, and the Asdex Upgrade Team. Review of data processing techniques for density profile evaluation from broadband FM-CW reflectometry on ASDEX Upgrade. *Nuclear Fusion*, 46(9):S693–S707, 2006. URL http://stacks.iop.org/0029-5515/46/i=9/a=S05?key=crossref.ad84a6a5a6b1a3760bec0a26fddc76db.

[231] A. Silva, P. Varela, L. Meneses, and M. Manso. Novel mono-static arrangement of the ASDEX Upgrade high field side reflectometers compatible with electron cyclotron resonance heating stray radiation. *Review of Scientific Instruments*, 83(10):10E317, 2012. URL http://aip.scitation.org/doi/10.1063/1.4732804.

[232] R. Nazikian and E. Mazzucato. Reflectometer measurements of density fluctuations in tokamak plasmas (invited). *Review of Scientific Instruments*, 66(1):392, 1995. URL http://scitation.aip.org/content/aip/journal/rsi/66/1/10.1063/1.1146357.

[233] R. Nazikian, G. J. Kramer, and E. Valeo. A tutorial on the basic principles of microwave reflectometry applied to fluctuation measurements in fusion plasmas. *Physics of Plasmas*, 8(5):1840, 2001. URL http://scitation.aip.org/content/aip/journal/pop/8/5/10.1063/1.1362534.

[234] L. Cupido, J. Sánchez, and T. Estrada. Frequency hopping millimeter wave reflectometer. *Review of Scientific Instruments*, 75(10):3865–3867, 2004. URL http://scitation.aip.org/content/aip/journal/rsi/75/10/10.1063/1.1788834.

[235] L. Cupido, S. Graca, G. D. Conway, et al. Frequency hopping millimeter-wave reflectometry in ASDEX upgrade. *Review of Scientific Instruments*, 77(10):10E915, 2006. URL http://scitation.aip.org/content/aip/journal/rsi/77/10/10.1063/1.2235206.

[236] D. Prisiazhniuk, A Krämer-Flecken, G. D. Conway, et al. Magnetic field pitch angle and perpendicular velocity measurements from multi-point time-delay estimation of poloidal correlation reflectometry. *Plasma Physics and Controlled Fusion*, 59(2):025013, 2017. URL https://iopscience.iop.org/article/10.1088/1361-6587/59/2/025013.

[237] H J Hartfuss, T Geist, and M Hirsch. Heterodyne methods in millimetre wave plasma diagnostics with applications to ECE, interferometry and reflectometry. *Plasma Physics and Controlled Fusion*, 39(11):1693–1769, 1997. URL https://iopscience.iop.org/article/10.1088/0741-3335/39/11/001.

[238] D Prisiazhniuk, G D Conway, A Krämer-Flecken, and U Stroth. Density fluctuation correlation measurements in ASDEX Upgrade using poloidal and radial correlation reflectometry. *Plasma Physics and Controlled Fusion*, 60(7):075003, 2018. URL http://stacks.iop.org/0741-3335/60/i=7/a=079602?key=crossref.cff95a7b6f3af432b9d9cf48a1fa7a99.

[239] K. McCormick, S. Fiedler, G. Kocsis, J. Schweinzer, and S. Zoletnik. Edge density measurements with a fast Li beam probe in tokamak and stellarator experiments. *Fusion Engineering and Design*, 34-35:125–134, 1997. URL https://linkinghub.elsevier.com/retrieve/pii/S0920379696006850.

[240] M. Willensdorfer, G. Birkenmeier, R. Fischer, et al. Characterization of the Li-BES at ASDEX Upgrade. *Plasma Physics and Controlled Fusion*, 56(2):025008, 2014. URL https://iopscience.iop.org/article/10.1088/0741-3335/56/2/025008.

[241] M. Willensdorfer, E. Wolfrum, R. Fischer, et al. Improved chopping of a lithium beam for plasma edge diagnostic at ASDEX Upgrade. *Review of Scientific Instruments*, 83(2): 023501, 2012. URL http://aip.scitation.org/doi/10.1063/1.3682003.

[242] Dustin H. Froula, Siegfried H. Glenzer, Neville C. Luhmann, and John Sheffield. *Plasma Scattering of Electromagnetic Radiation*. Elsevier, 2011. URL http://linkinghub.elsevier.com/retrieve/pii/B9780123748775000014.

[243] H. Murmann, S. Götsch, H. Röhr, H. Salzmann, and K. H. Steuer. The Thomson scattering systems of the ASDEX upgrade tokamak. *Review of Scientific Instruments*, 63(10):4941, 1992. URL http://scitation.aip.org/content/aip/journal/rsi/63/10/10.1063/1.1143504.

[244] B. Kurzan and H. D. Murmann. Edge and core Thomson scattering systems and their calibration on the ASDEX Upgrade tokamak. *Review of Scientific Instruments*, 82(10): 103501, 2011. URL http://aip.scitation.org/doi/10.1063/1.3643771.

[245] S. K. Rathgeber, L. Barrera, T. Eich, et al. Estimation of edge electron temperature profiles via forward modelling of the electron cyclotron radiation transport at ASDEX Upgrade. *Plasma Physics and Controlled Fusion*, 55(2):025004, 2013. URL https://iopscience.iop.org/article/10.1088/0741-3335/55/2/025004.

[246] R. Fischer, C. J. Fuchs, B. Kurzan, et al. Integrated Data Analysis of Profile Diagnostics at ASDEX Upgrade. *Fusion Science and Technology*, 58(2):675–684, 2010. URL http://epubs.ans.org/?a=10892.

[247] R. C. Isler. A Review of Charge-Exchange Spectroscopy and Applications to Fusion Plasmas. *Physica Scripta*, 35(5):650–661, 1987. URL https://iopscience.iop.org/article/10.1088/0031-8949/35/5/007.

[248] R. C. Isler. An overview of charge-exchange spectroscopy as a plasma diagnostic. *Plasma Physics and Controlled Fusion*, 36(2):171–208, 1994. URL https://iopscience.iop.org/article/10.1088/0741-3335/36/2/001.

[249] R. M. McDermott, R. Dux, T. Pütterich, et al. Evaluation of impurity densities from charge exchange recombination spectroscopy measurements at ASDEX Upgrade. *Plasma Physics and Controlled Fusion*, 60(9):095007, 2018. URL https://iopscience.iop.org/article/10.1088/1361-6587/aad256.

[250] S. K. Rathgeber, R. Fischer, S. Fietz, et al. Estimation of profiles of the effective ion charge at ASDEX Upgrade with Integrated Data Analysis. *Plasma Physics and Controlled Fusion*, 52(9):095008, 2010. URL https://iopscience.iop.org/article/10.1088/0741-3335/52/9/095008.

[251] R. Fischer, K. M. Hanson, V. Dose, and W. von der Linden. Background estimation in experimental spectra. *Physical Review E*, 61(2):1152–1160, 2000. URL https://link.aps.org/doi/10.1103/PhysRevE.61.1152.

[252] Ralph Dux, Marco Cavedon, Arne Kallenbach, et al. Influence of CX-reactions on the radiation in the pedestal region at ASDEX Upgrade. *Nuclear Fusion*, 60(12):126039, 2020. URL https://iopscience.iop.org/article/10.1088/1741-4326/abb748.

[253] T. Pütterich, R. Neu, R. Dux, A. D. Whiteford, and M. G. O'Mullane. Modelling of measured tungsten spectra from ASDEX Upgrade and predictions for ITER. *Plasma Physics and Controlled Fusion*, 50(8):085016, 2008. URL https://iopscience.iop.org/article/10.1088/0741-3335/50/8/085016.

[254] T. Odstrčil, T. Pütterich, M. Odstrčil, et al. Optimized tomography methods for plasma emissivity reconstruction at the ASDEX Upgrade tokamak. *Review of Scientific Instruments*, 87(12):123505, 2016. URL http://dx.doi.org/10.1063/1.4971367.

[255] M. Brusati, J.P. Christiansen, J.G. Cordey, et al. Analysis of magnetic measurements in tokamaks. *Computer Physics Reports*, 1(7-8):345–372, 1984. URL https://linkinghub.elsevier.com/retrieve/pii/0167797784900091.

[256] E. J. Strait, E. D. Fredrickson, J.-M. Moret, and M. Takechi. Chapter 2: Magnetic Diagnostics. *Fusion Science and Technology*, 53(2):304–334, 2008. URL https://www.tandfonline.com/doi/full/10.13182/FST08-A1674.

[257] W. Schneider, P.J McCarthy, K. Lackner, et al. ASDEX upgrade MHD equilibria reconstruction on distributed workstations. *Fusion Engineering and Design*, 48(1-2):127–134, 2000. URL https://linkinghub.elsevier.com/retrieve/pii/S0920379600001095.

[258] R. Fischer, A. Bock, M. Dunne, et al. Coupling of the Flux Diffusion Equation with the Equilibrium Reconstruction at ASDEX Upgrade. *Fusion Science and Technology*, 69(2):526–536, 2016. URL https://www.tandfonline.com/doi/full/10.13182/FST15-185.

[259] Felician Mink, Elisabeth Wolfrum, Marc Maraschek, et al. Toroidal mode number determination of ELM associated phenomena on ASDEX Upgrade. *Plasma Physics and Controlled Fusion*, 58(12):125013, 2016. URL http://stacks.iop.org/0741-3335/58/i=12/a=125013?key=crossref.c85dabfb71712cc67d14b5af1550c3eb.

[260] L. Giannone, D. Queen, F. Hellman, and J. C. Fuchs. Prototype of a radiation hard resistive bolometer for ITER. *Plasma Physics and Controlled Fusion*, 47(12):2123–2143, 2005. URL https://iopscience.iop.org/article/10.1088/0741-3335/47/12/004.

[261] H. Meister, T. Eich, N. Endstrasser, et al. Optimization of a bolometer detector for ITER based on Pt absorber on SiN membrane. *Review of Scientific Instruments*, 81(10):10E132, 2010. URL http://aip.scitation.org/doi/10.1063/1.3499637.

[262] M. Bernert, T. Eich, A. Burckhart, et al. Application of AXUV diode detectors at ASDEX Upgrade. *Review of Scientific Instruments*, 85(3):033503, 2014. URL http://aip.scitation.org/doi/10.1063/1.4867662.

[263] A. Kallenbach, A. Carlson, G. Pautasso, et al. Electric currents in the scrape-off layer in ASDEX Upgrade. *Journal of Nuclear Materials*, 290-293:639–643, 2001. URL https://linkinghub.elsevier.com/retrieve/pii/S0022311500004451.

[264] A. Kallenbach, R. Dux, J. C. Fuchs, et al. Divertor power load feedback with nitrogen seeding in ASDEX Upgrade. *Plasma Physics and Controlled Fusion*, 52(5):055002, 2010. URL https://iopscience.iop.org/article/10.1088/0741-3335/52/5/055002.

[265] G. F. Matthews. Tokamak plasma diagnosis by electrical probes. *Plasma Physics and Controlled Fusion*, 36(10):1595–1628, 1994. URL https://iopscience.iop.org/article/10.1088/0741-3335/36/10/002.

[266] M Weinlich and A. Carlson. Flush mounted probes in ASDEX Upgrade - Can they be operated as triple probes? *Contributions to Plasma Physics*, 36(S1):53–59, 1996. URL http://doi.wiley.com/10.1002/ctpp.19960360109.

[267] B. Sieglin, M. Faitsch, A. Herrmann, et al. Real time capable infrared thermography for ASDEX Upgrade. *Review of Scientific Instruments*, 86(11):113502, 2015. URL http://dx.doi.org/10.1063/1.4935580.

[268] A. Herrmann, W. Junker, K. Gunther, et al. Energy flux to the ASDEX-Upgrade diverter plates determined by thermography and calorimetry. *Plasma Physics and Controlled Fusion*, 37(1):17–29, 1995. URL https://iopscience.iop.org/article/10.1088/0741-3335/37/1/002.

[269] S. Potzel, R. Dux, H. W. Müller, A. Scarabosio, and M. Wischmeier. Electron density determination in the divertor volume of ASDEX Upgrade via Stark broadening of the Balmer lines. *Plasma Physics and Controlled Fusion*, 56(2):025010, 2014. URL https://iopscience.iop.org/article/10.1088/0741-3335/56/2/025010.

[270] S.S. Henderson, M. Bernert, S. Brezinsek, et al. Determination of volumetric plasma parameters from spectroscopic N II and N III line ratio measurements in the ASDEX Upgrade divertor. *Nuclear Fusion*, 58(1):016047, 2018. URL https://iopscience.iop.org/article/10.1088/1741-4326/aa96be.

[271] S.S. Henderson, M. Bernert, S. Brezinsek, et al. An assessment of nitrogen concentrations from spectroscopic measurements in the JET and ASDEX upgrade divertor. *Nuclear Materials and Energy*, 18(December 2018):147–152, 2019. URL https://doi.org/10.1016/j.nme.2018.12.012.

[272] L. Gil, C. Silva, T Happel, et al. Stationary ELM-free H-mode in ASDEX Upgrade. *Nuclear Fusion*, 60(5):054003, 2020. URL https://iopscience.iop.org/article/10.1088/1741-4326/ab7d1b.

[273] F. Ryter, S.K. Rathgeber, L. Barrera Orte, et al. Survey of the H-mode power threshold and transition physics studies in ASDEX Upgrade. *Nuclear Fusion*, 53(11):113003, 2013. URL http://iopscience.iop.org/0029-5515/53/11/113003/article/{%}5Cnhttp://stacks.iop.org/0029-5515/53/i=11/a=113003?key=crossref.c8c733cd8b06749ba4388dc37003934d.

[274] E.J. Doyle (Chair Transport Physics), W.A. Houlberg (Chair Confinement Da Modelling), , et al. Chapter 2: Plasma confinement and transport. *Nuclear Fusion*, 47(6):S18–S127, 2007. URL https://iopscience.iop.org/article/10.1088/0029-5515/47/6/S02.

[275] P. C. Stangeby. *The Plasma Boundary of Magnetic Fusion Devices*. Institute of Physics Publishing, 2000.

[276] J. Neuhauser, D. Coster, H. U. Fahrbach, et al. Transport into and across the scrape-off layer in the ASDEX Upgrade divertor tokamak. *Plasma Physics and Controlled Fusion*, 44 (6):855–869, 2002. URL https://iopscience.iop.org/article/10.1088/0741-3335/44/6/316.

[277] C. Angioni, R.M. McDermott, E. Fable, et al. Gyrokinetic modelling of electron and boron density profiles of H-mode plasmas in ASDEX Upgrade. *Nuclear Fusion*, 51 (2):023006, 2011. URL http://stacks.iop.org/0029-5515/51/i=2/a=023006?key=crossref.aa3d37c129c0fed41cb1f9fc1b90580b.

[278] Clément Gallet and Claude Julien. The significance threshold for coherence when using the Welch's periodogram method: Effect of overlapping segments. *Biomedical Signal Processing and Control*, 6(4):405–409, 2011. URL http://linkinghub.elsevier.com/retrieve/pii/S1746809410000881.

[279] P. Welch. The use of fast Fourier transform for the estimation of power spectra: A method based on time averaging over short, modified periodograms. *IEEE Transactions on Audio and Electroacoustics*, 15(2):70–73, 1967. URL http://ieeexplore.ieee.org/document/1161901/.

[280] A Medvedeva, C Bottereau, F Clairet, et al. High frequency edge coherent modes studied with the ultra-fast swept reflectometer on ASDEX Upgrade. *Plasma Physics and Controlled Fusion*, 61(8):085011, 2019. URL https://iopscience.iop.org/article/10.1088/1361-6587/ab2575.

[281] M. Griener, J M Muñoz Burgos, M Cavedon, et al. Qualification and implementation of line ratio spectroscopy on helium as plasma edge diagnostic at ASDEX Upgrade. *Plasma Physics and Controlled Fusion*, 60(2):025008, 2018. URL https://iopscience.iop.org/article/10.1088/1361-6587/aa97e8.

[282] M. Griener, E. Wolfrum, M. Cavedon, et al. Helium line ratio spectroscopy for high spatiotemporal resolution plasma edge profile measurements at ASDEX Upgrade (invited). *Review of Scientific Instruments*, 89(10):10D102, 2018. URL http://dx.doi.org/10.1063/1.5034446.

[283] A. Silva, L. Cupido, M. Manso, et al. Microwave reflectometry diagnostic for density profile and fluctuation measurements on ASDEX Upgrade. *Review of Scientific Instruments*, 70(1):1072–1075, 1999. URL http://aip.scitation.org/doi/10.1063/1.1149439.

[284] S. Potzel, M. Wischmeier, M. Bernert, et al. Formation of the high density front in the inner far SOL at ASDEX Upgrade and JET. *Journal of Nuclear Materials*, 463:541–545, 2015. URL http://dx.doi.org/10.1016/j.jnucmat.2014.12.008.

[285] L. Guimarais, S. Potzel, C. Silva, et al. Poloidal asymmetries in the edge density profiles on ASDEX Upgrade. *Nuclear Fusion*, 58(2):026005, 2018. URL http://stacks.iop.org/0029-5515/58/i=2/a=026005?key=crossref.6dd7ad0cd57434747aaddebed381730f.

[286] G. Birkenmeier, J. Galdon-Quiroga, V. Olevskaia, et al. Beam modelling and hardware design of an imaging heavy ion beam probe for ASDEX Upgrade. *Journal of Instrumentation*, 14(10):C10030–C10030, 2019. URL https://iopscience.iop.org/article/10.1088/1748-0221/14/10/C10030.

[287] J A Snipes, R S Granetz, M Greenwald, et al. ELMs and fast edge fluctuations in Alcator C-Mod. *Plasma Physics and Controlled Fusion*, 40(5):765–770, 1998. URL http://stacks.iop.org/0741-3335/40/i=5/a=039?key=crossref.b7ea54672a9cd41506a1d346c7fc6612.

[288] S. Coda, M. Agostini, R. Albanese, et al. Physics research on the TCV tokamak facility: from conventional to alternative scenarios and beyond. *Nuclear Fusion*, 59(11):112023, 2019. URL https://iopscience.iop.org/article/10.1088/1741-4326/ab25cb.

[289] M. G. Dunne, L. Frassinetti, M N A Beurskens, et al. Global performance enhancements via pedestal optimisation on ASDEX Upgrade. *Plasma Physics and Controlled Fusion*, 59(2):025010, 2017. URL https://iopscience.iop.org/article/10.1088/1361-6587/59/2/025010.

[290] A. Kallenbach, M. Bernert, R. Dux, et al. Impurity seeding for tokamak power exhaust: from present devices via ITER to DEMO. *Plasma Physics and Controlled Fusion*, 55(12):124041, 2013. URL https://iopscience.iop.org/article/10.1088/0741-3335/55/12/124041.

[291] F. Reimold, M. Wischmeier, M. Bernert, et al. Divertor studies in nitrogen induced completely detached H-modes in full tungsten ASDEX Upgrade. *Nuclear Fusion*, 55(3):033004, 2015. URL https://iopscience.iop.org/article/10.1088/0029-5515/55/3/033004.

[292] N. Asakura, K. Hoshino, S. Suzuki, et al. Studies of power exhaust and divertor design for a 1.5 GW-level fusion power DEMO. *Nuclear Fusion*, 57(12):126050, 2017. URL https://iopscience.iop.org/article/10.1088/1741-4326/aa867a.

[293] A. Kallenbach, M. Bernert, R. Dux, F. Reimold, and M. Wischmeier. Analytical calculations for impurity seeded partially detached divertor conditions. *Plasma Physics and Controlled Fusion*, 58(4):045013, 2016. URL https://iopscience.iop.org/article/10.1088/0741-3335/58/4/045013.

[294] Arne Kallenbach, Matthias Bernert, Pierre David, et al. Developments towards an ELM-free pedestal radiative cooling scenario using noble gas seeding in ASDEX Upgrade. *Nuclear Fusion*, 2021. URL https://iopscience.iop.org/article/10.1088/1741-4326/abbba0.

[295] A. Drenik, L. Laguardia, R. McDermott, et al. Evolution of nitrogen concentration and ammonia production in N 2 -seeded H-mode discharges at ASDEX Upgrade. *Nuclear Fusion*, 59(4):046010, 2019. URL https://iopscience.iop.org/article/10.1088/1741-4326/aafe23.

[296] T. Pütterich, E. Wolfrum, R. Dux, and C. F. Maggi. Evidence for Strong Inversed Shear of Toroidal Rotation at the Edge-Transport Barrier in the ASDEX Upgrade. *Physical Review Letters*, 102(2):025001, 2009. URL https://link.aps.org/doi/10.1103/PhysRevLett.102.025001.

[297] M. Cavedon, G. Birkenmeier, T. Pütterich, et al. Connecting the global H-mode power threshold to the local radial electric field at ASDEX Upgrade. *Nuclear Fusion*, 60(6):066026, 2020. URL https://iopscience.iop.org/article/10.1088/1741-4326/ab8777.

[298] E. Viezzer, T. Pütterich, C. Angioni, et al. Evidence for the neoclassical nature of the radial electric field in the edge transport barrier of ASDEX Upgrade. *Nuclear Fusion*, 54(1):012003, 2014. URL https://iopscience.iop.org/article/10.1088/0029-5515/54/1/012003.

[299] F. Jenko, W. Dorland, M. Kotschenreuther, and B. N. Rogers. Electron temperature gradient driven turbulence. *Physics of Plasmas*, 7(5):1904–1910, 2000. URL http://aip.scitation.org/doi/10.1063/1.874014.

[300] T. Görler, X. Lapillonne, S. Brunner, et al. The global version of the gyrokinetic turbulence code GENE. *Journal of Computational Physics*, 230(18):7053–7071, 2011. URL https://linkinghub.elsevier.com/retrieve/pii/S0021999111003457.

[301] J.W. Hughes, A. Loarte, M.L. Reinke, et al. Power requirements for superior H-mode confinement on Alcator C-Mod: experiments in support of ITER. *Nuclear Fusion*, 51

(8):083007, 2011. URL http://stacks.iop.org/0029-5515/51/i=8/a=083007?key=crossref.a0a798ac019a07c7ee405975cb50f77f.

[302] C.D. Challis, J. Garcia, M. Beurskens, et al. Improved confinement in JET high β plasmas with an ITER-like wall. *Nuclear Fusion*, 55(5):053031, 2015. URL https://iopscience.iop.org/article/10.1088/0029-5515/55/5/053031.

[303] G.T.A Huysmans and O. Czarny. MHD stability in X-point geometry: simulation of ELMs. *Nuclear Fusion*, 47(7):659–666, 2007. URL https://iopscience.iop.org/article/10.1088/0029-5515/47/7/016.

[304] Olivier Czarny and Guido Huysmans. Bézier surfaces and finite elements for MHD simulations. *Journal of Computational Physics*, 227(16):7423–7445, 2008. URL https://linkinghub.elsevier.com/retrieve/pii/S0021999108002118.

[305] E. Joffrin, S. Abduallev, M. Abhangi, et al. Overview of the JET preparation for deuterium–tritium operation with the ITER like-wall. *Nuclear Fusion*, 59(11):112021, 2019. URL https://iopscience.iop.org/article/10.1088/1741-4326/ab2276.

[306] H. Shirai, P. Barabaschi, and Y. Kamada. Recent progress of the JT-60SA project. *Nuclear Fusion*, 57(10):102002, 2017. URL https://iopscience.iop.org/article/10.1088/1741-4326/aa5d01.

[307] G. Giruzzi, M. Yoshida, N. Aiba, et al. Advances in the physics studies for the JT-60SA tokamak exploitation and research plan. *Plasma Physics and Controlled Fusion*, 62(1):014009, 2020. URL https://iopscience.iop.org/article/10.1088/1361-6587/ab4771.

[308] G. Zhuang, G.Q. Li, J. Li, et al. Progress of the CFETR design. *Nuclear Fusion*, 59(11):112010, 2019. URL https://iopscience.iop.org/article/10.1088/1741-4326/ab0e27.

[309] B. LaBombard, J.L. Terry, J.W. Hughes, et al. Divertor heat flux footprints in EDA H-mode discharges on Alcator C-Mod. *Journal of Nuclear Materials*, 415(1):S349–S352, 2011. URL http://dx.doi.org/10.1016/j.jnucmat.2010.07.021.

[310] E.A. Tolman, J.W. Hughes, S.M. Wolfe, et al. Influence of high magnetic field on access to stationary H-modes and pedestal characteristics in Alcator C-Mod. *Nuclear Fusion*, 58(4):046004, 2018. URL http://stacks.iop.org/0029-5515/58/i=4/a=046004?key=crossref.2c832c0b451650de97f6746e794409ac.

[311] M N A Beurskens, J. Schweinzer, C. Angioni, et al. The effect of a metal wall on confinement in JET and ASDEX Upgrade. *Plasma Physics and Controlled Fusion*, 55(12): 124043, 2013. URL https://iopscience.iop.org/article/10.1088/0741-3335/55/12/124043.